NUMERICAL MODELING OF SEISMIC WAVE PROPAGATION IN UNDERGROUND MINES

by

Xin Wang

A thesis submitted in partial fulfillment
of the requirements for the degree of
Doctor of Philosophy (PhD) in Natural Resources Engineering

The Faculty of Graduate Studies
Laurentian University
Sudbury, Ontario, Canada

THESIS DEFENCE COMMITTEE/COMITÉ DE SOUTENANCE DE THÈSE
Laurentian Université/Université Laurentienne
Faculty of Graduate Studies/Faculté des études supérieures

Title of Thesis Titre de la thèse	NUMERICAL MODELING OF SEISMIC WAVE PROPAGATION IN UNDERGROUND MINES
Name of Candidate Nom du candidat	Wang, Xin
Degree Diplôme	Doctor of Philosophy
Department/Program Département/Programme	Natural Resources Engineering
Date of Defence Date de la soutenance	November 04, 2015

APPROVED/APPROUVÉ

Thesis Examiners/Examinateurs de thèse:

Dr. Ming Cai
(Supervisor/Directeur(trice) de thèse)

Dr. Peter Kaiser
(Committee member/Membre du comité)

Dr. Marty Hudyma
(Committee member/Membre du comité)

Dr. Philip Dirige
(Committee member/Membre du comité)

Dr. Bernd Milkereit
(External Examiner/Examinateur externe)

Dr. Richard Smith
(Internal Examiner/Examinateur interne)

Approved for the Faculty of Graduate Studies
Approuvé pour la Faculté des études supérieures
Dr. David Lesbarrères
Monsieur David Lesbarrères
Acting Dean, Faculty of Graduate Studies
Doyen intérimaire, Faculté des études supérieures

ACCESSIBILITY CLAUSE AND PERMISSION TO USE

Abstract

The phenomenon of rockburst damage localization, which is not well understood, has been observed in deep underground mines. Analysis of seismic wave propagation in underground mines is of great interest for improved understanding of the dynamic rock failure problem. This thesis aims at making a contribution for improving understanding of the seismic wave propagation in deep underground mines. Advanced numerical modeling tools are used and new modeling techniques are developed to attain this goal.

In this thesis, research is emphasized on the ground motion around excavations due to seismic wave propagation that results from a fault-slip seismic event in the far-field and the near-field. It is found that moment tensor point source model seems to be suitable for the source representation in the far-field and the non-point source model (such as kinematic rupture source model) seems to be suitable for the source representation in the near-field. The modeling results confirm that ground motion is influenced by many factors such as target-source distance, slip direction, spatial location, and geometrical and geological conditions.

Influence of wavelength-to-excavation span (λ/D) ratio on the wavefield is investigated to gain insights of ground motion behavior under both quasi-static and dynamic loading conditions. It is revealed that PPV (peak particle velocity) values increase as the λ/D ratio increases and the amplification effect increases as the λ/D ratio decreases. The loading condition maybe changed from the dynamic loading to the quasi-static condition when the λ/D is larger than 30. Strong dynamic loading should be considered when the λ/D ratio is small (less than 10, with a shear

wavelength less than 50 m and an excavation span greater than 5 m) for most underground excavations.

A method is proposed to estimate the quality factor (a measure of energy loss per oscillation cycle) for shear waves propagating in underground hard rocks so as to gain insight into the influence of internal attenuation on seismic wave propagation. A proper shear wave quality factor can be obtained by comparing modeling results with that from a scaling law, even if there are no high quality data for quality factor back analysis. Furthermore, the influence of different geological structures on seismic wave propagation is studied. It is shown that wave propagation patterns around an excavation can be altered and PPV amplification and shielding effect can occur near the excavation boundaries amongst other reasons due to heterogeneities such as tunnels, open and backfilled stopes, and dykes in underground mines.

Finally, a coupled numerical procedure, which couples FLAC and SPECFEM2D, is developed to consider the excavation effect on ground motion. The FLAC model considers the excavation-induced stress change and rock mass failure, and passes the input data to SPECFEM2D by invoking FISH scripts. In addition, a new nonlinear velocity model that considers the influence of confinement and rock mass failure on wave velocity is presented. This nonlinear velocity model and the coupled numerical technique are used to model a simple stope excavation problem. It is found that there is a large difference in the wavefields and ground motions between the results from the uniform and non-uniform velocity models. A relatively stronger amplification is observed in the low confinement zones and on the excavation surface in the non-uniform velocity models. Because stress redistribution and rock mass failure around an excavation are considered, a realistic non-uniform velocity field can be obtained. The proposed coupled

numerical procedure offers a method to improve the understanding of the site amplification effect and ground motion near excavation boundaries.

This thesis presents some insights with regard to seismic wave propagation due to fault-slip seismic events in underground mines. If seismic wave propagation in underground mines can be modeled properly using techniques such as these presented in this thesis, then it is possible to conduct forensic analysis after a large seismic event so as to explain one of many factors that caused rockburst damage localization. Alternatively, the modeling approach may provide valuable inputs for decision-making with regard to strengthening high risk areas to prevent rockburst, thus improving mine safety.

Keywords

Rockburst Damage Localization, Numerical Simulation, Seismic Wave Propagation, Wavefield Simulation, Ground Motion, Non-uniform Velocity Model, Coupling, FLAC, SPECFEM2D/3D, PPV (Peak Particle Velocity), Rock Failure, Underground Mines.

Original Contributions

This thesis aims at making a contribution for improved understanding of seismic wave propagation in underground mines. Some challenging issues are addressed and new methods are developed in this thesis and the results are presented in respective chapters. Major contributions of the thesis are summarized and listed below.

1) Advocated using the SPECFEM2D/3D tools to study wave propagation problems in underground mines and revealed the influence of different source parameters on ground motion around excavations (Chapter 2).
2) Ripened the understanding of ground motion and amplification effect under different wavelength-to-excavation span ratios (Chapter 4).
3) Developed a method to estimate the shear quality factor for hard rocks in underground mines through comparing PPV (Peak Particle Velocity) from a background scaling law with that from numerical modeling (Chapter 5).
4) Explored the combined influence of typical heterogeneities in underground mines (i.e., tunnels, open and backfilled stopes, and dykes) on wave propagation using SPECFEM2D, which was the first attempt in this field (Chapter 6).
5) Established a confinement and rock quality dependent nonlinear velocity model which can be used to capture ground motions around underground excavations better than the traditional uniform velocity model (Chapter 7).
6) Developed a new coupled numerical method for wavefield simulation considering the excavation effect that includes stress redistribution and rock failure. The coupling

between FLAC and SPECFEM2D is unique and is the first of its kind in the field (Chapter 7).

7) Enhanced the understanding of ground motions around excavations due to the interaction of seismic wave propagation with geological structures and excavations in underground mines. This work provides an alternative method for rockburst damage potential analysis. In the meantime, this work may be beneficial for improving mine safety in deep underground mines (Chapters 2 to 7).

Acknowledgements

It is my great pleasure to express my sincerest gratitude to all individuals and institutes that offered me the kind support during my PhD study at Laurentian University since Sept. 2012. I cherished the past three years with valuable experience which has shaped my thinking and my life. I would not able to come to this point and finish my study without the help and care from many people, including my dear supervisor, academic committing members, colleagues and officemates at MIRARCO, my parents and my wife, as well as my friends.

First and foremost, I would like to deeply thank my supervisor Prof. Ming Cai for his tremendous patience, eminently helpful guidance, and encouragement throughout my study at Laurentian University. I am very grateful to Dr. Cai for providing me the opportunity to study in Sudbury. His in-depth of knowledge in the field, research attitude and passion, distinct academic knack, and attention to details are impressive. During the past three years, I learned a lot from him and these would remain with me as a great treasure in the rest of my life. Whenever I encountered a challenging problem, he is always there, always gives me good advices, and always provides me confidence. I would like to thank him for training me to form a good research habit after the countless productive discussions, which really saved me a lot of time and many brain cells. I also want to thank his generosity for offering me the opportunity to attend academic workshops and conferences such as the SUMIT annual meetings in 2014 and 2015 and international conference of Deep Mining 2014 in Sudbury and ISRM 2015 in Montreal, which extend my view of research. In addition, I appreciate his thorough proof-reading and correcting my “Chinglish” academic writings, from the research proposal, the progress report, to this final thesis. Thank you so much for being such a wonderful mentor. I am so lucky!

I also wish to express my gratitude to the academic committee members for sharing with me your valuable knowledge, comments, and suggestions. I would like to express my thanks to Prof. Peter Kaiser, Prof. Marty Hudyma, and Prof. Philip Dirige. Thanks Dr. Kaiser for your enlightening short course at MIRARCO and valuable suggestions during my study. Thanks Dr. Hudyma for the course of mining seismicity and very useful comments and suggestions during my study. I am also grateful to Dr. Dirige for his insightful comments and helpful ideas. Appreciation is also extended to Prof. Dean Millar for his wonderful research method course and Prof. Ramesh Subramanian for his support and guidance. I am so grateful!

I want say thanks to the financial support provided by the Ontario Research Fund (through a project entitled "Smart Underground Monitoring and Integrated Technologies (SUMIT) for Deep Mining"), Vale, Rio Tinto, and Glencore. I am also indebted to Dr. Cai for helping me get an international student tuition fee waiver at Laurentian University, which helped me to focus on my study in this "small size" but "big content" famous mining university. I am so blessed!

Special thanks to MIRARCO – Innovation for providing the vivid academic atmosphere and the opportunity to know so many talented people working in a broad range of mining related projects. I am fortunate to be a member of GRC at MIRARCO. I am more than grateful for the great experience of collaborating with the following colleagues in Prof. Ming Cai's group: Nader Golchinfar, Christopher Groccia, Yuhang Xu, Amin Manouchehrian, Reza Noorani, and Subash Bastola, who provided many helps and invaluable inspiration in all the constructive group discussions. In the meantime, I want say thanks to friends in the GRC group: Sean Maloney, Salina Yong, Navid Bahrani, and Marta Rios, who assisted me in many aspects and provide the friendly environment. Moreover, many friends from MIRARCO, such as Kim Trapani, Vijay Kumar Sharma, Negar Saeidi, Alberto Romero, and Harvard Farrant, have made my academic

life colorful and joyful. In addition, the friendly contacts with Jun Peng and Songfeng Guo are very supportive to my work and thanks for all the helpful advices you gave before and after my oral exams. I am also indebted to Ms. Qin Liang for all the solicitude and help during the past years, which make everything so convenient and make me feel at home. Thank you for everything, like the valuable life advices, the fancy Chinese food, the unforgettable parties, etc. I will not forget all the beautiful things that came from your efforts. Many thanks to the friends I met at Laurentian University for the wonderful time, namely: Fangqiu Gu, Zhuo Chen, Yang Ge, Zhongming Dong, and Yongxin Li. I also want thank Haohua Ren, Zhengbao Lu, Fangjie Wang, Juan Yan, Lei Wang, Zhiheng Chen, Zhiqiang Zhao, Chengjian Wang, Longli Li, and Fan Zhang for your great friendship and support. All of you are thankfully acknowledged. I am so enjoyable!

Last but not least, I would like to express my cordially thank to my parents, Qinyu Wang and Xiuyun Hu, and my family in China for their life-long love and constant moral support during my PhD study. Their unselfish love has always provided me with great power for growing up and moving forward throughout my life. I am incredibly thankful for my wife, Jia Zheng, who sacrificed her nice job in Beijing and is accompanying me in Canada. My life becomes more colorful and meaningful during my studies since she came to Sudbury. Her endless love and understanding are important during my study time and in my life. I am so grateful!

I am indebted to the mentioned and non-mentioned individuals and institutions. Thanks a million!

Xin Wang
MIRARCO – Mining Innovation
Laurentian University
Sudbury, Canada, 25th July, 2015

Table of Contents

List of Tables

List of Figures

List of Symbols

ψ^{c}_{ijkl}	Fourth-order tensorial relaxation function
f_0	Corner frequency (Hz)
μ	Displacement field
$\boldsymbol{\sigma}(\mathbf{x})$	Stress tensor at position **x**
$\boldsymbol{\varepsilon}(\mathbf{x})$	Strain tensor at position **x**
$\mathbf{u}$	Displacement field
$\mathbf{C}$	4th order stiffness tensor
$\mathbf{f}$	External body force
Ω	Physical domain of the model
Γ	Model boundary
ΔE_v	Energy loss
$P_v^{\max}$	Peak energy density stored per cycle
ϕ_0^v	Constant complex quantity
k_v	Complex wave number
Q_μ	Shear modulus quality factor
Q_k	Bulk modulus quality factor
$\mathbf{k}_\mathbf{v}$ / $\boldsymbol{\alpha}_\mathbf{v}$	Real vectors indicate the direction / magnitude
μ^R / μ^I	Real / imaginary parts of displacement field
A	Rupture area (m^2)
a and C	Site specific constants for design scaling law
A_p	Peak amplitude of the recorded seismograms (mm)
c	Cohesion (MPa)
C_s / C_r	Correction factors for site / receiver
D	Excavation span (m)
d	Dislocation displacement (m)
D_s	Slip displacement over a fault surface (m)
E	Elastic or Young's modulus (GPa)
E_0	Minimum elastic modulus at the excavation boundary (GPa)
E_{max}	Elastic modulus of a rock mass in the in situ stress state (GPa)
f	Dominant frequency (Hz)
$\mathbf{F}$	External source term
F_c	Correction factor for amplitude variation
H	Overburden depth (m)
$H(t)$	Heaviside function
K	Site-specific constant
L_v	Number of relaxation mechanism
M	Complex moduli
$\mathbf{M}$	Diagonal mass matrix

M_0	Seismic moment (dyne·cm)
M_b	Body-wave magnitude
M_L	Local (or Richter) magnitude
M_N	Nuttli magnitude
M_s	Surface-wave magnitude
M_v	Elastic or relaxed modulus of the medium
M_w	Moment magnitude
P	Confining pressure (MPa)
P_c	Critical confining pressure (MPa)
Q	Quality factor
Q_c	Rock mass quality
Q_B	Rock mass quality index of Barton'system
Q_p	P-wave quality factor
Q_s	S-wave quality factor
r	Distance (m)
R_c	Critical distance that divides the velocity change profile
SH/SV, P	Shear waves in horizontal plane/vertical plane, P wave
T	Transmission coefficient
t	Time (s)
T_d	Dominant period for seismograms (s)
U	Ground displacement (m)
U_x / U_y / U_z	Displacements in the x / y / z directions
V	Velocity (m/s)
V_p / V_s	P-wave velocity / S-wave velocity (m/s)
V_x/ V_y/ V_z	Velocity components in the x / y / z directions
λ_c / μ_c	Complex Lamé constants
λ_L / μ_L	Lamé constants (scalar)
β	Dimensionless model constant for the nonlinear velocity model
α	Amplification factor
$\delta(t)$	Dirac's function
ε_{ps}	Plastic shear strain
ϕ_f	Friction angle (°)
ϕ_s / δ_d / γ_r	Strike / dip / rake (°) of a plane
ϕ_1	Spherical coordinate azimuth angle (°)
ϕ_2	Inclination angle (°)
ϕ_A	Azimuths (°)
λ	Wavelength (m)
μ_s	Shear rigidity (dyne/cm^2)
μ / κ	Shear modulus / bulk modulus
ν	Poisson's ratio
ρ	Density (kg/m^3)
σ_c	Uniaxial compressive strength (MPa)
σ_{ij} / ε_{kl}	Stress / strain tensors
σ_t	Tensile strength (MPa)
σ_1 / σ_2 / σ_3	The maximum/intermediate/minimum principal stress

$t^{v}_{\sigma l}$ /$t^{v}_{\varepsilon l}$	Material relaxation times for the l_{th} mechanism
ω	Angular frequency
ψ	Dilation angle (°)

Preface

This research work has been accomplished at MIRARCO – Mining Innovation and the Bharti School of Engineering, Laurentian University, under the supervision of Prof. Ming Cai, and under the financial support of the Ontario Research Fund (through a project entitled "Smart Underground Monitoring and Integrated Technologies (SUMIT) for Deep Mining"), Vale, Rio Tinto, and Glencore.

The results presented in Chapter 6 are published in the proceedings of the 7th International Seminar on Deep and High Stress Mining, Deep Mining 2014, which was organized by the Austrian Center for Geomechanics (ACG) and held in Sudbury, Canada (Wang and Cai, 2014). The study of Wavelength-to-Excavation-Span ratio on ground motions with results presented in Chapter 4 has been published in the journal of *Tunnelling and Underground Space Technology* (Wang and Cai, 2015). The nonlinear velocity models and part of the results of the coupled FLAC/SPECFEM2D numerical method presented in Chapter 7 are published in the proceedings of the 13th International ISRM Congress 2015, which is organized by the ISRM and held in Montreal, Canada (Cai and Wang, 2015). More comprehensive results that are obtained in Chapter 7 have been submitted for journal publication. The preliminary results presented in Chapters 5 and 6 will be prepared for publication in a journal.

Chapter 1

1 Introduction

1.1 Research background

As mining occurs increasingly at greater depths, rockburst is inevitable due to high in situ stress and complex geological and geometrical conditions in underground hard rock mines. Considerable progress has been made in understanding rockburst in underground mines since the 1980s (Cai, 2013b; Cai and Champaigne, 2009; Holub and Rusajova, 2011; Kaiser and Cai, 2013; Kaiser et al., 1996; Konicek et al., 2013; Lightfoot et al., 1996; Simser et al., 2002; Stacey and Ortlepp, 2000; Tannant et al., 1993; Wang et al., 2009); however, many burst-prone mines in Canada, China, Chile, Australia, South Africa, and some other countries are still facing the rockbursts. Rockbursts occasionally lead to severe damage to excavations and mining equipment, as well as injuries and fatalities (Heal et al., 2006; Kaiser and Cai, 2012; Ortlepp and Stacey, 1994; Potvin et al., 2000).

In general, rock support design in burst-prone mines needs to consider both static loading (e.g., rock mass weight, stress redistribution due to excavation) and dynamic loading (e.g., blast waves and seismic waves generated by induced seismic events). The static loading has been extensively investigated by many researchers (Cai, 2008a; Cai and Kaiser, 2005; Dou et al., 2012; Jing et al., 2002; Kontogianni and Stiros, 2005; Martin et al., 2003; Roth and Ranta-Korpi, 2007; Tajdus et al., 1997; Tang and Xia, 2010; Wang et al., 2010). Compared with research on static loading around excavation boundaries, analysis of seismic dynamic loading (seismic wave propagation from a remote seismic event) has been studied extensively but various complexities lead to much

greater uncertainties. Hence, an improved understanding of seismic wave propagation in a complex mining context is essential for a better understanding rockburst damage localization and for improved rock support design in burst-prone mines.

At present, the analysis of wave propagation is of great interest for solving engineering problems in a number of industries such as mining, civil, oil extraction, and nuclear waste disposal (Dubinski and Mutke, 1996, 2005; Goldstein, 1995; Hildyard et al., 2005a; Šílený and Milev, 2008; Triviño et al., 2012; Wright et al., 2003; Yoshimitsu et al., 2012). In the context of underground mines, both analytical and experimental methods are of limited use in solving seismic wave propagation problems due to complex geological, geometrical, and stress conditions in the mines. Hence, ground motion patterns near excavation in underground mines are currently not well understood. Fortunately, with the rapid advancement of computer technology and many powerful numerical techniques, numerical modeling is becoming an important and irreplaceable tool in investigating seismic wave propagation (Fichtner 2011; Hatherly, 2013; Komatitsch and Tromp, 1999; Komatitsch et al., 1999; Sato et al.; Triviño et al., 2012; Yoshimitsu et al., 2012).

1.2 Problem statement and research questions

Mining-induced seismicity and rockburst increase continually and cannot be prevented as mining progresses to deeper levels. It is often observed that after a large seismic event, damage is often localized. In other words, the damage extent along a tunnel varies for the same seismic event. Damage does not necessarily occur only at locations nearest the seismic source. It has been reported that damage can occur quite far from the seismic source and in unexpected areas (Hildyard and Young, 2002; Hildyard et al., 2005a; Hildyard, 2007b). It is possible that tunnels

located at a large distance from the seismic source may suffer more severe damage, while tunnels near the seismic source may experience less damage, as illustrated in Figure 1-1. This phenomenon, in turn, reveals a need for improved dynamic support design methodologies. Dynamic support design against larger seismic events usually involves uncertainty in input design parameters, such as PPV/PPA (peak particle velocity/acceleration) and these parameters should be estimated carefully.

The first question arises considering the phenomenon above is why the seismic response of tunnels is different at different locations during a given seismic event? Once the potential causes (seismic magnitude, rock mass properties, mining activities, etc.) are found and several important factors are focused (this thesis focuses only on some factors that can alter ground motion patterns around excavations), then the second question is what kind of approach we can take to address the issue? Next, can we offer reliable input design parameters (PPV/PPA) at the

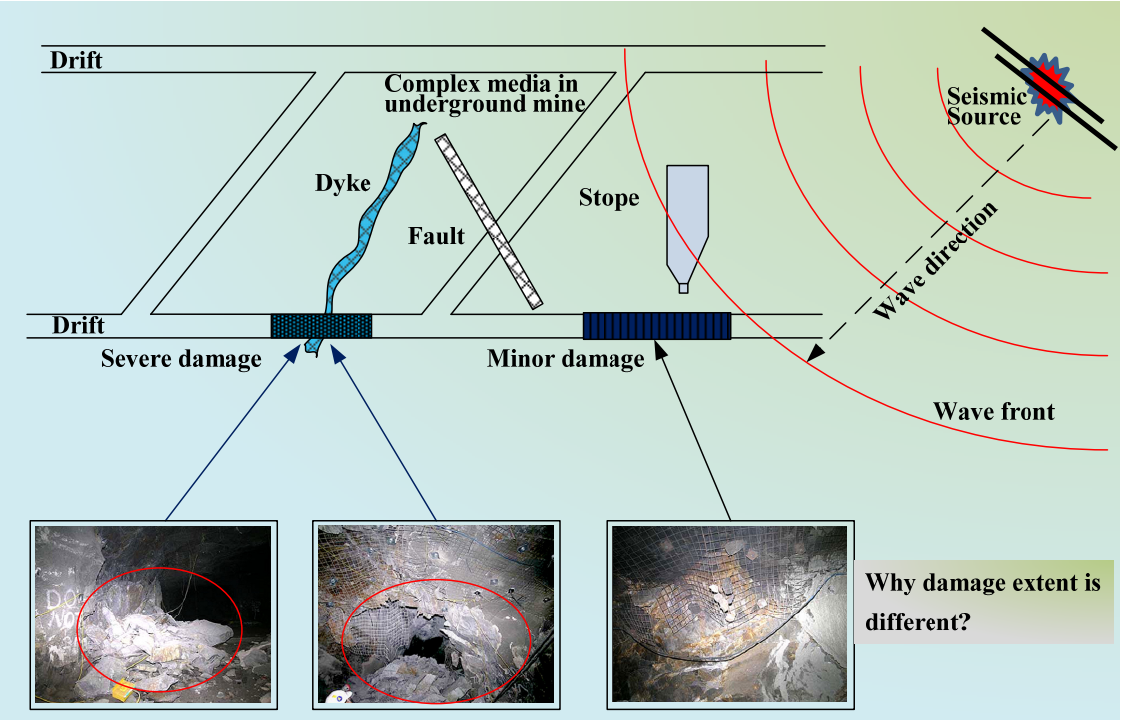

Figure 1-1: A sketch to illustrate different degrees of rockburst damage at various locations in a mine (reproduced from Kaiser et al. (1996) and Hudyma (2013) with some amendments).

design stage and can we get accurate ground motion (i.e., PPV) information at damage locations for forensic analyses?

1.3 Research objectives

This study attempts to address some outstanding issues related to rockburst damage localization and seismic wave propagation in deep underground mines, as stated in Section 1.2, with a particular emphasis on the ground motion near excavation boundaries due to seismic wave propagation that results from a remote fault-slip seismic event. Specifically, by using advanced numerical tools and a proposed coupled numerical method, this thesis aims at:

(1) studying the influence of different geometrical and geological structures (mining openings, faults, dykes) on ground motions, which can deepen the understanding of the wave patterns during the seismic wave interaction with these structures;

(2) investigating the influence of wavelength-to-excavation span on ground motions, which can provide additional insights into the ground motion behavior around excavations under both quasi-static and dynamic seismic wave loadings;

(3) establishing a non-uniform velocity model which can better model wave patterns near excavations than the uniform velocity model;

(4) developing a methodology for estimating ground motion (PPV) distribution near excavations in underground mines, which can assist in the interpretation of site amplification effect near excavation boundaries and for forensic analyses;

(5) increasing the confidence of rational dynamic support design against damage accounted by ground motions, which is important for reducing seismic hazard and improving mine safety.

1.4 Thesis summary

The main research components of this thesis are presented in Figure 1-2, which consist of (1) seismic source in underground mines, (2) influence of complex medium (geology) on wave propagation, and (3) interaction effect of wave propagation with mining excavations. Due to limitation of time and computation power, this thesis focuses primarily on 2D wave propagation modeling (Chapters 3 to 7) and contains with some preliminary studies on 3D wave propagation modeling (Appendices D and E). A brief summary of the eight chapters of this thesis is provided below.

- **Chapter 2** provides a review of the literature that is closely related to this research work. Rockburst damage mechanisms are first reviewed and various influence factors on rockburst damage localization are summarized. Three aspects, i.e., seismic source, wave propagation medium, and interaction of seismic wavefield with mine

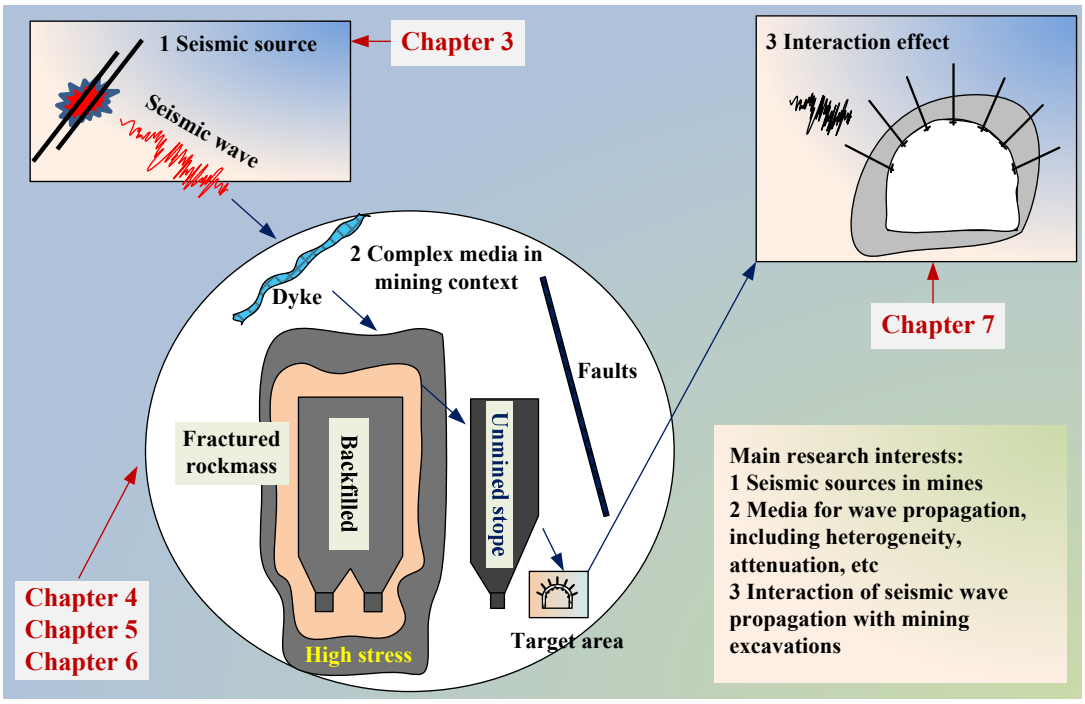

Figure 1-2: A sketch illustrating the linkage of the three main research topics addressed in this thesis.

excavations, are then briefly reviewed. The main numerical techniques used in rock mechanics and for seismic wave propagation analysis are also summarized in the Chapter 2. After a brief introduction of the SEM (Spectral Element Method), the SPECFEM2D and the SPECFEM3D codes are introduced.

- **Chapter 3** provides a validation example of the SPECFEM2D code. The numerical solution of the classical Garvin's problem, which has an analytical solution, is successfully verified with high accuracy. After that, a parametric study of source parameters for the point source model is conducted. As expected, it is found that the ground motion (PPV) depends not only on the target-source distance, but also on the source models and other factors. This shows that extreme care is needed when selecting source parameters to conduct seismic wave propagation modeling.
- **Chapter 4** assesses the influence of wavelength-to-excavation span ratio (λ/D ratio) on ground motion patterns around underground excavations. It is found that, in general, the PPV values at the excavation boundary increase as the λ/D ratio increases. The amplification effect around an excavation boundary increases as the λ/D ratio decreases, by either increasing the excavation span or decreasing the wavelength. It was also found that dynamic loading condition should be considered when the λ/D ratio is small (e.g., λ/D less than 10, with a shear wavelength less than 50 m and for a typical excavation span of 5 m).
- **Chapter 5** deals with the attenuation effects on wave propagation and a simple method is proposed to estimate the shear quality factor Q_s for hard rock mines. Based on the analysis in this chapter, $Q_s = 60 \pm 20$ can be chosen for wave

propagation simulation in underground hard rock mines when no high quality recorded data are available for back analysis.

- **Chapter 6** focuses on investigating the effect of geological and mine structures such as tunnels, open stopes, backfilled stopes, and dykes on ground motions. It is found that wave propagation patterns around an excavation can be altered significantly due to various heterogeneities in underground mines. In addition, it is found that PPV amplification and shielding effect can occur around excavation boundaries.
- **Chapter 7** deals with the excavation effect on ground motions. A nonlinear velocity model linking wave velocity to confinement and rock mass quality is proposed and a FLAC/SPECFEM2D coupled approach is developed and implemented to simulate ground motions. Compared with uniform velocity model, it is found that strong amplification occurs in low confinement zones and excavation damage zones in the non-uniform velocity model. Ground motion amplification at the excavation surface is larger in the non-uniform velocity models than that in the uniform velocity model due to the influence of extent of excavation damage.
- **Chapter 8** summaries the main achievements of this thesis and closes it with some suggestions for future work.

In the Appendices, the author presents: (A) additional modeling results; (B) magnitude scales of seismic event are reviewed; (C) results of joint time frequency analysis (JTFA) of synthetic seismograms of different models conducted in Chapter 6; (D) results of a simple excavation modeling using SPECFEM3D, and (E) a preliminary case study of a seismic event in a gold mine in South Africa.

Chapter 2

2 Literature Review

This chapter gives a background literature review that covers some concerns related to this thesis in order to understand the tunnel damage localization and tackle the seismic wave modeling problems in underground mines. The main areas of the review are: the rockburst damage mechanism, influence factors of tunnel damage localization, the seismic source models, wave propagation medium, interactions of wavefield with geological structures and excavation openings, main numerical methods in rock mechanics and seismic wave propagation. A brief introduction of SPECFEM2D/3D is provided in the last subsection.

2.1 Seismic events and rockburst damage mechanisms

Various mechanisms for mining-induced seismic events have been proposed by some researchers (Gibowicz, 1990; Gibowicz and Kijko, 1994b; Kaiser et al., 1996; Ortlepp and Stacey, 1994). According to Gibowicz (1990), two types of seismic events can be identified: Type I is directly connected with mining operations (i.e., associated with blasting and excavations) and Type II is not directly connected with mining activities (i.e., associated with the movement of geological discontinuities). According to these two damage mechanisms (Type I and Type II), as suggested by Potvin and Wesseloo (2013), Type I and Type II can be associated with near-field and far-field situations, respectively. Ortlepp and Stacey (1994) and Ortlepp (1997) proposed five rockburst mechanisms in underground mines, as shown in Table 2-1. Three rockburst types (strainburst, bulking, and facing crush/pillar burst) can be related to Type I, which is closely associated with excavations.

Strainburst is the most common rockburst near excavation boundaries. Buckling most likely occurs in laminated or transversely anisotropic rocks. Shear rupture and fault-slip rockbursts listed in Table 2-1 can be related to Type II.

In a broad sense, buckling and shear rupture rockbursts would be grouped into strainburst and fault-slip rockbursts respectively, as stated in Kaiser and Cai (2012). Thus, only three rockburst mechanisms, strainburst, pillar burst, and fault-slip burst need to be classified. In underground mines, strainburst can be expected when there is a high tangential stress associated with a relatively soft loading environment of the surrounding rock mass around the openings. Strainburst can be mining-induced due to static stress change caused by nearby mining or dynamically-induced due to dynamic stress change. Pillar burst can occur when the extraction ratio is high at a late mining stage, which also can be grouped into mining-induced and dynamically-induced pillar bursts. Fault-slip rockburst will occur when dynamic slippage occurs along a pre-existing fault or along a newly generated shear rupture and a large amount of seismic

Table 2-1: **Five mechanisms of damaging rockbursts proposed by Ortlepp (1997)**

Seismic source	Postulated source mechanism	First motion from seismic records	Richter Magnitude
Strainburst	Superficial spalling with violent ejection of fragments	Usually undetected, could be implosive	- 0.2 to 0.0
Buckling	Outward expulsion of large slabs pre-existing parallel to surface of opening	Implosive	0.0 to 1.5
Face crush / Pillar burst	Violent expulsion of rock from stope face or pillar sides	Mostly implosive, complex	1.0 to 2.5
Shear rupture	Violent propagation of shear facture through intact rock mass	Double-couple shear	2.0 to 3.5
Fault-slip	Violent renewed movement on existing fault or dyke contact	Double-couple shear	2.5 to 5.0

energy will be released. Fault-slip rockburst may generate strong ground motions that can cause shake down of damaged rocks locally and/or trigger strainburst or pillar burst in the far-field (Kaiser and Cai, 2012).

Once the consideration is focused on an excavation, Kaiser et al. (1996) proposed three distinct rockburst damage mechanisms: rock mass bulking due to rock fracturing, rock ejection due to seismic energy transfer, and rockfall due to seismic shaking. Rock mass bulking occurs when the broken rock volume increases directionally towards the opening due to rock mass disintegration. Rock mass bulking can be caused by both a remote seismic event and the bursting event itself. Rock ejection can be caused by a strainburst event, a pillar burst event, or by a remote seismic event through dynamic moment transfer. In other words, both the near- and far-field seismic events can contribute to this damage mechanism. It should be noted that the rock ejection velocity is not directly related to the momentum from the seismic source but more closely related to the energy stored in the near-wall rock and how this stored energy is released (Kaiser and Cai, 2012). Seismically-induced rockfall is caused by strong ground shaking due to a large remote seismic event, which could be a pillar burst or a fault-slip event. In the meantime, it is also possible that the subsequent ground motion can trigger the rockfall if the main ground shaking has already fractured a volume of rock mass without shaking them down.

In summary, rockburst damage mechanisms for an excavation are either mining-induced by energy release from a local seismic event in the near-field (e.g., strainburst/ejection without an additional dynamic loading) or dynamically-induced by energy transfer (e.g., strainburst/ ejection/rock falls with dynamic loading from the seismic waves) from a remote seismic event in the far-field.

2.2 Influence factors of damage localization in underground mines

In general, many factors can cause damage localization in underground mines (Durrhem, 2012; Heal et al., 2006; Hildyard and Young, 2002; Hildyard et al., 2005a; Kaiser and Cai, 2012; Potvin et al., 2000; Potvin and Wesseloo, 2013). The influencing factors can be categorized into four aspects: seismic source condition, geology conditions, geotechnical conditions, and mining activities, as shown in Figure 2-1.

(1) Seismic source: the first main factor related to tunnel damage is the seismic source itself, which generates seismic waves and governs the energy radiation patterns. For a potential large fault-slip seismic event, the initial wave patterns are determined by the seismic source mechanisms (i.e., normal fault, reverse fault, strike slip fault) (Aki and Richards, 2002; Chapman, 2004). Different fault mechanisms will cause a large variation of wave amplitude in the temporal and spatial spaces (Šílený and Milev, 2008), which can partially contribute the localized damage in a tunnel regardless of the tunnel location (far-field or near-field). In general, the larger the seismic event and the closer the seismic event is to a tunnel, the higher the potential that it will cause more rock mass damage. Furthermore, if a tunnel is located in the near-field, factors such as slip direction, rupture velocity, static and dynamic stress drop of the seismic source can cause different rock mass damage response to the seismic event.

(2) Geology: regardless of the tunnel location (far-field or near-field), the influence factors in this group have a large influence on the seismic wave propagation, which can cause extremely complex wavefields and wave patterns around a tunnel. In deep mining, high in situ stress and complicated mine geometries are common in mature underground mines. Two subgroups can be considered here. 1) Discontinuity: lithological interfaces, joints, and fractures (Hildyard and

Young, 2002; Zhu et al., 2012); 2) Heterogeneity: lithological units and geological structures (Kühn and Vavryčuk, 2013; Potvin and Wesseloo, 2013). Because of these factors, very complex wave radiation patterns and attenuation effect would be expected around tunnels due to reflection and refraction, and the interaction between seismic waves and the geological features. Under static and dynamic stress loading conditions, for example, when a tunnel is intersected by a geological weakness (e.g., faults or shear zones) or stress raisers (e.g., dykes), relatively large released energy and damage can be expected due to the unfavorable stress field and loading system conditions (Kaiser and Cai, 2012). Furthermore, different attenuation effect around the tunnel can also be expected due to these geology factors. For instance, different degrees of wave attenuation may be observed if seismic waves travel through various rock domains near the tunnel.

(3) Geotechnical: factors in this category have a large influence on site seismic response due to the interaction between seismic wave and the tunnel, both in the near-field and the far-field.

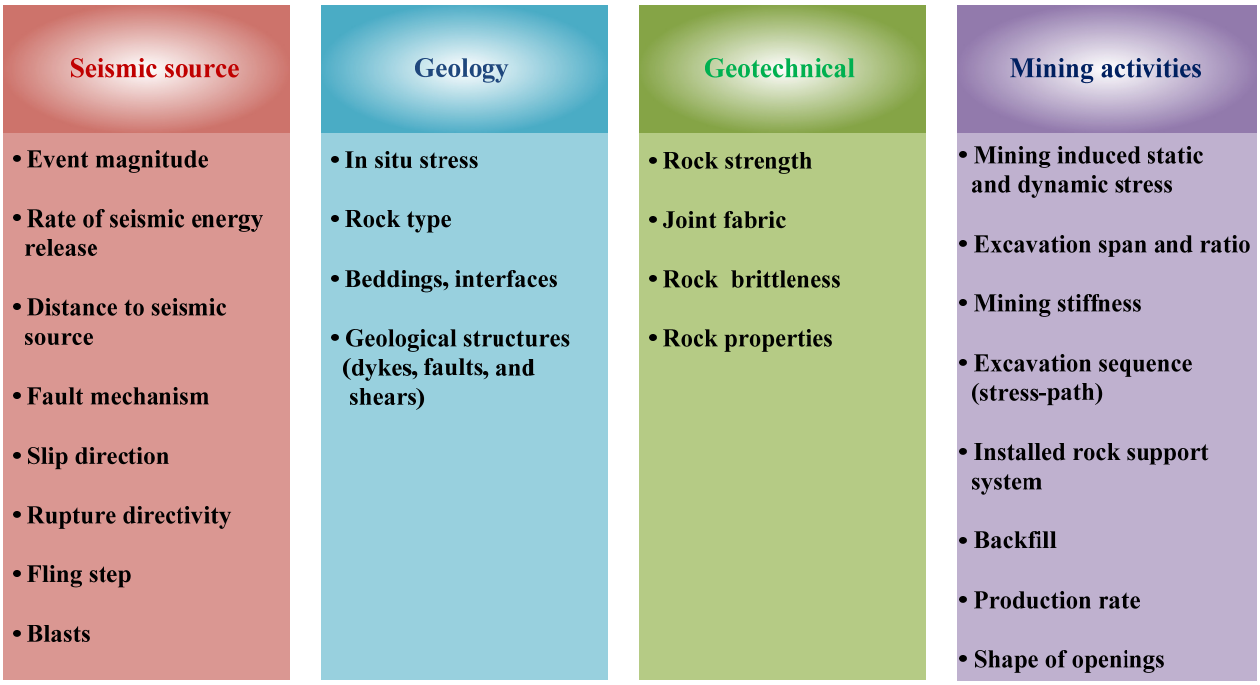

Figure 2-1: Main factors influence tunnel damage localization (modified from Kaiser and Cai (2012)).

Factors such as rock mass properties, rock and joint strength, rock brittleness, and anisotropy can influence tunnel damage locally (Kaiser and Cai, 2012; Kgarume, 2010). For instance, if a volume of rock mass in a tunnel has already reached a stress state very close to its peak strength due to static stress increase, then even a relatively small dynamic stress wave may be sufficient enough to trigger a localized rock mass failure in the tunnel. Furthermore, Hildyard (2007a) stated that rock mass anisotropy also has a large influence on wave radiation pattern. More wave attenuation can be expected if the seismic waves propagate across lamination than along the lamination.

(4) Mining activities: it is accepted that mining activities near a tunnel can have a large impact on the local site effect and lead to rock mass damage localization. Hence, factors such as mine layout and mining sequence, pillar width and height, working face orientation, size and shape (concave or convex curvature) of stopes and/or excavation faces, capacity of ground support system, and the relative orientation of rock mass deformation should be considered (Durrhem, 2012; Heal, 2010; Kaiser and Cai, 2012; Potvin and Wesseloo, 2013). For instance, when multiple openings are created near a tunnel, it can reduce loading system stiffness and hence rockburst damage is more likely to occur.

In summary, rockburst damage localization in tunnel is not controlled by only one factor, although there may exist a dominant factor; instead, it is the cumulative effect caused by multiple factors (Figure 2-1). Therefore, it should be governed by a combination of different factors and should be treated as site-specific. Among them, complex seismic waves (e.g., reflection, refraction, scattered, and coda waves) and their interaction with other factors may be a major cause of localized damage in tunnels.

2.3 Key aspects in modeling seismic wave propagation in underground mines

2.3.1 Seismic source model in underground mines

2.3.1.1 A brief introduction of seismic wave and seismic source models

In the earthquake field, a tectonic earthquake is generated by a sudden rupture of the Earth's crust when the stress in the rock reaches its strength, and it usually occurs along pre-existing faults but can sometimes occur along newly formed faults (Bormann et al., 2002). As a result, a seismic wave is generated. A seismic wave is a mechanical disturbance or energy packet, which can propagate in the Earth's media (Chapman, 2004; Sato et al., 2012). There are several types of seismic waves, which can be classified as body waves (that propagate through the volume of the Earth) and surface waves (that travel along the surface of the Earth). For body waves, P-waves (longitudinal or dilatational waves) and S-waves (shear waves or transverse waves) are the two main types. For the surface waves, Rayleigh and Love waves are the most common types.

In general, there are two types of seismic source models in numerical modeling of wave propagation, which are point source and non-point source models (Frohlich and Apperson, 1992; Rebetskii, 2005; Stickney and Sprenke, 1993), as shown in Figure 2-2.

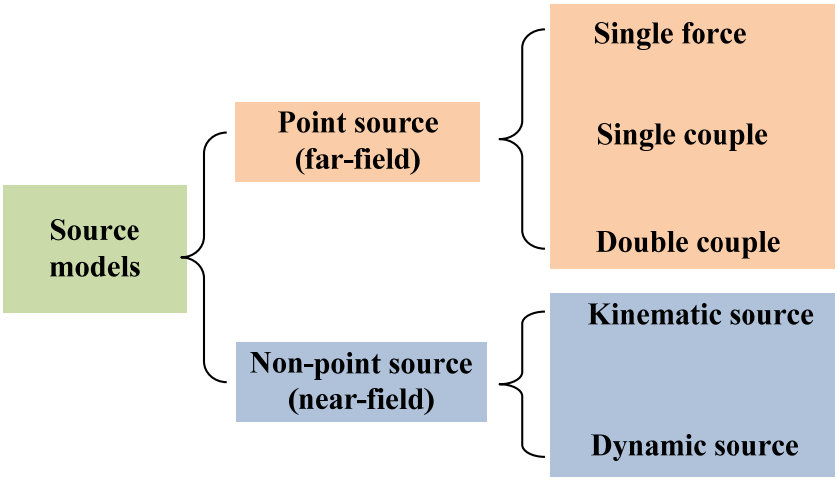

Figure 2-2: Typical source models in seismic wave propagation modeling.

A point source model is appropriate for far-field seismic wave modeling because the seismic source can be viewed as a point source if the distance between an observation station and the seismic hypocenter is far enough and the influence of the type of source models on site response is negligible. Three point source models are normally used, which are SF (single force), SC (single-couple), and DC (double-couple) models. However, a seismic source cannot be considered as a point source in the near-field and it should be taken as a non-point seismic source. When conducting research on the near-field seismic response, several factors involved in the seismic source model such as fault rupture area, orientation of rupture, rupture speed, stress drop, etc., should be considered. The kinematic dislocation model and the dynamic crack source model are the main two models. Several non-point source models, i.e., circular-shear dislocation model, stochastic source models (k-squared slip model), finite moving-source model (unilateral rupture and bilateral rupture models), finite fault rupture model, asperity source model, barrier model, slip-weakening friction model, have been developed (Dalguer et al., 2004; Guatteri et al., 2003; Mai and Beroza, 2000; Miyake et al., 2003; Motazedian and Atkinson, 2005).

2.3.1.2 Seismic sources in underground mines

As stated in Section 2.1, there are several seismic sources in underground mines, such as slip on geological features, crushing of pillars, and violent failure of wall rocks (Hudyma, 2013). In the meantime, high stress concentrations around openings and the existence of mined-out cavities can cause non-double-couple components in seismic sources (Baker and Young, 1997; Fletcher and McGarr, 2005; Kühn and Vavryčuk, 2013; Lenhardt and Pascher, 1996; McGarr, 1992a, b, c, 2005; Stickney and Sprenke, 1993). Šílený and Milev (2008) analyzed five seismic events through different seismic mechanisms in an underground gold mine. Source models were used to interpret the seismic events (Figure 2-3). The first event was induced by a pillar burst, which was

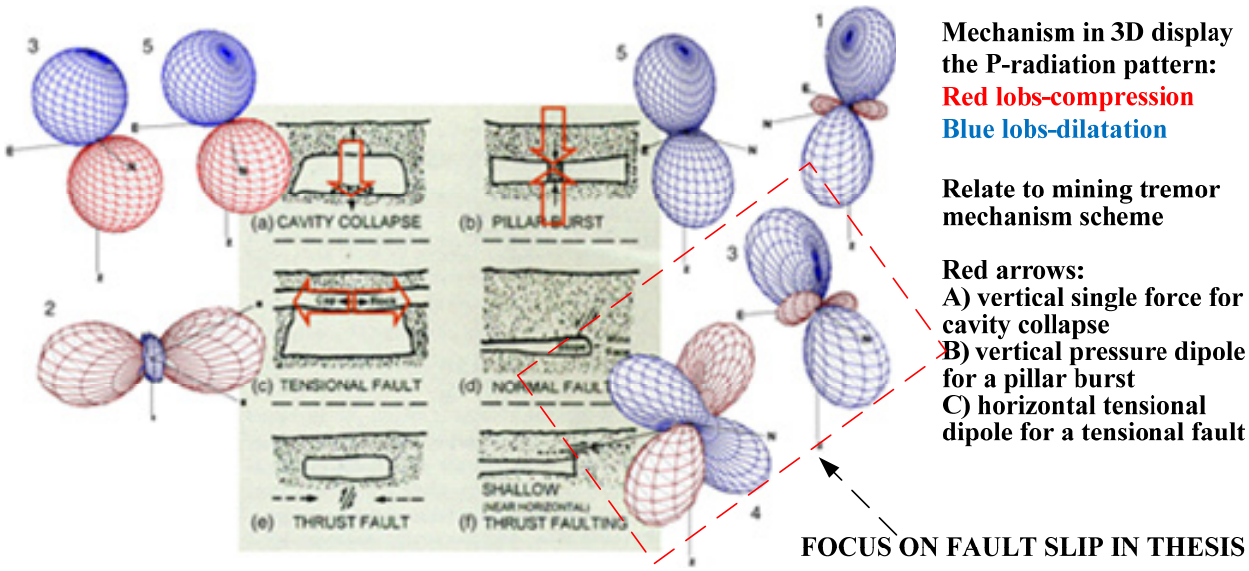

Figure 2-3: Common seismic source mechanisms (center part from Hasegawa et al. (1989)) and radiation patterns of P-waves (from Šílený and Milev (2008), with some modifications) in underground mines.

accompanied with P-wave radiation patterns indicated by "1" in Figure 2-3. The second event was generated by breaking of a hanging wall in a mined-out area (P-wave radiation pattern indicated by "2"). The force system of the third event was close to a pillar burst (compressional single-couple) and the rest was a cavity collapse (downward single force). The double-couple orientations of the fourth event corresponded to a sub-horizontal slip. The fifth event was linked to the mechanisms of pillar burst and the collapse of mined-out areas. In general, seismic sources in an underground mine are very complex due to non-uniform stress distribution and complex wave propagation medium. Compared with other seismic sources, fault-slip induced seismic events are usually associated with high energy release and thus could have a great potential to damage underground openings.

Figure 2-4 shows the three typical point source models (SF, SC, and DC). The upper panel indicates the force forms in 3D and the lower panel shows force forms in 2D. In the context of underground mining environment, the SF, SC, and DC models can be used to model cavity collapse, pillar burst, and fault-slip seismic events, respectively. As stated above, fault-slip

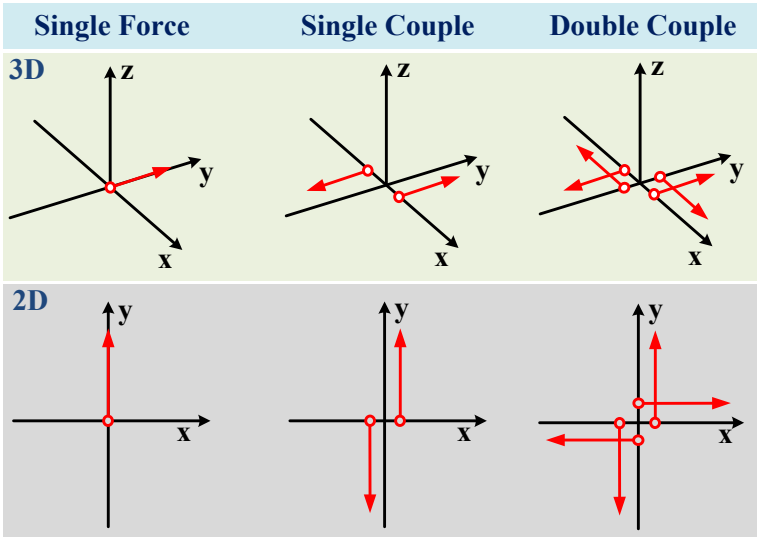

Figure 2-4: Typical point source models for numerical wave modeling; the upper panel shows forces in 3D and the lower panel indicates forces in 2D.

seismic events usually cause a large area of damage in underground mines. Hence this study will focus on seismic source caused by fault-slip events. As shown in Figure 2-4, a double-couple model can represent pure shear failure along a planar fault surface. The two force vectors acting on the surface are equal in magnitude, pointing in opposite direction and are separated by a small distance. In the double-couple source model, two force couples are present and each couple can be quantified by its moment.

2.3.1.3 Moment tensor model in P-SV system of 2D wave simulation

The moment tensor model, which includes double-couple forces and other force couples, is a more general representation of seismic source. A moment tensor has nine elements and each element can denote a force couple, which is shown in Figure 2-5.

In general, a full solution of a moment tensor can be decomposed to three components in terms of ISO (isotropic components, such as explosion or implosion, which can be represented by the single-couple point source model), DC (double-couple components), and CLVD (compensated linear vector dipole), as shown in Figure 2-6.

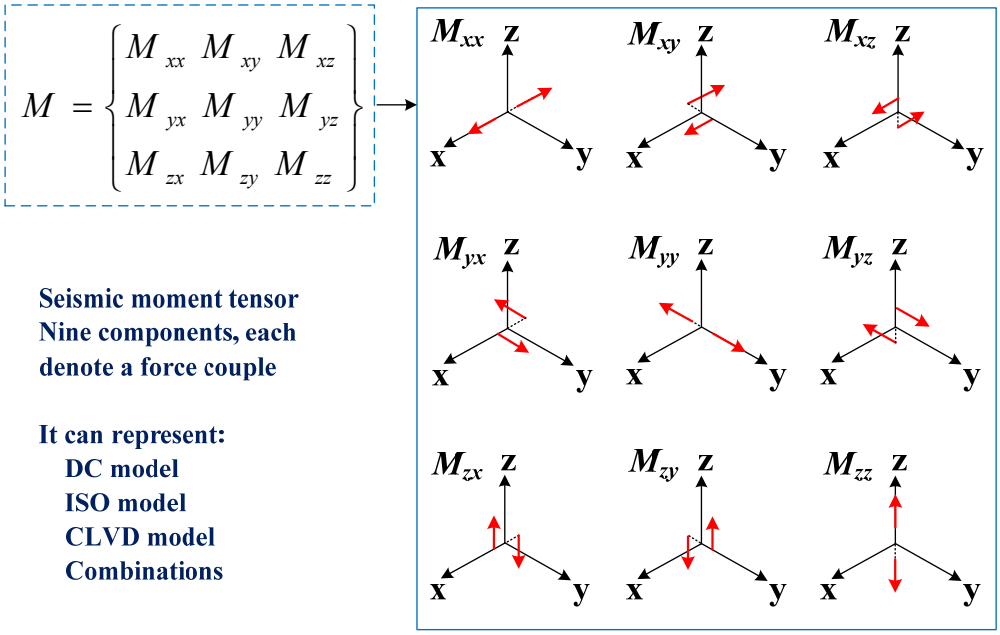

Figure 2-5: Moment tensor and nine elements in a moment tensor. Each element is denoted by a single force couple (red arrow), which comprises two equal and opposite forces (reproduced from Aki (1980a)).

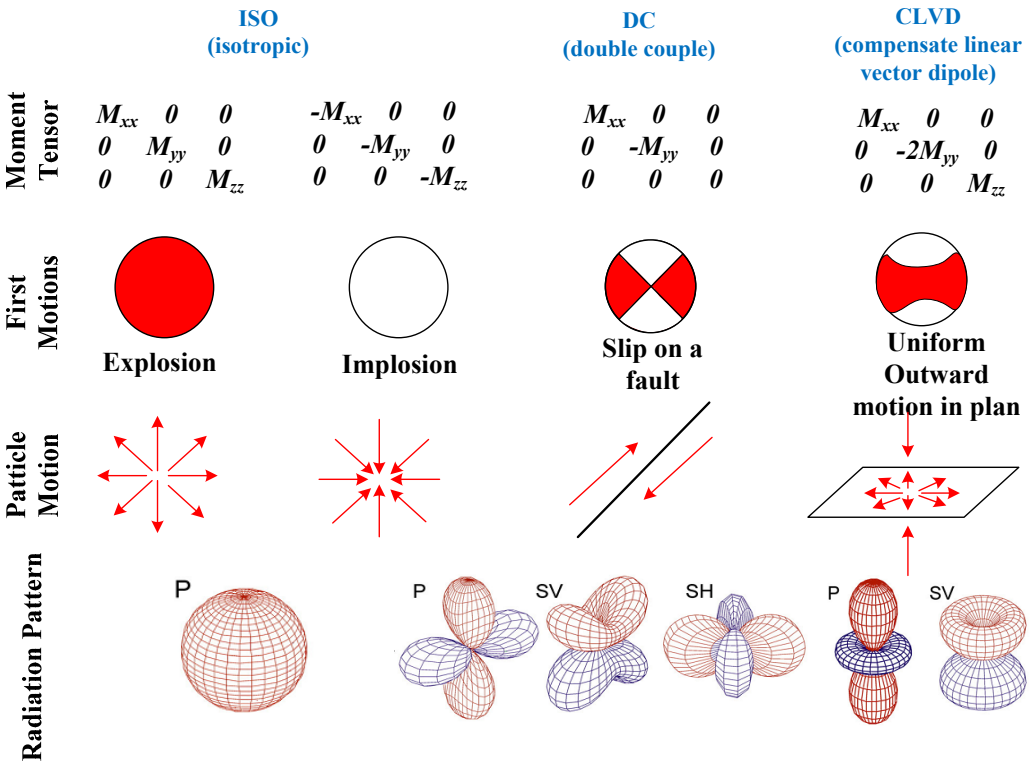

Figure 2-6: Moment tensor decomposition in terms of isotropic (ISO), double-couple (DC), and compensate linear vector dipole (CLVD) and radiation patterns of P, SH, and SV waves (red for compression and blue for dilatation) (from Frohlich and Apperson (1992) and Kühn and Vavryčuk (2013) with some modifications).

This research focuses mostly on 2D modeling of seismic wave propagation caused by a far-field fault-slip event. It is therefore necessary to derive 3D moment tensor model components in a 2D model that involves the application of the P–SV and the P–SH systems. Figure 2-7 shows a shear fault source located at the origin of the coordinate system (red dot) and the fault plane (light red area) is associated with the following parameters: strike ϕ_s, rake γ_r, and dip δ_d. Assume that two receivers R_1 and R_2 (denoted by green triangles) are located at two locations with azimuths ϕ_A and $\phi_A + \pi$, respectively. In such a configuration, two 2D computation planes can be realized: one in the P–SV system (vertical plane) and the other in the SH system (horizontal plane). The displacement components are V for SH displacement, S for P displacement and W for SV displacement. In this research, the focus is on the 2D simulation in the P–SV system.

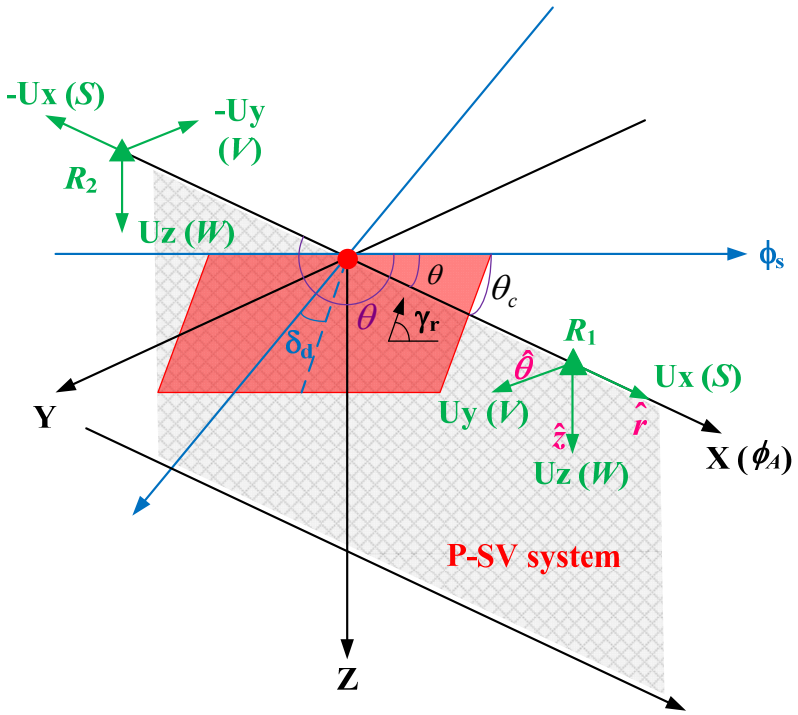

Figure 2-7: Cylindrical and Cartesian coordinates systems for a fault plane. In the Cylindrical coordinate system, θ is the clockwise angle from the strike to the receivers. In the Cartesian coordinate, X points to the receiver direction and Z points the downward direction. The displacements for the P, SV, and SH components are depicted by *S*, *W*, and *V*, respectively (after Li et al. (2014)).

For a pure double-couple source, Aki and Richards (2002) proposed the following equations to calculate the elementary moment tensor:

$$
\begin{aligned}
M_{xx} &= -M_0(\sin\delta_d\ \cos\gamma_r\ \sin 2\phi_s + \sin 2\delta_d \sin\gamma_r \sin^2\phi_s) \\
M_{xy} &= M_0(\sin\delta_d\ \cos\gamma_r \cos 2\phi_s + 0.5\times\sin 2\delta_d \sin\gamma_r \sin 2\phi_s) \\
M_{xz} &= -M_0(\cos\delta_d\ \cos\gamma_r\ \cos\phi_s\ + \cos 2\delta_d \sin\gamma_r \sin\phi_s) \\
M_{yy} &= M_0(\sin\delta_d\ \cos\gamma_r\ \sin 2\phi_s\ - \sin 2\delta_d \sin\gamma_r \cos^2\phi_s) \\
M_{yz} &= -M_0(\cos\delta_d\ \cos\gamma_r\ \sin\phi_s\ - \cos 2\delta_d \sin\gamma_r \cos\phi_s) \\
M_{zz} &= M_0 \sin 2\delta_d\ \sin\gamma_r \\
M_{zx} &= M_{xz} \\
M_{zy} &= M_{yz} \\
M_{yx} &= M_{xy}
\end{aligned}
\tag{2.1}
$$

In 2D modeling, there is no need to consider all the components. Based on the work of Chapman (2004), Li et al. (2014) proposed far-field radiation patterns for three components as

$$
\begin{aligned}
P(M;\phi_1,\phi_2) &= (M_{xx}\cos^2\phi_1 + M_{yy}\sin^2\phi_1 + M_{xy}\sin 2\phi_1)\sin^2\phi_2 + M_{zz}\cos^2\phi_2 \\
&\quad + (M_{zx}\cos\phi_1 + M_{yz}\sin\phi_1)\sin 2\phi_2 \\
SV(M;\phi_1,\phi_2) &= 0.5\times(M_{xx}\cos^2\phi_1 + M_{yy}\sin^2\phi_1 - M_{zz} + M_{xy}\sin 2\phi_1)\sin 2\phi_2 \\
&\quad + (M_{zx}\cos\phi_1 + M_{yz}\sin\phi_1)\cos 2\phi_2 \\
SH(M;\phi_1,\phi_2) &= (0.5\times(M_{yy} - M_{xx})\sin 2\phi_1 + M_{xy}\cos 2\phi_1)\sin\phi_2 \\
&\quad + (M_{yz}\cos\phi_1 - M_{zx}\sin\phi_1)\cos\phi_2
\end{aligned}
\tag{2.2}
$$

where ϕ_1 and ϕ_2 are the spherical coordinate azimuth angle and inclination angle, respectively. If the azimuth angle ϕ_1 is equal to zero, then Eq. (2.2) becomes

$$
\begin{aligned}
P(M;\phi_2) &= M_{xx}\sin^2\phi_2 + M_{zz}\cos^2\phi_2 + M_{zx}\sin 2\phi_2 \\
SV(M;\phi_2) &= 0.5\times(M_{xx} - M_{zz})\sin 2\phi_2 + M_{zx}\cos 2\phi_2 \\
SH(M;\phi_2) &= M_{xy}\sin\phi_2 + M_{yz}\cos\phi_2
\end{aligned}
\tag{2.3}
$$

It is seen from Eq. (2.3) that only the components of M_{xx}, M_{zz}, and M_{xz} contribute to the far-field P–SV system in the x–z plane, and for far-field SH system only M_{xy} and M_{yz} can be used to denote its radiation. In this manner, the moment tensor can be used to investigate the wave radiation in 2D and only three components (M_{xx}, M_{zz}, and M_{xz}) are required in the seismic source representation in the P–SV system.

2.3.1.4 Radiation patterns from a moment tensor point source

A good understanding of wave radiation patterns is essential for this study and the following section discusses radiation patterns for P- and S-waves from a point moment tensor seismic source.

Figure 2-8 shows a few typical faults, which are considered as seismic sources in the earthquake field (Stein and Wysession, 2003). Seismic waves are emitted and propagated in the medium once the fault-slip seismic source is triggered. To represent a fault-slip seismic source, several aspects shown in Figure 2-9 need to be considered.

The actual forces on the fault plane can be described by superposition of equivalent forces (Feignier and Young, 1992; Gibowicz, 1993; Hazzard and Young, 2002), leading to a double-couple force model. According to research conducted by some investigators (Feignier and Young, 1992; Gibowicz, 1993; Kühn and Vavryčuk, 2013; McGarr, 1992a; Trifu, 2001), a moment tensor can be used as a mathematic description of the equivalent force couples. In other words, a moment tensor model can be employed to describe the pure shear fault-slip process and this is very well suited to examining the seismic source using a point source model.

The seismic moment can be expressed as (Aki and Richards, 2002)

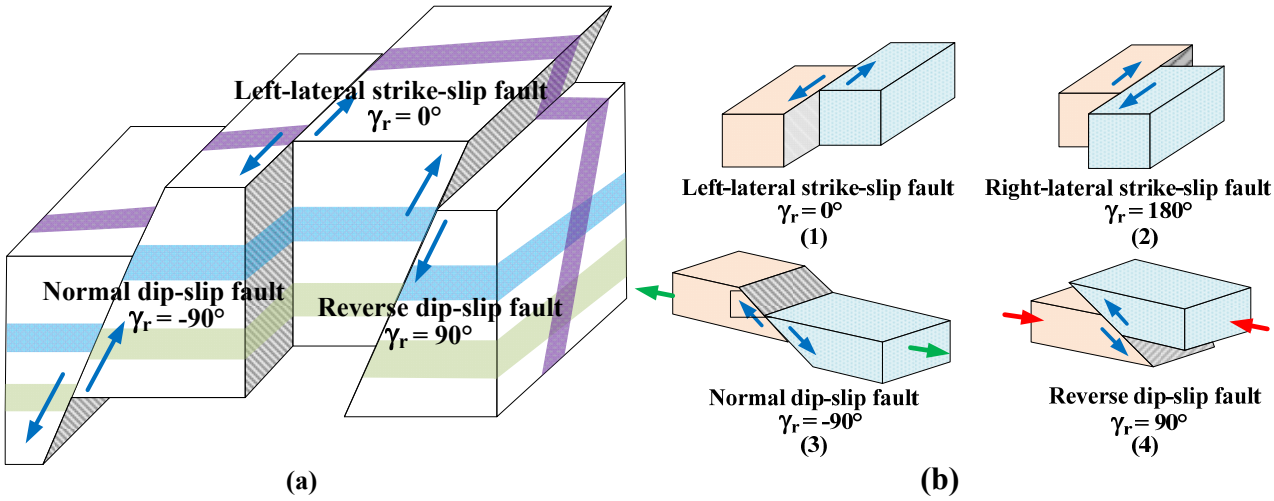

Figure 2-8: Geometrical configuration of a fault after slip. (a) Shows the typical formation and motion of faults; (b) shows basic types of fault motion. Strike-motion can either be (1) left-lateral or (2) right-lateral and dip motion can either be (3) normal or (4) reverse. Oblique motions are also possible with different rake directions. The red arrows and the green arrows represent compression and tension forces (reproduced from Stein and Wysession (2003)).

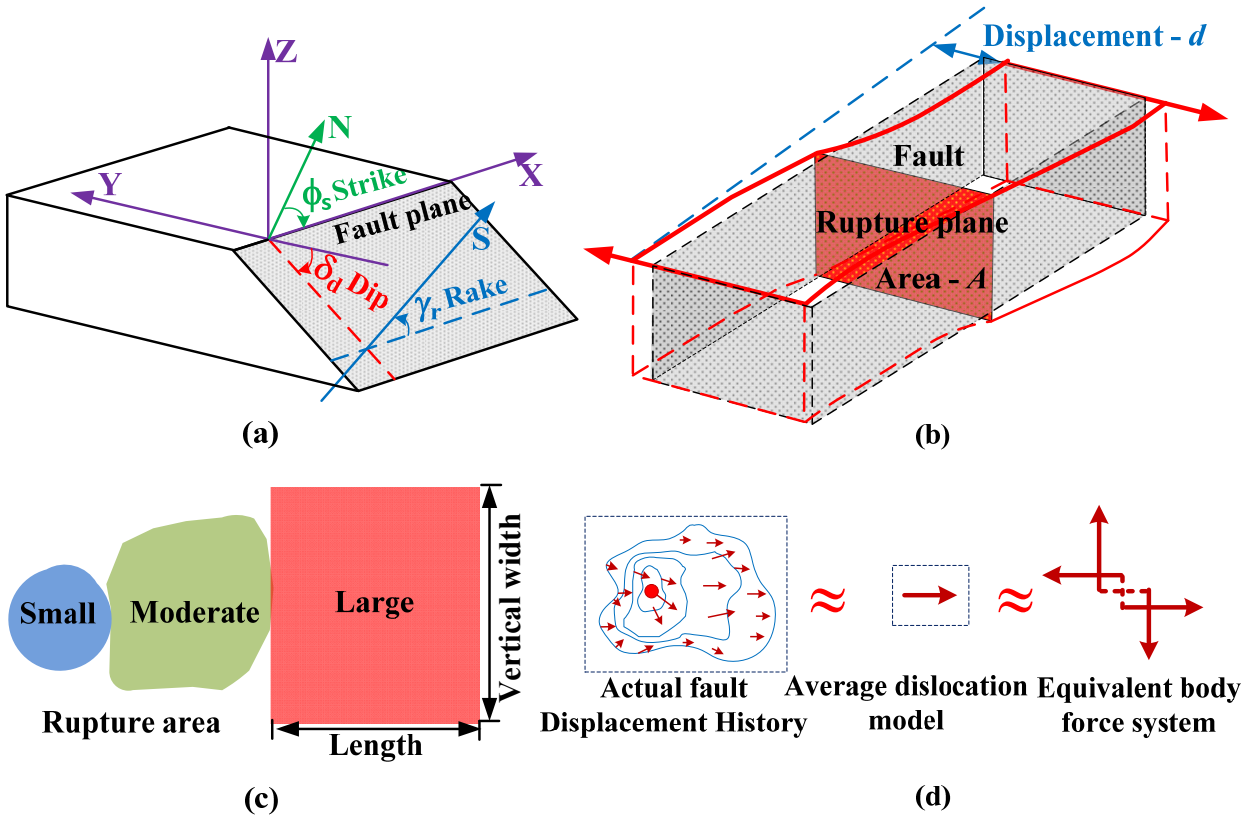

Figure 2-9: Several considerations for viewing a fault-slip event as a seismic source. (a) Fault plane associated with the characteristic parameters of strike, dip, and rake angle; (b) a sketch to show the rupture area and slip distance for a fault-slip source; (c) various rupture areas can be connected to different intensity of the seismic event; (d) simplification of the actual fault-slip process to a double-couple equivalent forces (reproduced from Stein and Wysession (2003)).

$$M_0 = \mu_s A D_s \tag{2.4}$$

where μ_s (dyne/cm^2) is the average shear rigidity of the faulted rocks, A (cm^2) is the area of the fault face, and D_s (cm) is the average slip displacement over the entire fault surface. To illustrate the wave propagation pattern, Figure 2-10 represents a point DC source model with a rupture area of A and the fault plane is in the x-y plane and the slip direction is along the x direction. If the seismic source is a point dislocation source in an unbounded homogeneous space, the general representation of the complete displacement field can be expressed as

$$\begin{aligned} u(\mathrm{x},\mathrm{t}) = {} & \frac{1}{4\pi\rho} A^N \frac{1}{r^4} \int_{r/V_P}^{r/V_S} \tau M_0(\mathrm{t}-\tau) d\tau \\ & + \frac{1}{4\pi\rho V_P^2} A^{IP} \frac{1}{r^2} M_0(\mathrm{t}-\mathrm{r}/V_p) + \frac{1}{4\pi\rho V_S^2} A^{IS} \frac{1}{r^2} M_0(\mathrm{t}-\mathrm{r}/V_S) \\ & + \frac{1}{4\pi\rho V_P^3} A^{FP} \frac{1}{r^1} \dot{M}_0(\mathrm{t}-\mathrm{r}/V_P) + \frac{1}{4\pi\rho V_S^3} A^{FS} \frac{1}{r^1} \dot{M}_0(\mathrm{t}-\mathrm{r}/V_S) \end{aligned} \tag{2.5}$$

where

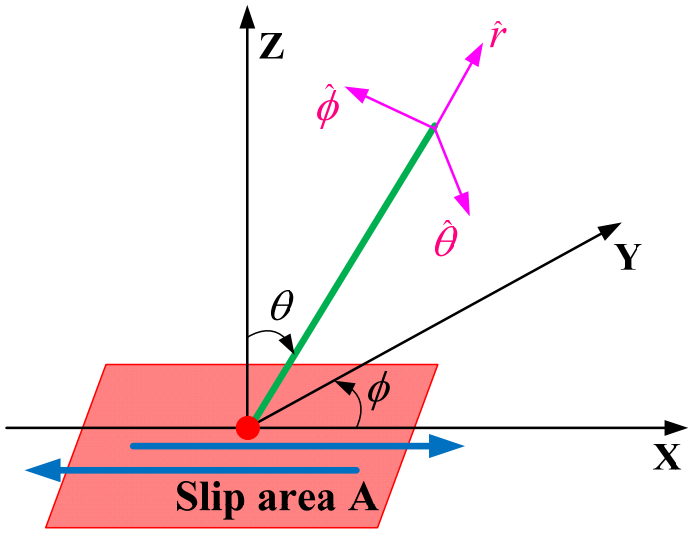

Figure 2-10: Cartesian and polar coordinate systems for the analysis of radiation pattern from a pure shear fault-slip with a rupture area of A (Aki and Richards, 2002; Chapman, 2004).

$$
\begin{aligned}
A^{N} &= 9\sin 2\theta\cos\phi\hat{\mathbf{r}} - 6(\cos 2\theta\cos\phi\hat{\boldsymbol{\theta}} - \cos 2\theta\cos\phi\hat{\boldsymbol{\varphi}}) \\
A^{IP} &= 4\sin 2\theta\cos\phi\hat{\mathbf{r}} - 2(\cos 2\theta\cos\phi\hat{\boldsymbol{\theta}} - \cos\theta\sin\phi\hat{\boldsymbol{\varphi}}) \\
A^{IS} &= -3\sin 2\theta\cos\phi\hat{\mathbf{r}} + 3(\cos 2\theta\cos\phi\hat{\boldsymbol{\theta}} - \cos\theta\sin\phi\hat{\boldsymbol{\varphi}}) \\
A^{FP} &= \sin 2\theta\cos\phi\hat{\mathbf{r}} \\
A^{FS} &= \cos 2\theta\cos\phi\hat{\boldsymbol{\theta}} - \cos\theta\sin\phi\hat{\boldsymbol{\varphi}}
\end{aligned}
\tag{2.6}
$$

where u is the ground displacement as a function of space and time, M_0 is the time-dependent seismic moment, ρ is the density of the medium, r is the source-site distance, V_p and V_s are the P- and S-wave velocities, respectively, N means the near-field, IP and IS stand for the intermediate field, and FP and FS stand for the far-field.

According to Eq. (2.6), the radiation patterns depend on angles θ and φ, which determine the source-site position with respect to the fault slip. The wave amplitudes depend on the distance from the source to the point of calculation. Clearly, for the near-field terms (N) at a small distance, the wave is a combination of both P- and S-waves, and it is difficult to separate these two waves for a short propagation distance. For the intermediate terms (IP and IS), the ground motion will be attenuated at a pace of $1/r^2$. For the far-field terms (FP and FS), which are at a relatively large distance r, the amplitudes will be attenuated as a pace of $1/r$. Again, this thesis will focus mostly on the far-field wave simulation using a selected point source mode. The radiation patterns from the DC source model will be discussed.

The orientation of a DC model determines the wave radiation patterns. Figure 2-11 shows a typical wave propagation pattern for a pure normal fault-slip source with a dip of 45°. The highest ground motion for P-waves is at 45° to the slip direction (see upper panel of the figure), and the maximum ground motion for S-waves is exactly along with the slip direction (middle panel). The contributions of P- and S-waves to the wave pattern are shown in the lower panel of

Figure 2-11. Clearly, the maximum ground motions for P- and S-waves are notable at different directions. In a normal fault, the maximum seismic response results from P-waves can be located at the x and z-axes and the strong ground motion for S-waves can be observed at 45°/135° to the x coordinate axis.

In summary, a moment tensor model can be employed to examine wave propagation in the P–SV coordinate system and only three components of the moment tensor are required to represent the seismic source in 2D modeling.

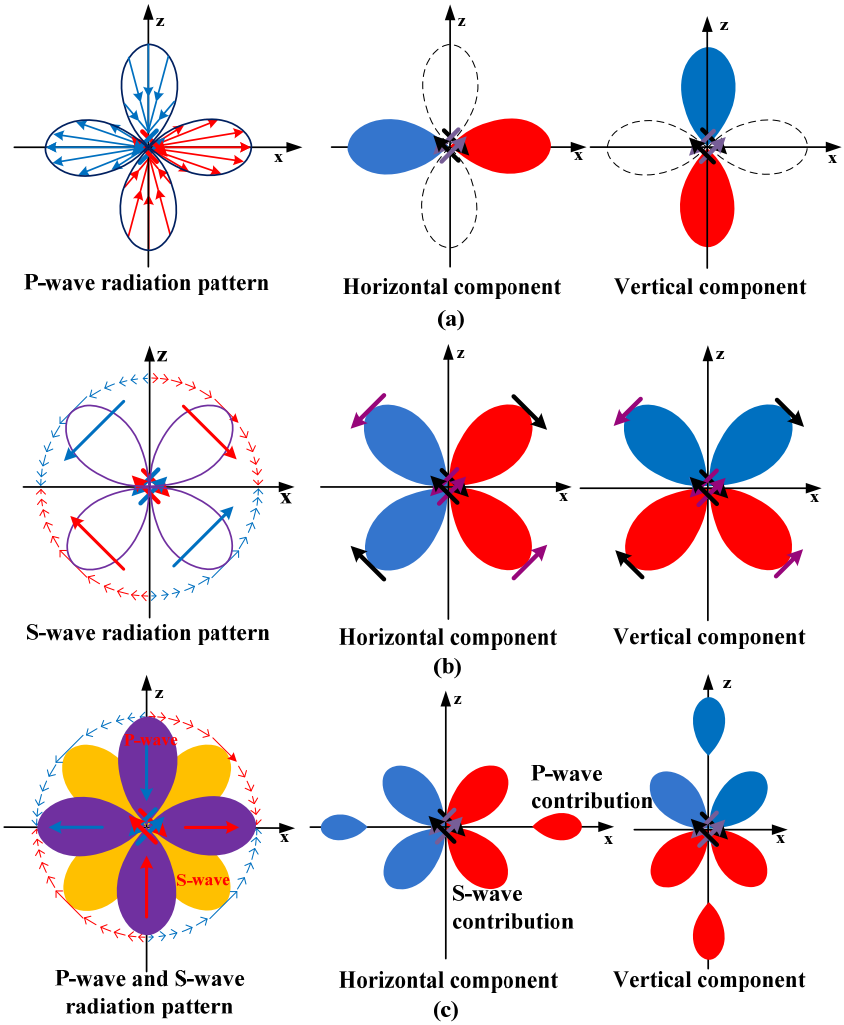

Figure 2-11: Wave propagation patterns for a DC source model (normal fault slip with a dip of 45°). Wave propagation pattern and two components of P- and S-waves are denoted by different colors. Red and blue denote right and left movements for horizontal component, and up and downward movements for vertical component, respectively (after Aki and Richards (2002) and Stein and Wysession (2009)).

2.3.2 Medium and seismic wave propagation

2.3.2.1 General medium models

Seismic wave propagation in earth is extremely complicated, and it is impossible to model it exactly. Various assumptions and approximations must be made to quantitatively study the excitation and propagation of seismic waves and their relation to physical properties of the earth (Aki, 1980b; Berkhout, 1987; Carcione, 2007b; Sato and Fehler, 1998; Udias, 1999).

For a linear elastic, heterogeneous, and anisotropic medium, the generalized Hooke's law and the governing equation of motion can be written as (Aki, 1980b; Berkhout, 1987; Chapman, 2004; Fichtner, 2011):

$$\sigma(\mathbf{x}) = \mathbf{C}(\mathbf{x}) : \varepsilon(\mathbf{x}) = \mathbf{C}(\mathbf{x}) : \frac{1}{2}(\nabla \mathbf{u} + \mathbf{u}\nabla) \tag{2.7}$$

$$\rho(\mathbf{x})\ddot{\mathbf{u}}(\mathbf{x},t) - \nabla \cdot [\mathbf{C}(\mathbf{x}) : \nabla \mathbf{u}(\mathbf{x},t)] = \mathbf{f}(\mathbf{x},t) \tag{2.8}$$

where $\sigma(\mathbf{x})$ is the stress tensor at position $\mathbf{x}$, $\mathbf{C}$ is a 4^{th} order stiffness tensor, $\varepsilon(\mathbf{x})$ is the strain tensor, $\mathbf{u}$ is the displacement field, $\mathbf{u}\nabla$ stands for the transpose of $\nabla\mathbf{u}$, ":" denotes for the double inner product of tensors, $\rho(\mathbf{x})$ is the mass density of the medium, and $\mathbf{f}$ is an external body force. The governing equation of motion is a linearized version of Newton's second law; it balances the momentum of particle displacement and forces resulting from both the internal stresses and the external forces. Various idealized physical medium models will be presented based on Eq. (2.8).

(1) Homogeneous, isotropic medium model: in this medium model, it is assumed that both $\rho(\mathbf{x})$ and $\mathbf{C}$ are independent of position $\mathbf{x}$ in the homogeneous medium, and the model has only two independent elastic constants (the Lamé constants). Hence, Eq. (2.8) becomes

$$\rho(\mathbf{x})\,\ddot{\mathbf{u}}(\mathbf{x},t)-(\lambda_L+2\mu_L)\nabla\cdot(\nabla\cdot\mathbf{u})+\mu\nabla\times(\nabla\times\mathbf{u})=\mathbf{f}(\mathbf{x},t) \tag{2.9}$$

where λ_L and μ_L are the Lamé constants. Eq. (2.9) governs two types of body wave propagation in an isotropic medium, namely, the compressional wave (P-wave or longitudinal wave) and the shear wave (S-wave, or secondary wave, or transverse wave). The P-wave will cause an arbitrary element of the medium to change its volume without rotation, whether it is contraction or expansion. The S-wave will cause an element of the medium to distort without changing its volume. S-wave may be resolved into vertical and horizontal components.

(2) General anisotropic elastic medium: in an anisotropic medium, **C** has 21 independent elastic constants in a 3D problem, and 6 independent components in a 2D problem. A rock medium in underground mines usually exhibits a wide range of anisotropic features. To represent this medium, the classical reduced Voigt notation can be used and more details can be found in Carcione (2007b). Because of the variations of elastic properties with direction in anisotropic media, polarizations of seismic waves are no longer longitudinal or transverse to the direction of wave propagation anymore. The transverse wave will split into two quasi-shears (*qS*) waves with quasi-transverse polarizations and *qS* will propagate at different velocities. In general, three waves propagate through an anisotropic medium, referred as quasi-compressional or quasi-P (*qP*) wave, fast (qS_1) and slow (qS_2) quasi-shear or quasi-S waves.

(3) Transversely isotropic (TI) medium: a TI medium is the simplest form of anisotropic media. For a TI medium, **C** has five independent elastic constants and an axial symmetry with respect to the Z-axis Figure 2-12. It means that all physical properties are isotropic in the plane perpendicular to the Z-axis, while the properties vary as a function of an angle with respect to the Z-axis. In modeling, a TI model can be used to represent layered rocks or rocks with one

dominant joint set. A shear wave will split into a slow S-wave and a fast S-wave when its moving direction is at an angle with respect to the symmetry axis. Thomsen (1986) introduced a practical way to measure anisotropy by three effective parameters. These constants include P-wave anisotropy, near-vertical P-wave anisotropy and S-wave anisotropy for the anisotropy of the medium (Li et al., 2004).

(4) Heterogeneous medium: compared with a homogeneous medium, the elastic properties of a heterogeneous medium vary with location. For a heterogeneous medium, $\rho(\mathbf{x})$ and/or $C(\mathbf{x})$ are not constants but rather vary in space. Wavefields will be scattered due to material heterogeneity, and a detailed study on wave scattering in heterogeneous media can be found in (Wu, 1996; Wu and Aki, 1985).

2.3.2.2 Attenuation of seismic wave propagation

Seismic wave amplitude generally will decrease as travel distance (spatial) increases. This is due to wave attenuation or damping, which can be viewed as a natural consequence of the energy conservation (Gibowicz and Kijko, 1994a; Sato and Fehler, 1998; Sato et al., 2012). The attenuation mechanisms for seismic waves have been studied for many years and two main

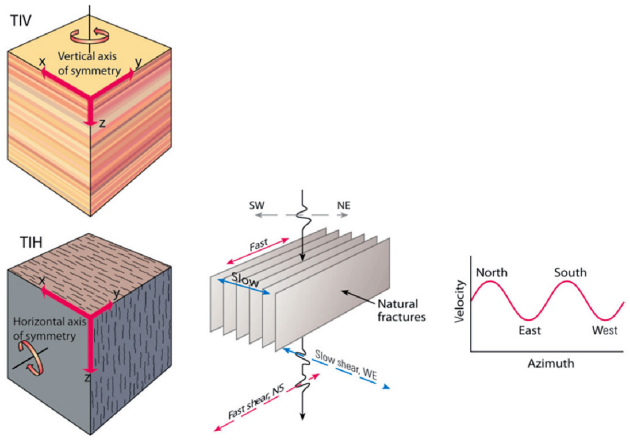

Figure 2-12: A sketch of a transversely isotropic medium with a vertical axis and a horizontal axis (left hand side), and a shear wave splits into a slow and a fast S-waves (middle and right hand side) (Close et al., 2009).

mechanisms, which are called scattering and intrinsic mechanisms, have been proposed. In general, six different mechanisms can contribute to wave attenuation; they are geometric spreading, radiation damping, reflection and transmission at interfaces, scattering, multi-paths, and intrinsic damping (Chapman, 2004; Sato et al., 2012). For the first five attenuation mechanisms, they redistribute wave energy within the medium without removing energy from waves. On the contrary, the intrinsic damping mechanism does not conserve energy and it will convert vibration energy into heat and other forms of energy due to anelasticity, which will cause permanent deformation of the medium. Hence, the total attenuation is the sum of the external and intrinsic attenuations. In the following discussion, geometrical damping, reflection and transmission at interfaces, and intrinsic damping will be further explained.

(1) Geometrical damping: different types of seismic waves will present different radiation patterns. Typically, as spherical waves (i.e., P- and S-waves) or cylindrical (i.e., Rayleigh waves) move forward in the medium, the density of energy at the surface of the wave front will decrease due to the conservation of elastic energy. For the spherical and cylindrical waves, the energy per unit wave front will decrease as a function of $1/r^2$, and $1/r$, respectively, where r is the source-target distance. In addition, the wave amplitude will decrease as a function of $1/r$ for body waves, and $1/r^{0.5}$ for Rayleigh waves. In underground mines, if a seismic event is caused by shear slip on a pre-existing fault, triggering of damage to mine infrastructures will in part depend on wave radiation patterns, particularly the shear wave radiation patterns.

(2) Reflection, transmission and scattering at interfaces: during wave propagation, a seismic wave will scatter when it encounters a discontinuity in the medium. Discontinuity is a term often used to refer to any change in stiffness or geometry of the medium, such as cavities, joints, inclusions, and free surfaces of underground structures. In such a situation, scattering will appear

in various forms, such as reflection, refraction, and diffraction. The relation between the amplitudes of incident and transmitted waves can be expressed by the transmission coefficient (T), which is the amplitude quotient of transmitted and incident waves. The transmission coefficient depends on the product of density and velocity of each medium.

(3) Intrinsic damping: due to nonlinear friction between the molecules and grains of the material of the medium, intrinsic damping can result and it refers to the mechanism of converting mechanical energy into other types of energy such as heat (Gibowicz and Kijko, 1994a; Sato et al., 2012). This process is not reversible. There is energy loss due to shear heating at grain boundaries and mineral dislocation. The energy loss is commonly measured by a dimensionless parameter called quality factor Q, which represents the ratio of the total stored energy to the dissipated energy per volume per cycle of vibration. Q is independent of wave frequency. A large value of Q indicates a low energy loss medium, and vice versa.

2.3.2.3 Complex medium in underground mines

In underground mines, the media of seismic wave propagation are characterized as complex heterogeneities in the forms of various geological and geometrical structures and highly non-uniform stress distribution around openings. For example, a seismogram from a microseismic monitoring system is often composed of two parts: the primary waves and the scattered waves (S-coda wave). S-coda waves are generated by the interaction between the primary waves and the heterogeneities medium (Gibowicz and Kijko, 1994a; Sato et al., 2012), and they can be viewed as one of the most compelling pieces of evidence of random heterogeneity in the medium. It was demonstrated from many studies that P-waves can be converted to S-waves if the P-waves travel through a non-uniform medium (Kondrat'yev et al., 1984). Mandal and Toksoz (1991) showed that a significant amount of shear wave energy will be generated if an explosive source

is contained in an anisotropic medium, and the generated wavefield is more complex compared with that in an isotropic medium. The shape of underground structures also has an influence on wave propagation in transversely isotropic and isotropic media (Gibson et al., 1996). Additional discussion on this problem can be found in Bouchon (1976), Lee and Balch (1982), Faccioli et al. (1989), and McLaughlin et al. (2004).

As stated above, two main tasks, i.e., the influence of different geological structures on wavefield and the interaction of wavefield with excavations, are addressed in this thesis. Clearly, both topics are related to the propagation medium in underground mines. The complex underground medium therefore imposes a challenge in wave propagation simulation.

2.3.3 Interaction of seismic wave with fractures and openings in underground mines

When a seismic wave reaches underground excavations, the wave propagation pattern can be altered significantly. At the excavation boundary, the amplification effect can increase the wave amplitude and hence PPV. It is well known that the wave velocity of a rock mass is confinement dependent (Maxwell and Young, 1995; Prikryl et al., 2005). Stress field near the excavation boundary is not uniform, which means that the velocity field will not be uniform as well. This in turn will have a significant effect on the seismic wave propagation. It is therefore important to consider the stress field change near excavation boundaries to model seismic wave propagation accurately.

Rock masses contain discontinuities such as faults and shears. In seismic wave propagation studies, these discontinuities have been termed as fractures. In general, fractures can alter and complicate the seismic wavefield (Hildyard and Young, 2002). In order to represent the fractures, Schoenberg (1980) proposed a displacement discontinuity method. This approach can capture

the frequency effect on waves (Pyrak-Nolte et al., 1990a, b), but it cannot consider multiple fractures and is not suitable for 3D modeling (Cai and Zhao, 2000). Another approach to model the influence of fractures on wave propagation is based on the effective wave velocity and the attenuation effects (Liu et al., 2000; Sayers and Kachanov, 1991). Some assumptions such as 2D modeling, plane wave propagation, low frequency relative to crack size, and uniform stress sate are commonly made in these methods (Hildyard and Young, 2002). In addition, assumptions such as point source, homogeneous, and isotropic material are often made, which make the underlying model less representative of the real rock masses in underground mines.

In summary, the effect from the interaction of wave propagation with fractures and excavations can be very strong, leading to altered wave amplitudes and complex wavefield. Previous studies focused more on the effect of fractures on wave propagation. However, this thesis concentrates more on the interaction of seismic wave with mine openings through considering the non-uniform velocity model resulted from the stress redistribution due to excavation.

2.4 Review of numerical methods

Main numerical methods and tools in the rock mechanics field and wave propagation field are reviewed. The goal of this section is to understand the advantages and disadvantages of each method and tool, and to identify proper tools for the thesis research.

2.4.1 Main numerical methods in rock mechanics

Broadly speaking, the most commonly used numerical methods in rock mechanics can be classified into three categories: continuum methods, discontinuum methods, and hybrid continuum/discontinuum methods (Jing, 2003).

2.4.1.1 Continuum methods

FDM (Finite Difference Method): FDM is one of the oldest numerical techniques used for the solution of a set of PDEs (Partial Differential Equations). No interpolation functions are needed, but this method does suffer inflexibility in dealing with fractures, complex boundary conditions and material heterogeneity. Several methods, such as FVM (Finite Volume Method), FDTD (Finite-difference time-domain), GFDM (Generalized Finite Difference Method), and FPM (Finite Point Method), were developed based on the basic idea of FDM. A comprehensive review can be found in Jing and Hudson (2002) and Jing (2003).

FEM (Finite Element Method): First used by Clough (1960) for plane stress problems, FEM has become the most powerful numerical method in engineering and science research (Jing and Hudson, 2002), due to its great flexibility in handling material heterogeneity, nonlinear deformability, complex boundary conditions, etc. Many commercial codes based on the FEM are developed, such as ATENA (http://www.cervenka.cz/products/atena), FRANC (Agrawal and Sun, 2004), ANSYS (http://www.ansys.com), and ABAQUS (http://www.3ds.com/products-services/simulia/portfolio/abaqus). Examples of FEM application in rock mechanics can be found in Goodman et al. (1968), Mahtab and Goodman (1970), Huang et al. (2005), and Jiang et al. (2010), Silva and Einstein (2013).

BEM (Boundary Element Method): BEM tries to find a weak solution at a global level through a numerical solution of an integral equation which is derived from the original PDEs. BEM reduces one dimension of the problem and considers only the boundary in the calculation domains (Jing, 2003). In light of this, it is more suitable for solving homogeneous and linearly elastic problems, and in turn, it is not ideal for solving problems involving nonlinear material behavior and damage evolution process. For more details on the BEM method, refer to

Nagarajan et al. (1996), Mukherjee et al. (1997), Pan et al. (1997), Pan et al. (1998), Gray and Monaghan (2004), and Phan and Mukherjee (2008).

The continuum assumption in continuum-based methods makes them not suitable for dealing with problems of complete detachment and large-scale fracture opening (Jing, 2003). Hence, it is not suitable to use it to solve complex discontinuity problems.

2.4.1.2 Discontinuum methods

DEM (Discrete Element Method): This method was first proposed by Cundall (1971) for solving rock mechanics problems involving discrete fracturing processes. The soul of this method is to divide the modeling domain into an assemblage of rigid or deformable blocks/particles/bodies (Williams and Mustoe, 1987). Explicit formulation is used in DEM, and PFC, PFC3D, UDEC, and 3DEC (Cundall, 1988; Hart et al., 1988; ITASCA, 1995) are the most representative explicit DEM codes in geotechnical engineering. Rock mass in a DEM model can be assembled by blocks or particles, and the fracturing process can be represented by the breakage of inter-block contacts or inter-particle bonds.

DDA (Discontinuous Deformation Analysis), developed by Shi (1988), is an implicit code which can simulate discontinuous behavior of rock masses.

It is required to input the geometry of the fracture network to use discontinuum methods,. DFN (Discrete Fracture Network) models can be used to generate stochastic fracture networks for that purpose. DFN models were created for the fluid flow and transport processes in fractured rock masses through a system of connected fractures (Jing, 2003; Yu et al., 1999; Zimmerman and Bodvarsson, 1996). This method is most useful for the research of flow and transport in fractured

rocks, due to its capability to consider fracture system geometry and transmissivity of individual fractures.

2.4.1.3 Hybrid continuum/discontinuum methods

It is noticed that continuum based methods require less computational resources but they are not ideal for simulating post-failure behavior of rock mass. Discontinuum-method-based models are computationally expensive to run. Therefore, there is a need to couple these two methods (continuum methods and discontinuum methods) to take advantages of the two methods and avoid drawbacks of the two methods. A large number of studies have been conducted using the coupled technique. Fox example, a FLAC/PFC coupled method was used to simulate AE (Acoustic Event) in large-scale underground excavations (Cai et al., 2007c). A coupled method was proposed to model both the pre-failure and post-failure behavior of geomaterials (Darve et al., 2004). A hybrid FEM/DEM code was used to study joint surface damage and near-surface intact rock tensile failure (Ariffin et al., 2006). In addition, methods of hybriding DEM and BEM (Lorig et al., 1986), combining DEM and BEM (Wei and Hudson, 1988), and coupling DEM and FEM for the blast wave propagation (Chen and Zhao, 1998) have been developed and used.

The FEM/DEM combined method has been used to simulate rock fracturing processes from continuum to discontinuum (Beer et al., 2004; Cai, 2008a, 2013a; Cai and Kaiser, 2004; Elmo et al., 2007; Latham et al., 2008; Mahabadi et al., 2010; Rousseau et al., 2008). Multi-scale coupled methods have been shown as a promising methodology for simulating material fracturing processes (Guidault et al., 2007; Hettich et al., 2008).

2.4.2 Main numerical methods in seismic wave modeling

This thesis focuses on numerical modeling of seismic wave propagation in underground mines. Because of the complex media in underground mines, both analytical and experimental methods are of limited use to solve seismic wave propagation problems. Rapid development in computer technology and advances in numerical schemes have made it possible to study seismic wave motion at much more detailed scale and in less time. This section reviews some numerical methods for seismic wave propagation simulation.

2.4.2.1 A brief review of wave modeling methods

There are three main methods in wavefield numerical simulation; they are (1) the geometric ray tracing method (Rizk et al., 1997), (2) the integral equation method (Marfurt, 1984; Rizzo et al., 1985), and (3) the wave equation method (Chapman, 2004; Fichtner, 2011; Li et al., 2007). The ray tracing method is based on a high frequency asymptotic of ray theory and it involves expressions of eikonal equations and transfer equations. It is suitable for seismic wave propagation in homogeneous media. This method simplifies wave theory for ray theory and focuses on kinematic features of wave without considering dynamic features of the wave. The integral equation method is based on wave superposition of the Huygens principle considering mathematical expressions of the Green function and boundary integral function. The wave equation method is based on the Newtonian mechanics theory and elastic or viscoelastic theory to solve the wave equations (a hyperbolic PDE (partial different equation)). Hence, complete information of kinematic and dynamic of the wavefield is included in the wave equation method (Li et al., 2007). The wave equation method is widely used to investigate features of wavefield but it requires high computation power.

2.4.2.2 A brief review of numerical methods for solving wavefield equations

(1) FDM: FDM is considered as the classical and most frequently applied method for solving seismic wavefield equations (Fichtner, 2011; Moczo et al., 2007a; Moczo et al., 2007b). Because spatial derivatives are approximated by difference quotients, FDM can cause numerical dispersion error that depends, among other factors, on the number of grid points per wavelength. Conventional grids (all field variables are defined at the same grid positions) are used for this method at an early stage in seismological study (Alford et al., 1974; Boore, 1970; Kelly, 1976). A breakthrough of staggered grid (field variables are defined at different grid positions) approach was created (Madariaga, 1976; Virieux, 1984), which increased the effectiveness of the method and reduced numerical dispersion. FDM can be used in more complex models that incorporate general anisotropy (Igel et al., 1995), consider free surfaces (Kristek et al., 2002), and handle material discontinuities (Moczo et al., 2007a).

(2) FEM: FEM is based on a weak or a variational form of the wave equation (Fichtner, 2011). In an FEM model, a computational domain is decomposed into sub-domains, and the dynamic fields are approximated by polynomials of different orders within each element. Hybrid schemes can be used to solve the wave propagation problem. To model wave propagation along irregular surface topography, an FEM/DEM or FEM/BEM coupled methods can be used (Bangash and Munjiza, 2002; Eibert et al., 1997; Moczo et al., 2007a). Recently, an irregular mesh has been used to model the wavefield base on GPU computing (Cherry et al., 2013), which can accelerate computation speed drastically. The FEM scheme can account for irregular geometries and free surfaces (i.e., element types of triangles, tetrahedral, hexahedra, shells, etc.), but it has a large numerical dispersion if low-order polynomial approximation is used. In addition, it is computational expensive if the mass matrix is not diagonal.

(3) Pseudo-spectral method: Similar to the FDM, this method directly discretizes the spatial derivatives (Furumura et al., 1998; Kosloff and Baysal, 1982; Wang et al., 2001b). The method comprises three distinct steps. The wavefield is first sampled at a finite number of grid points, and then transferred to wave number domain using FFT (Fast Fourier Transform) to execute space discretization, and finally transferred back to space domain employing inverse FFT. A highly heterogeneous medium can be considered (Seriani and Su, 2012). The advantage is that there is a small amount of numerical dispersion (Mizutani et al., 2000).

(4) SEM (Spectral-Element Method): SEM was originally developed in the field of computational fluid mechanics (Maday and Patera, 1989; Patera, 1984) and was later applied to addressing problems in seismic wave modeling (Faccioli et al., 1997; Komatitsch, 1997; Seriani et al., 1995). The SEM is a halfway between the FEM (higher-order) and the PSM, which is based on a high-order piecewise polynomical approxiamtion of the weak formulation of the wave equations (Komatitsch and Tromp, 1999). It combines the accuracy of the PSM with the flexibility of the FEM. In the SEM, a computation domain is divided into disjoint elements that are mapped onto a reference element. The dynamic wavefield on each element is discretized in terms of high-degree Lagrange polynomials, which are computed on the Gauss-Lobatto-Legendre (GLL) points (Cristini and Komatitsch, 2012; Komatitsch and Tromp, 2002a). As a result, a higher accuracy can be obtained. A perfectly diagonal mass matrix of the assembled discrete system is formed due to the selection of the GLL points, which greatly simplifies the algorithm and in turn leads to a fully explicit time scheme that makes it easy for parallel computation implementation. For more details on the SEM method, one can refer to Komatitsch et al. (1999), Komatitsch and Tromp (2002a), Komatitsch and Tromp (2002b), and Tromp et al. (2008).

(5) DGM (Discontinuous Galerkin method): This is a new method, developed recently by Käser et al. (2007) and Puente et al. (2007) for seismic wavefield modeling. It represents a class of finite-element methods where neighboring elements are linked by numerical fluxes, not by continuity constraints. This allows for solutions that are discontinuous across element boundaries. It is particularly suitable for modeling earthquake rupture processes (Puente et al., 2009).

2.5 A brief introduction of SEM and SPECFEM2D/3D

2.5.1 SEM and solution algorithm

SEM has been successful used to simulate seismic wave propagation resulting from earthquakes or from active seismic acquisition experiments (Komatitsch et al., 2010b; Komatitsch and Vilotte, 1998). The SEM solves the variational form of the elastic wave equation in the time domain on a non-structured mesh of elements (spectral elements) (Komatitsch and Tromp, 1999, 2002a).

For a linear anisotropic elastic rheology for a heterogeneous medium, as stated in Section 2.3.2.1, the governing equation of motion (strong form, i.e., differential formulation) is expressed by Eq. (2.8). Because the SEM solves the wave motion equation in a weak form (i.e., integral formulation), the strong system needs to be transformed into a weak form. When the physical domain of the model (Ω) and its boundary (Γ) are introduced to the strong system, the weak form of the wave motion equation is obtained by dotting Eq. (2.8) with an arbitrary test function **w** and integrating by parts over the whole model volume; then, it becomes

$$\int_{\Omega} \rho(\mathbf{x}) \cdot \ddot{\mathbf{u}}\, d\Omega + \int_{\Omega} \nabla \mathbf{w} : \mathbf{C} : \nabla \mathbf{u}\, d\Omega = \int_{\Omega} \mathbf{w} \cdot \mathbf{f}\, d\Omega + \int_{\Gamma} (\sigma \cdot \hat{\mathbf{n}}) \cdot \mathbf{w}\, d\Gamma \tag{2.10}$$

Note that the free traction-free condition is implicitly (last term in Eq. (2.10) vanished at the free surface) because the traction vector must be zero at the free surface. In SEM, the physical domain (Ω) is subdivided into a series of hexahedral non-overlapping mesh elements (Ω_e, e = 1, 2, …, n_e, $\Omega = \bigcup_{e=1}^{n_e} \Omega_e$) and the absorbing boundary Γ is also subdivided into a series of surface elements Γ_b. Variables are approximated by high order interpolants for the mesh and surface elements. Mapping between Cartesian points within a deformed, hexahedral element (Ω_e) and the reference cube is defined through a Jacobin transform. Furthermore, a combination of Lagrange polynomials interpolants with Gauss-Lobatto-Legendre (GLL) quadrature points is used to represent the displacement field in the spectral elements (Peter et al., 2011b). This combination greatly simplifies the algorithm due to the formation of a diagonal mass matrix, which permits the implantation of fully explicit time schemes (Tromp et al., 2008).

Numerical integrations over the spectral elements are required to solve the weak form of the wave equation shown in Eq. (2.10). As stated above, a GLL integration rule is used to solve the integration. The weak system in Eq. (2.10) can be rewritten in matrix form as:

$$\mathbf{M}\ddot{\mathbf{U}} + \mathbf{K}\mathbf{U} = \mathbf{F} \tag{2.11}$$

where **U** is the displacement vector that needs to be computed, **M** is the diagonal mass matrix, **K** is the stiffness matrix, **F** is the source term, and a double dot over a symbol denotes the second derivative with respect to time. More details about these matrices and the application of weak form of the wave equation can be found in Chaljub et al. (2007) and Liu (2006).

2.5.2 Introduction of SPECFEM2D/3D packages

SPECFEM2D/3D software packages, which are based on the SEM, are powerful tools for modeling seismic wave proagation at local, regional, and global scales. SPECFEM2D/3D are particularly well-suited for handling complex geometries and interfaces. They facilitate 2D and 3D simulations of acoustic, (an) elastic, and poro-elastic seismic wave propagation (SPECFEM2D, 2012; SPECFEM3D, 2014).

As stated above, the SEM method is based on a weak formulation of the equations of motion, which are solved on a mesh of elements that is adapted to the free surface. It is very suitable for handling distorted mesh elements (Oliveira and Seriani, 2011), and it can consider internal discontinuities in the model. A diagonal mass matrix can be obtained due to the combination of discretization and integration, which will greatly simplify its algorithm and reduce computing time (Tromp et al., 2008). For example, Figure 2-13 shows the application of SPECFEM3D to modeling seismic wave propagation around a mountain.

The SEM is very efficient to simulate seismic wave propagation because it combines good accuracy properties of the pseudo-spectral method with geometrical flexibility of the FEM.

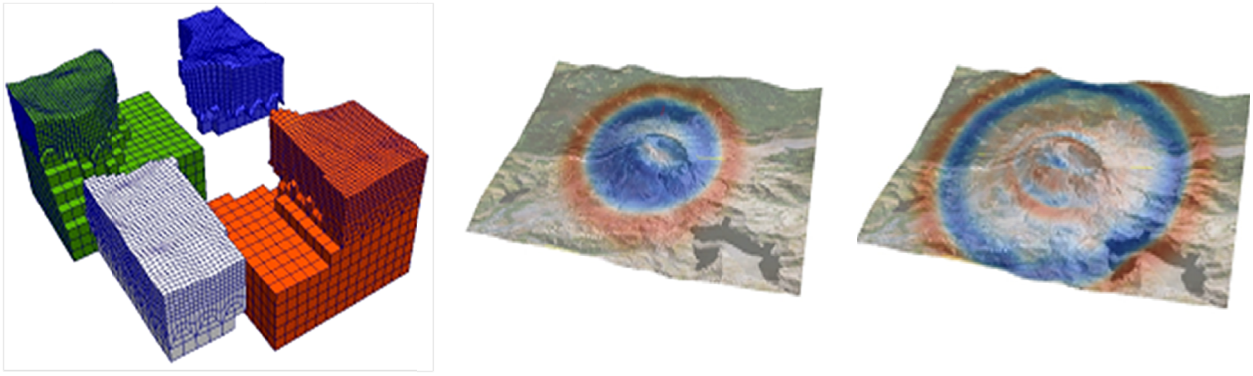

Figure 2-13: Wave propagation modeling using SPECFEM3D (from Peter et al. (2011b)). Left panel: mesh partitioned and load balanced can run in parallel (four cores that are indicated by different colors). Middle and right panels: wavefield snapshots for seismic wave modeling around a mountain, showing the vertical displacements (up and down colored by red and blue, respectively) at the free surface of the model.

Complex problems that include fluid, elastic, viscoelastic, anisotropic, or porous media can be modeled (Morency and Tromp, 2008), making it a good choice for modeling seismic wave propagation through various rock domains in underground mines.

In seismic wave modeling, boundary conditions are very important in terms of artificial wave reflection. In the SPECFEM2D/3D codes, the spectral-element solver accommodates convolution Perfect Match Layer (PML) as artificial boundaries, and convolution or auxiliary differential equation perfectly matching absorbing layers can be used in a simulation (Komatitsch and Tromp, 2003; Martin and Komatitsch, 2006). In addition, the calculation of sensitivity kernels can be performed based on adjoint modeling. Furthermore, the codes are well-suited for parallel computation on supercomputers with clusters of CPUs (Komatitsch et al., 2010b). Clusters of GPU graphics cards can also be used in numerical simulations (Komatitsch et al., 2010a; Komatitsch et al., 2009).

Many researchers have proved that these codes have very good accuracy and convergence properties. For example, a discussion on high-order numerical methods can be found in Cohen (2002), a study of high-order time stepping and high-order finite elements for acoustic or elastic wave propagation can be found in Basabe and Sen (2007, 2010), and research on dispersion analysis of SEM can be found in Seriani and Oliveira (2008).

In summary, the SPECFEM2D/3D codes have many merits in the context of seismic wave modeling in academia and in different industries such as oil and gas, ocean acoustics/sonar, non-destructive testing, and underground mining. The tools can handle distorted mesh elements accurately, take advanced PML absorbing layers, use high-order spatial and time schemes, possess relatively good convergence, obtain high degree of accuracy, demand less computation

power by hybrid (GPU) computing, consider heterogeneous and anisotropic materials, and save time by taking parallel computation.

2.6 Final remarks

This chapter provides a literature review that covers several topics related to the thesis work. To understand the phenomenon of tunnel damage localization, rockburst damage mechanisms are firstly reviewed in this chapter. For a tunnel, rockburst damage are either mining-induced from a local seismic event (near-field) or dynamically-induced from a remote seismic event (far-field). Both near-field and far-field seismic events may trigger rockburst around the tunnel. With respect to the near-field and far-field in underground mines, four groups of influence factors that may cause tunnel damage are reviewed and summarized. Due to local site effect and superposition of complex seismic waves, very high localized load can build up and lead to rock failure. Because there are many challenges in trying to study all the influence factors on rockburst damage, for simplicity, this thesis focuses on some factors such as geological structures, excavation size and shapes, internal attenuation, and excavation effect on ground motions near excavation boundaries.

Three key aspects, i.e., seismic source model, wave propagation medium, and interactions of wavefield with geological structures and excavations are briefly reviewed to have a broad understanding of seismic wave propagation in underground mines. Subsequently, main numerical methods in rock mechanics and seismic wave propagation simulation are summarized for the selection of proper research tools. Many numerical techniques have been developed and the SEM is considered as a preferred method to study wave propagation. A brief introduction of SEM and SPECFEM2D/3D is provided.

Many investigations have been conducted in wave propagation in earthquake engineering using SPECFEM; however, very few works have been conducted in using the SPECFEM codes to simulate wave propagation in underground mines. Because of the merits of the SPECFEM codes, it opens the door to close the gap between wave modeling in earthquake engineering and mining engineering. It is expected that the SPECFEM codes can find their application in mining engineering.

Chapter 3

3 Validation of SPECFEM2D and Parametric Study

From the literature review presented in Chapter 2, SPECFEM2D software was selected as the research tool to simulate seismic wave propagation in underground mines in this thesis. Prior to conducting further simulation, a validation of the SPECFEM2D tool is needed. After the validation, a parametric study of seismic source is required to examine the influence of input source parameters on ground motions.

3.1 Validation example: Garvin's problem

The SEM has been well benchmarked against several classical problems with exact analytical solutions (Komatitsch and Vilotte, 1998), such as the Lamb's problem (Lamb, 1904; Virieux, 1986), the Garvin's problem (Ricciardello et al., 2011; Sánchez-Sesma et al., 2013), and the two-layer model (Komatitsch and Tromp, 1999; Peter et al., 2011a). To further validate the SPECFEM2D code, the Garvin's analytical solution is selected to validate the modeling results. The source of the Garvin's problem (Figure 3-1(a)) is a compressional point source that is buried in an elastic, homogenous, and isotropic half-space with a free surface, which can be used to mimic a seismic source located in underground mines. The solution of the seismic response is obtained analytically using the Cagniard-De Hoop technique and is convolved with the source-time function and the solution can be obtained by the code of EX2DVAEL from SPICE (http://www.spice-rtn.org).

The validation model has a horizontal width of 4 km and a buried depth of 2 km, and is discretized into 200 × 100 spectral elements with an element size of 20 m, as shown in Figure

3-1(b). Absorbing boundaries are applied to the bottom, left, and right edge model boundaries. The top edge of the model is set as free surface which allows wave refraction and reflection. Two cases of validation are considered. Two lines of receivers are placed from x = 2 km to x = 3 km at the free surface (Case A: z = 0 m) and inside the model (Case B: z = -200 m). A moment-tensor point source is placed at (x, z) = (2000, -500) m and (x, z) = (2000, -700) m for Cases A and B, respectively. The source time function is a Ricker wavelet with a dominant frequency of 14.5 Hz. The model runs 6000 steps with a time step of 0.2 ms, which lasts 1.2 s for the simulation.

The main events of the Garvin's problem are direct P waves, reflected P waves, and a P-to-S wave conversion at the surface, which can be clearly identified in the modeling results indicated

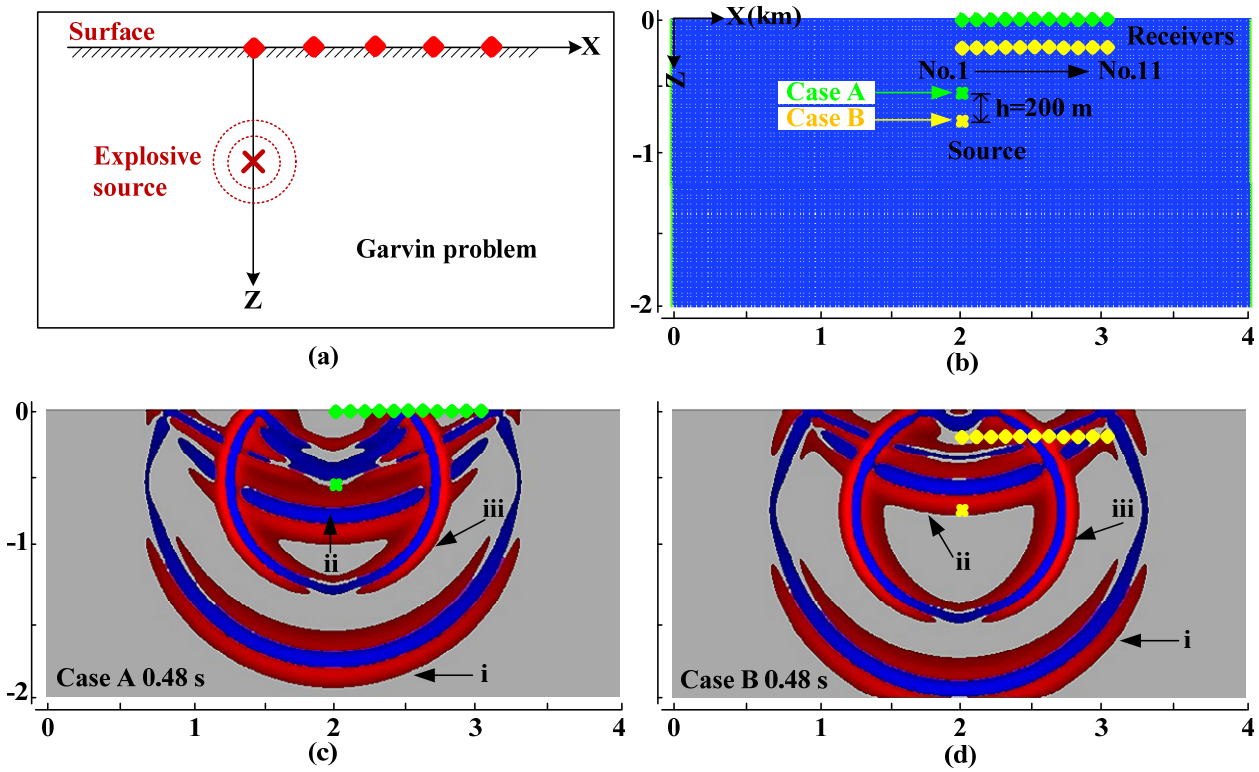

Figure 3-1: The Garvin's problem (a) and the validation model (b) and typical snapshots of vertical displacement field showing wave propagation at 0.48 s for Cases A and B, which are shown in (c) and (d). The green and yellow crosses indicate the source locations for Cases A and B. 11 receivers with a 100 m spacing from x = 2 km to x = 3 km are placed for each case. Upward and downward movements are colored as red and blue in (c) and (d), respectively.

by i, ii, iii respectively in Figure 3-1(c) and (d). Figure 3-2 presents the analytical solutions of the displacement seismograms at receiver No.6, which is located at (x, z) = (2500, 0) m and (x, z) = (2500, -200) m for both Cases A and B. It is seen that the seismograms from the numerical modeling match well with those from the analytical solutions, which exhibit almost identical displacements In the meantime, absolute residuals between the amplitude results of modeling and analytical are also plotted in Figure 3-2 and the maximum waveform differences remain a very small value which further validates the accuracy of SPECFEM2D. Good agreements are also found for other receivers, and Figure A - 1 presents a comparison of the numerical and the

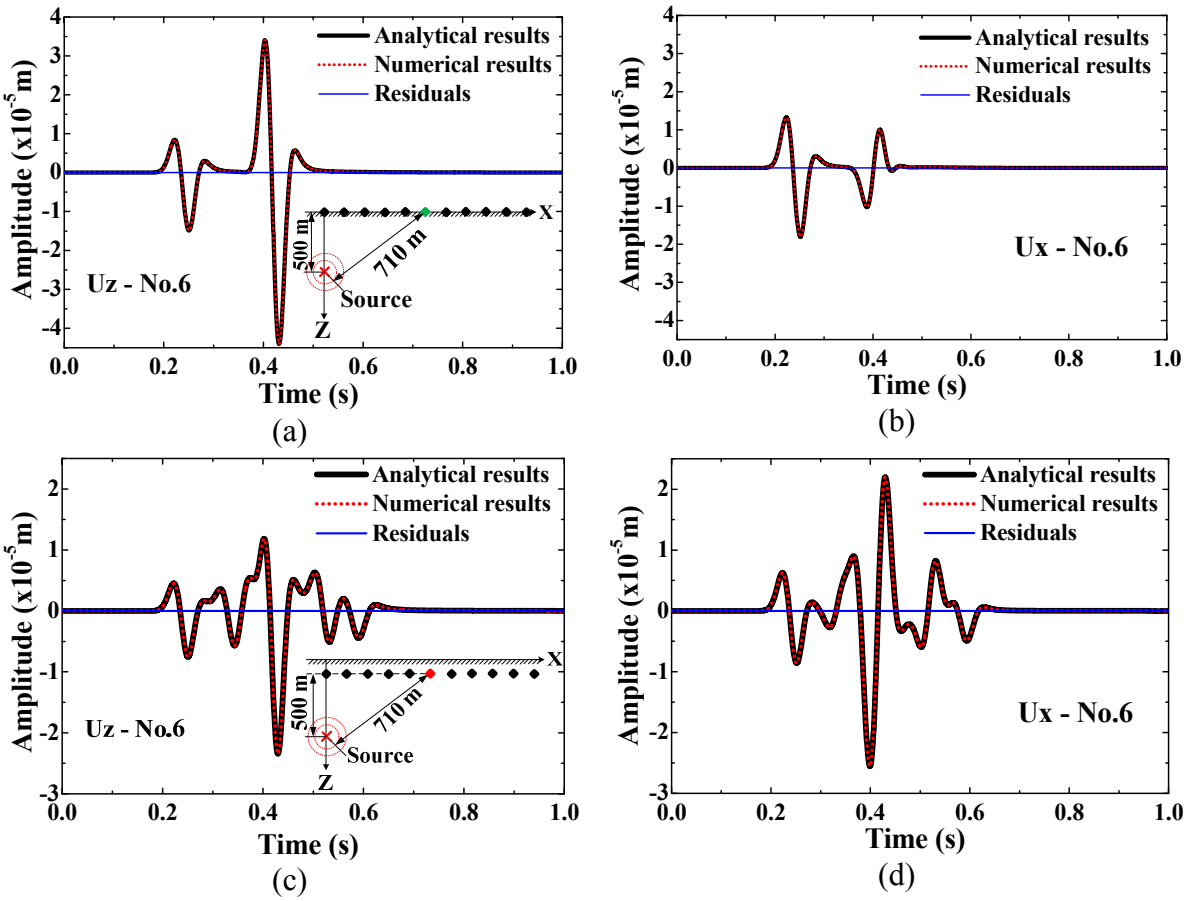

Figure 3-2: Seismograms of displacement for receiver No.6 for two validation cases. Receiver No.6 is placed at the free surface/inside the model for Cases A and B, which is shown as green/red dot in the small insert in the lower-right of (a) and (c), respectively. Components of vertical (U_z) and horizontal (U_x) displacements are shown in (a)/(c) and (b)/(d), respectively. The modeling results of displacement (red dot line) are plotted against the analytical solution (black solid line), and the absolute residuals (blue solid line) are displayed in the same plot.

analytical results for receiver of No.11 located at (x, z) = (3000, 0) m and (x, z) = (3000, -200) m for the Cases A and B.

It is seen from Figure 3-2 that the Garvin's problem is successfully solved by SPECFEM2D and the modeling results agree with the analytical solution very well. As mentioned above, SPECFEM2D has been verified by other researchers using classic problems such as the Lamb's problem and the two layer media model problem. It is hence confirmed that the implementation of SPECFEM2D is accurate for this simple case of the analytical solutions and it can be used for seismic wave propagation modeling.

3.2 Wave patterns of SF and DC source models

Two point source models (SF – single force and DC – double force) are used to simulate wave propagation in a homogenous isotropic medium to further demonstrate the application of SPECFEM2D and illustrate the wave pattern differences due to different point source models. The seismic source is placed at the center of the model with a dimension of 308 m × 308 m, and the source types are shown in the left-insert in Figure 3-3.

Figure 3-3 shows snapshots of displacement wavefields for the SF and DC point source models. It is shown that different radiation patterns are observed for the SF and DC point source models. The most significant difference is the direction of ground motion and the rotation angle between the horizontal U_x and the vertical U_z components. For the SF model, a outer (P-wave) and inner (S-wave) wavelets have the same direction of motion; however, for the DC model, the wave pattern follows that caused by a normal fault slip (as discussed in Chapter 2) and the outer (P-wave) and inner (S-wave) wavelets do not have the same motion direction. Compared the first two columns of wavefield caused by the SF model with the last two columns of wavefield

caused by the DC model and recall the fault-slip radiation pattern shown in Chapter 2, it is concluded that the DC point source model is suitable for far-field wave propagation modeling due to a fault-slip seismic event.

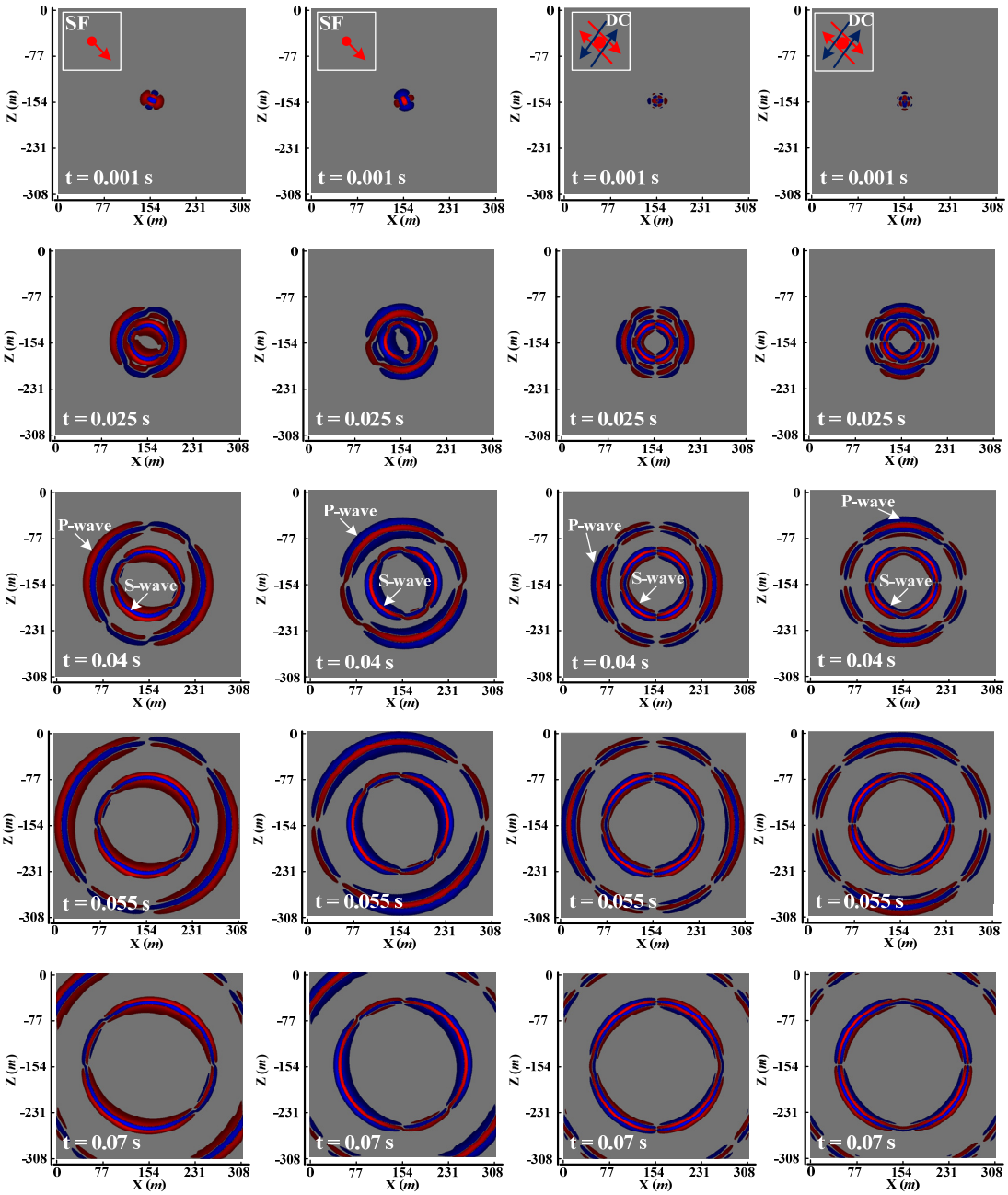

(a) SF U_x (b) SF U_z (c) DC U_x (d) DC U_z

Figure 3-3: Wave propagation patterns simulated using SPECFEM2D for seismic sources of SF (single-force) and DC (double-couple) in a homogenous and isotropic medium. Red and blue denote upward and downward or right and left movements, respectively. Snapshots of displacement wavefields of the SF and DC source models are selected to show different wave patterns at five wave propagation times (0.001, 0.025, 0.04, 0.055, 0.07 s).

3.3 Application of PML (perfect match layer) absorbing boundary

Artificial absorbing boundaries are needed at the four computation edges in numerical modeling of seismic wave propagation to absorb wave energy and eliminate spurious wave reflections from the model boundaries. Numerous techniques such as sponge, paraxial conditions, asymptotic operator have been developed for this purpose over the past decades (Martin et al., 2010; Sochacki et al., 1987; Stacey, 1988). However, a large amount of spurious energy reflection at boundary and the requirement for large computation power are two main issues. On the other hand, perfect matched layer (PML) absorbing boundary has proven to be very efficient for the absorption of elastic waves in numerical modeling (Komatitsch and Tromp, 2003).

In the SPECFEM2D/3D codes, the PML absorbing boundary is incorporated and it can be assigned to different parts of the boundary in a model, such as the top, bottom, left, right, left top and bottom corner, right top and bottom corner, as shown in Figure 3-4. The model simulations are conducted with and without PML to illustrate efficiency of the PML absorbing boundary.

Figure 3-5 presents a comparison of vertical displacement snapshots with and without the PML absorbing boundary. The dimension of computation domain is 208 m × 248 m. A horse-shoe shaped tunnel (6 m × 8 m) is located in the lower part of the model (highlighted by a blue area). The top panel (a) shows modeling results without using the PML absorbing boundary, and spurious reflection waves can be observed. When the PML absorbing boundary is applied, no reflection results from the outer boundary. The only reflection in the model is coming from the tunnel located in the model where no PML absorbing boundary is applied.

As can be seen from Figure 3-5, spurious reflection waves (highlight by yellow dash lines) in model (a) are suppressed efficiently in model (b) by imposing the PML boundaries at all

computation edges for both P- and S-waves. Clearly, the PML absorbing boundary is efficient for both P and S-waves. Using the PML absorbing boundary, a smaller model can be used without worrying about the influence of model boundary on the waveform (i.e., causing spurious waves). The PML absorbing boundary will be used throughout the thesis research.

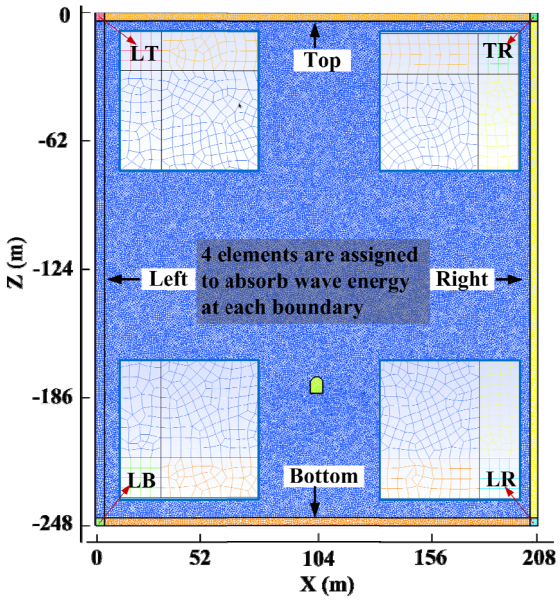

Figure 3-4: PML absorbing boundaries are imposed around the computation domain. The dimension of this model is 208 m × 248 m, which is meshed by the Gmsh tool kit. Eight PML absorbing boundaries are placed around the domain, i.e., top, left, bottom, and right side, plus the left-top and bottom corners and the right-top and bottom corners (see the insert for close-up views). The width of the PML is four elements for each absorbing layer.

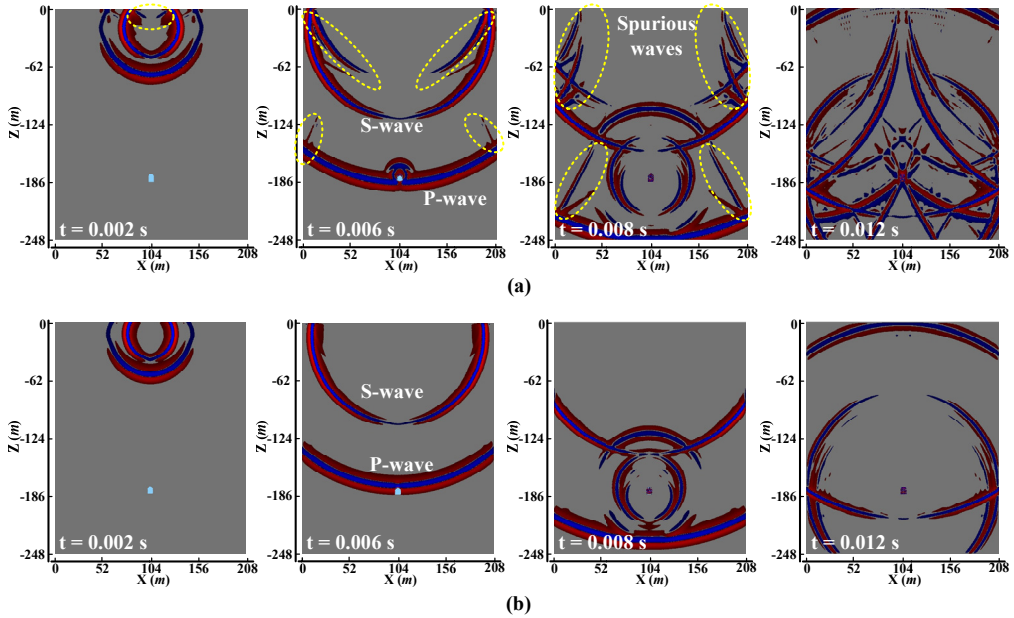

Figure 3-5: Snapshots of vertical displacement component of propagating seismic waves at four times (t = 0.002, 0.006, 0.008, and 0.012 s) without (a) and with (b) the PML absorbing boundary.

3.4 A parametric study using SPECFEM2D

The purpose of this section is to investigate the influence of model source parameters on seismic wave propagation and ground motions. In the SPECFEM2D package, source parameters include location, source types (elastic point force or moment tensor source), time function, source angle, dominant frequency, etc. A systematical parametric study will assist in a proper use of the tool for wave propagation modeling.

3.4.1 Models and model parameters for the parametric study

For the parametric study, wave propagation due to a seismic source in a homogeneous and isotropic medium with a horse-shoe shaped tunnel located in the center of the model is considered. The model setup is shown in Figure 3-6, along with the model parameters and the types of seismic sources that are studied in the work. Receivers (red and blue) are placed along the boundary of the tunnel and in eight monitoring lines to capture the waveforms and to calculate the PPV.

The dimension of the computation domain is 308 m × 360 m. The size of the horse-shoe shaped tunnel is 6 m × 8 m (highlighted by the blue area in the center of model). The computation domain contains 15,300 spectral elements, meshed at about 1 m grid spacing. A time step of $\Delta t = 6.0 \times 10^{-6}$ s is used and the waves will propagate 0.084 s (i.e., 14000 time steps). As shown in Figure 3-6(a), 75 receivers are placed around the tunnel (denoted by the blue and red dots) and the position of each receiver is displayed and zoomed in on the upper left corner (red dots show the receivers around the tunnel surface) and lower right corner side (blue dots denote the receivers placed in the vicinity of the tunnel). The spacing between two adjacent receivers is 1 m.

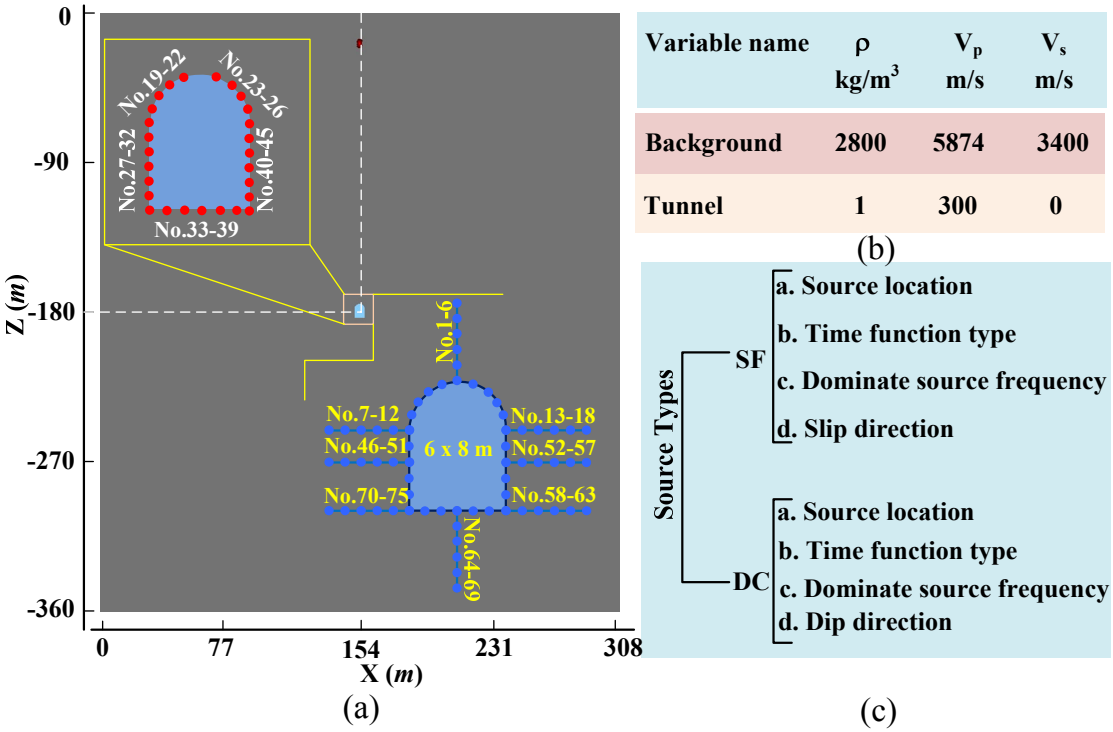

Figure 3-6: 2D model for the parametric study of wave propagation in a homogenous and isotropic medium.

The properties of the model are tabulated in the left upper corner panel in Figure 3-6(b), where ρ, V_p, and V_s are the density, P- and S-wave velocities, respectively. The tunnel is filled with air so that the air properties are assigned to the tunnel region. The main source parameters, which will be discussed in the following, are summarized in Figure 3-6(c). All the source parameters are important for wave propagation study and a thorough investigation is conducted. All the external boundaries are set as the PML absorbing boundaries.

3.4.2 Parametric study of seismic source

3.4.2.1 Source time functions

In numerical seismic wave modeling, many factors such as source time function and geological structures can alter synthetic seismograms. As discussed extensively in some books and papers (Chapman, 2004; Fichtner, 2011; Hatherly, 2013; Hildyard et al., 2005b; Sato et al., 2012), source time function is one of the most important factors in seismic wave modeling. Different

time functions, such as the Ricker time function, the Gaussian time function, and the Dirac time function, are investigated.

For a SF (Single Force) point source model, a seismic source with a high dominant frequency of 300 Hz is located at the upper-right corner (x = 270 m, z = -20 m), and the slip direction is assumed to be 135°. For the a DC (Double Couple) model, the seismic event is assumed caused by a normal fault with 45° dip and with a dominant frequency of 300 Hz. It should be mentioned that 300 Hz is a relatively high dominant frequency, which is not normal found in underground mine for a relatively large seismic event. The reason to use 300 Hz as the dominant frequency in this chapter is that the ground motion is more sensitive to high frequency waves. A receiver is placed exactly at the source location for the purpose of recording the seismogram for each case. Figure 3-7 shows the velocity seismograms of a source receiver for different source time functions. Different velocity amplitudes can be found at t = 0 for different time functions. The Dirac and the Heaviside time functions produce large velocities at the source (the largest values are roughly 130 m/s and 61 m/s respectively), while the Ricker and Gaussian time functions produce relatively low velocities at the source (the highest values are about 21 m/s and 13 m/s for the Ricker and the Gaussian time function, respectively).

PPV values at the receivers placed around the tunnel are presented in Figure 3-8. The PPV distributions around the tunnel surface ((a) and (b)) and inside the rock mass ((c) and (d)) for the SF and the DC source models show a similar trend for all the four time functions. However, different time functions will lead to different PPV values at the same location. The Heaviside time function produces the highest PPV compared with that from other three time functions. When the DC point source model (as shown in Figure 3-8(b) and (d)), for instance, it is evident that similar PPV distributions are found for the surface receivers and for the inside rock mass

receivers (assumed borehole receivers) for all the four time function cases. In addition, the Heaviside time function produces the highest PPV values and the Gaussian time function produces the lowest PPV values for the receivers.

Different time functions can be used as the source time function in seismic wave propagation modeling. One should be careful to select the source time function. As known, the Ricker time wavelet (the second derivative of a Gaussian function) is a zero-phase wavelet and it is a widely used source time function for numerical modeling of seismic wave propagation. The Ricker time function will be selected as the source time function in the subsequent analysis.

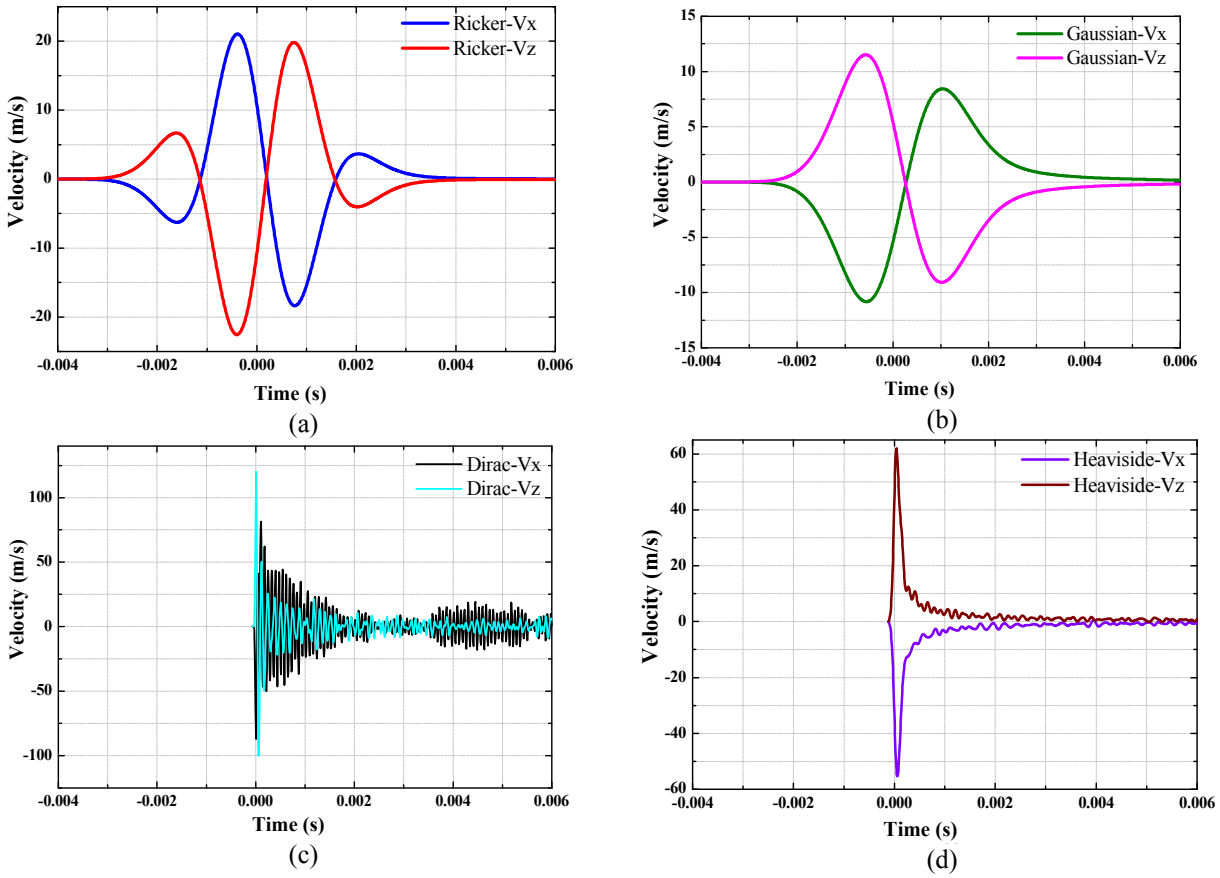

Figure 3-7: Various source time functions used in the simulations for the SF and DC models. Different line colors denote vertical (V_z) and horizontal (V_x) velocity components for the Ricker (a), Gaussian (b), Dirac (c), and Heaviside (d) time functions.

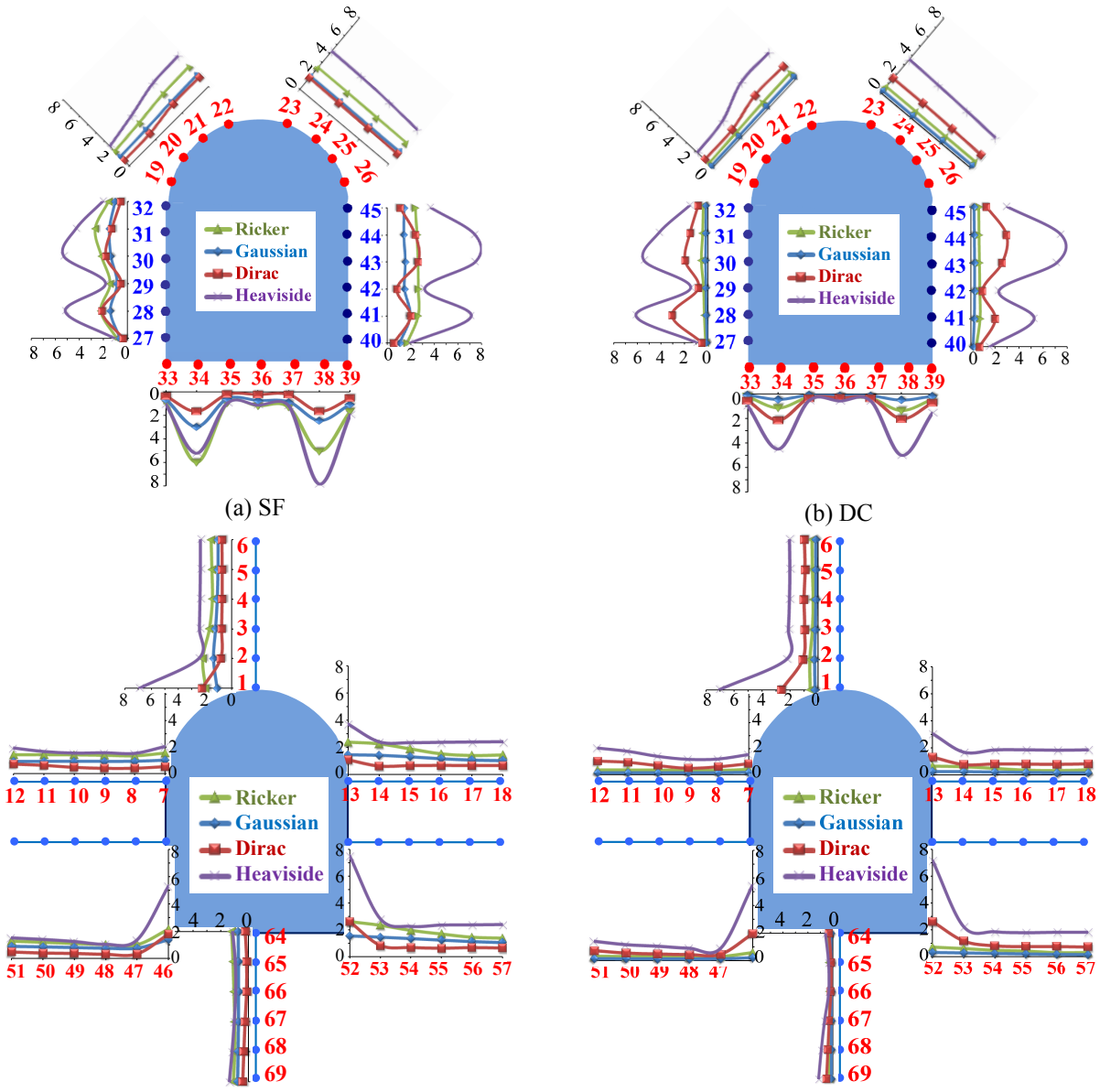

Figure 3-8: PPV (m/s) distributions of receivers around the tunnel when receivers are located at the tunnel surface ((a) and (b)) and in the assumed borehole lines ((c) and (d)) for the SF and DC point source models.

3.4.2.2 Dominant source frequency

It is known that a faulting process of a fault slip is normally associated with high spike impulse and high frequency components may excite near the source regions. The high frequency components will be absorbed due to attenuation effect in the medium and relatively stable dominant frequency components will exist in the seismic waves after a certain propagation

distance. In this section, dominant frequency is changed to examine the influence of the dominant frequency on ground motions. The seismic source is represented by the SF and DC point source models with a Ricker time function. The seismic source is assumed at the upper-right corner of the model, which is at x = 270 m, z = -20 m. It should be mentioned that only dominant frequency is changed and other source parameters are not changed in this modeling practice to check the influence of dominant frequency on ground motions. The seismic energy will increase as the dominant frequency increase in the numerical modeling. In other words, this is just a numerical practice and the modeling results do not necessary link to the physical reality.

Figure 3-9 shows the PPV distributions around the tunnel for four dominant frequencies. From Figure 3-9, high PPV are observed when relatively high dominant frequencies are used. PPV increases around the tunnel with the increases of the dominant frequency for both the SF and DC seismic source models. Ground motions at the receivers under different dominant frequencies follow basically the similar trend. As expected, the synthetic seismograms at receivers No.38 (the SF model) and No.52 (the DC model) (Figure 3-10) indicate that more oscillations can be observed and the particle motion velocity is higher with the increase of the dominant frequency.

According to field observations from some investigators (Gibowicz et al., 1990; Larsson, 2004; Salamon, 1981; Yang et al., 2009), dominant frequency of recorded seismograms ranges from several to a few hundred Hz in underground mines for seismic events. The dominant frequency range corresponds to the size of seismic event. In general, low dominant frequency is found for a relatively large source event and vice versa. Furthermore, because of the complex reflection and refraction of seismic wave propagation in underground mines, high frequency components are usually observed in the recorded seismograms. A detailed study of the influence of different frequency components on ground motion are conducted in Chapter 4.

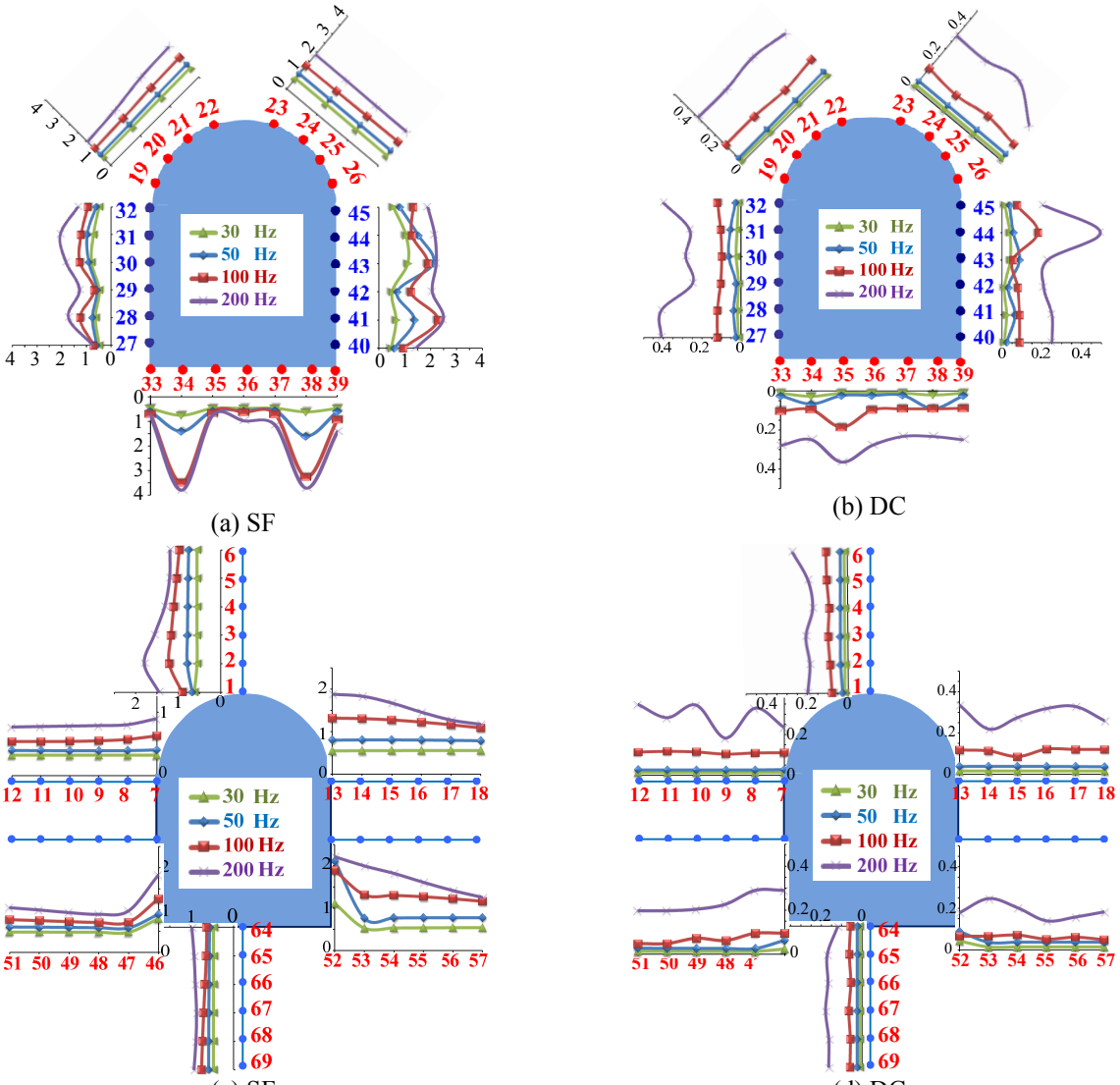

Figure 3-9: PPV (m/s) distributions at receivers around the tunnel under four dominant frequencies for the SF ((a) and (c)) and the DC ((b) and (d)) point source models.

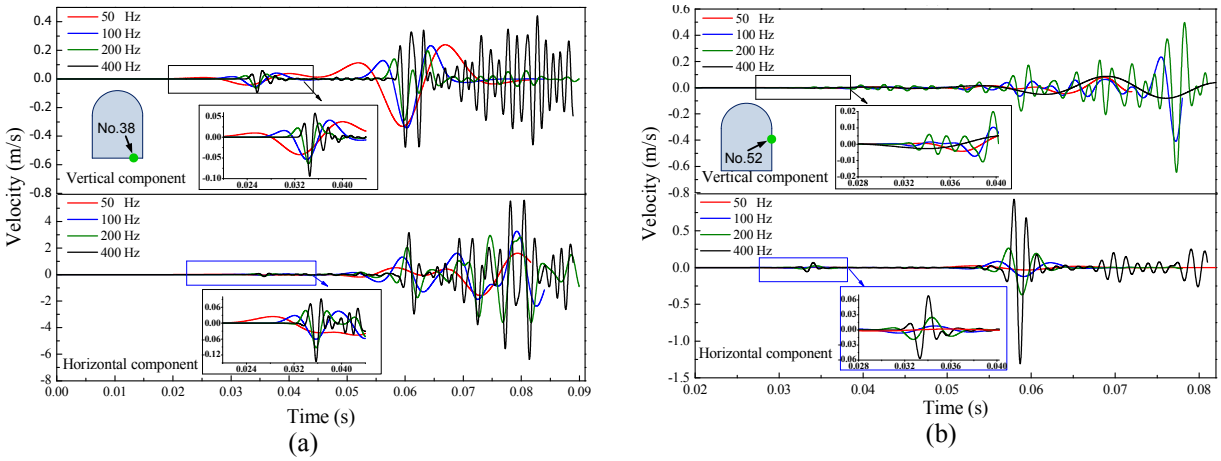

Figure 3-10: Synthetic seismograms at two selected receivers (No.38 and No.52) for four dominant frequencies for the SF (a) and DC (b) models. The locations of receivers No.38 and No.52 are denoted by the insert sketches).

3.4.2.3 Source location

High uncertainty of seismic source location is expected in underground mines, even when the fault location is known. In mine design considering potential future seismic events, sometimes, the event locations may not be determined with a high degree of confidence. A design seismic source is placed at different positions in the model (Figure 3-11) to reveal the ground motion around the tunnel and identify potential high PPV areas. In Figure 3-11, the seismic sources are located at the top side (Case 1 to Case 4), bottom side (Case 5 to Case 11), and right side (Case 12 to Case 15) of the computation domain. A total of 15 source locations are considered for both the SF and the DC source models. The source parameters are kept the same for different cases to reveal the influence of source location on ground motions.

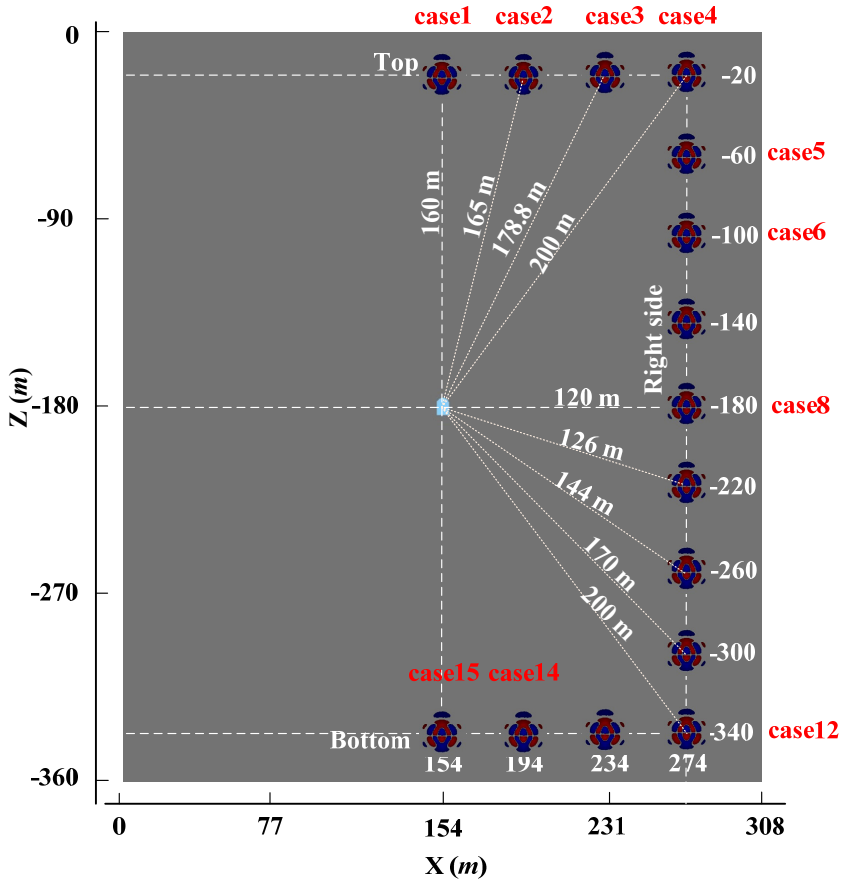

Figure 3-11: Locations of various seismic sources in the computation domain. Only source locations in the right part of the model are shown because of the model symmetry. The interval of each source location is 40 m for both the x and z directions. The source is initiated by either the SF or the DC source model.

Figure 3-12 depicts the PPV distributions of the receivers around the tunnel at different seismic source locations for the SF and DC source models. In Figure 3-12, the x axis shows the source-receiver distance for all the receivers around the tunnel for each modeling case. It should be mentioned that the PPV values of two neighbor points in Figure 3-12 do not necessarily correspond to the PPV values of two adjacent receivers. From Figure 3-12, firstly, for both the two source models, the PPV distributions for most receivers show the same trend except for some receivers. For instance, certain receivers such as receivers No.34, No.38, No.41, and No.44 (the insert small figure) for the SF and DC models show relatively high PPV values for the top source cases (Figure 3-12(a) and (b)).

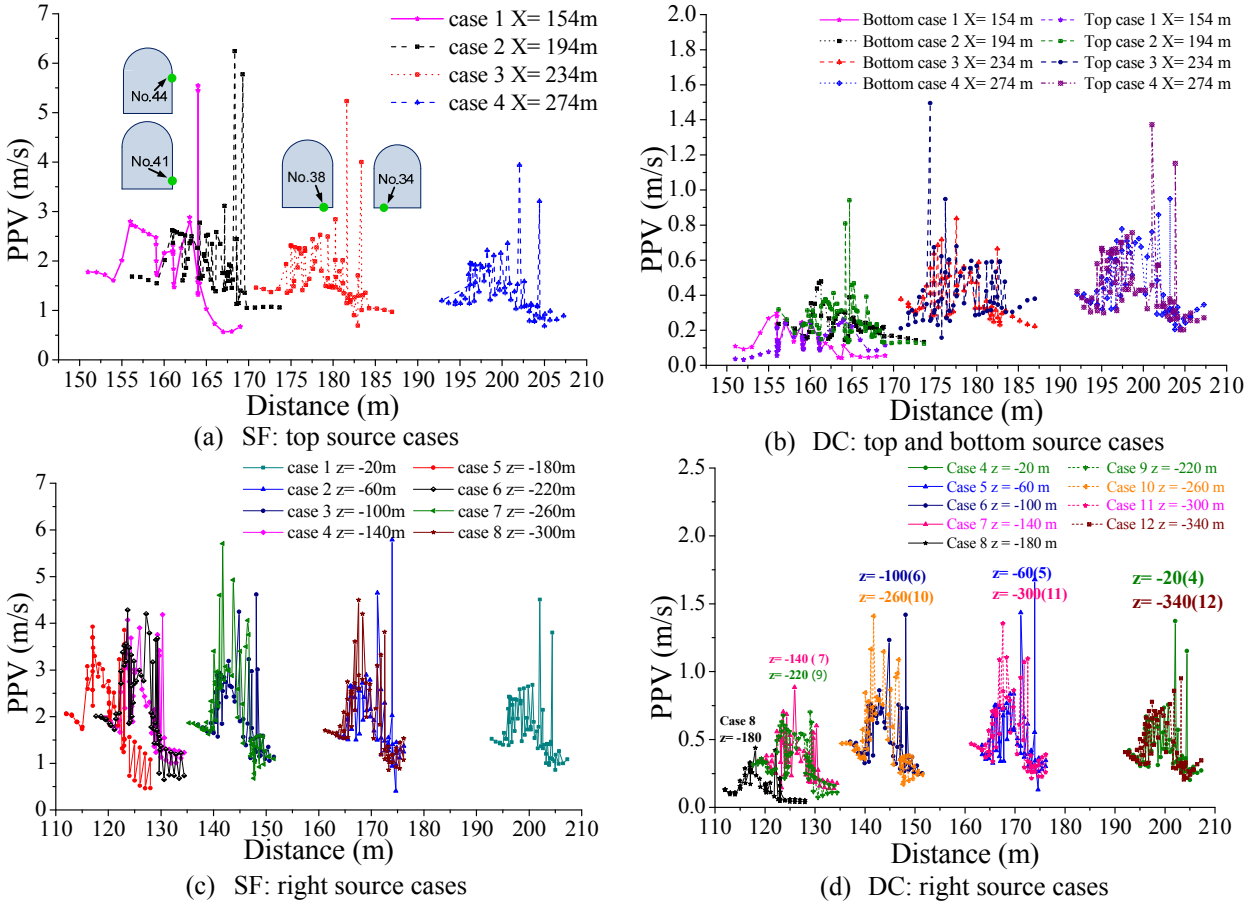

Figure 3-12: PPV distributions at 75 receivers that are placed around the tunnel for the SF and DC source models. (a) and (c) present top source and right source cases for the SF source model, respectively. (b) and (d) present top and bottom and right source cases for the DC source model, respectively. The x-axis is sorted by the source-receiver distance and the PPV values of two neighbor points in this figure do not necessarily correspond to the PPV values of two adjacent receivers.

Secondly, Figure 3-12(b) shows the PPV distributions for the top and bottom source location cases of the DC models. Compared with the PPV distributions of the bottom seismic source cases (Case 15, Case 14, Case 13, and Case 12), some higher PPV values can be observed for the top source location cases (Case 1, Case 2, Case 3, and Case 4). This may indicate the PPV distribution is affected, more or less, by the geometry or shape of the tunnel.

Thirdly, Figure 3-12(c) and (d) present the right side source location cases (Case 4 to Case 12) for the SF and DC source models. It is seen that the PPV distribution of each source location case shows similar trends, albeit the different peak velocity amplitude. At the same time, what is the most interesting in the PPV distribution is that the source-receiver distance is not the only control factor that influences PPV value. For example, relatively high PPV values can be found at a relatively large source-receiver distance. The smallest distance is 120 m for the right source location Case 8 (z = -180 m). However, the smallest PPV value can be identified for this case. The PPV values around the tunnel depends not only on source-target distance, but also on other factors such as seismic source, spatial location of the tunnel, propagation direction of the seismic wave which may cause a large alteration to the ground motions. Some extreme PPV values of ground motion around the tunnel (mostly occurred on the tunnel surface) are expected due to the high dominant frequency (e.g., 300 Hz) is used. These high PPV values may result from the complex wave interaction with the opening (more notable for very high dominant frequency), and as mentioned above, which are not necessarily linked to the physical reality.

3.4.2.4 Slip direction of the SF model

As stated in Section 3.2, the radiation patterns for a SF model are different with various slip directions. Figure 3-13 presents a simple sketch that describes the influence of slip direction (for SF source model) on wave pattern. The slip direction is varied from 0° to 360° at an increment of

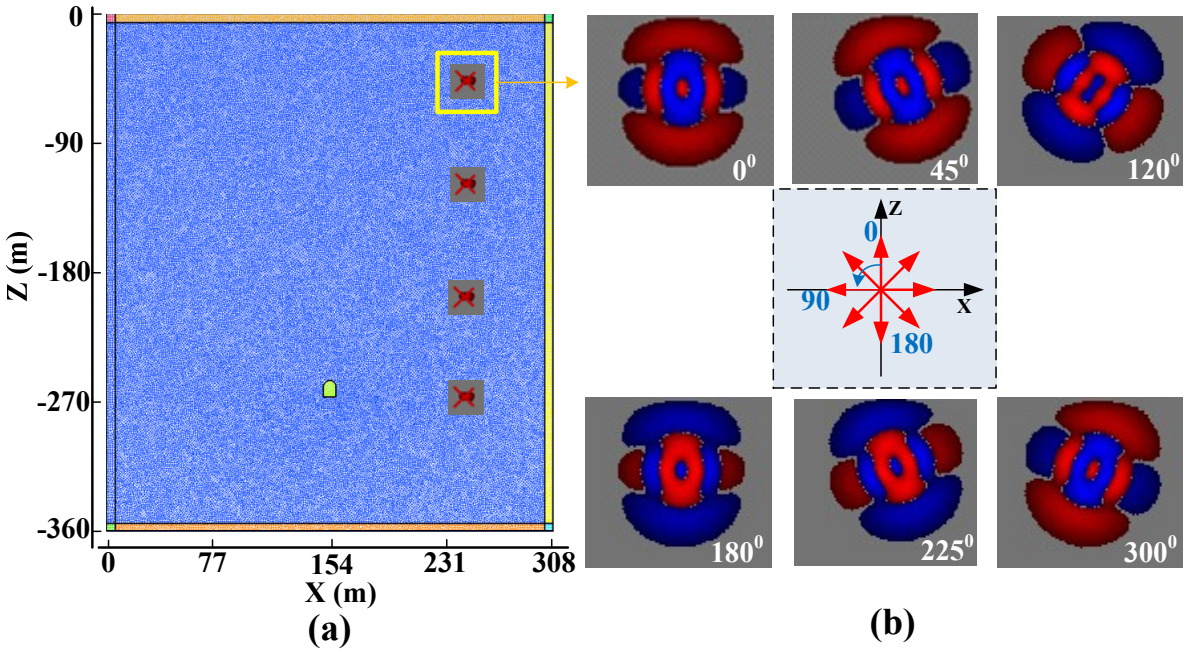

Figure 3-13: A sketch of slip direction of the SF seismic source model. 0^0 is defined along the positive z-axial direction and the slip direction increases in the anticlockwise direction (see the right middle panel). The radiation pattern is symmetric by 180^0; however, the radiation direction is exactly the opposite.

15° at each source location to study the influence of slip direction on wave propagation patterns. As mentioned above, 15 source location cases (with a 300 Hz dominant frequency) are considered, and 24 slip directions (from 0° to 360°) are considered for each source location. PPV value at each receiver is calculated and analyzed to identify the highest PPV location around the tunnel. The slip direction that corresponds to the maximum PPV can thus be identified.

The seismic sources are placed at three sides of model: the top side (Case 1 to Case 4, z = -20 m, x range from 154 to 274 m), the bottom side (Case 12 to Case 15, z = -340 m, x range from 154 to 274 m), and the right side (Case 5 to Case 11, x = 274 m, z ranges from -20 to -340 m with an increment of 40 m). For each source location, PPV due to various slip direction is obtained. Figure 3-14 shows the PPV distributions at some selected receivers around the tunnel for Case 5 when the seismic source is located at x = 274 m, z = -60 m for various slip directions. As can be seen from the figure, the PPV distribution is symmetric by 180° when the slip directions change

from 0° to 360°. PPV presents increasing and decreasing phases as the slip direction changes. The maximum PPV is reached at all receiver locations when the slip direction is about 45°/225°. Moreover, the floor area (Figure 3-14(e)) and the right wall area (Figure 3-14(f)) show a high PPV magnification compared with the PPV from other receivers around the tunnel, meaning that these areas may suffer more ground motion. The extremely high PPV values for receivers No.34 and No.38 in the floor area are caused by the high dominant frequency used in this modeling.

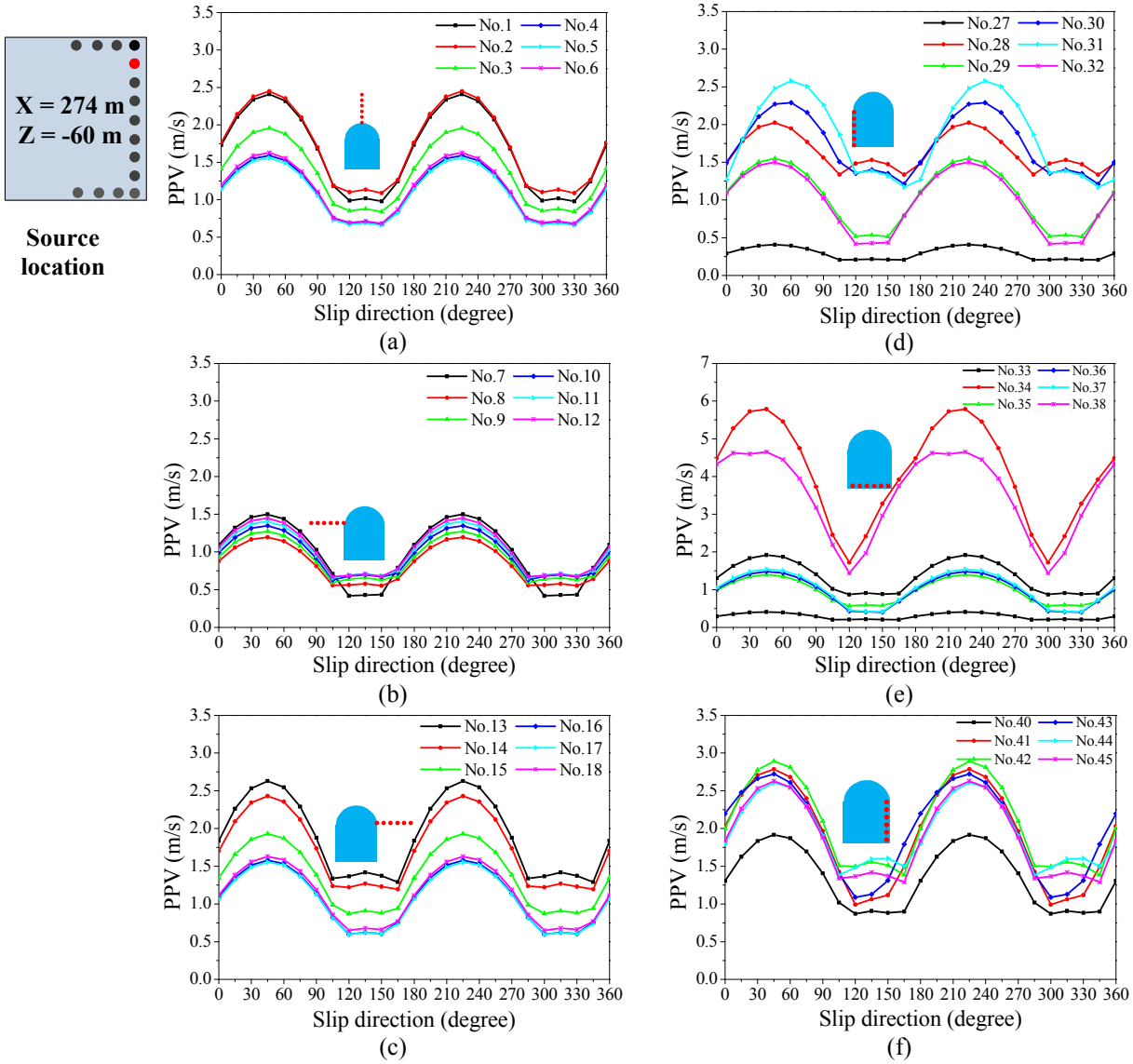

Figure 3-14: PPV at receivers placed in some boreholes around the tunnel ((a), (b), and (c)) and at the tunnel surface ((d), (e), and (f)) for various slip directions in the SF source model. The numbering of receivers can be seen in Figure 3-6. In Case 5, a SF source is located at x = 274 m, z = -60 m (see the top-left small insert sketch). The slip direction is changed from 0° to 360° and the maximum PPV can be found at slip directions of 45° and 225° at all the receivers.

Similar analyses are conducted for different sources located at the top, bottom, and right sides as shown in the illustration figures in Figure 3-15, and the results are presented in the same figure. The PPV distributions against the slip direction are calculated for receivers No.1 to No.6, which are placed in the roof of the tunnel. The slip directions that correspond to the maximum PPV for each source location are shown in Figure 3-15. The results imply that the slip direction of the SF source model has a large influence on the ground motions. The maximum slip directions keep changing as the seismic source locations change. A 40 m increment change in the top and bottom source locations corresponds to a ±15° changing of the maximum slip direction and similar

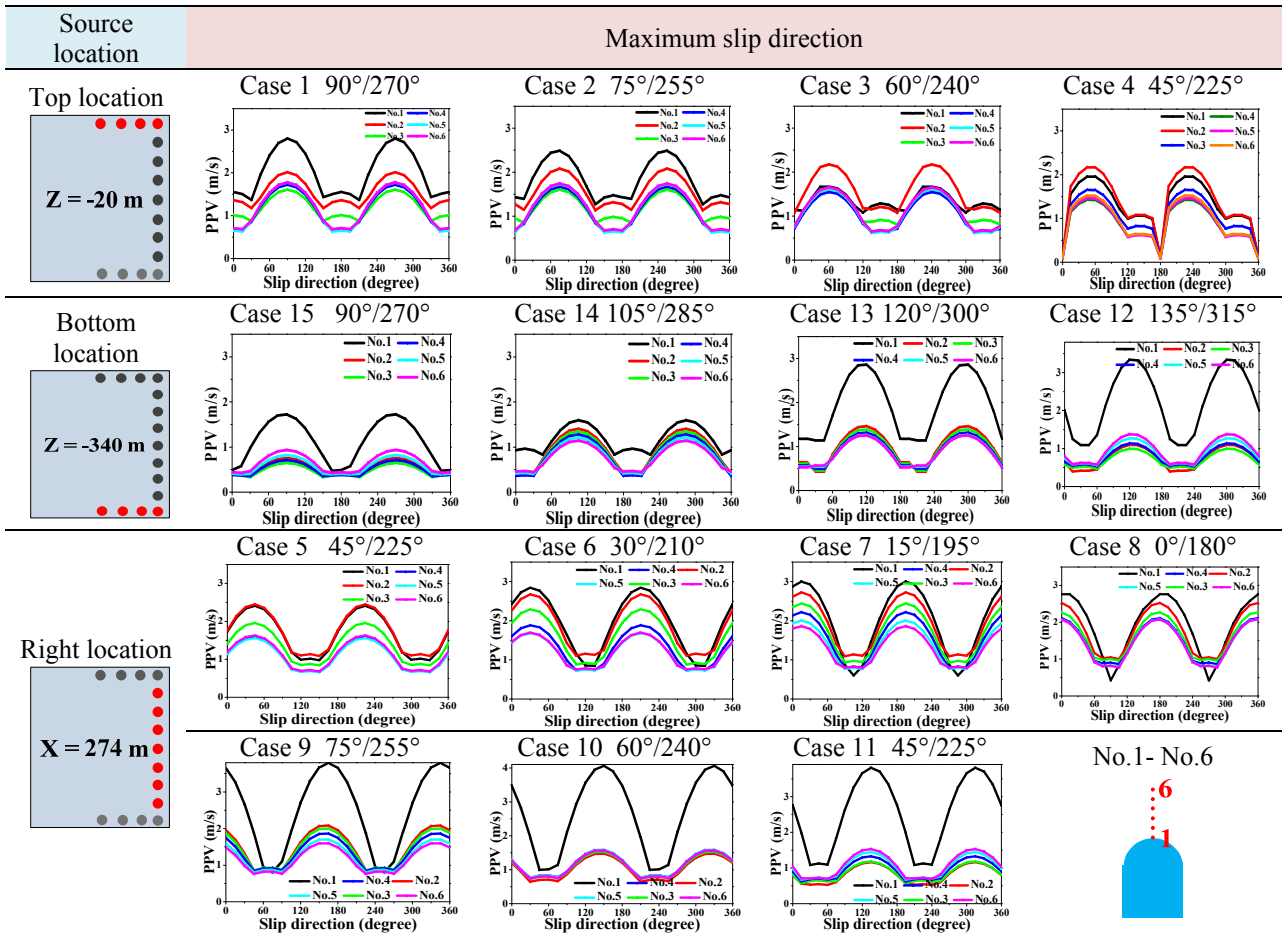

Figure 3-15: Slip directions that correspond to the maximum PPV at different source location cases (from Case 1 to Case 15) for the SF source model.

tendency can also be found in the cases where the sources are located on the right side (Case 5 to Case 11) of the model. The results indicate that the slip direction can lead to different seismic responses around the tunnel. In addition, higher ground motions are observed when the receivers are located close to the tunnel surface and at the tunnel surface. The closer a receiver is to the tunnel surface, the higher the PPV will be observed (i.e., No.1 and No.2).

Receivers associated with the maximum PPV for each set of receivers are selected and the results are presented in Figure 3-16 to identify the area of the highest ground motion around the tunnel. The maximum ground motion changes as the seismic source changes its location spatially. Although the ground motion patterns are complex, several potential high PPV areas can be identified. The high PPV areas are highlighted as light red areas in Figure 3-16. When the seismic source is located at the top (Case 2 and Case 3) and bottom (Case 13 and Case 14) sides of the model, the right floor and wall as well as part of the right roof of the tunnel will be subjected high ground motions. Compared with the roof, the right floor and wall will experience higher ground motion (Figure 3-16(a) and (b)). In the meantime, the right wall side of the tunnel will experience larger ground motions higher than that on the left wall side of the tunnel. This is because that the seismic source is located in the right hand side of the tunnel, meaning that a tunnel may have a higher ground motion in the side of the tunnel that faces the direction of incoming seismic waves. Similar high ground motion areas can be found in the top of the tunnel if the seismic source is located in the upper-right hand side (i.e., Case 5 in Figure 3-16(c)). However, the left roof and wall will have a high ground motion when the source is located in the lower-right side of the model (i.e., Case 11 in Figure 3-16(c)). The results indicate that different tunnel responses to seismic wave loadings, such as floor heave, spalling and rock falls, can be potentially linked to various radiation patterns around the tunnel caused by the interaction of the

incoming seismic waves and the tunnel. Because very dominant frequency (300 Hz) is used and a strong velocity contrast is introduced in the models, large wave amplification at certain area of the tunnel is expected, particularly on the tunnel surface (e.g., No.34 and No.38).

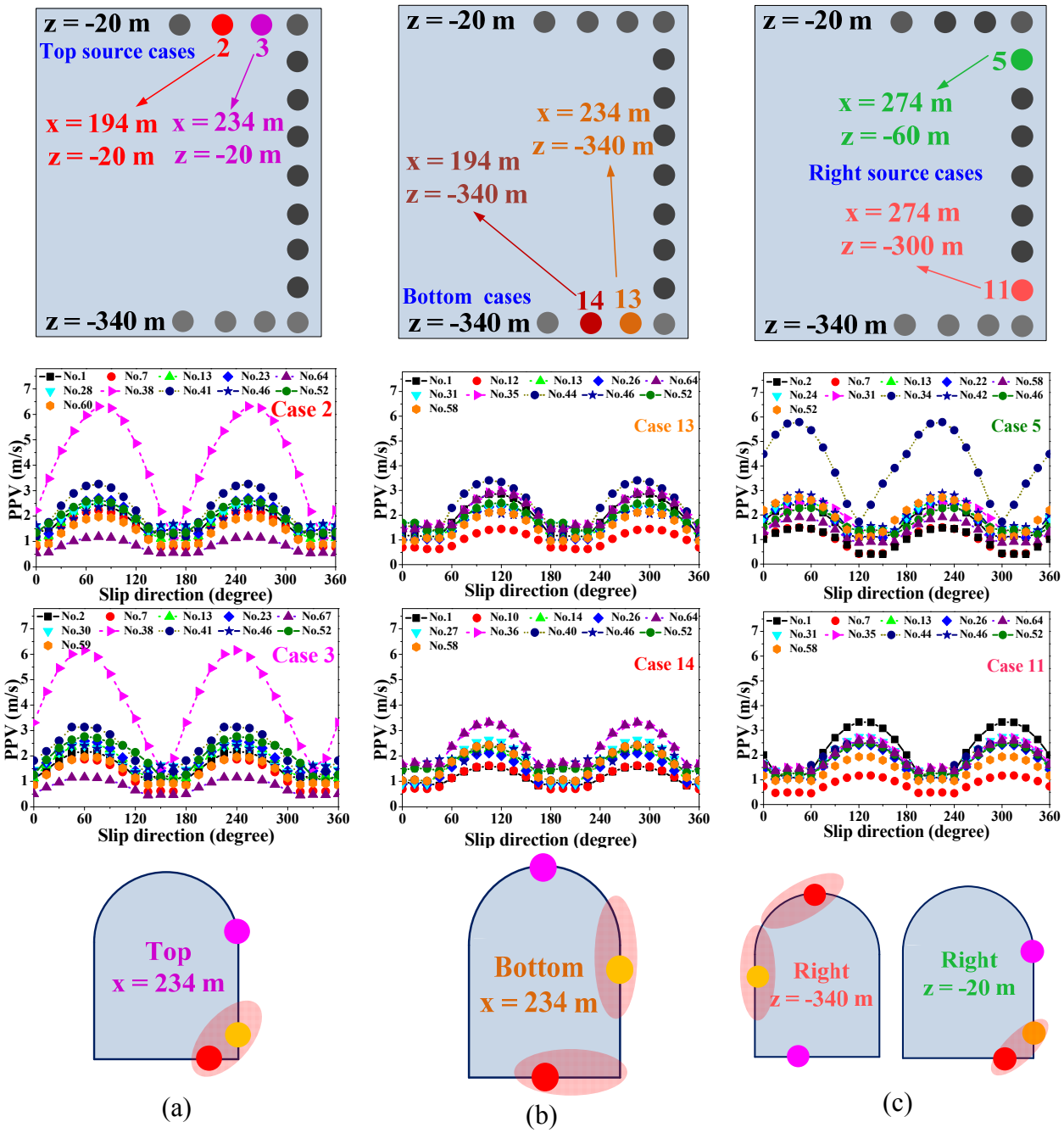

Figure 3-16: Comparison of the maximum PPV distribution of at selected set of receivers for the seismic source located at the top (a), bottom (b), and right (c) side of the model. Three receivers are selected and denoted in the last row according to different PPV values with red/yellow/pink denote the first/second/third highest PPV values around the opening, respectively. The potential high PPV areas are highlighted in light red.

3.4.2.5 Dip of the DC model

As noted in Chapter 2, seismic waves emitted from a DC point model (moment tensor source) can be modeled in the P-SV system in 2D; however, the 2D assumption leads to a variation of dip ranging from 0° to 90° only with the rake angle restricted to normal and reverse faults (with slip angles of -90° and 90°, respectively). A normal fault is selected as the seismic source in the following discussion.

The maximum PPV distributions under different dips are plotted in Figure 3-17. The seismic source is located at x = 270 m, z = -50 m (Case 4). Different seismic responses can be expected under different dips of the assumed fault-slip seismic source. In general, higher PPV values can be observed when the dips range from 30° to 45°. This is because that the maximum wave front will cover the tunnel area and a relatively high ground motion can be induced due to the wave

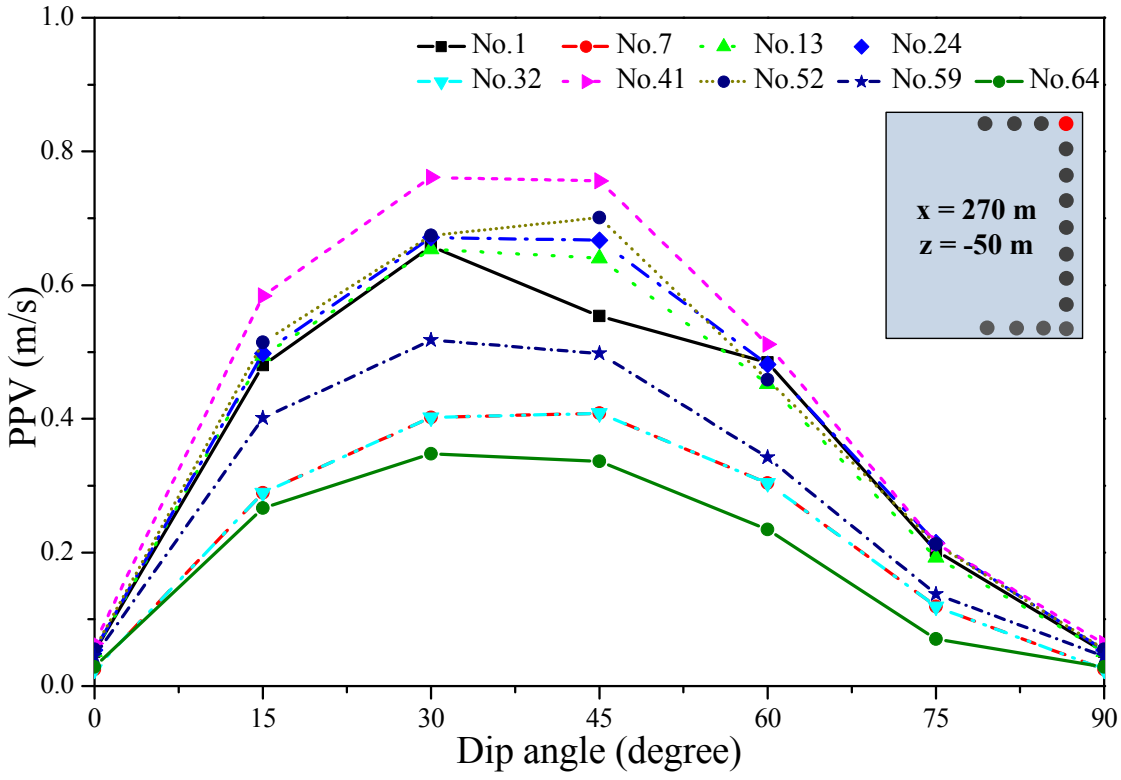

Figure 3-17: The maximum PPV values at some receivers as a function of the dip of the assumed normal fault. The seismic source of a normal fault is placed at the top right-corner of the model (Case 4: see the red dot in the insert).

pattern around the tunnel. The results imply that the dip of the fault influences the ground motions. Similar tendency can be found in other source location cases, which show that strong ground motion can be expected when the tunnel is located along the maximum shear wave front propagation direction.

3.5 Final remarks

SPECFEM2D has been validated using some classical analytical solutions of elastic seismic wave propagation. In this chapter, SPECFEM2D is successfully verified using the Garvin's problem which has a closed-form solution. This increases the confidence of using SPECFEM2D for seismic wave propagation simulation.

Point source models (SF and DC) are used to simulate far-field seismic wave propagation. A homogeneous and isotropic medium model with a horse-shoe tunnel subjected to a point seismic source is used to conduct a parametric study to better understand the sensitivity of the source parameters. It is seen from the modeling results that seismic response around a tunnel is closely related to wave pattern; in the meantime, wave radiation patterns resulted from a seismic source are, in general, dependent on source parameters such as the source time function and the dominant frequency used in the numerical modeling.

It is found from the parametric study that different source time functions leads to different ground motions around the tunnel. In addition, the dominant frequency of a seismic source plays an important role in influencing the ground motions around the tunnel. In wave modeling in underground mines, we are interested more in lower frequency waves. Ground motion is more intense for high frequency waves compared with that of lower frequency waves. High dominant frequency waves (300 Hz) is used only in this parametric study to check different source

parameters on ground motions. In other chapters, the dominant frequency is related to the intensity of a seismic source.

Source location also influences the wave pattern around an excavation significantly. The obtained ground motion (PPV) demonstrates that the PPV values depend not only on the receiver-source distance, but also on other factors such as source locations, wave propagation path, and tunnel spatial location.

For the SF point source model, the slip direction has a large effect on the ground motions. The simulation results imply that the slip direction (slip along the dip direction) of a normal fault in the DC model also has a large influence on the ground motions around a tunnel, especially when the tunnel is located along the slip direction that carries the maximum shear wave front. The wave pattern can be altered locally near a tunnel, which may cause local amplifying or shielding. The amplifying and shielding effects will be further discussed in Chapters 6 and 7.

Chapter 4

4 Influence of Wavelength-to-excavation Span Ratio on Ground Motion near Underground Excavations

From the seismic source parametric study conducted in the previous chapter, it was found that the moment tensor point source model is suitable for a fault-slip seismic event in the far-field. In the meantime, it was shown that one should be very careful when selecting the seismic source parameters. Excavations with different spans usually exist in mature underground mines. Various wavelength (or frequency) components can be generated due to the seismic source and the complex interaction between the seismic wave and geological structures and excavations. Both the above two factors, excavation span and wave frequency, can influence ground motions around excavations. The influence of wavelength-to-excavation span ratio (λ/D) on ground motion near excavations is investigated in this chapter. This content in this chapter was written as a paper and it was published in ***Tunnelling and Underground Space Technology***.

4.1 Introduction

Compared with surface structures, underground structures such as subways, railway and highway tunnels, powerhouse caverns and nuclear waste repositories are more earthquake resistant (Chen et al., 2012a; Chen et al., 2012b; Hashash et al., 2001; Ji et al., 2009; St John and Zahrah, 1987; Wang et al., 2001a). Despite of this fact, many underground structures have experienced damage in recent large earthquakes and considerable effort has been devoted to addressing tunnel damage due to seismic loading (Abokhalil, 2007; Alejano et al., 2009; Aydan et al., 2010; Geniş, 2010b; Kontoe et al., 2008).

The fact that deep civil tunnels (overburden depth H > 60 m) seem to be less vulnerable to earthquake shaking than shallow tunnels (H < 60 m) (Abokhalil, 2007; Hashash et al., 2001; Wang et al., 2001a) can be attributed to several factors such as higher moduli of competent rock masses, smaller excavation dimensions relative to the dominant wavelength in deep grounds (Barton, 1984; Bhasin et al., 2008). For tunnels located in deep underground mines (H > 1000 m), seismic loading caused by fault-slip rockbursts can cause large damage to the openings. Several factors, such as high in situ stress and highly non-uniform mining-induced stress, can alter ground motion in rock masses around underground excavations (Cai and Kaiser, 2002; Cai and Wang, 2015; He, 2006). Complex geology (e.g., dykes, faults, shear zones) and layout of the tunnel system (e.g., haulages, stopes, crosscuts, orepasses) can affect wave propagation. As shown in Figure 4-1, a few high risk areas (denoted by red) such as highly stressed pillars and locations where dykes intersect mine openings can be expected in an active underground mine. More attention should be paid to these areas because additional seismic wave loading can lead to rock mass failure in these areas.

Rockburst can cause large damage to underground mine infrastructures and pose a threat to the safety of mine personnel (Cai, 2013b; Cai and Champaigne, 2009; Kaiser et al., 1996; Ortlepp and Stacey, 1994; Potvin et al., 2000; Zhang and Fu, 2008). Incoming seismic waves may be altered in their intensity near the excavation boundary which in turn can shake down loose rocks directly or trigger ejection of rocks in these high risk areas. As noted in Chapter 2, Kaiser et al. (1996) proposed three rockburst damage mechanisms: bulking due to rock fracturing, ejection due to seismic energy transfer, and rockfall due to seismic shaking (right insert in Figure 4-1). All the three damage mechanisms can be triggered by seismic wave loading caused by a remote seismic event. If a rock mass has already reached a stress state near failure, a small seismic wave

disturbance is sufficient to trigger failure. If a rock mass is in a stress state not near failure, a large seismic wave disturbance can also cause rock mass failure.

Both the absolute values of PPV (Peak Particle Velocity) and the site amplification around excavations are of concerns in engineering design. Rock deformation moduli are reduced in fractured zones around excavations and various frequency contents (waves with multiple wavelengths) can be produced due to reflection and refraction of waves. Hence, seismically induced rockburst in underground excavations is complex and site-dependent.

The factors that affect ground motion in underground mines can be grouped into: (1) structure factors, e.g., shape and dimension of openings, rock mass properties, in situ stress, geological structures, rock support conditions, and rock discontinuities (Cai, 2013b; Cai et al., 2012; Deng

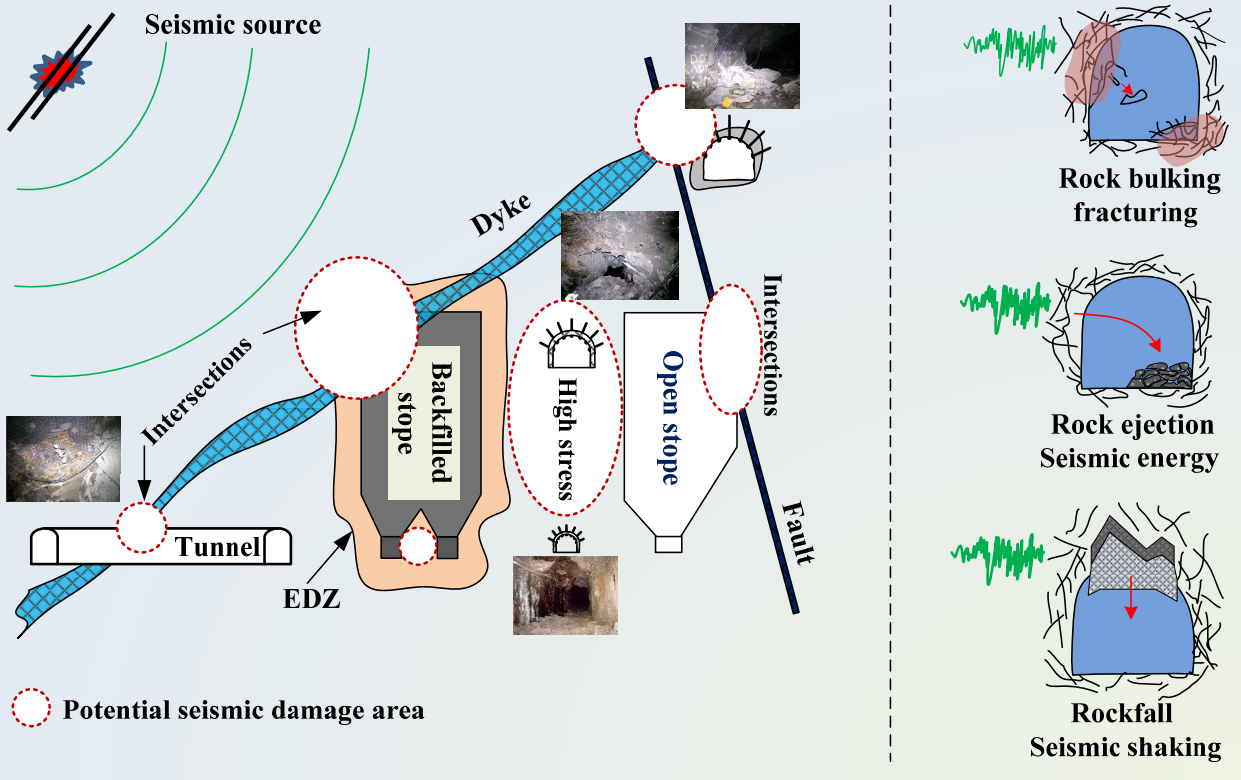

Figure 4-1: A schematic drawing showing the complex environment in underground mines (left) and three rockburst damage mechanisms (right). All three rockburst damage mechanisms can be triggered by seismic wave loading. Modified from Hudyma (2013) and Kaiser et al. (1996).

et al., 2014; Zhu et al., 2012); (2) seismic event factors, e.g., seismic event magnitude, seismic source-target distance, duration of strong ground motion shaking, wave-passage effects, and angle between incidence wave and tunnel axes (Dowding, 1984; Hashash et al., 2001; St John and Zahrah, 1987). Among these factors, wavelength λ to excavation span D ratio (λ/D) has a large influence on ground motion, as discussed in some studies (Chen and Chen, 2004; Chen et al., 2012a; Chen, 2005; Wang et al., 2014). For instance, Chen et al. (2012a) found that seismically induced stresses were strongly related to the wavelength of the seismic wave. Chen and Chen (2004) and Chen (2005) found that a strong impact on tunnel lining occurred when the λ/D ratio was between 1.0 and 4.5; less impact to the tunnel lining could be expected as the λ/D ratio increased. The above results revealed that ground motion in shallow tunnels are related to tunnel dimension and the corner frequency of an earthquake and the tunnels can become vulnerable if the λ/D ratio is small.

The corner frequency f_0 of seismic waves can be derived from displacement or acceleration amplitude spectrum analysis (Abercrombie, 1995; Aki, 1967); it can also be estimated from a scaling relation (e.g., $M_0 \propto f_0^{-3}$) between the corner frequency (f_0) and seismic moment (M_0) (Brune, 1970; Hashash et al., 2001; Izutani and Kanamori, 2001; Kanamori and Rivera, 2004). One major difference between a rockburst event and a natural earthquake event is that the frequency of the rockburst event is higher (Cai et al., 2007a). For a seismic event of a certain magnitude, complex frequency components can be generated due to seismic wave propagation involving wave reflection, refraction, and interaction in underground mines. Waves of different frequencies can cause various degrees of amplification and shielding effect around mine openings. High frequency ground motions may cause local spalling of rocks along weakness planes (Hashash et al., 2001).

Most previous studies on the influence of the λ/D ratio on ground motion focused on different tunnel spans under the same seismic source (fixed f_0) and the λ/D ratio is more than 10 or 20 for quasi-static loading problems (quasi-static loading is assumed if the λ/D ratio has a large value, e.g., > 20); only a few studies considered dynamic loading problems (dynamic loading is assumed if the λ/D ratio has a small value, e.g., < 10) when the wavelength is close to the tunnel span (Dowding, 1984; Tshering, 2011). Because of the need to better understand the complex seismic waves traveling in underground mines, engineers are interested in seismic waves generated from fault-slip rockbursts that have higher frequencies than natural earthquakes; engineers are also interested in not only the absolute value of ground motions (PPV) but also the relative values of ground motions that can be indicated by amplification factors (α). α is defined as the ratio of PPV from a model with an excavation to that from a model without any excavation. Hence, two unanswered questions are focused on in this chapter: are the ground motions around tunnels with different λ/D ratios the same if one fixes the tunnel span and changes the wavelength or fixes the wavelength and changes the tunnel span? What are the amplification factors of ground motions around the excavations?

This chapter attempts to shed light on the above two questions by carrying out a series of numerical experiments to study the effect of the λ/D ratio on ground motion, with a focus on finding the distribution of PPV and the amplification factors using SPECFEM2D. Again, seismic source is modeled using the moment tensor source model. Two tunnel cross-sections (circular and arched back) are considered.

4.2 Seismic source representation and numerical model description

4.2.1 Seismic source representation

As shown in Figure 4-2, three simplified deformation models of tunnels under seismic wave loading can be considered for engineering design: (a) compression-extension, (b) longitudinal bending, and (c) ovaling/racking (Owen and Scholl, 1981). Among these models, the ovaling of tunnel cross-section (distortion of the cross-section) is the most critical deformation and it can occur when shear waves (or S-waves) propagate normal or near normal to the tunnel axis (Hashash et al., 2005; Penzien, 2000). S-waves, which transmit a large proportion of the seismic energy, have greater energy and amplitude than the P-waves (Aki and Richards, 2002; Kaiser et al., 1996). Compared with the seismic energy and amplitude in the horizontal plane, typically 66% more seismic energy can be observed in the vertical plane (Hashash et al., 2001). Hence, a 2D approximation can be used to analyze the effect of the λ/D ratio on ground motion in the vertical plane (P-SV system).

As stated in Section 2.3.1 in Chapter 2, it is appropriate to employ a moment tensor source model to represent the point source of a fault-slip source in the far-field (Aki and Richards, 2002). In this fashion, only three components (M_{xx}, M_{zz}, and M_{xz}) of a moment tensor are used to represent a fault-slip source to study ground motion in the P-SV system.

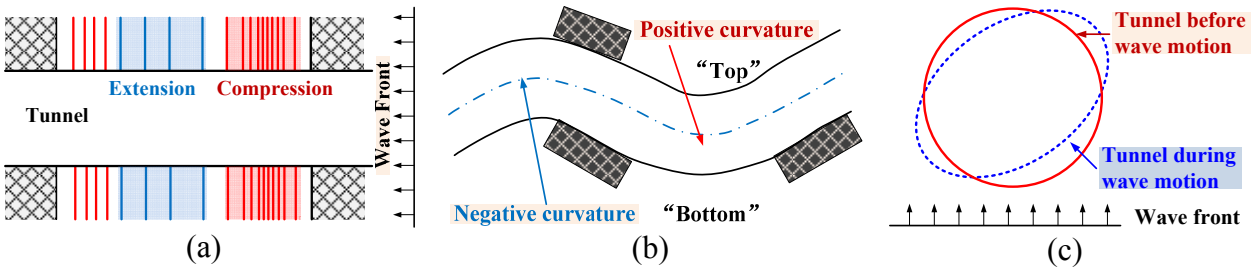

Figure 4-2: Three simplified deformation models of tunnels under seismic wave loading: (a) compression-extension; (b) longitudinal bending; (c) ovaling of tunnel section (Owen and Scholl, 1981).

4.2.2 Models with different tunnel spans

Ten cases with two tunnel cross-section shapes (arched back and circular) are considered to study the influence of the λ/D ratio on ground motions around excavations due to a fault-slip seismic event. Each with five λ/D ratios (λ/D = 0.5, 1, 2, 5, 10, listed in Table 4-1) are considered (Figure 4-3). The largest tunnel span is 60 m and the smallest span is 3 m; the wavelength of the S-waves is fixed at 30 m.

As shown in Figure 4-3, the dimension of the computation domain is 508 m × 508 m. The arched back shaped or circular shaped tunnel is located in the center of the model. The rock mass is

Table 4-1: Different λ/D ratios for the five model cases when λ is fixed

Case no.	Shear wavelength (m)	Tunnel span (m)	λ/D ratio
1	30	60	0.5
2	30	30	1
3	30	15	2
4	30	6	5
5	30	3	10

Notes: The determination of tunnel span (D) is different for two cross-section shapes, see Figure 4-3.

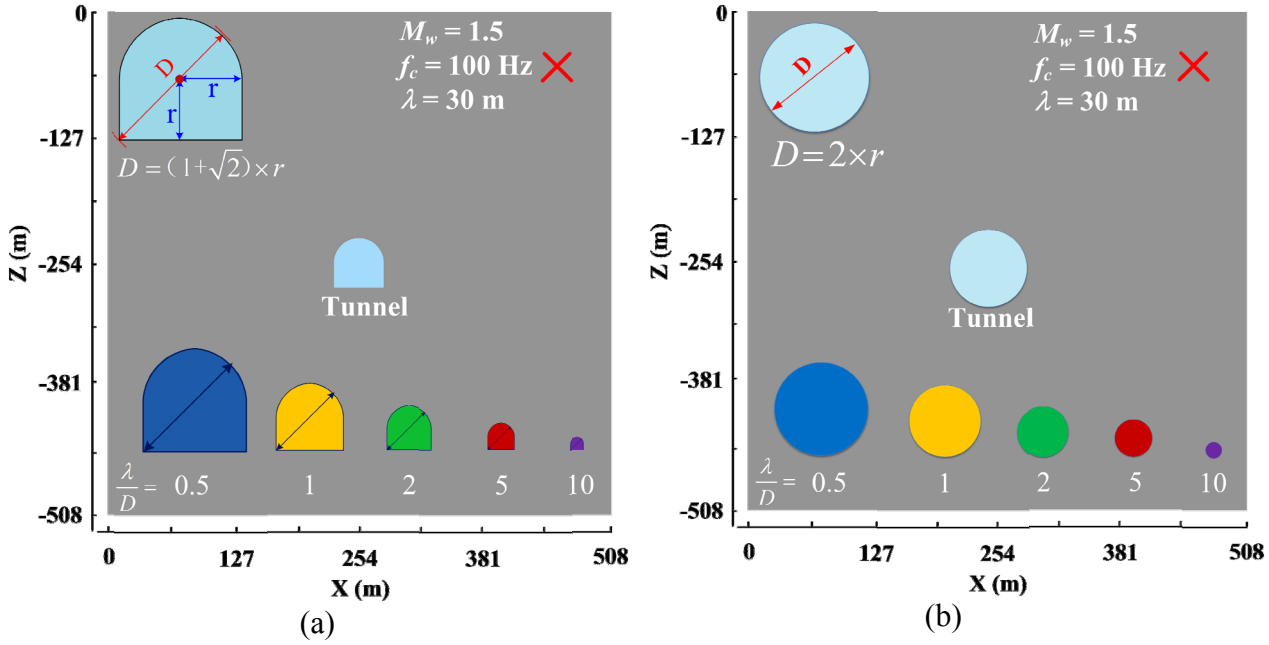

Figure 4-3: 2D models for arched back (a) and circular (b) excavations under five λ/D ratio scenarios. The seismic source (red cross) is located at the top right (x = 454 m, z = - 54 m) and the excavation is located in the center of the model (x = 254 m, z = - 254 m).

homogeneous and the density, Young's modulus, and Poisson's ratio of the rock mass are 2600 kg/m^3, 60 GPa, and 0.25, respectively. Constant wave velocities are assigned to the rock mass (V_p = 5.2 km/s, V_s = 3.0 km/s) and the excavated areas (V_p = 0.3 km/s, V_s = 0.0 km/s) in the model. A normal fault with a dip of 45° is simulated using the moment tensor source model. The moment magnitude of the seismic event is M_w = 1.5, with a Ricker wavelet source time function and with a dominant frequency of 100 Hz. This results in a shear wavelength of λ = 30 m. The seismic source is placed at the top right (x = 454 m, z = - 54 m) in the model, shown as a red cross (X).

The four boundaries of the model are set as PML absorbing boundaries (4 m wide for each boundary) to avoid spurious seismic wave reflection of outward propagating waves. As mentioned in Chapter 3, the PML boundaries are efficient to absorb seismic waves in numerical modeling (Komatitsch and Tromp, 2003).

4.2.3 Models with different wavelengths

As noted in Section 4.1, different corner frequencies (f_0) correspond to seismic events of different intensities. A series of numerical simulations using a arched back shaped excavation (D = 10 m) subjected to waves generated from seismic events of different magnitudes are conducted to examine the influence of seismic wavelength on ground motions around a tunnel for a given size. Once the moment magnitude (M_w) of a seismic source is known, the seismic moment can be determined from Aki and Richards (2002)

$$M_0 = 10^{\frac{3}{2}(M_W + 10.73)} \tag{4.1}$$

where M_0 (dyne-cm) is the seismic moment and M_w is the moment magnitude. The corner frequency is linked to the seismic moment M_0 by

$$M_0 \propto f_0^{-3} \tag{4.2}$$

Once the strike ϕ_s, rake γ_r, and dip δ_d of the fault-slip seismic source are known, the three moment tensor components M_{xx}, M_{zz}, and M_{xz} in the P-SV system for 2D analysis can be expressed by

$$\begin{aligned} M_{xx} &= -M_0(\sin\delta_d \cos\gamma_r \sin 2\phi_s + \sin 2\delta_d \sin\gamma_r \sin^2\phi_s) \\ M_{xz} &= -M_0(\cos\delta_d \cos\gamma_r \cos\phi_s + \cos 2\delta_d \sin\gamma_r \sin\phi_s) \\ M_{zz} &= M_0 \sin 2\delta_d \sin\gamma_r \end{aligned} \tag{4.3}$$

As shown in Figure 4-4, an arched back shaped excavation with a 10 m excavation span is located in the center of the model (1008 m × 1008 m). The modeling conditions (e.g., material

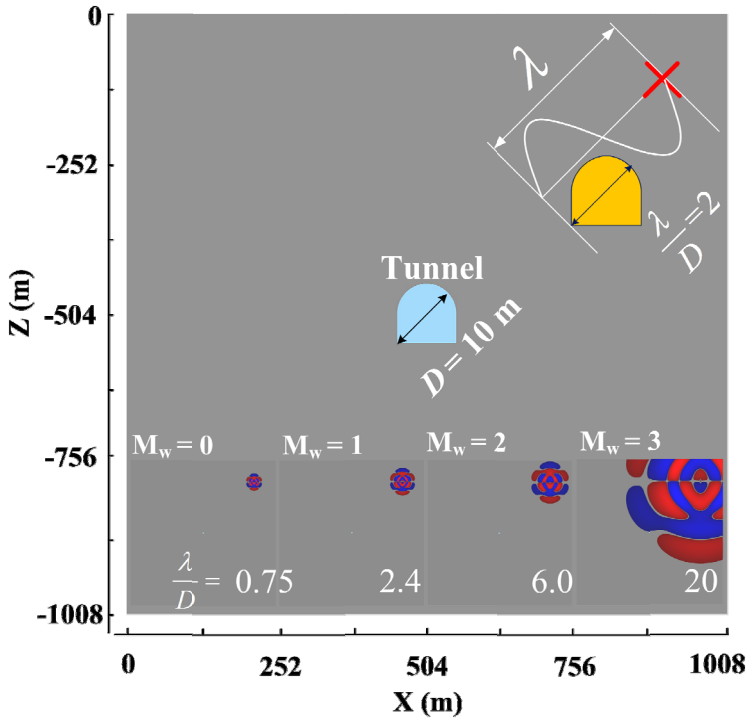

Figure 4-4: 2D models for a arched back shaped excavation with constant D and variable λ. The seismic source (red cross) is located at the top right (x = 454 m, z = - 54 m) and the excavation is located at the center of the model (x = 254 m, z = - 254 m).

Table 4-2: Parameters for different seismic magnitudes and nine λ/D ratios when D is fixed

Case No.	M_w	M_0 (N·m)	f_0 (Hz)	λ (m)	D (m)	λ/D ratio
1	- 0.5	2.21e8	700	4.3	10	0.43
2	0.0	1.24e9	400	7.5	10	0.75
3	0.5	6.99e9	250	12.0	10	1.20
4	1.0	3.94e9	125	24.0	10	2.40
5	1.5	2.21e11	100	30.0	10	3.00
6	2.0	1.24e12	50	60.0	10	6.00
7	2.5	6.99e12	25	120.0	10	12.00
8	3.0	3.94e13	15	200.0	10	20.00
9	3.5	2.21e14	10	300.0	10	30.00

Note: f_0 is determined from $f_0 = K \times V_s \times M_0^{-0.33}$, where K is a site-specific constant and V_s is the shear wave velocity.

properties, PML absorbing boundaries, etc.) are the same as that described in Section 4.2.2, except that the magnitudes of the seismic sources are different. Nine case studies are conducted and the seismic source parameters are listed in Table 4-2. For each modeling case, the seismic source parameters (i.e., M_0 , f_0, M_{xx}, M_{zz}, and M_{xz}) are determined using Eqs. (4.1) to (4.3).

4.2.4 Receiver layout

A number of receivers are placed around the excavation to capture PPV distribution around the excavation. The receiver layouts are presented in Figure 4-5 for different modeling cases. For the case that has constant λ and variable D, 41 by 41 receivers are placed regularly in a square around the excavations for both the arched back (Figure 4-5(a)) and the circular shaped excavations (Figure 4-5(b)).

It should be noted that the areas covered by these receivers are different for each case. For instance, an area of 20 m × 20 m is covered by the receivers around the excavation when the λ/D ratios are equal to 10 and 5. An area of 40 m × 40 m is covered by the receivers for the cases of λ/D = 1 and 2 and an area of 80 m × 80 m is covered when the λ/D ratio is 0.5 (represented by different color dots).

The receiver spacing is different for each case. For example, the receiver spacing is 0.5 m for cases of λ/D = 1 and 2 and the spacing is 1.0 m for cases of λ/D = 5 and 10, and with a 2.0 m spacing when λ/D = 0.5 in Figure 4-5(a) and (b). In addition, Figure 4-5(c) shows the layout of the 41 × 41 receivers (1.0 m receiver spacing and a covered area of 40 m × 40 m) around the back arched excavation with a cross section of 8 m by 8 m (D is approximately 10 m) for the

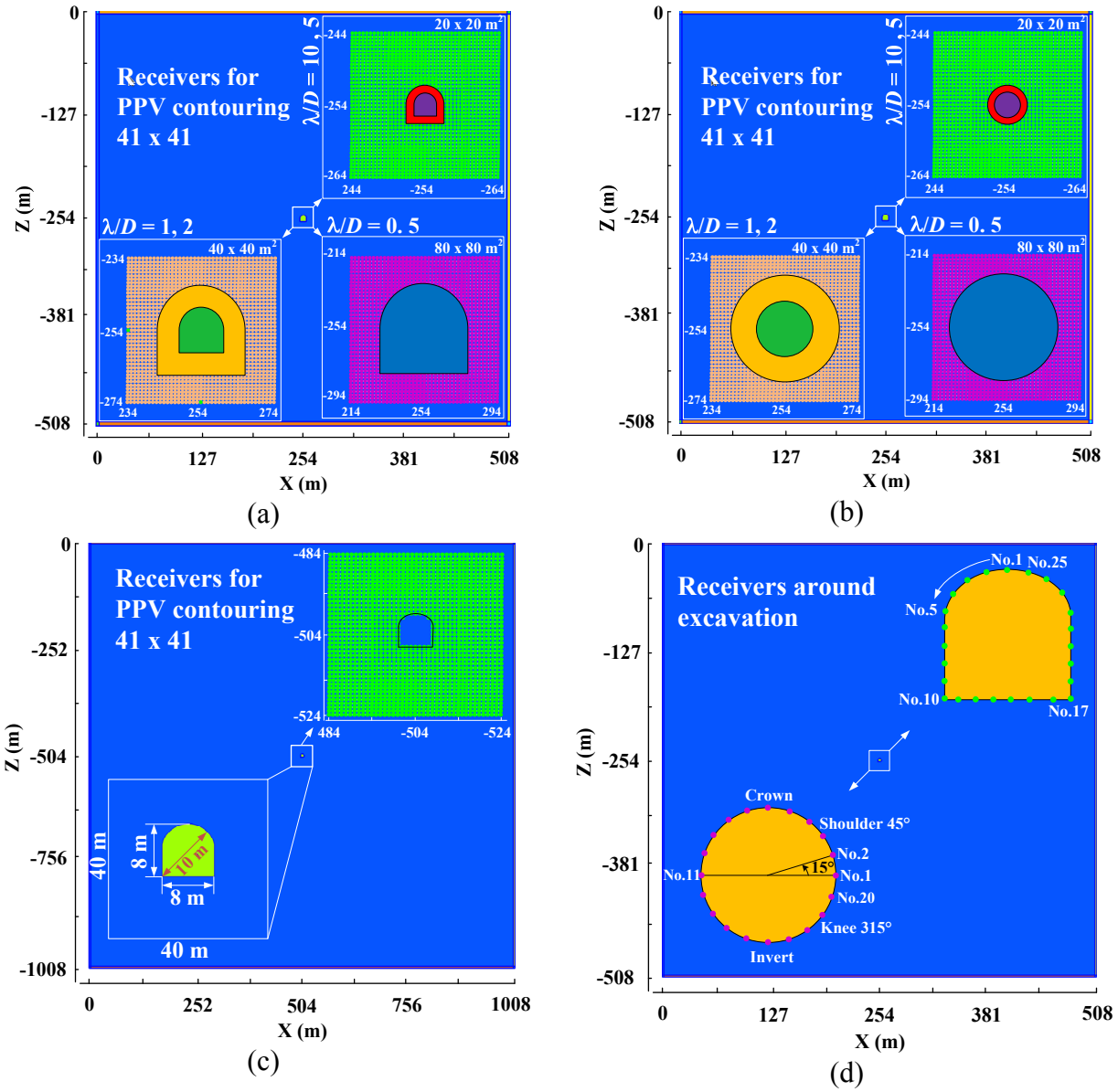

Figure 4-5: Layout of receivers around the excavation. 41 × 41 receivers for the back arched and circular excavations of different tunnel span are shown in (a) and (b). (c) Layout of the receivers for models with different wavelengths. (d) Layout of the receivers around the surface of the arched back and circular excavations.

models with variable wavelengths. A total of 25 receivers are placed on the surface of the back arched shaped tunnel, numbered from 1 to 25 in the counter clockwise direction and 20 receivers are placed on the surface of the circular tunnel and the receiver location is denoted by the angle, as shown in Figure 4-5(d).

4.3 Modeling results and discussion

In the numerical modeling, wave propagation analysis for a background model (without an excavation) is performed first, and then analysis is conducted for the model with an excavation. Subsequently, PPV distribution around the excavation is obtained from recorded synthetic seismograms at each receiver. An amplification factor at each receiver is then calculated. The amplification factor (α) is equal to the ratio of PPV_E in the excavation model to PPV_B in the background model.

4.3.1 Results of models with different tunnel spans

Figure 4-6 shows snapshots of the vertical velocity component of four cases with λ/D = 0.5, 1.0, 2.0, and 5.0, at five propagating times for the arched back excavation. The plots show the process of wave propagation from seismic waves emitting from the source, transmitting in the medium, and then passing through the excavation area. Direct P- and S- waves are observed in all cases. Because the selected seismic source represents a normal fault with a dip of 45°, the P-wave-induced disturbance around the excavation is small but the S-wave-induced disturbance to the wavefield is large (Figure 4-6).

As can be seen from Figure 4-6, scattering seismic waves are generated and are more pronounced when the S-waves reach to the right shoulder of the excavation (at t = 0.105 and 0.12

s). However, there is a difference in wavefield around the excavation as the direct S-waves pass through the excavation for different λ/D ratios. Comparing Figure 4-6(d) with Figure 4-6(c), (b), and (a), it is noticed that as the λ/D ratio decreases, dynamic wave interaction between the S-waves and the excavation increases. This large dynamic wave interaction can lead to strong

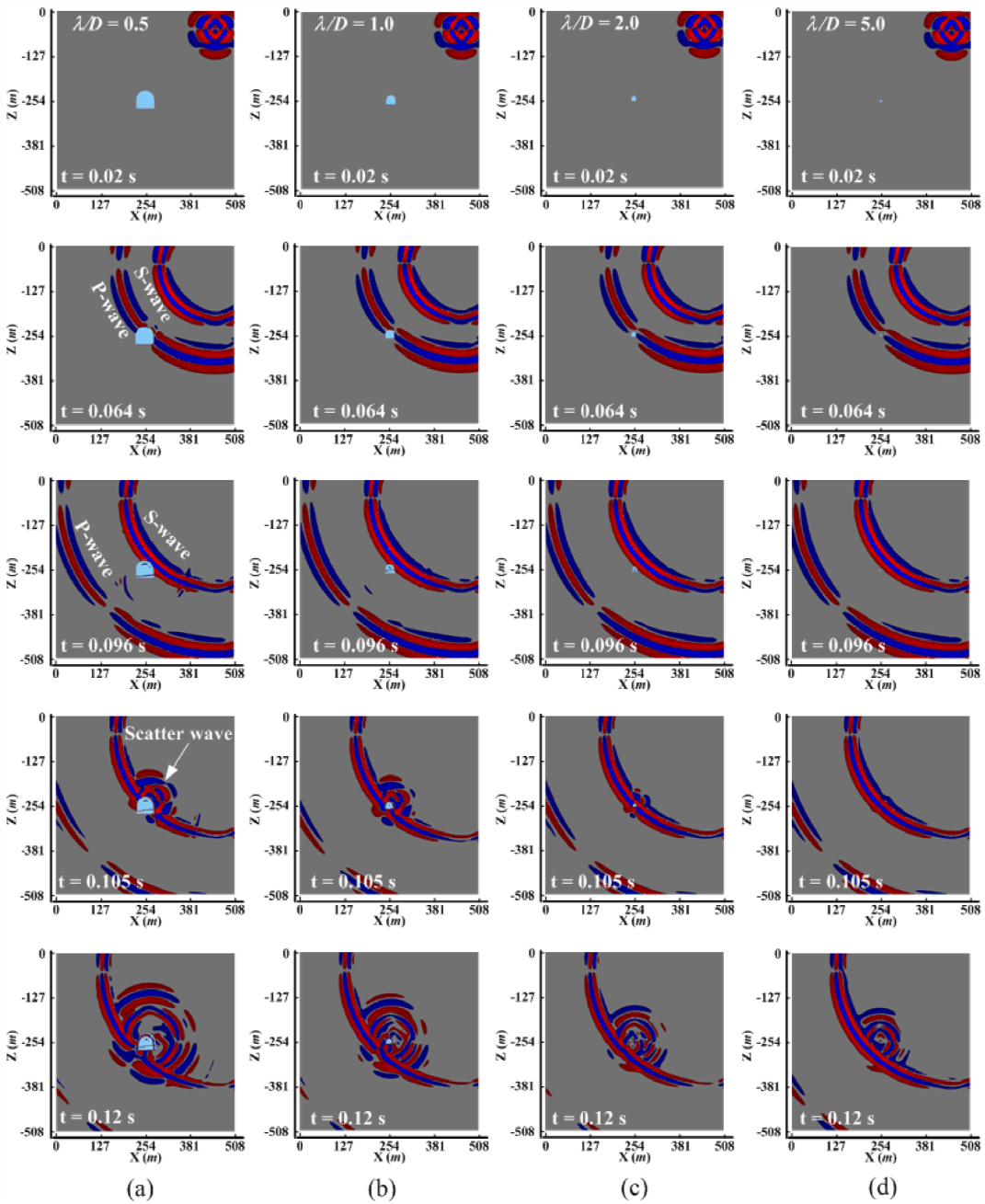

Figure 4-6: Snapshots of the vertical velocity field for the arched back excavation at 0.02, 0.064, 0.096, 0.105, and 0.12 s for models with λ/D ratios of 0.5 (a), 1 (b), 2 (c), and 5 (d). The positive (upward movement) and negative (downward movement) vertical velocities are denoted by red and blue, respectively. Figure A - 2 shows the snapshots of vertical velocity field for the circular shaped excavation.

scattering waves and more complex wavefield around the excavation. This observation holds true for the case of circular excavation (see results in Appendix A, Figure A - 2).

As noted in the literature, PPV is an important parameter that is widely used to quantify ground motion for dynamic rock support design in burst-prone mines (Cai et al., 2012; Kaiser and Maloney, 1997; Kaiser et al., 1996). PPV contours in the mapping area covered by the 41 by 41 receivers for models without and with excavations are generated to find out the influence of the λ/D ratio on the ground motion around the excavations and the results are presented in Figure 4-7, for λ/D = 2.0 and 10.0. The color scale of the contours is 0.00 - 0.08 m/s for the background model (Figure 4-7(a)) and the excavation model for the cases of λ/D = 2.0 and 10.0 (Figure 4-7(b) and (c)).

It can be seen from Figure 4-7 that zones of PPV increase and decrease exist in both the arched back and the circular excavation models for λ/D = 2.0 and 10.0. In general, large PPV increase zones appear in the roof and on the right wall region and PPV decrease zones appear at the lower-left side of the excavation, as a result of the direction of seismic wave propagation.

The PPV values have roughly the same value range (0.00 to 0.07 m/s) and similar distribution patterns around the excavation when the λ/D ratio is equal to 2.0 for both the arched back and circular shaped excavations (Figure 4-7). Although the PPV distributions around the two excavations look similar (Figure 4-7(b)) when the λ/D ratio is equal to 10.0, higher PPV values (e.g., 0.08 m/s) are observed in the floor area around the corners for the arched back tunnel, but not in the circular tunnel (Figure 4-7(c)). This indicates that different cross-sections of excavations (such as circular, ellipse, back arched, rectangle, and horse-shoe) may influence the seismic response and ground motion near the excavation boundary.

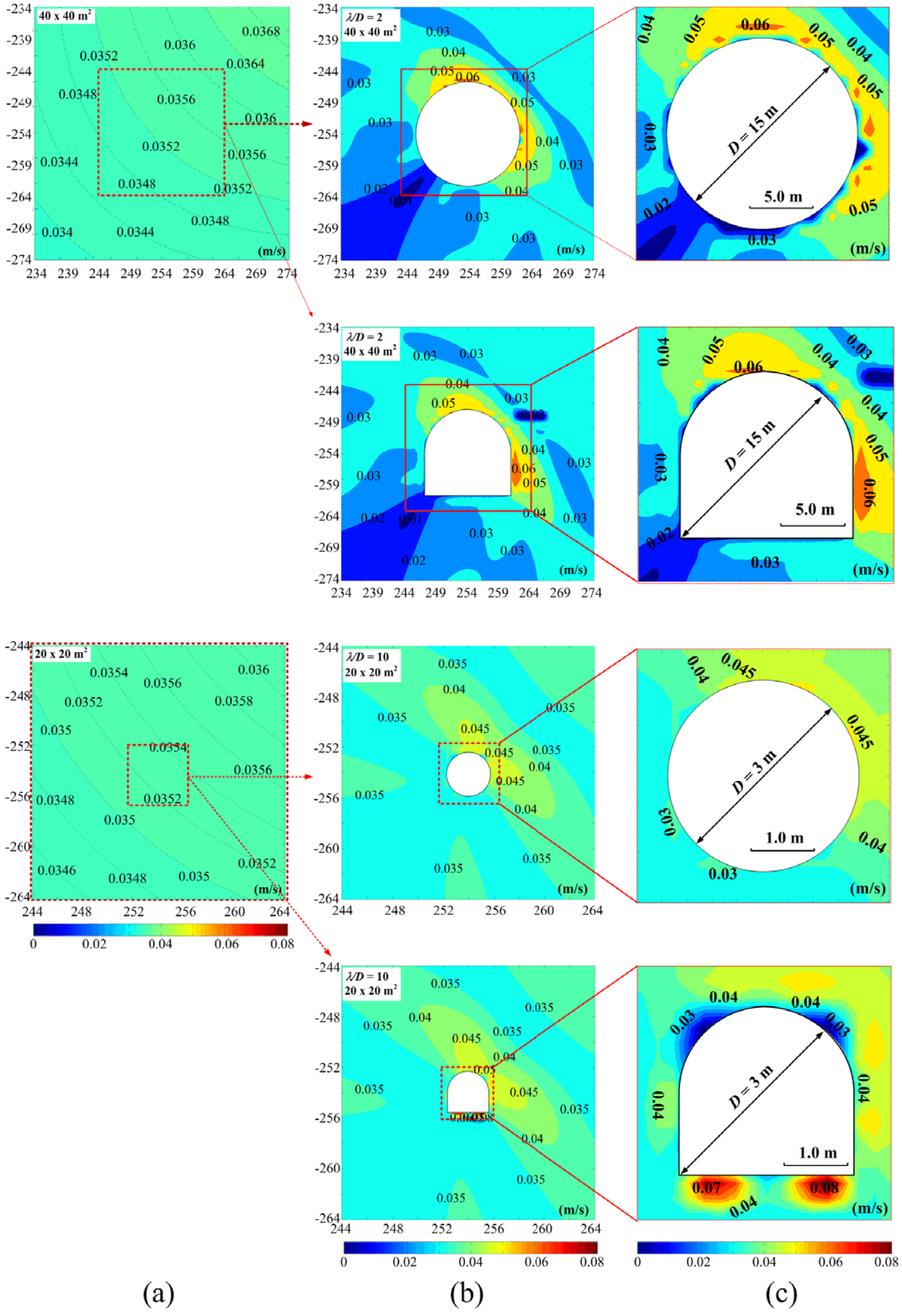

Figure 4-7: PPV contours of background (a) and excavation models (b) with circular and back arched shaped openings for λ/D ratio = 2.0 and 10.0. (c) Zoom-in plots showing detailed PPV distribution around the excavations. The PPV mapping areas are 40 m × 40 m and 20 m × 20 m for the two cases. The details of the receivers are shown in Figure 4-5.

It is seen from Figure 4-7 that the PPV distributions are similar in the right-upper area (i.e., the right wall and the roof) for the arched back and circular excavations. Hence, this area is selected to further examine the influence of the λ/D ratio on ground motions.

Figure 4-8 presents the influence of the λ/D ratio on the amplification factor around the excavation. All contours are plotted on the same color scales, from 0.0 to 2.5 for the arched back excavation (Figure 4-8(a)) and from 0.0 to 2.0 for the circular excavation (Figure 4-8(c)) to facilitate an easy comparison. Figure 4-8(b) shows zoom-in figures in order to illustrate detailed amplification factor distribution in the upper right area that faces the incoming seismic waves in the models.

Due to computation resource limitation, the maximum λ/D ratio considered is 10.0 in this model. This ratio seems not large enough to ensure that the whole excavation can experience quasi-static seismic loading (Owen and Scholl, 1981), but this is not a problem for dynamic loading. Most previous research works on studying the influence of the λ/D ratio on seismic response focused on quasi-static seismic loading, with a λ/D ratio greater than 20.0. The modeling results for λ/D ratios of 0.5, 1.0, 2.0, 5.0, and 10.0 in this study are applicable to seismic response around excavations under the dynamic loading conditions. As can be seen from Figure 4-8(a) and (c), the degrees and areas of PPV amplification and shielding around the excavation are not the same for different λ/D ratios. The amplifying and shielding areas concentrate in the upper-right and lower-left areas of the excavations, respectively, and correspond well with the PPV distributions shown in Figure 4-7.

For both the arched back and the circular excavations (Figure 4-8(b)), the amplification factors increase with the decrease of the λ/D ratios. Taking the circular excavation as an example, the

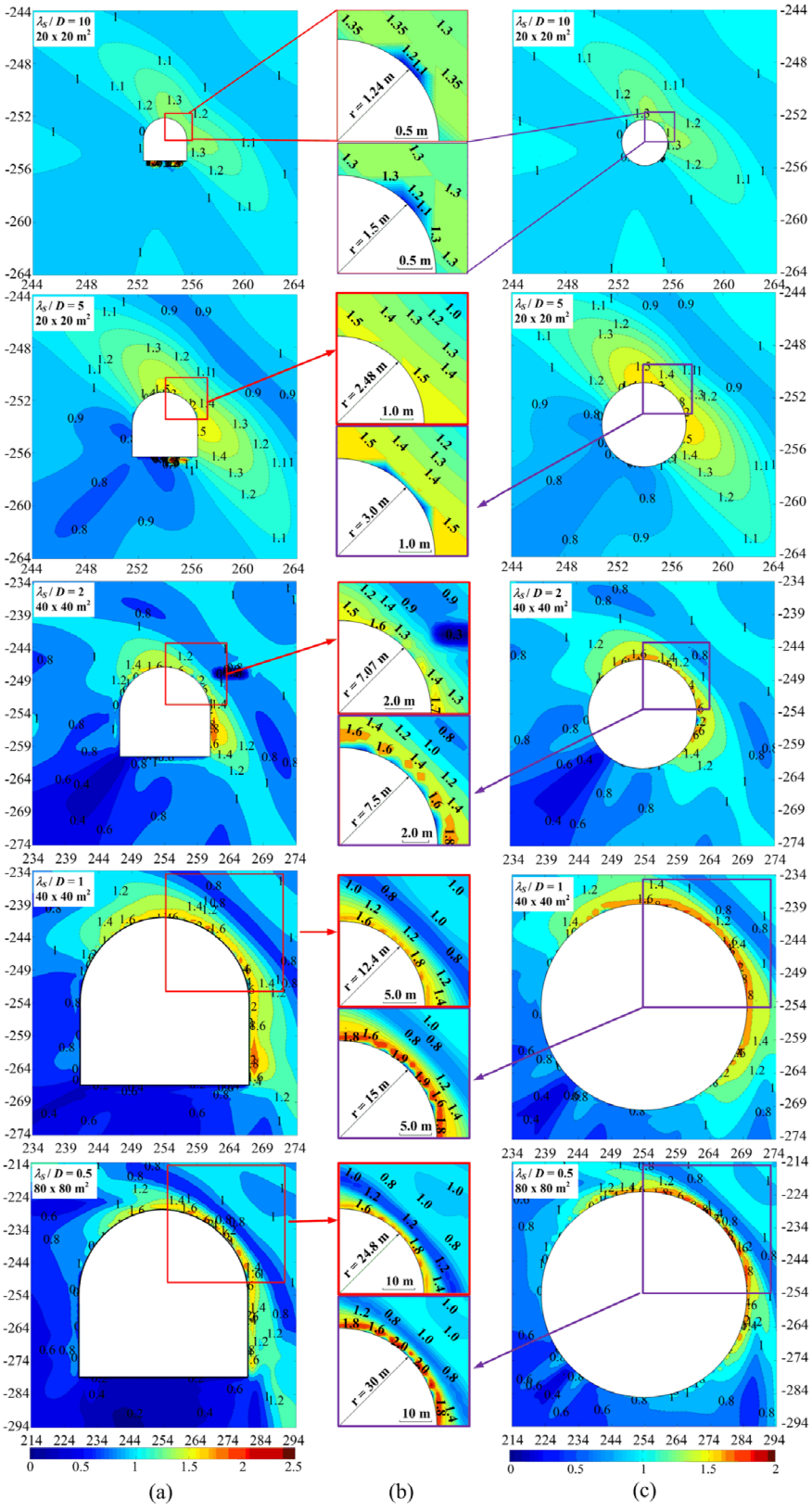

Figure 4-8: Amplification factor distributions around arched back (a) and circular (c) shaped excavations with five λ/D ratios. (b) Zoom-in plots showing detailed amplification factor distribution in the upper right areas.

maximum amplification factors in the upper-right area are 1.3, 1.5, 1.8, 1.9, and 2.0 when the corresponding λ/D ratios are 10.0, 5.0, 2.0, 1.0, and 0.5, respectively. This means that excavation size has a profound effect on the ground motion and an excavation with a larger span may experience stronger seismic amplification compared with that of an excavation with a smaller span for the seismic wave loading generated by the same seismic event.

The amplification factor distribution along the periphery of the circular excavation is shown in Figure 4-9. The abscissa is the receiver's location (measured by the angle from zero) and the convention used to denote a particular location is shown in Figure 4-5(d). Small circle inserts with different colors are added in Figure 4-9 to provide a simplified view of the distribution of the amplification factor. A green dot line in Figure 4-9 means that PPV_E is equal to PPV_B.

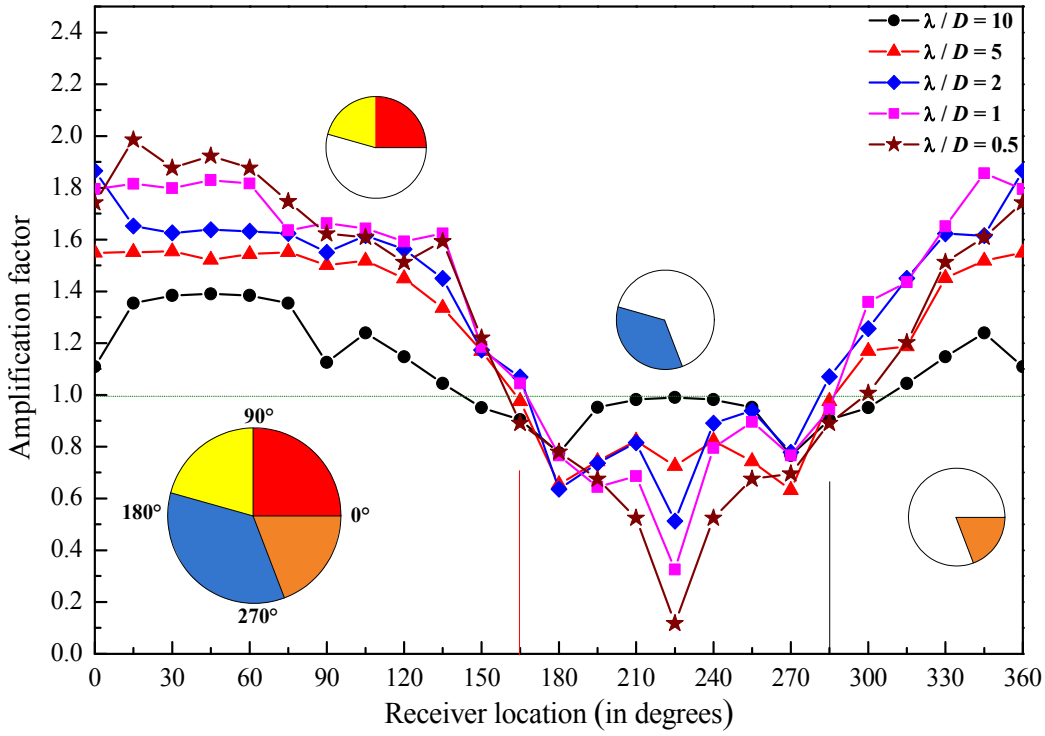

Figure 4-9: Amplification factor distribution along the periphery of the circular excavation. The location around the excavation is denoted by angle measured from 0 shown in the figure. The amplification effects are denoted by color in the inserted circles, with high to low amplifications denoted by red, yellow, light yellow, and blue.

Figure 4-9 shows that there is a large variation in the amplification factor at different locations around the excavation for different λ/D ratios. Larger amplification (red area of the inserted circle) occurs at the right shoulder and crown areas (from 0° to 90°) and the amplification factor increases when the λ/D ratio decreases from 10.0 to 0.5. Similarly, larger shielding effect (blue area) appears at the lower-left shoulder and the invert areas (from 165° to 285°) and the amplification factor decreases as the λ/D ratio decreases. The results show that an excavation with a larger span will experience higher ground motion than a smaller excavation under the same seismic event.

4.3.2 Results of models with different seismic wavelengths

The results presented in Section 4.3.1 were obtained by fixing the wavelength (λ) and varying the excavation span (D). This section focuses on studying the influence of wavelength on ground motion in an excavation with a fixed span. An arched back excavation with a 10.0 m span is considered. Because seismic sources of different intensities have different corner frequencies, the amplification factor is determined by the PPV ratio of the excavation model to the background model under the same seismic event with a moment magnitude of M_w. The moment magnitudes for all studied cases are listed in Table 4-2.

Figure 4-10 presents snapshots of the vertical velocity component of four λ/D ratios (2.4, 3.0, 6.0, and 12.0) at five wave propagation times. The selected propagation times differ in each case because the wavelengths are not the same. Similar to the results shown in Figure 4-6, direct P- and S- waves are observed in all cases. Because the corner frequency is different for each case, the wavelengths of the P- and S-waves are different in each case (Figure 4-10). For example, the P- and S-waves are separated at t = 0.1 s for λ/D = 2.4 but are still entangled at t = 0.13 s for λ/D

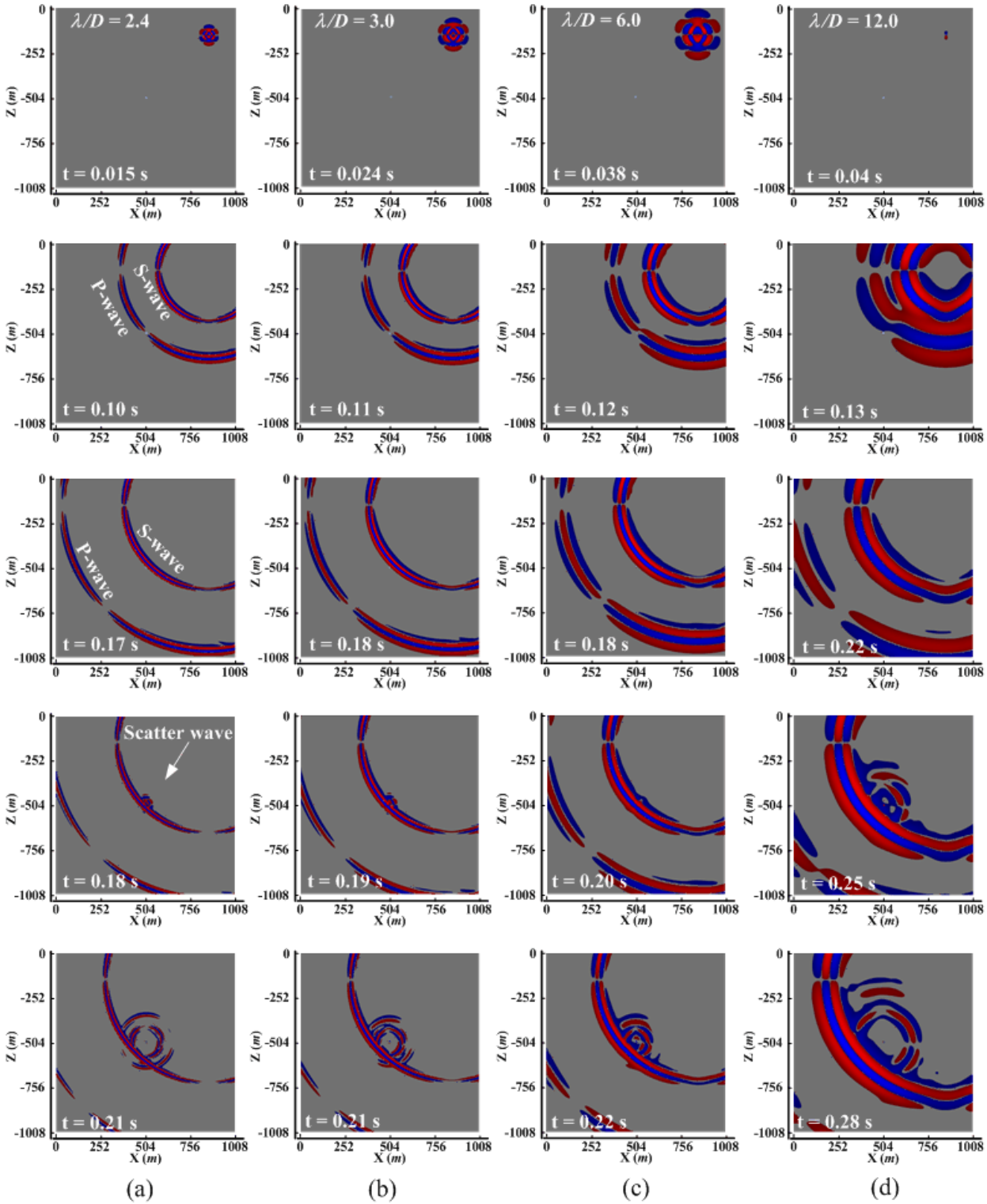

Figure 4-10: Snapshots of the vertical velocity component for the back arched excavation at five different times for λ/D ratios of 2.4 (a), 3.0 (b), 6.0 (c), and 12.0 (d). The positive (upward movement) and negative (downward movement) vertical velocity components are denoted by red and blue, respectively.

= 12.0. In addition, the time for the S-wave passing through the excavation has a large variation and is dependent on the λ/D ratio. The result indicates that an excavation with a large λ/D ratio may be subjected to longer seismic loading than an excavation with a smaller λ/D ratio.

The PPV contours are presented in Figure 4-11 for models without and with the excavation for λ/D = 0.43, 2.40, 12.00, and 30.00 to further inspect the influence of the λ/D ratio on ground motion. The color scales of the contours are different for the four cases that have seismic moment magnitude of M_w = -0.5, 1.0, 2.5, and 3.5, respectively. It can be seen from Figure 4-11 that the absolute PPV values are proportion to the intensity of the seismic event. As expected, higher PPV values are observed in the mapping area in the background model when the λ/D ratio is large (Figure 4-11(a)).

Figure 4-11(b) presents the PPV contours around the excavation. The areas of PPV increase and decrease are not the same for the results of different λ/D ratios. When the λ/D ratios are small, the PPV increase and decrease zones are large and are located at the right-side and lower-left side for λ/D = 0.43 and 2.40, respectively. However, when the λ/D ratios are large (λ/D = 12.0 or 30.0), the PPV increase and decrease zones become less notable and the areas that show some changes in PPV values are concentrated only near the excavation boundary. As can be seen from Figure 4-11(c), a relatively large PPV value (0.016 m/s) is observed at the right-floor side of the excavation for λ/D = 0.43, but the PPV values around the whole excavation are comparable (around 0.18 m/s) for λ/D = 30.0. This modeling result indicates that the λ/D ratio has a large effect on the ground motion – more dynamic wave interaction may occur when the λ/D ratio is small (e.g., < 20). For very large λ/D ratios, the assumption of uniform quasi-static loading is valid.

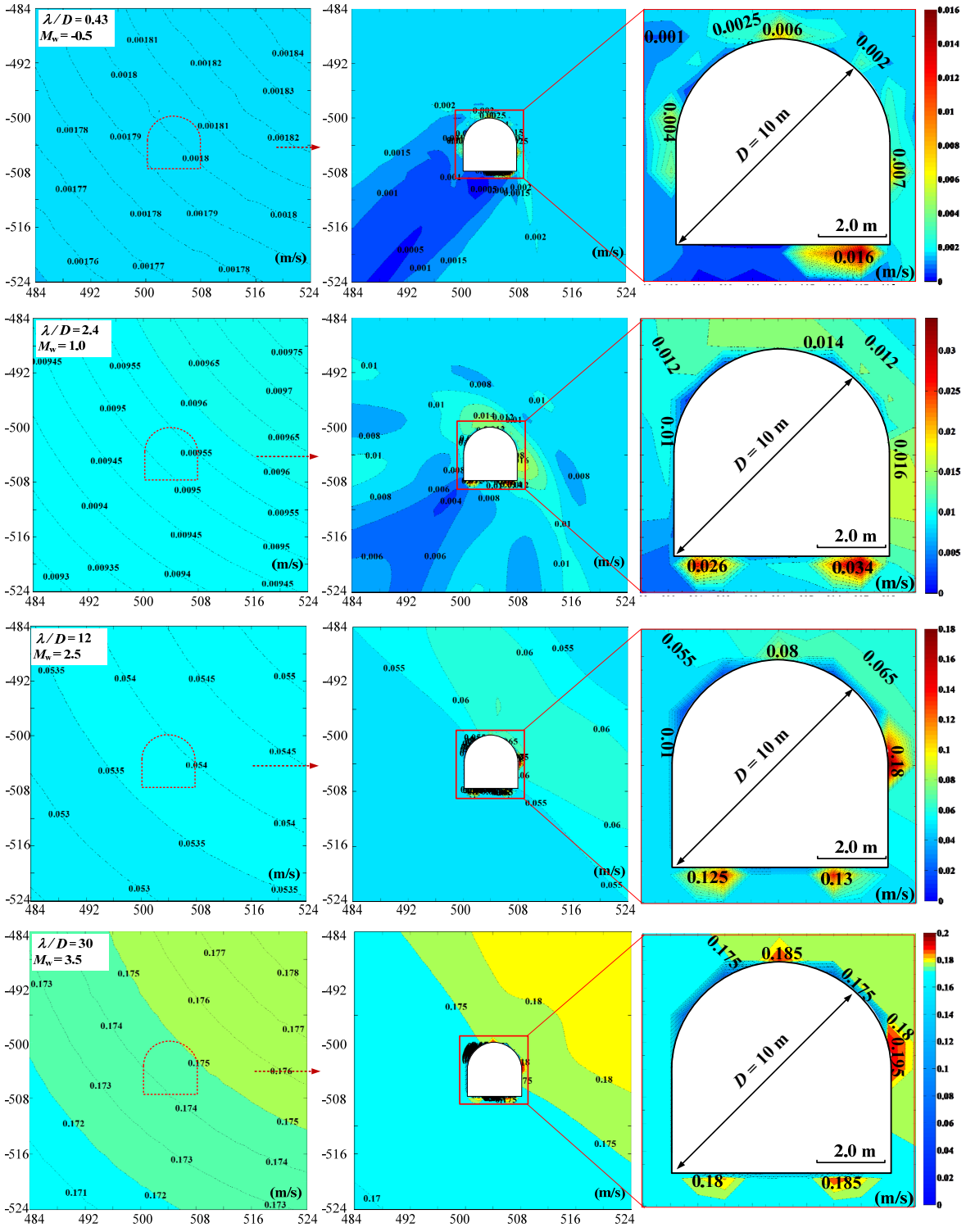

Figure 4-11: PPV contours of the background (a) and excavation models (b) with a 10.0 m span arched back excavation for *λ/D* ratios of 0.43, 2.4, 12.0, and 30.0. (c) Zoom-in plots showing detailed PPV distribution around the excavation boundary. The distance between the seismic source and the right-corner of the contouring area is 467 m. The PPV mapping area is 40 m × 40 m and with a 1.0 m receiver spacing. The detailed receiver layout is shown in Figure 4-5.

The amplification factors are calculated for λ/D ratios varying from 0.43 (M_w = -0.5) to 30.0 (M_w = 3.5) to understand the influence of the λ/D ratio on ground motion amplification. The results are presented in Figure 4-12. The color scales for all the contours are set to the same range (0.0 - 5.0) in order to compare the results easily. It should be noted that the amplification factors are greater than 5.0 in some cases.

Figure 4-12 shows the difference in the amplification factors for various λ/D ratios. The amplification factors decrease as the λ/D ratio increases and this trend is consistent with the results presented in Section 4.3.1. In addition, the area shows a large increase of the amplification factor decreases as the λ/D ratio increases. When the λ/D ratio is small (e.g., < 12), the amplifying and shielding areas can be observed clearly in the contours. In general, the areas that face the incoming seismic wave propagation (roof, right-wall, and floor side) have a relatively strong amplification (pink and red areas in the contours). The amplification factors decrease significantly with the increase of the λ/D ratio. For example, the amplification factor at the right wall side area decreases from 2.4 to 1.2 when the λ/D ratio increases from 0.75 to 20.0. This indicates that ground motion amplification effect can be expected when the λ/D ratio is small. High frequency seismic waves could potentially cause more damage to tunnels due to the amplification effect.

When the λ/D ratio is large (i.e., λ/D = 20.0 or 30.0), the amplification effect becomes less pronounced. For instance, when the λ/D ratios are equal to 20.0 and 30.0, the largest amplification factors around the excavation are 1.2 and 1.1, respectively. According to Dowding (1984) and Penzien (2000), there is no dynamic interaction between the opening and the seismic waves when the wavelength is many times (e.g., in the order of 20 times) larger than the opening

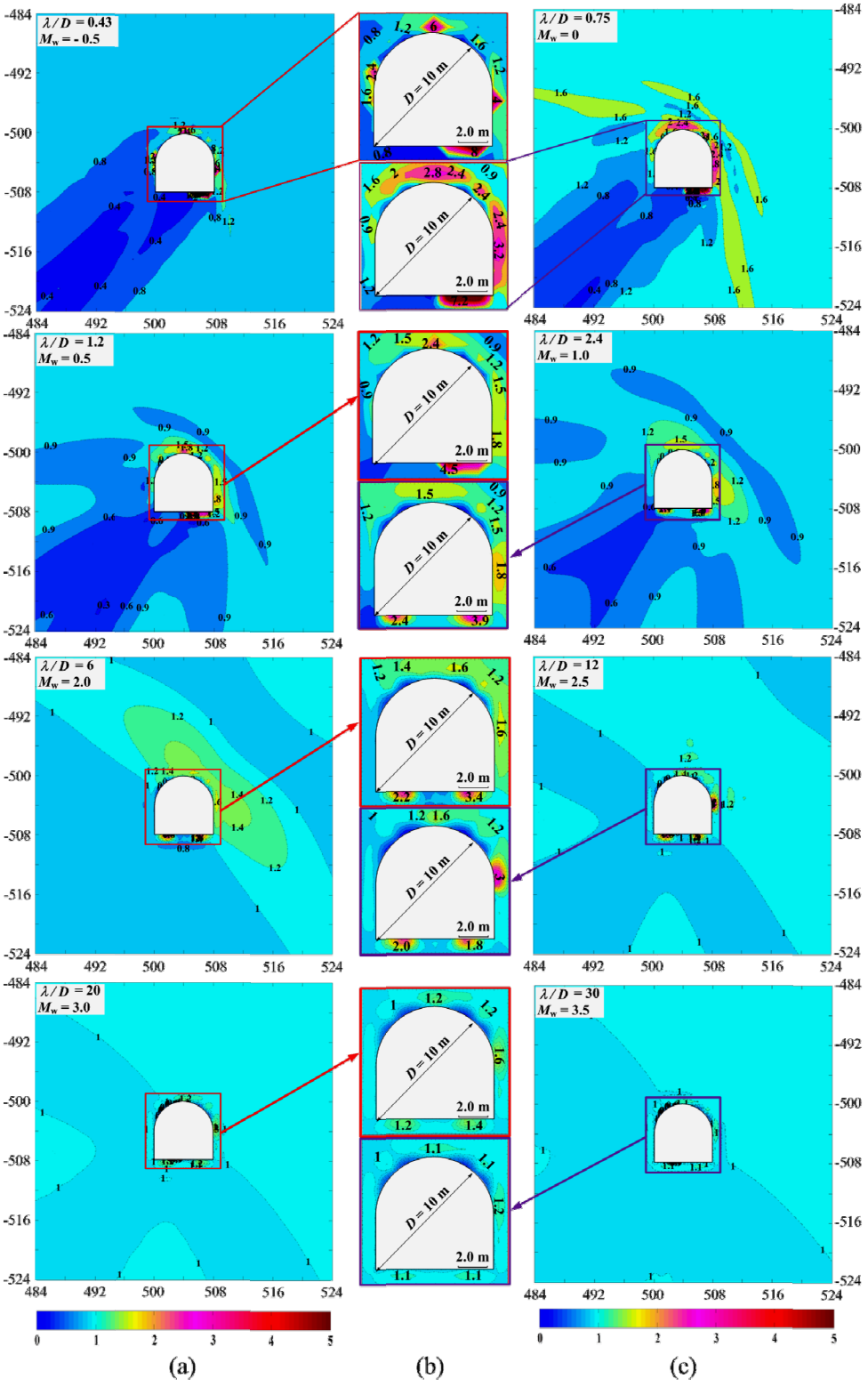

Figure 4-12: (a) & (c) Amplification factor distribution around the arched back excavation for eight λ/D ratios ranging from 0.43 to 30.0. (b) Zoom-in plots show detailed amplification factor distribution around the excavation boundary.

diameter. Tshering (2011) stated that under such a condition the whole excavation experiences almost the same loading and the loading can be viewed as a quasi-static loading instead of a dynamic interaction loading. It should be noted that the terms quasi-static loading condition and dynamic loading condition used in this thesis are referred to conditions with a larger λ/D ratio (e.g., > 30) and a small λ/D ratio (e.g., < 10), respectively. The modeling results are consistent with their findings.

4.3.3 Discussion

The modeling simulates ground motions around underground excavations that can be used for engineering design. The findings agree with the results of previous studies that define the quasi-static loading condition based on the λ/D ratio and provide convincing evidence of dynamic interaction loading condition when the λ/D ratio is small. The results from both types of models (fixed wavelength and variable tunnel size; fixed tunnel size and variable wavelength) show a similar trend. For a given seismic event, the ground motions around openings of different sizes (Section 4.3.1) are different. As the size of the excavation increases, wave amplification also increases. At the same time, an excavation can respond differently to seismic events of different intensities (Section 4.3.2). As the seismic source intensity increases, the PPV values increase but the amplification factor decreases around the excavation. This agrees with the conclusions from previous studies (Chen and Chen, 2004; Chen, 2005; Hashash et al., 2001) and the microseismic monitoring observation from underground mines (Milev and Spottiswood, 2005).

As stated in Section 4.3.2, for seismic events of different magnitudes, the ground motion is characterized by the dominant frequency. Normally, seismic waves generated from a seismic event contain multiple frequency components due to complex interaction between the seismic

waves and various structures in underground mines. Hence, high and low frequency components in the seismic waves can influence the seismic response of an excavation differently. Compared with high frequency components, low frequency components normally contain a large portion of the wave energy and can propagate a distance with a small attenuation. Higher ground motion (larger absolute PPV) can be generated due to the low frequency components, and this phenomenon can be used to explain rockburst damage in deep underground mines. As stated in Genis and Gercek (2003), the failure zone around a tunnel increases as the PPV amplitude increases. Moreover, although high frequency components (e.g., produced by complex reflection and refraction) have a relatively low seismic energy, the amplification effect can amplify the PPV value near the excavation boundary and this may contribute to triggering rockburst damage if a rock mass is already in a state near failure. Hence, both the high and low frequency components in the seismic waves play important roles in inducing rockburst damage.

4.4 Final remarks

Ground motion behavior around excavations is studied through the analysis of velocity wavefields, PPV contours, and amplification factors under different λ/D ratios. Both quasi-static and dynamic interaction loading conditions are considered in the modeling and a good understanding on how the λ/D ratio affects ground motion is obtained. The numerical modeling results seems to be consistent with most field observations and findings from previous studies and provide additional insight to ground motion near underground excavations.

The λ/D ratio does play an important role in modifying ground motion behavior around an excavation, including the distribution of PPV and the areas of wave amplification and de-amplification. In general, the PPV values increase as the λ/D ratio increases. The amplification

effect around an excavation increases as the λ/D ratio decreases, by either increasing the excavation span or decreasing the wavelength. Due to large wave amplification, an excavation with a large span may be more vulnerable to dynamic failure for the same seismic event. A relatively large value of λ/D ratio (e.g., 30) can be used to distinguish between dynamic and quasi-static seismic loading conditions. Once the λ/D ratio is larger enough (e.g., $\lambda/D > 30$), the amplification factor is almost independent of the λ/D ratio and a quasi-static loading condition can be used. Otherwise, dynamic loading condition should be considered. For most mine openings and fault-slip seismic events, the λ/D ratio is less than 10 (e.g., with a shear wave length less than 50 m for an excavation span of 5 m) and dynamic loading should be considered.

Complex dynamic wave interaction due to multiple frequency components in the seismic waves can cause ground motion amplification around underground excavations and this effect can be considered in dynamic rock support design. This chapter contributes to obtaining a deep understanding of the influence of λ/D ratio on ground motions near underground excavation boundaries.

Chapter 5

5 Influence of attenuation on wave propagation

In the parametric study conducted in Chapter 3 and in the wavelength to excavation span ratio study conducted in Chapter 4, the PPV values obtained from the numerical modeling are somewhat higher than the PPV values estimated directly from the scaling law. One possible reason can be the attenuation effects. The medium of the computation domain was assumed to behave as an ideal elastic medium and the attenuation was not considered in the previous chapters to reduce computation time. This chapter aims at studying the effect of medium attenuation on wave propagation so that wavefields can be modeled accurately. A method is proposed to estimate the shear quality factor for rocks in hard rock mines.

5.1 Introduction

In contrast to the ideal behavior of a perfectly elastic medium, seismic wave propagation in rocks is always accompanied with wave attenuation and frequency modulation, which can be described macroscopically in terms of internal friction. The internal friction effect usually results from irreversible movements along mineral dislocations and shear heating at grain boundaries, which lead to an anelastic medium (Aki, 1980b; Carcione, 2007b; Carcione et al., 1988). Many factors, such as geological structures, backfilled stopes, discontinuities, and fractured rocks, can cause wave attenuation in underground mines. A dimensionless quality factor of Q, which is a measure of energy loss per oscillation cycle, is used in this chapter.

5.1.1 Constitutive relations of the linear viscoelastic medium

Three main theories have been developed to explain the wave attenuation mechanism. The first one considers the Earth medium as a viscoelastic medium and the absorbing features are studied using models such as the Maxwell, the Kelvin-Voight, and the SLS (Standard Linear Solid) models (Carcione, 1993, 1995; Du et al., 2007; Vavrycuk, 2008). The second one views the Earth medium as an inhomogeneous medium and the loss of seismic energy is investigated by the multiple scattering theory (Kang and Chen, 2003; Mangriotis et al., 2013). The third one considers the Earth medium as a two-phase medium and the attenuation effect is analyzed by the Biot theory and the squirt-flow theory (Diallo and Appel, 2000; Saenger et al., 2005; Yang and Zhang, 2000).

Within a viscoelastic medium, current stress depends not only on the instant stress, but also on the previous stress and the strain condition. A viscoelastic medium combines the solid-like and liquid-like behaviors. For an anisotropic linear viscoelastic material, the general relation between stress and strain is given by Christensen (1982)

$$\sigma_{ij}(\mathbf{x},\mathrm{t}) = \psi^{c}{}_{ijkl}(\mathbf{x},\mathrm{t}) * \dot{\varepsilon}_{kl}(\mathbf{x},\mathrm{t}), \quad \mathrm{k},\mathrm{l},\ldots,\mathrm{n} \tag{5.1}$$

where t is time, $\mathbf{x}$ is the position vector, and ψ^{c}_{ijkl} is a fourth-order tensorial relaxation function, σ_{ij} and ε_{kl} are the stress and strain tensors, respectively. The dot above a variable denotes a time derivative. In Eq. (5.1), the Cartesian tensor notation is used, and i and j are in the range of 1, 2,. . . , n, where n is the spatial dimension.

The relaxation function $\psi^{\varepsilon}_{ijkl}$ can be expressed in an explicit form and the one proposed by Carcione et al. (1988) is

$$\psi_v(\mathrm{t}) = \mathrm{M}_v[1-\sum_{l=1}^{L_v}(1-\frac{t^v_{\varepsilon l}}{t^v_{\sigma l}})e^{-(t/t^v_{\sigma l})}],\ \ v=1,2 \tag{5.2}$$

where $t^v_{\sigma l}$ and $t^v_{\varepsilon l}$ stand for material relaxation times for the l_{th} mechanism, L_v is the number of relaxation mechanisms, M_v is the elastic or relaxed modulus of the medium that corresponds to dilatational (v = 1) or shear (v = 2) behavior of the medium. The relaxation function can represent L_v numbers of SLS elements connected in parallel for each deformation state, whether it is dilatational or shear. In this way, the basic Maxwell and Kelvin behavior models can be included by different relaxation functions.

5.1.2 Quality factor

Based on Eqs. (5.1) and (5.2), the attenuation effect of a medium can be controlled by the relaxation functions, governed by a set of relaxation parameters. In numerical modeling, the attenuation effect will, in most cases, be directly related to the shear modulus (μ) and the bulk modulus (κ). Instead of using particular relaxation functions, more emphasis is placed on Q (quality factor) in numerical modeling. Therefore, the quality factor will be briefly reviewed.

The energy loss per cycle is given by Carcione et al. (1988)

$$\Delta E_v = 2\pi\left|\phi_0^v\right|^2 \exp\{-2\boldsymbol{\alpha}_{\mathbf{v}}\cdot\mathbf{x}\}\times\left[\rho\omega^2\mathbf{k}_{\mathbf{v}}\cdot\boldsymbol{\alpha}_{\mathbf{v}}+2\mu^I\left|\mathbf{k}_{\mathbf{v}}\times\boldsymbol{\alpha}_{\mathbf{v}}\right|^2\right] \tag{5.3}$$

where ΔE_v is the energy loss, ϕ_0^v is a constant complex quantity, k_v is the complex wave number, which is defined as $k_v(\omega)=\omega/v_v(\omega)$, $\mathbf{k}_{\mathbf{v}}$ and $\boldsymbol{\alpha}_{\mathbf{v}}$ are real vectors that indicate the direction and magnitude of propagation and attenuation, respectively. μ is the displacement field.

The peak energy density stored per cycle is expressed by

$$P_v^{\max} = \frac{1}{2}\left|\phi_0^v\right|^2 \exp\{-2\boldsymbol{\alpha}_\mathbf{v}\cdot\mathbf{x}\}\times\left[\rho\omega^2(\mathrm{k}_v^2-\alpha_v^2)+2\mu^R\left|\mathbf{k}_\mathbf{v}\times\boldsymbol{\alpha}_\mathbf{v}\right|^2\right] \tag{5.4}$$

The quality factor is defined by

$$Q_V = 2\pi\frac{p_v^{\max}}{\Delta E_v} = \frac{\rho\omega^2(\mathrm{k}_v^2-\alpha_v^2)+2\mu^R\left|\mathbf{k}_\mathbf{v}\times\boldsymbol{\alpha}_\mathbf{v}\right|^2}{2\rho\omega^2\mathbf{k}_\mathbf{v}\cdot\boldsymbol{\alpha}_\mathbf{v}+4\mu^I\left|\mathbf{k}_\mathbf{v}\times\boldsymbol{\alpha}_\mathbf{v}\right|^2} \tag{5.5}$$

where μ^R and μ^I are the real and imaginary parts of μ.

The complex moduli is defined by Carcione et al. (1988)

$$\begin{aligned} M_v^c(\omega) &= \mathbf{F}[\delta(t)\psi_v(t)+H(t)\times\sum_{l=1}^{L_v}\frac{M_v}{\tau_{\sigma l}^v}(1-\frac{\tau_{\varepsilon l}^v}{\tau_{\sigma l}^v})\exp(\frac{-t}{\tau_{\sigma l}^v})] \\ &= M_v[1-\mathrm{L}_v+\sum_{l=1}^{L_v}\frac{1+i\omega\tau_{\varepsilon l}^v}{1+i\omega\tau_{\sigma l}^v})] \end{aligned} \tag{5.6}$$

where $\delta(t)$ is the Dirac's function. ω is angular frequency. $H(t)$ denotes the Heaviside function. Operator **F** means performing the time Fourier transform.

Based on the complex moduli, the complex Lamé constants are defined as

$$\begin{aligned} \lambda_c(\omega) &= \frac{1}{n}[M_1^c(\omega)-M_2^c(\omega)] \\ \mu_c(\omega) &= \frac{1}{2}M_2^c(\omega) \end{aligned} \tag{5.7}$$

The complex bulk modulus of the medium is then defined by Carcione et al. (1988) as

$$k(\omega) = \lambda_c(\omega)+\frac{2}{n}\mu_c(\omega) = \frac{1}{n}M_1^c(\omega) \tag{5.8}$$

Combining the terms of the dilatational and shear complex moduli, the quality factor can be written as

$$Q_\mu = \frac{\mathrm{Re}\,(M_2^c)}{\mathrm{Im}\,(M_2^c)} \qquad \text{for shear modulus}$$
$$Q_k = \frac{\mathrm{Re}\,(M_1^c)}{\mathrm{Im}\,(M_1^c)} \qquad \text{for bulk modulus} \tag{5.9}$$

Finally, the quality factors for P-wave and S-wave can be written as

$$Q_p^{-1} = (1 - \frac{4}{3} V_s^2 / V_p^2) Q_\kappa^{-1} + \frac{4}{3} (V_s^2 / V_p^2) Q_\mu^{-1}$$
$$Q_s^{-1} = Q_\mu^{-1} \tag{5.10}$$

From the above equations, it is seen that S-wave attenuation results from the relaxation of the μ and P-wave attenuation is caused by both μ and κ relaxations. Because the bulk attenuation is two orders of magnitude larger than the shear attenuation, Q_κ^{-1} can be ignored safely. Hence, Eq. (5.10) can be rewritten as

$$Q_s^{-1} = Q_\mu^{-1}$$
$$Q_p^{-1} \approx \frac{4}{3} (V_s^2 / V_p^2) Q_\mu^{-1} \tag{5.11}$$

Based on Eq. (5.11), the attenuation effect of seismic waves can be considered by using quality factors. For instance, for a Poisson solid (the Poisson's ratio is equal to 0.25), $Q_p = (9/4) \times Q_s$. In seismology, wave attenuation is observed to be relatively constant over a broad frequency range. It should be noted that waves of different frequencies will experience different attenuation effects.

Q is independent of wave frequency, which means that each frequency loses the same amount of energy. Consequently, high frequency waves, which have more oscillations, will introduce more attenuation. For low frequency waves, fewer oscillations will lead to less attenuation. This explains, more or less, why high frequency waves decay rapidly.

In the SPECFEM2D/3D codes, the SLS (Standard Linear Solid) model is used to model the attenuation effect. The SLS model describes the stress–strain relation as a convolution of a linear combination of relaxation functions in the time domain. Once the shear and bulk quality factors of the medium and a set of parameters for the SLS model (such as frequency for viscous attenuation, number of SLS for attenuation) are determined, the wave attenuation effect can be modeled properly.

5.2 Design scaling law for dynamic support design

Kaiser and Cai (2013) stated that the design scaling law presents a valid engineering approach to estimate upper bound ground motion parameters (PPV/PPA) for dynamic rock support design in burst-prone ground, especially when rock damage is caused by block ejection due to seismic energy transfer. The purpose is to provide a background of the design scaling law and further provide a baseline for the subsequent study of wave attenuation effect.

5.2.1 Design scaling law

In burst-prone ground, dynamic support is essential for safe and productive mining. The ejection velocity of a rock block is usually assumed equal to the PPV at the excavation surface (Kaiser and Maloney, 1997), and PPV is accepted as a representative parameter to determine dynamic support demands when damage is caused by rock block ejection (Kaiser and Cai, 2013). In light of this, knowledge of PPV/PPA generated by incoming seismic waves is required to determine demands of rock support and to analyze rockburst damage.

Near-field PPV and far-field PPV should be considered separately based on the distance between design location and the seismic source because the radiation patterns are completely different in

the near-field and the far-field. In the case of far-field, the PPV is roughly inversely proportional to the distance to the seismic source. However, this relation is not applicable to the near-field (Hudyma, 2013; Kaiser et al., 1996; Potvin and Wesseloo, 2013).

Currently, scaling laws are used widely to estimate PPV values for ground support design when damage is caused by rock ejection. McGarr (1984) proposed the following scaling law to estimate the PPV in the far-field

$$PPV = \frac{C \times 10^{(a * M_L)}}{r} \tag{5.12}$$

where PPV is the peak particle velocity (m/s), M_L is the local magnitude of the seismic event, r (m) is the source-target distance, and a and C are site-specific constants. After a regression analysis on seismic data from some Canadian mines (such as Brunswick mine and Creighton mine) and mines from other countries (such as EI Teniente mine), Kaiser et al. (1996) recommended that for prefeasibility type studies that a = 0.5 and C = 0.1 or 0.25 m^2/s (which correspond to 50% or 90 to 95% confidences, respectively) can be used to estimate PPV values when there is a lack of seismic data in a mine.

Using the design scaling law, upper bound PPV values can be obtained at different target source distances from various intensities of seismic events. Figure 5-1 shows the relation among PPV, source-target distance, and seismic event magnitude. It should be noted that even very small seismic events can trigger severe rock damage if the excavations are already in a condition of a marginal equilibrium due to mining. Figure 5-1 indicates that the maximum ground motion PPV_D can be estimated at various source-target distances for seismic events of different magnitudes.

5.2.2 Application of design scaling law

When scaling law is used to estimate the PPV, it assumes a point source of the seismic event and the waves propagate in an isotropic medium without reflection and refraction in a typical underground mining environment. Two limitations of the design scaling law are listed below (Kaiser and Cai, 2013):

a) The design scaling law cannot be applied to obtaining PPV properly in the near-field

In the near-field, the wave radiation pattern is extremely non-uniform and complex and the velocity field could also be different when comparing it with that in the far-field. Hence, according to the Canadian Rockburst Handbook (Kaiser et al., 1996), for magnitudes in the range of $1.0 < M_L < 3.5$, the design scaling law is not appropriate for locations closer than 5 to 30 m for a stress drop of 10 MPa, and 35 to 75 m for a stress drop of 1 MPa, respectively.

b) The design scaling law cannot be used in forensic analyses of rockburst damage

The PPV_D estimated from the design scaling law represents a possible upper bound condition of observed data from word-wide data. In other words, the values given by the scaling laws are not necessarily equal to actually measured field data in a seismic event, at a given source-target

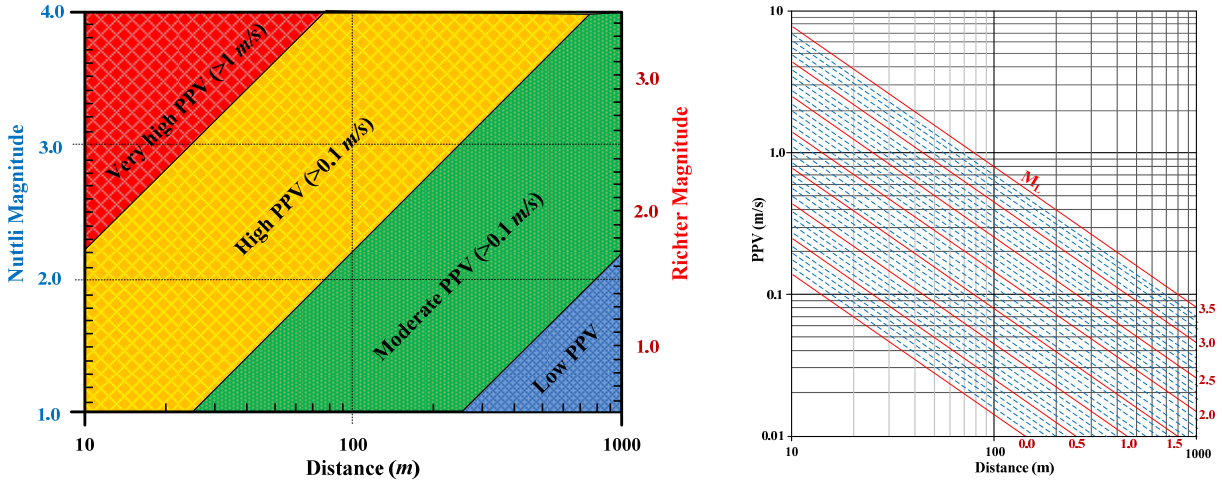

Figure 5-1: Relation among PPV, source-target distance, and seismic event magnitude (Kaiser et al., 1996).

distance (Kaiser and Cai, 2013). In general, field recorded ground motion differ from the PPV_D due to various factors such as source parameters, fault-slip direction, medium, site sensor location, site amplification effects, etc., which may lead to various ground motions.

In dynamic rock support design, it is reasonable to consider the worst-case scenario and hence it is valuable to provide a threshold value of PPV_D in design. Although there are limitations in the approach of the design scaling law, the design scaling law is still a robust engineering approach for dynamic support design when ejection due to a remote seismic event constitutes the applicable damage source. The scaling law can offer meaningful design inputs (Kaiser and Cai, 2013). However, for forensic analysis, it is necessary to determine the actual ground motion at a give damage location.

5.3 Models and parameters of 2D homogeneous medium

The design scaling law corresponds to a near worst case scenario and provides the maximum anticipated ground motion for design. The design scaling law has to be calibrated using real data from underground mines. Hence, the maximum ground motion obtained from a numerical simulation with the same assumptions (isotropic and homogeneous medium, point source model) should not be higher than the values given by the design scaling law. In other words, the numerical simulation results can be adjusted by comparing the results with that given by the design scaling law. For design purpose, a 90 to 95% confidence level for estimating PPV is typically required. However, a 50% average confidence level for estimating PPV should be considered to determine the quality factor for hard rocks in underground mines. The purpose of this forward modeling exercise is to investigate the influence of attenuation on wave propagation and the scaling law is used as the base for determining the quality factor in an attenuation model.

5.3.1 2D homogeneous medium model

A simple homogeneous viscoelastic medium is considered to investigate the attenuation effect of the medium and to determine a proper shear quality factor for future modeling work. The model setup is shown in Figure 5-2(a). The model is configured as a square (608 m × 608 m) and the seismic source is placed right on the diagonal line of the model, at x = 550 m, z = -58 m. Based on the parametric study, the diagonal line direction is identified as the maximum wave front propagation direction. In this manner, the PPV can be captured in the diagonal direction if the source parameters are selected properly. A total of 50 receivers are placed in this model. 40 receivers are set at an interval of 20 m from the source to the left corner of the model (green triangles), and 10 receivers are placed at a 1 m interval located 10 m from the seismic source (yellow triangles). The four edges are set as absorbing boundaries and four elements of PML (perfect match layer) are used for each boundary in the model.

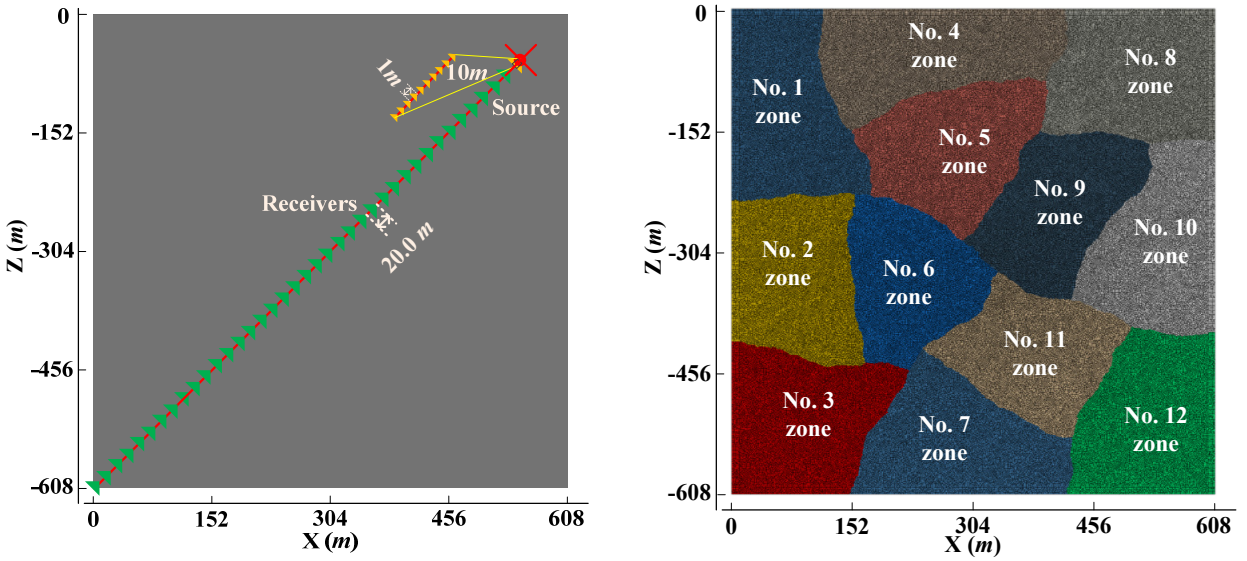

(a) (b)

Figure 5-2: (a) 2D simulation model of seismic wave propagation in a homogeneous viscoelastic medium whose properties are summarized in Table 5-1. The model dimension is 608 m × 608 m, and a seismic source with a dominant frequency of 100 Hz (denote by the red cross) is located at (x = 550 m, z = -58 m). Receivers (denote by green and yellow triangles) are placed in the model to capture the PPV. (b) 2D simple homogenous modeling mesh is partitioned to run in parallel on 12 CPU cores. The 12 partitions are indicated by different colors.

12 CPU cores are used for parallel computation to reduce computation time (as shown in Figure 5-2(b)). For this model, about 6.5 and 17 hours (12 cores) are required to complete the modeling for the elastic and viscoelastic models, respectively. Longer times would be required to finish the job if only one or two CPUs were used.

5.3.2 Description of the seismic wave attenuation model

In most attenuation models, the shear quality factor is often significantly lower than the bulk quality factor, which lead to shear-dominated attenuation (Dziewonski and Anderson, 1981; Romanowicz and Mitchell, 2007). As a result, most seismic wave attenuation is predominantly dependent on the shear quality factor. It is important to emphasize that because the intrinsic attenuation is predominantly caused by shear lattice effects at grain boundaries that lead to the shear-dominated attenuation. Moreover, because the bulk attenuation factor (Q_κ) is usually hundreds of times greater than shear attenuation factor (Q_μ), hence, only the Q_μ will be incorporated and considered and the Q_κ will be neglected (Komatitsch et al., 2000; Lee et al., 2009; Savage et al., 2010). This greatly simplifies the attenuation model.

The viscoelastic medium properties are summarized in Table 5-1. These values are for typical hard rocks in underground metal mines. In the numerical modeling, the perturbation is initiated by a moment tensor with a Ricker time function with a dominant frequency of 100 Hz. A normal fault with a dip of 45° is modeled, and this seismic event will produce the maximum seismic response on the receivers that are placed in the model. $M_w = 1.5$ is selected as the design moment magnitude. The seismic moment of the source event and the components of the moment tensor are determined following the method described in Chapter 2.

Table 5-1: Medium properties of the viscoelastic model

Variable name	Symbol	Unit	Value
Elastic modulus	E	GPa	58
Poisson's ratio	ν	-	0.24
P-wave velocity	V_p	m/s	5874
S-wave velocity	V_s	m/s	3400
Bulk quality factor	Q_κ	-	9999
Shear quality factor	Q_μ	-	40-1000

A high quality mesh of the model is generated using the tool kit of Gmsh, and Delaunay for quadrangle is used as the 2D algorithm to discretize the computation domain. The grid spacing is roughly 1 m for each element and the total number of elements is 369,664. A time step increment of $\Delta t = 1.0 \times 10^{-5}$ s is used and the total time steps are set to 22,000, which means that about 220 ms will last for the seismic wave propagation.

5.4 Results and discussion

5.4.1 Wavefield of vertical displacement

Figure 5-3 presents snapshots of vertical displacement wavefield for different shear quality factors at t = 0.01, 0.05, 0.1, 0.15 and 0.2 s. It can be seen that body waves are excited and generated at first (Figure 5-3: t = 0.01 s) and body waves are then separated into fast P-waves and slow S-waves (Figure 5-3: t = 0.1 and t = 0.15 s). After 0.21 s, only the S-waves propagate in the domain and the P-waves have passed through the PML boundaries.

The attenuation effect is examined by three different shear quality factors (200, 150, and 100) and the results are compared with that without attenuation. The displacement wavefield of the elastic case is shown in the first column (a) and the other three cases with shear quality factors

200, 150, and 100 are shown in columns (b), (c), and (d) respectively in Figure 5-3. At t = 0.01 s and 0.05 s, arriving time and shapes of wave front of the P- and S-waves are similar in all four cases. As the waves propagate further, travel time and waveform are still similar to each other.

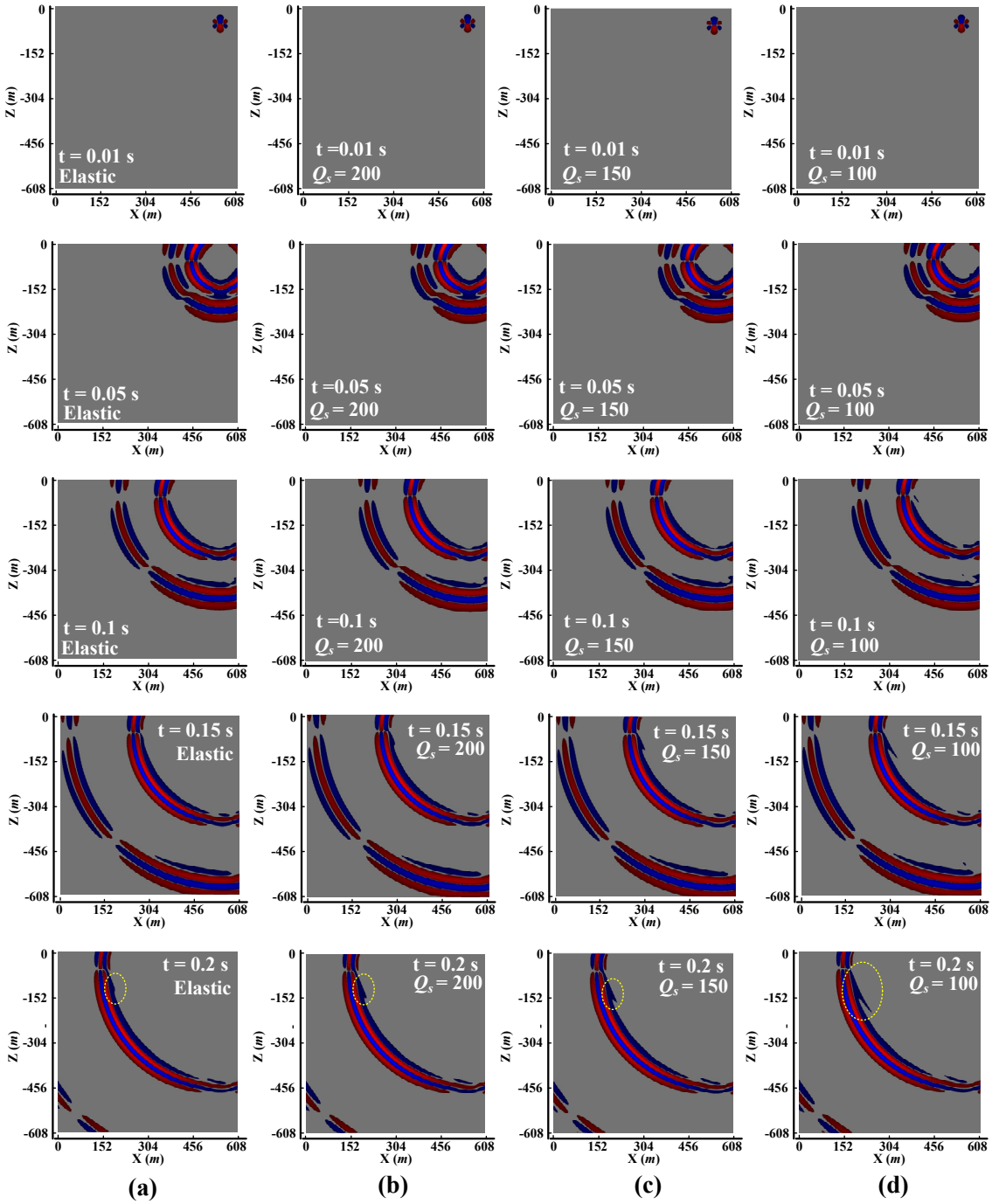

Figure 5-3: Snapshots of the vertical displacement at 0.01, 0.05, 0.1, 0.15 and 0.2 s for the elastic model (a), and for the viscoelastic models of (b), (c), and (d) with different shear quality factors (200, 150, and 100). The computation domain is represented by the grey background. Positive (upward) and negative (downward) displacements are represented by red and blue, respectively.

Although the differences are not notable, the attenuation effect is discernible when comparing the results with each other carefully. By observing the wave front of S-waves at 0.2 s, it is evidenced that there is a strong attenuation as the shear quality factors decrease gradually (changes of waveforms are highlighted by the yellow dash ovals in Figure 5-3). The attenuation effect is seen in the S-waveform, which is expected because the shear quality factors are used.

The difference in the vertical displacement wavefields in Figure 5-3 is not clearly notable. Velocity seismograms of each component are calculated separately and PPV values are calculated to further investigate the influence of the shear quality factor on wavefield. To place a series of receivers to generate the PPV contour, a tunnel to be excavated is included in this model. A total of 1681 receivers are placed in a rectangular region of 40 m × 40 m. The tunnel location and the receiver layout are shown in Figure 5-4(a). It should be noted again that the tunnel is placed here without excavation; the purpose is to generate the PPV contours around a potential excavation.

Figure 5-4(b) to (d) present the PPV contours for the elastic model and the attenuation models with Q_s = 200 and Q_s = 100, respectively. It is evident that attenuation affects the PPV distributions. As expected, the PPV contours follow basically the same distribution trend as the scaling law, showing a decreasing trend as the source-target distance increases. The maximum PPV value in the mapping region is located at the right upper corner. For the elastic model, the PPV is about 0.0566 m/s at the right tunnel arch, which is roughly 1.14 and 3.68 times higher than the PPV values for the Cases with Q_s = 200 (0.0495 m/s) and Q_s = 100 (0.0154 m/s), respectively.

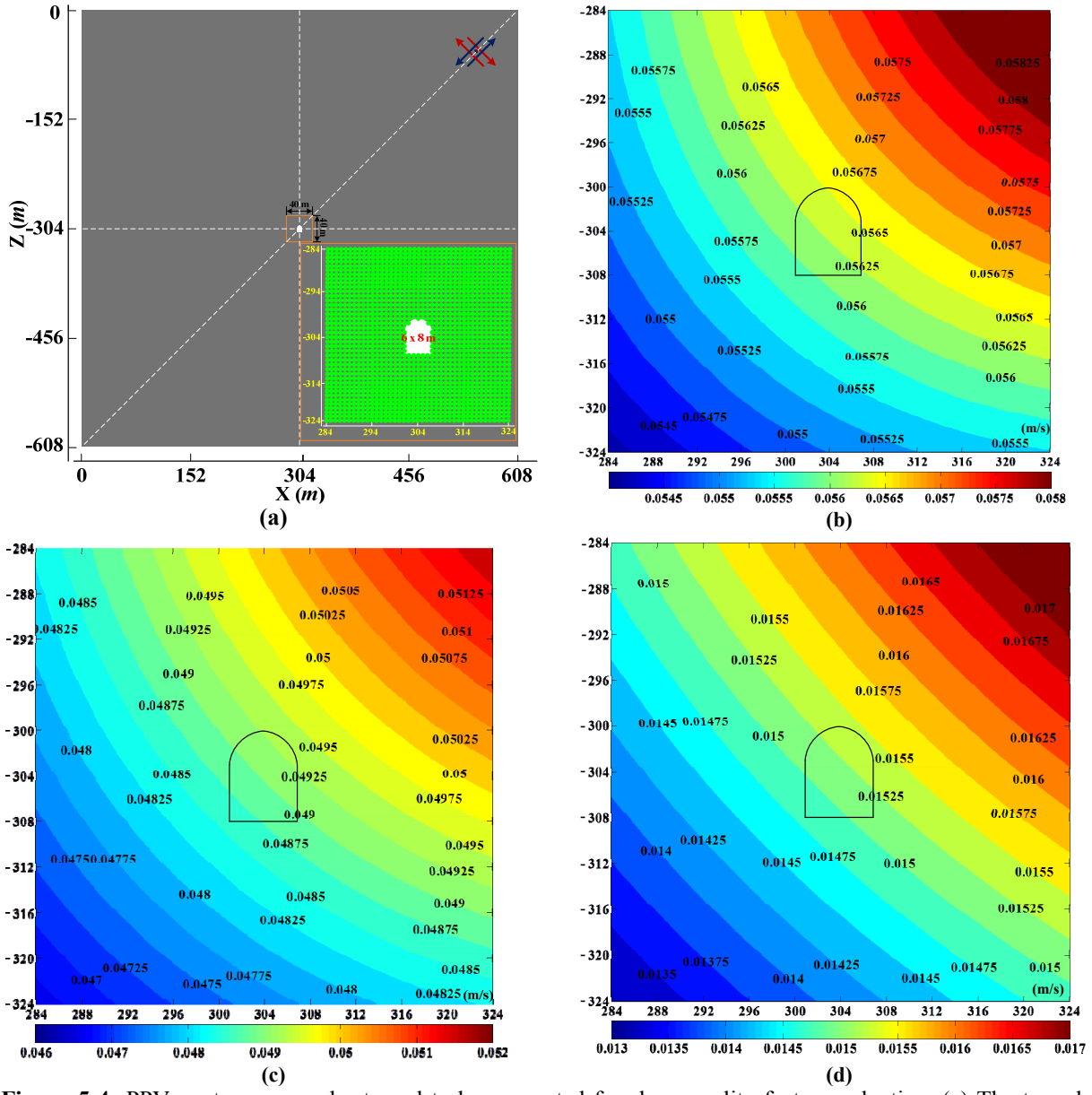

Figure 5-4: PPV contours around a tunnel to be excavated for shear quality factor evaluation. (a) The tunnel is placed at the center of the model. The yellow rectangle in the center, 40 m × 40 m in size, represents the range of the contour map. 41 × 41 receivers are placed in this range, with a 1.0 m spacing between each receiver, which are denoted by the small green dots in the insert in (a). (b) PPV contours for the elastic model, (c) and (d) are the PPV contours for the cases of $Q_s = 200$ and $Q_s = 100$, respectively.

5.4.2 Shear quality factor determination

As stated above, the scaling law provides upper bond PPV value based on the seismic intensity and the source-target distance. In this work, 50 receivers are placed along the diagonal line which represents the maximum ground motion direction. The distance between two receivers is

20 m. The PPV value of each receiver is calculated from the seismograms of the horizontal and vertical velocity components using Matlab. The PPV values estimated from the scaling law with a 50% confidence are compared with the PPV obtained from the numerical modeling.

Figure 5-5 shows the simulated PPV distribution along the diagonal line for various quality factors. It is shown that the PPV value decreases exponentially as the wave travel distance increases. This trend is evident for both the elastic and the attenuation models. Furthermore, it is seen that strong attenuation is associated with low Q_s values. The PPV distribution from the scaling law with the intensity of M_L = 1.5 is also shown in Figure 5-5. It is seen that the PPV distribution by the scaling law has already included the effect of attenuation in the field. The simulated PPV is less than the PPV value from the scaling law when Q_s is lower than 60.

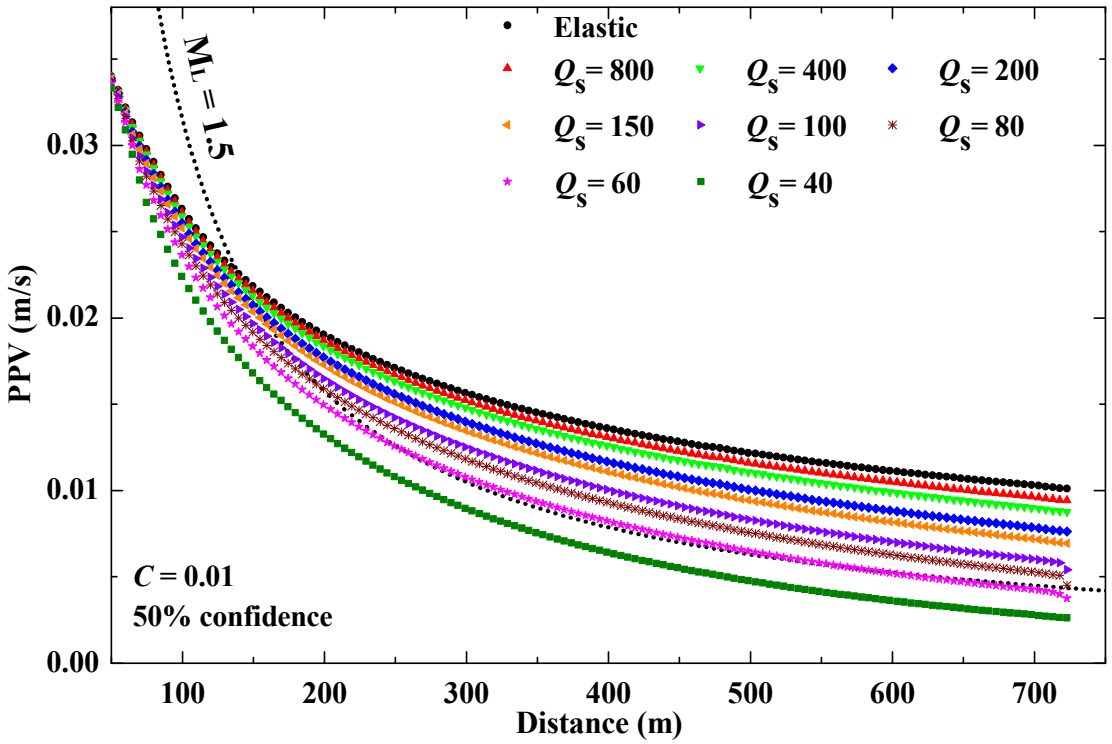

Figure 5-5: PPV versus source-receiver distance with different shear quality factors. The simulation results indicate that the PPV decreases exponentially with the seismic wave travel distance, which is in good agreement with field observation.

For a further comparison, PPV from the numerical simulation and PPV from the scaling law are shown in Figure 5-6. It is seen that by selecting a proper shear quality factor in the attenuation model, the PPV distribution from the modeling can match the PPV distribution from the scaling law well (Figure 5-6(b)), particularly for the far-field. The scaling law provides the upper bound PPV and the results from this simple homogenous numerical model should also produce the upper bound PPV (based on the assumptions made). Accordingly, the simulated PPV should not be greater than the scaling law PPV and the trend line should be roughly the same or very close to the one given by the scaling law. Hence, a proper shear quality factor can be chosen from the plot shown in Figure 5-6. When the source is represented by a moment tensor model, a shear quality factor of Q_s = 60 in the attenuation model will produce a realistic wave attenuation for the hard rocks in the far-field in underground mines when the results from the scaling law with a confidence of 50% are used for comparison.

Referring to the PPV distributions shown in Figure 5-6, it shows that there is a decreasing trend of PPV values as Q_s decreases. According to Figure 5-6(a) and (b), at a distance of 200 m, the PPV values reduce from about 0.0187 to 0.013 m/s when Q_s decreases from 800 to 40, respectively. This deduction indicates that the lower the shear quality factor is, the stronger the medium attenuation is. Moreover, the trend for each case can be seen in Figure 5-6(b). When Q_s = 60 is used, the simulated PPV is comparable with the estimated PPV from the scaling law (at the 50% confidence level) and the trend line is also close to that from the scaling law (see Figure 5-6). In this way, Q_s = 60 will be used to consider wave attenuation in hard rocks. It should be noticed that Q_s = 60 is a reference shear quality factor which corresponds to the scaling law derived from a hard rock mine in Canada. For other hard rock conditions, Q_s in the ranges of 40

to 80 can be considered. A relatively higher value of Q_s is expected to correspond the upper bound PPV from scaling law when 90 to 95% confidence level is considered.

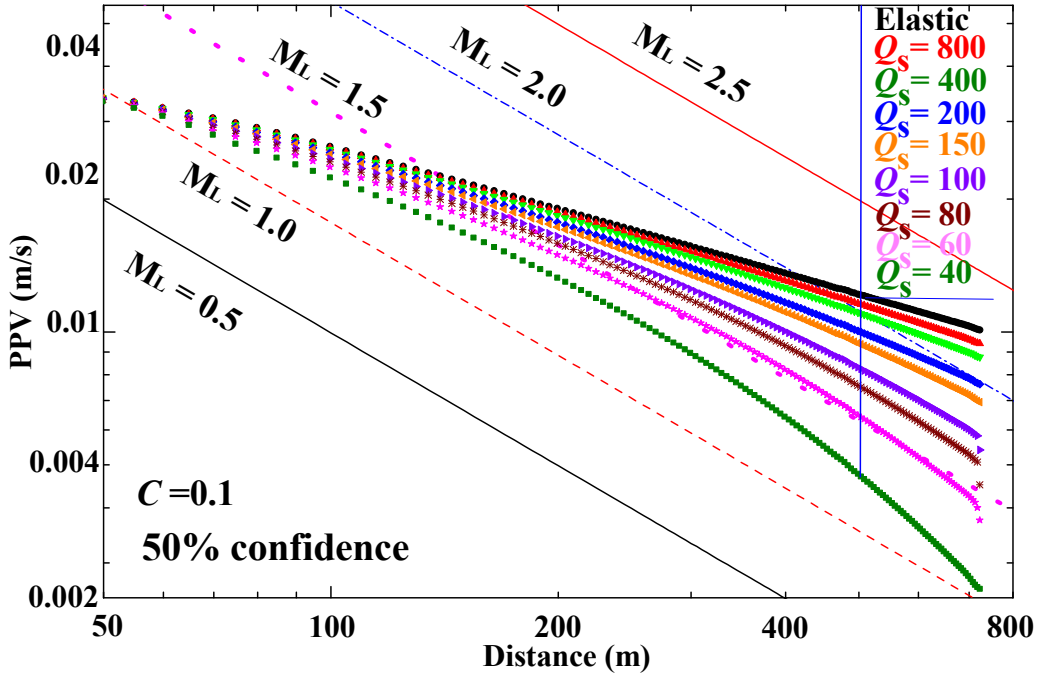

(a)

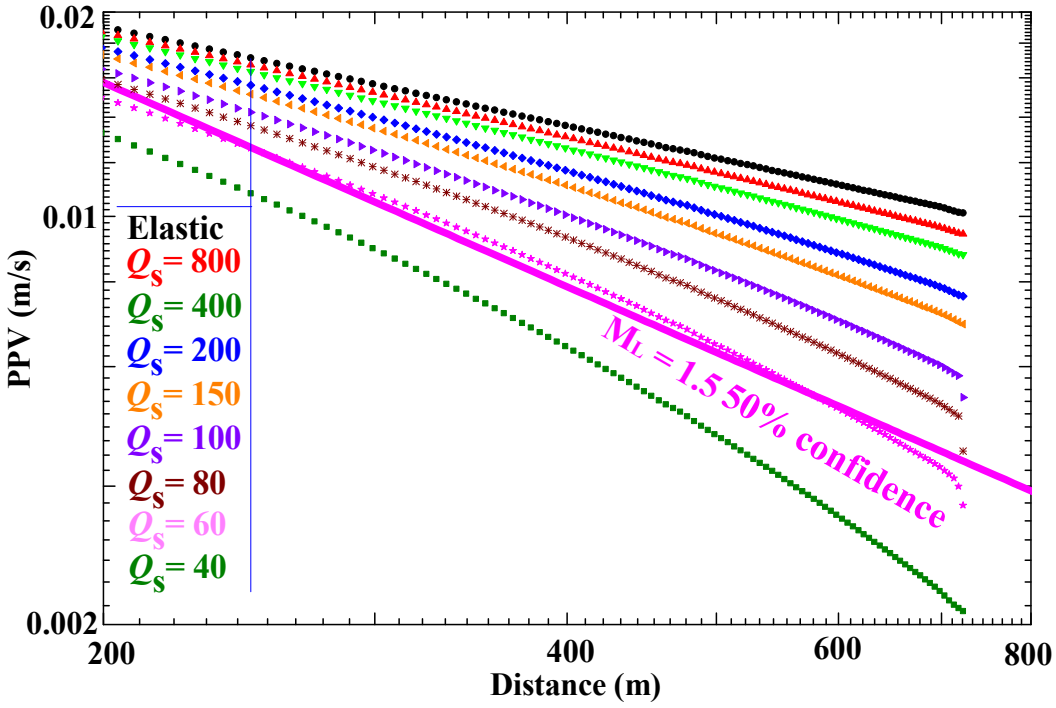

(b)

Figure 5-6: PPV distributions for various shear quality factors and PPV from the scaling law with a 50% confidence level. (a) and (b) are plotted using the same data, but (b) shows only the data for the far-field (distance > 200 m).

5.4.3 Discussion

It is difficult to estimate the quality factors for the P and S-waves in underground mines. Many factors such as rock type, voids, water content, and discontinuities can influence the quality factors in the context of a mining environment. Among different influencing factors, the source-sensor path has a large influence on the quality factor determination. It means that a large variation of the quality factor is expected at different sensor stations even in the same hard rock domain. For instance, in order to consider the attenuation effect for nine receiver stations in a South African gold mine, Richardson and Jordan (2002) employed a quality factor of $Q_s = 133$ to conduct waveform inversion work. Furthermore, for a better back analysis, Yamada et al. (2005) conducted waveform inversion by assigning different quality factors to each receiver station (Q_s ranges from 10 to 75). More reliable quality factor may be obtained by deriving a site-specific inversion based on data obtained from each receiver station in underground mines.

When field data are not available to conduct back analysis to calibrate the quality factor, the method discussed in this chapter provides a means to estimate the quality factor for hard rocks in underground mines.

5.5 Final remarks

Seismic wave propagation is strongly influenced by the attenuation effect, where the intrinsic attenuation is predominantly caused by the shear lattice effect at grain boundaries. The dimensionless quality factor Q can be used to describe the intrinsic attenuation effect. Because the intrinsic attenuation is mainly controlled by the shear quality factor Q_s, only the shear quality factor can be considered in numerical modeling and the bulk quality factor can be ignored.

PPV results from the numerical simulation of a homogenous model are compared with the PPV derived from the scaling law. The attenuation effect can be observed clearly in the modeling results when the modeling results are compared with the results from the elastic model and from the scaling law. When the average confidence level of PPV from the scaling law is considered, $Q_s = 60$ seems to be a proper representative value to account the attenuation effect. Due to the complexity of underground mining environment, a range of shear quality factor (e.g., 60±20) can be considered for wave propagation simulation using a moment tensor seismic source model for the far-field in hard rock mines.

Chapter 6

6 Influence of heterogeneity on wave propagation

In Chapter 5, the attenuation effect of the medium was studied and a method was proposed to determine the shear quality factor for hard rocks in underground mines when field data are not available. In this manner, the attenuation effect can be included in estimating PPV, especially for far-field ground motions. Furthermore, as stated in Chapter 2, wave pattern alteration due to geological structures and mine excavations was one of the important factors that contribute to localized rockburst damage. This chapter therefore focuses on investigating the effect of mining and geological structures, such as tunnel, open stope, backfilled stope, and dyke on ground motions. Part of the results in this chapter was published in the proceedings of the ***7th International Seminar on Deep and High Stress Mining, Deep Mining 2014***, held in Sudbury, Canada.

6.1 Introduction

Seismic waves emitted from a seismic event may cause localized tunnel damage and this phenomenon may in part be attributed to the complex wave pattern around the underground openings. The propagation patterns of seismic waves are influenced by various factors such as the characteristics of the seismic source and the transit medium and the local site (Carcione, 2007a; Kühn and Vavryčuk, 2013). It is known that heterogeneity contributes to the variation of wave patterns, which can make the wave patterns very complex. In general, heterogeneities in underground mines can be caused by the presence of faults, ore bodies, different rock types, mined and backfilled stopes, and tunnel systems. Among them, the mined-out openings will

introduce strong velocity contrasts, which may cause multiple scattering of waves and may result in a complex wavefield with long coda waves (Aki and Richards, 2002; Chapman, 2004). The phenomena of wave reflection, refraction, dispersion, and diffraction will be observed when the seismic waves encounter a material property change. Therefore, it is important to have a good knowledge of the wave pattern and ground motion (PPV) distribution near mine openings in order to conduct rational engineering design such as dynamic rock support design. In this chapter, wave propagation patterns due to heterogeneity are examined through synthetic seismograms, snapshots of velocity wavefield, and PPV contours around tunnels.

6.2 2D models with typical heterogeneities in underground mines

6.2.1 Model setup

In the SPECFEM2D computation models, heterogeneous models with different structures are considered to examine the influence of typical natural or man-made heterogeneities on wave propagation. The model types are summarized in Table 6-1 and Figure 6-1.

Table 6-1: 2D models with typical heterogeneities in underground mines

Model type	Model name		Description
Background	$M_{1\text{-}R}$	$M_{1\text{-}L}$	No excavation, homogenous medium, moment tensor source
Excavation	$M_{2\text{-}R}$	$M_{2\text{-}L}$	Tunnel T1 is excavated in the computation domain
Backfilled stope	$M_{3\text{-}1\text{-}R}$ $M_{3\text{-}2\text{-}R}$ $M_{3\text{-}3\text{-}R}$	$M_{3\text{-}1\text{-}L}$ $M_{3\text{-}2\text{-}L}$ $M_{3\text{-}3\text{-}L}$	3 levels of backfilled stopes (S1, S2, and S3) are added near tunnel T1, at a distance of 20 m from the tunnel
Dyke	$M_{4\text{-}1\text{-}R}$	$M_{4\text{-}1\text{-}L}$	A 3 m wide of dyke is added at the right side of tunnel T1
Multiple openings	$M_{5\text{-}1\text{-}R}$ $M_{5\text{-}2\text{-}R}$	$M_{5\text{-}1\text{-}L}$ $M_{5\text{-}2\text{-}L}$	Multiple openings (tunnels T2, T3, and T4) are considered at certain distance away from tunnel T1 in the stope and dyke models

Notes: In the above table, M_i (i = 1, 2, …, 5) indicates case number of the models. Subscripts -R and -L denote that seismic source is located at the upper-right and upper-left side of the model, respectively. Subscripts -1/-2/-3 means different mining stages of the stope in the backfilled model, -1 denotes the first level is mined out; -2 means the second level is excavated and the first level is backfilled; -3 means that the third level is mined and the other two levels are backfilled. In the multiple openings model, -1 and -2 mean three openings are considered in the backfilled stope models and the dyke models, respectively.

As can be seen from Figure 6-1, the size of the model is 608 m × 608 m. The four edges are set as absorbing boundaries and 4 elements of the PML (perfect match layer) are imposed for each boundary. A 6 m × 8 m tunnel is located at (x = 264 m, z = -405 m, tunnel T1 in the figure). A seismic source is located at a distance from the stopes and tunnels. Several cases are considered: Figure 6-1(a): Background model without any tunnel ($M_{1\text{-}R}$ and $M_{1\text{-}L}$) and with tunnel T1 ($M_{2\text{-}R}$

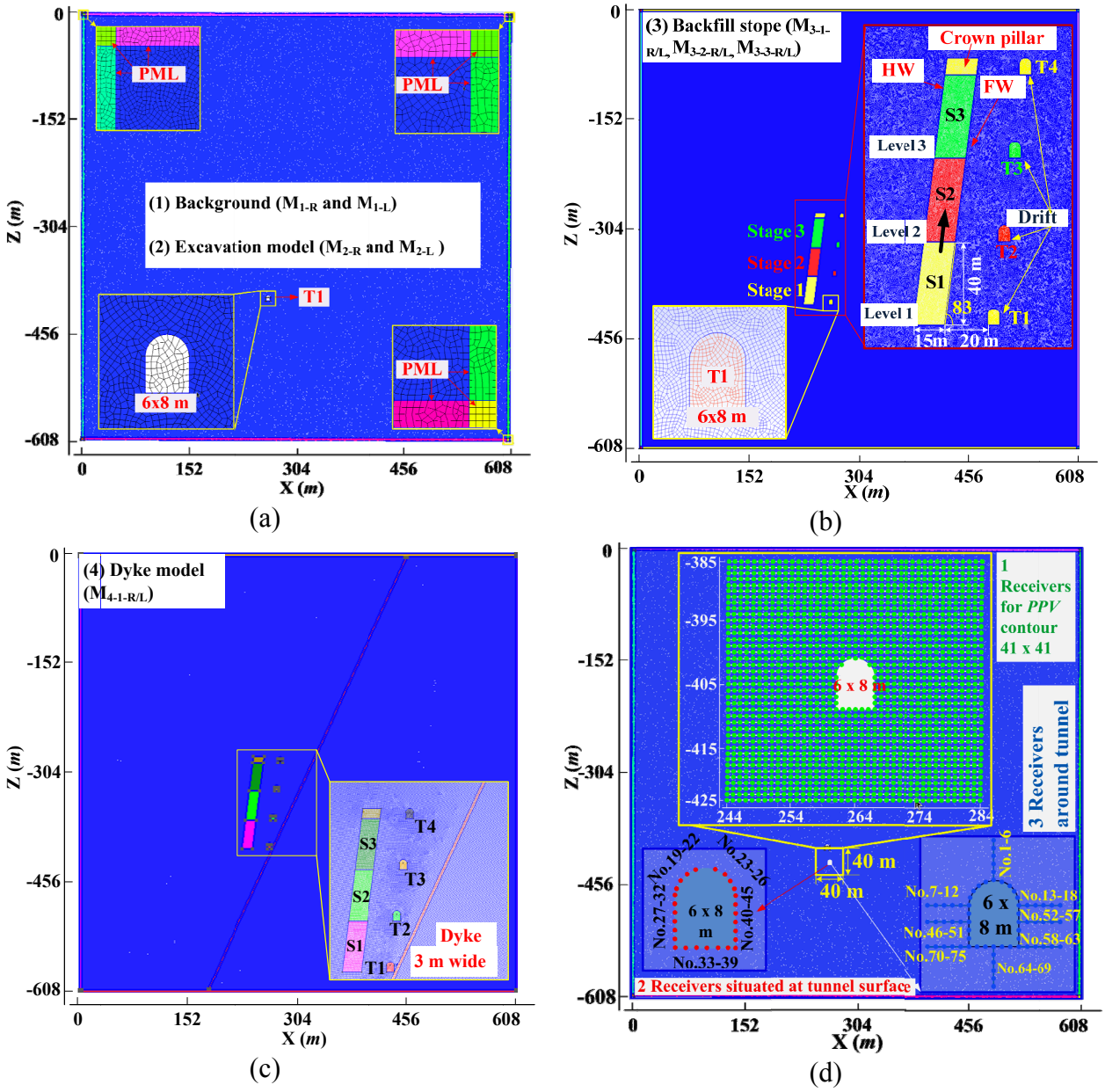

Figure 6-1: 2D models of typical heterogeneities in underground mines whose properties are tabulated in Table 6-2. (a), (b), and (c) show the background model, the stope model, and the dyke model, respectively. Layout of the receivers is shown in (d).

and $M_{2\text{-}L}$), where L and R in the model name denote that the seismic source is located at the upper-right and the upper-left corners of the model, respectively. The model responses with and without the tunnel can be compared with each other to examine the influence of the tunnel on wave propagation pattern. Figure 6-1(b): Backfilled stope models ($M_{3\text{-}1\text{-}R/L}$, $M_{3\text{-}2\text{-}R/L}$ and $M_{3\text{-}3\text{-}R/L}$), which have multi-level stopes with backfill. The width and height of the stope are 15 m and 40 m, respectively, and the dip of the stope is 83°. The distance from the stope to tunnel T1 is 20 m. Bottom-up stoping method is used to model the influence of different mining stages on wave propagation pattern. Figure 6-1(c): Dyke model ($M_{4\text{-}1\text{-}R}$ and $M_{4\text{-}1\text{-}L}$), in which a 3.0 m wide dyke is added. The dyke is very close to the tunnel T1.

Three types of receivers are placed at various locations in the model to capture synthetic seismogram and PPV distribution. The layout of the receivers is presented in Figure 6-1(d). 41 by 41 receivers (the blue dots) are placed regularly in a square to generate PPV contours. A set of receivers are placed at the surface of the tunnel T1 for examining the seismic response at the tunnel free surface (the red dots). In addition, a series of receivers are placed in the vicinity of tunnel T1 in some lines to identify PPV distributions at different depths from the wall (the blue dots). The grid spacing is about 1.0 m and the total number of elements in each model depends on the model configuration.

6.2.2 Seismic source parameters and model material properties

The same source parameters as presented in Chapter 5 are used to facilitate the comparison of the modeling results with that from the attenuation models. As mentioned above, the moment tensor point source is used to represent a normal fault with a dip of 45° and the Ricker wavelet source time function is used with a dominant frequency of 100 Hz. The intensity of the seismic

source is assumed as M_w = 1.5. Two seismic source locations, the upper-left (x = 50 m, z = -58 m) and the upper-right (x = 550 m, z = -58 m), are considered.

Material properties of the orebody, backfill, and dyke are listed in Table 6-2. It should be noted that the shear quality factors for the orebody, backfill, and dyke are assumed based on the relative strength of the materials when compared with that of the background rock material (Q_s = 60). According to some previously research work (Essen et al., 2007; Gharti et al., 2012), the P- and S-waves velocities of excavations filled with air are chosen as 300 and 0 m/s, respectively.

6.3 Modeling results

6.3.1 Influence of a single tunnel on wave propagation

Figure 6-2 presents snapshots of the wavefields for the vertical velocity component produced by the seismic event located on the upper-right or the upper-left corners. For comparison, results from the case without the tunnel are also presented.

As can be seen from Figure 6-2, the tunnel can alter the velocity wavefields. The wavefields of the background models ($M_{1\text{-}R}$ (a) and $M_{1\text{-}L}$ (c)) show direct P- and S-waves. With the introduction of tunnel T1, strong scattering of the S-waves around tunnel T1 can be observed clearly (at t = 0.13 s and t = 0.15 s). The slip direction of the seismic source is defined by a dip of 45°. When the source is located on the upper-right corner (x = 550 m, z = -58 m), it will have the

Table 6-2: Material properties of the heterogeneity models

Variable name	E (GPa)	ν	V_p (m/s)	V_s (m/s)	Q_s
Background	58	0.24	5874	3400	60
Orebody	100	0.15	6327	4100	120
Backfill	2.5	0.35	1830	878	35
Dyke	80	0.22	6726	4202	150
Tunnel	N/A	N/A	300	0	10

largest S-wave energy and the smallest P-wave energy along a propagation path connected from the source to the target tunnel. In this case, the influence of tunnel T1 on P-wave propagation is not significant (Figure 6-2(b), t = 0.08 s). Hence, there is relatively weak P-wave disturbance around tunnel T1. However, when the seismic source is on the upper-left corner, the minimum P-wave energy direction is not in the extension line from the seismic source to the tunnel. As a result, some P-wave disturbance can be seen (Figure 6-2(d), t = 0.08 s).

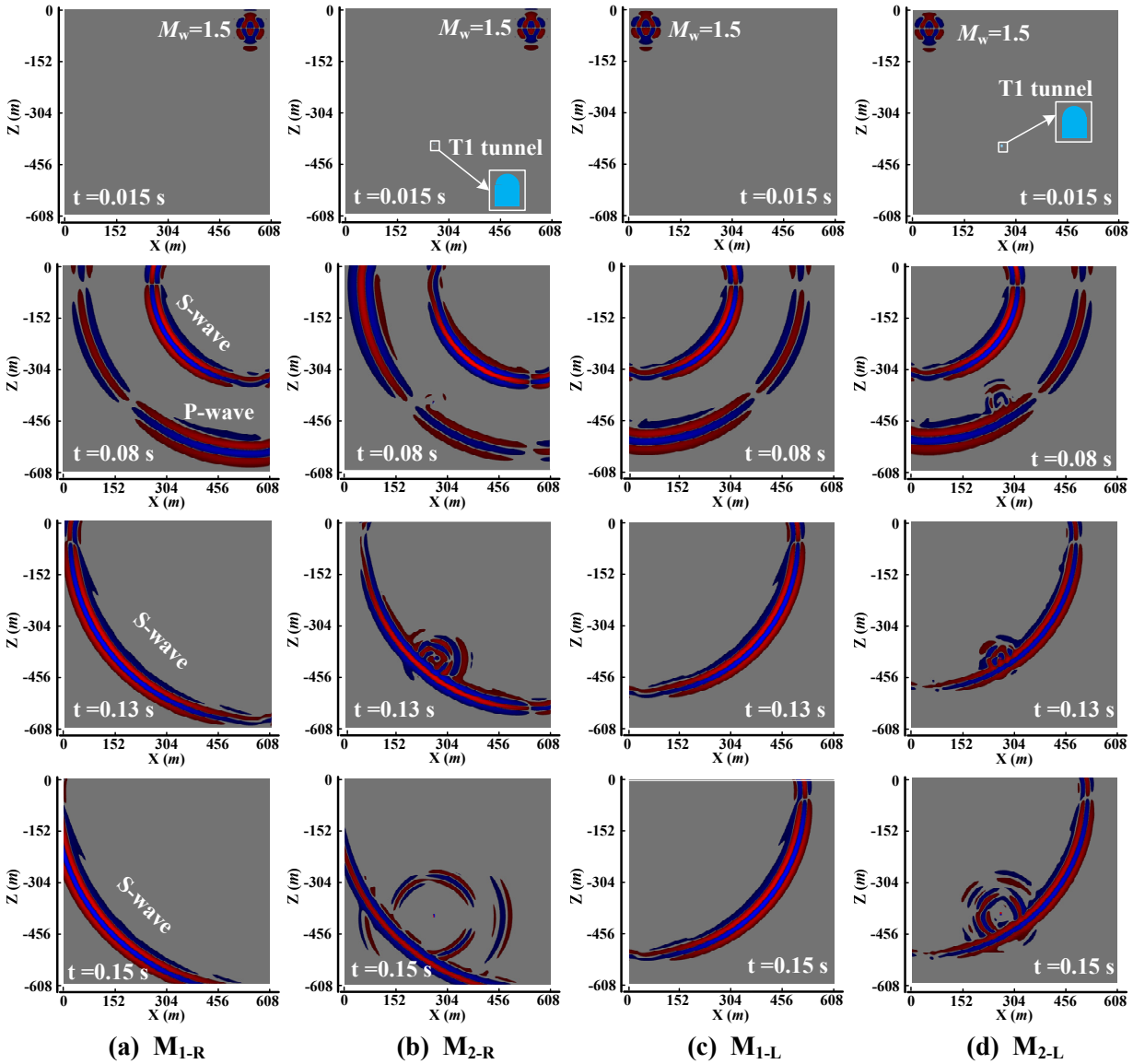

Figure 6-2: Snapshots of the vertical component of the velocity field at 0.015, 0.08, 0.13, and 0.15 s for four models. The 6 m × 8 m tunnel T1 is denoted by blue. The positive and negative values of the velocity components are denoted by red and blue (up and down toward are colored red and blue, respectively).

In the $M_{2\text{-}L}$ and $M_{2\text{-}R}$ models, although the energy reflected from the P-waves is less intense, strong energy redistribution of the S-waves is noticeable. This means that when the S-waves reach the tunnel, strong scattering waves are excited and they dominate the wave propagation after the S-waves pass the tunnel.

As stated in Chapter 5, PPV from a homogenous model without considering other influence factors (e.g., excavations, dykes, shear zones, etc.) is calibrated with the PPV from the scaling law with an average confidence level. Hence in this chapter, PPV_{SLB} is defined as the PPV from the background model in numerical modeling. The PPV_{SLB} is used to compare PPV among the different models (as shown in Table 6-1).

PPV contours, mapped from a 40 m × 40 m square area around tunnel T1 (see Figure 6-1(d)), are shown in Figure 6-3 and Figure 6-4 to show the influence of the tunnel on wave propagation. The distance between the seismic source and the center of tunnel T1 is about 450 m and 410 m for the upper-right and upper-left seismic sources, respectively. According to the PPV_{SLB}, the anticipated PPV values (at 50% confidence) at the tunnel center of the two cases are about 0.007 m/s and 0.0077 m/s, respectively. This is based on a point source and isotropic wave propagation assumption. It can be observed that seismic wave energy is redistributed around tunnel T1 due to the existence of the tunnel, showing a strong non-uniform PPV distribution around the tunnel with PPV amplified and shielded when compared with the PPV_{SLB} contours from the background model. Contrary to the result of the $M_{1\text{-}R}$ background model, in which PPV_{SLB} decreases gradually as a function of 1/r (where r is the source-target distance), PPV in the excavation model $M_{2\text{-}R}$ increases to various extents in areas near the T1 tunnel (see Figure 6-3(a) and (b)).

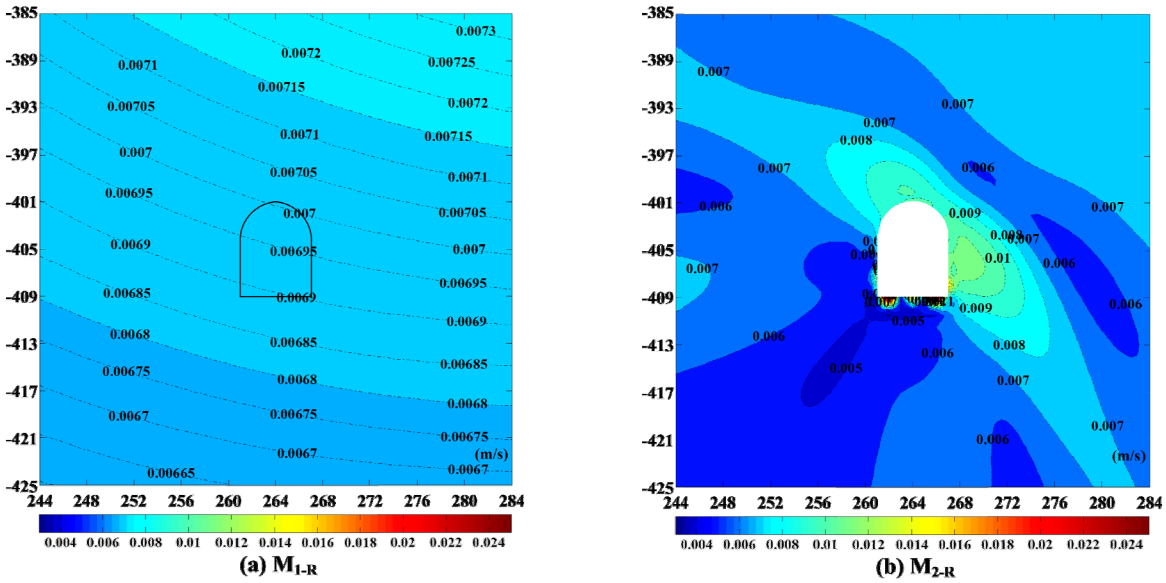

Figure 6-3: PPV contours in (a) the background model and (b) the model containing a tunnel (T1) when the seismic source is placed at the top right at (x = 550 m, z = -58 m). The scale of the color bar is from 0.003 to 0.025 m/s.

High PPV zones around tunnel T1 can be observed in the right wall areas and on the floor areas. The maximum PPV is roughly about 3.55 times higher than the maximum PPV_{SLB} in the background model at the floor (0.0245 m/s in $M_{2\text{-}R}$ and 0.0069 m/s in $M_{1\text{-}R}$). The right wall and the floor of the tunnel exhibit noticeable high ground motions. This may be attributed to the relative locations of the seismic source and tunnel T1. In the meantime, some shield PPV zones can also be identified because of the influence of tunnel T1. This example demonstrates that both the wave pattern and ground motions around a tunnel can be very complex. When conducting forensic analysis of rockburst damage, knowledge of the ground motion like this is important for correlating to correct PPV to tunnel damage.

Figure 6-4(a) and (b) show the PPV contours when the seismic source is located at the upper-left corner (x = 50 m, z = -58 m). Because the propagation path from the seismic source to tunnel T1 is not corresponding to the strongest ground motion in this case, the PPV value at the tunnel center (about 0.00735 m/s) is slightly smaller than that from the PPV_{SLB} (about 0.0076 m/s). This again shows the influence of source-tunnel path direction on wave pattern. When tunnel T1 is

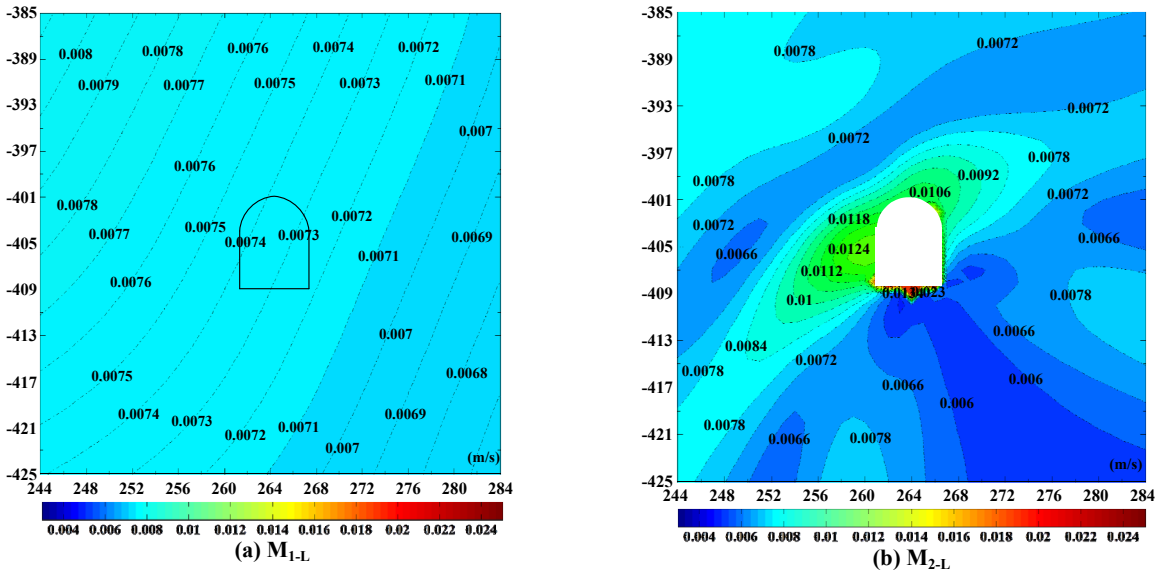

Figure 6-4: PPV contours in (a) the background model and (b) the model containing tunnel T1 when the seismic source is placed at upper-left corners (x = 50 m, z = -58 m). The scale of the color bar is from 0.003 to 0.025 m/s.

introduced (Figure 6-4(b)), the PPV distribution around the tunnel is altered and the PPV distribution approximately follows a mirrored pattern compared with that from the M_{1-L} model.

In Model M_{2-R} and M_{2-L}, the modeled PPV near the tunnel boundary can be several times higher than the PPV_{SLB} from the background model when tunnel T1 is present (Figure 6-3(b) and Figure 6-4(b)). As mentioned in Chapter 5, the PPV_{SLB} contour shows a similar PPV contour from the scaling law (with a 50% confidence level). One possible reason to explain the difference is that the data used for deriving the scaling law were not measured directly from the tunnel surface. Field monitoring sensors are often located in boreholes sufficiently away from the tunnel surface to avoid the influence of excavation. In this manner, localized amplification effect at tunnel surfaces is often not seen in the databases. If sensors are placed near or at the tunnel surfaces, large ground motions due to surface amplification should be captured. It is seen from Figure 6-3 and Figure 6-4 that PPV amplification and shielding zones exist around the tunnel and the wave patterns can be altered depending on the location of the seismic source, the source parameters, and the relative tunnel position.

Figure 6-5 presents the synthetic seismograms of four receivers placed on the tunnel surface. The seismograms at these locations for the $M_{1\text{-}R}$ model are also shown. The seismograms for each velocity component show variations due to existence of tunnel T1. Velocity increase for each component at all the receivers can be observed in the $M_{2\text{-}R}$ model. It is found that amplification is closely related to the spatial position of the tunnel, which means that different areas of the tunnel will have a different velocity increase. For instance, receivers No.41 and No.28 are located symmetrically at the tunnel wall and the seismograms at both locations show similar waveforms but the velocity amplitudes differ. The maximum V_z are 0.028 m/s and 0.0044 m/s for receivers No.41 and No.28 respectively. The velocity is higher at receiver No.41 because its location is facing the wave propagation direction. In addition, a delay of arrive time can be found. These modeling results indicate that even a single tunnel can alter the wave patterns significantly.

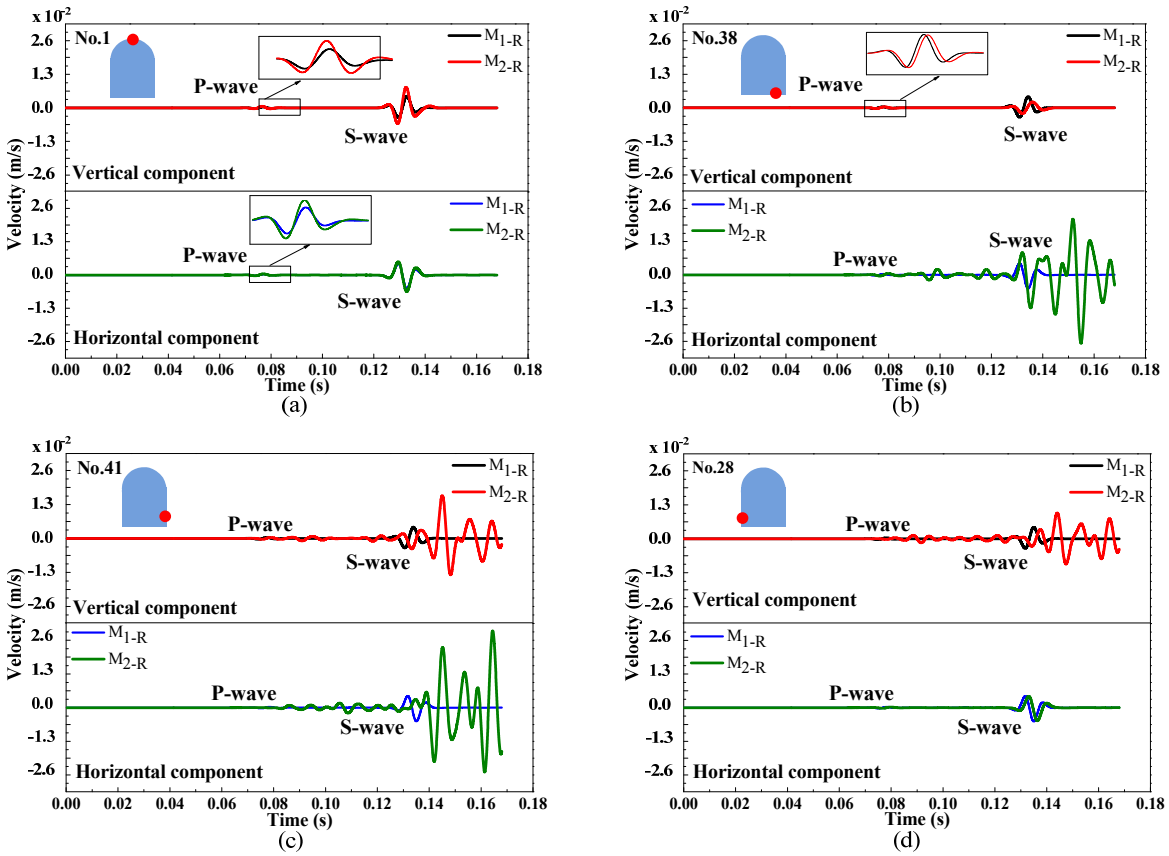

Figure 6-5: Synthetic seismograms at four receivers for the $M_{1\text{-}R}$ model and the $M_{2\text{-}R}$ model. The receiver locations are denoted by the red circle dots.

6.3.2 Influence of stope and backfill on wave propagation

In underground mines, mined-out and backfilled stopes can introduce high velocity contrasts and alter wave patterns. Models with three stope levels are considered to examine the influence of different mining stages on wave patterns around tunnel T1 in Figure 6-1(b). Bottom up mining method is used and backfill of the mined-out stopes is also considered. For example, model $M_{3\text{-}1\text{-}R}$ means that Stope 1 is excavated and remains open; model $M_{3\text{-}2\text{-}R}$ means Stope 1 is backfilled and Stope 2 is excavated and remains open; model $M_{3\text{-}3\text{-}R}$ means Stopes 1 and 2 are backfilled and Stope 3 is excavated and remains open. Snapshots of the vertical velocity components at three mining stages are shown in Figure 6-6, for the case when the seismic source is located at the upper-right (x = 550 m, z = -58 m).

Complex wavefields result from reflection and refraction due to the existence of the stopes. Strong scattering waves are observed when the P-waves reach the top of the stopes (t = 0.08 s). After the P-waves pass the stopes, S-waves arrive and interact with the orebody, the open stope, and the backfill materials (t = 0.13 s). Then, the wavefields become even more complex due to the co-existence of multiple reflection and refraction waves. The most notable feature is that complex scattering waves are generated and propagated due to multiple interactions among the host rock, the orebody, the open stopes, the backfill, and the tunnel (t = 0.18 s). The result can be used to explain the phenomenon of complex waveforms observed in actual underground mines, suggesting that extremely complex wave patterns are in part due to the complex environment in underground mines and in part due to fault slip that has a preferred slip direction.

PPV contours at different mining stages are presented in Figure 6-7. There are zones of PPV increase and decrease and in general high PPV values are on the right side of the tunnel, in areas

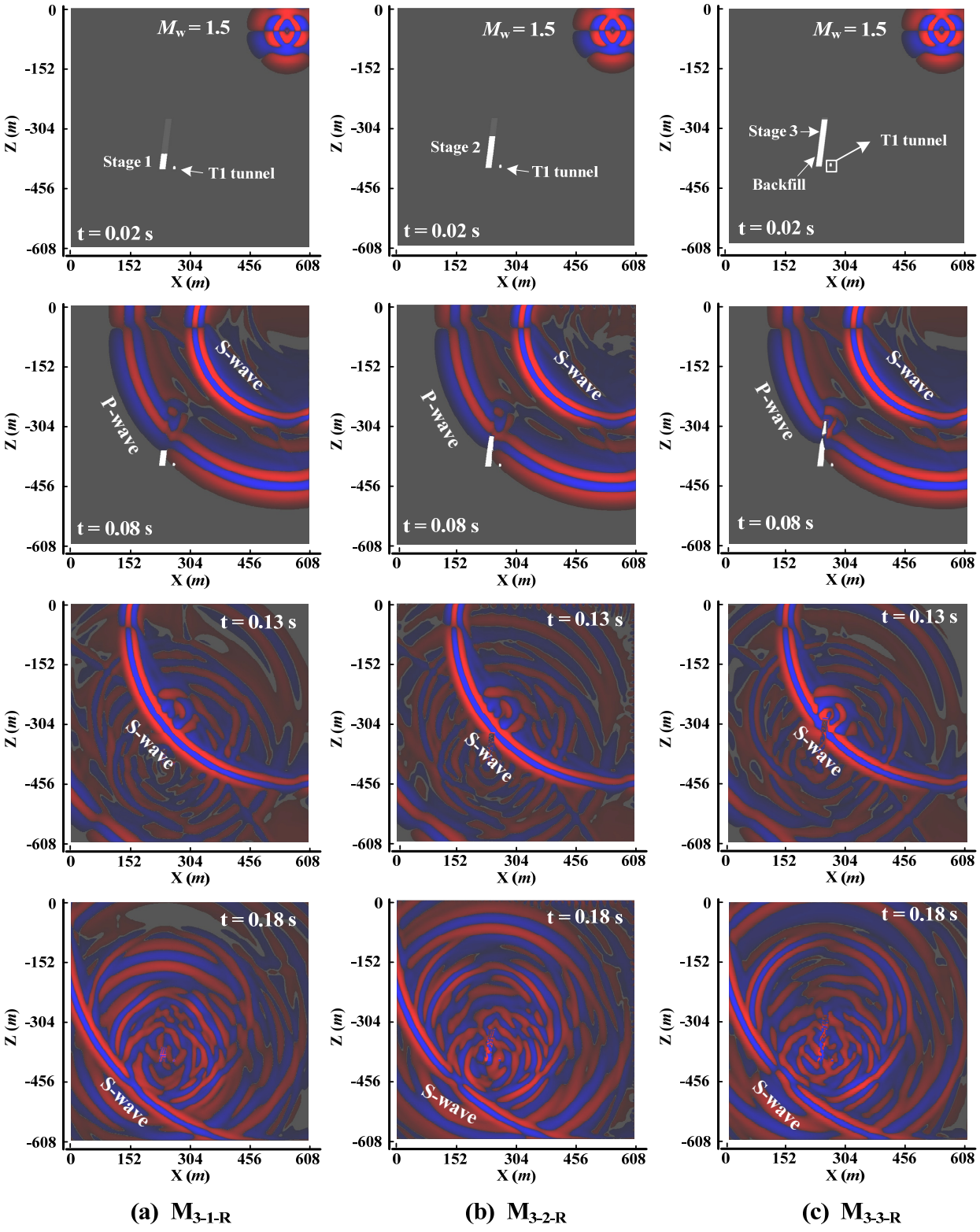

Figure 6-6: Snapshots of the vertical velocity components at 0.02, 0.08, 0.13, and 0.18 s at three mining stages. The positive and negative values (upward and downward movements) of the vertical velocity components are represented by red and blue, respectively.

10 to 20 m away from the tunnel. However, PPV variations around tunnel T1 (0 to 10 m) can be identified for all cases. In the $M_{3\text{-}1\text{-}R}$ model, PPV is enhanced on both sides of the walls of tunnel T1. The left tunnel wall suffers a slightly higher ground motion because the PPV ranges from 0.0082 to 0.021 m/s (Figure 6-7(b)). This is due to the interaction of multiple reflection waves between the mined-out stope and tunnel T1. As expected, higher PPV zones can be found around the mined-out area (see upper-left corner of Figure 6-7(b)). This result indicates that wave interaction between two openings can increase ground motion.

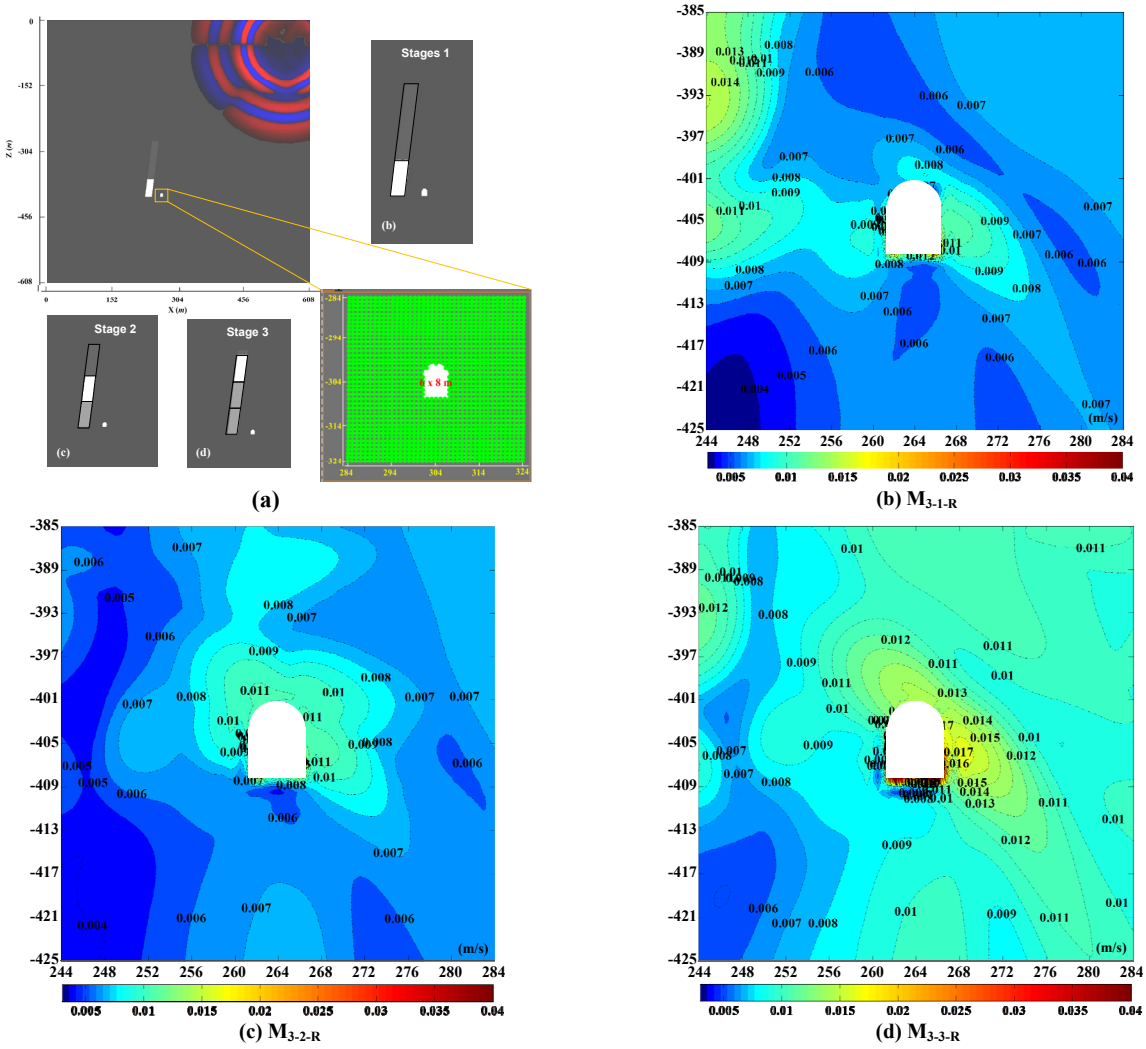

Figure 6-7: PPV contours around tunnel T1 at different mining stages. (a) Shows the mapping range of PPV and three mining stages; (b), (c), and (d) present PPV contours at the three mining stages. All contours have the same color scale: 0.003 – 0.04 m/s. The results for the seismic source located at the upper-left of the model (x = 50 m, z = -58 m) are presented in Figure A - 3.

In the $M_{3\text{-}2\text{-}R}$ model, Stope 1 is backfilled and Stope 2 is mined out. As the mining front progresses towards to Stage 2, the PPV contour (Figure 6-7(c)) changes when compared with the contour from that of $M_{3\text{-}1\text{-}R}$ model. The zone around the tunnel with high PPV values appears to migrate to the top (in a 6.0 m range) and to the right side (in a 10 m range). This indicates that areas of amplification can be expected when Stope 2 is mined. Relatively low PPV values appear in the result of the $M_{3\text{-}2\text{-}R}$ model. The range of PPV values is from 0.0078 to 0.014 m/s, compared with that up to 0.02 m/s in the $M_{3\text{-}1\text{-}R}$ model.

In the $M_{3\text{-}3\text{-}R}$ model, the first two stopes are backfilled and Stope 3 is mined out. The PPV contour changes again in this case (see Figure 6-7(d)). The enhanced/shield PPV zones, which are at the right parts and left parts of the mapping area, can be seen in the figure. High PPV zones in the vicinity of tunnel T1 appear on the right hand side of the floor and walls, with the maximum PPV (about 0.042 m/s) occurring on the floor. The results of the PPV distribution around the tunnel indicate that the wave patterns can be very different at different mining stages in a system that contains mined-out, backfilled, and un-mined stopes. Under ideal conditions, the seismic waves can be amplified due to complex wave interaction, leading to a very high PPV values which may cause potential unstable rock failure. High PPV is a major factor that may trigger violent rock failure and numerical tools such as SPECFEM2D provide a powerful approach to identify potential high risk areas.

6.3.3 Influence of dyke on wave propagation

Dykes are common geological structures in underground mines. Problems such as rockburst could occur when mining or tunneling near and in a dyke. The influence of dyke on seismic

wave patterns is investigated in this section. For easy comparison, the same model shown in Figure 6-1(b) is used by adding a 3.0 m wide dyke and the dyke model is shown in Figure 6-1(c).

Figure 6-8 presents some snapshots of the horizontal velocity component of the dyke model at four propagation times. In this model, only Stope 1 is mined. The most notable influence of the dyke is that strong reflection waves are generated and transmitted for both the P- and S-waves. At the same time, strong scattering waves are also observed when the P-waves reach the un-mined stopes (t = 0.08 s). After the P-waves pass the stopes, the S-waves arrive (t = 0.13 s) and they interact with the orebody, the open stope, and the tunnel. At a later stage of the simulation, the wavefields become more complex and it is hard to distinguish between the reflection and

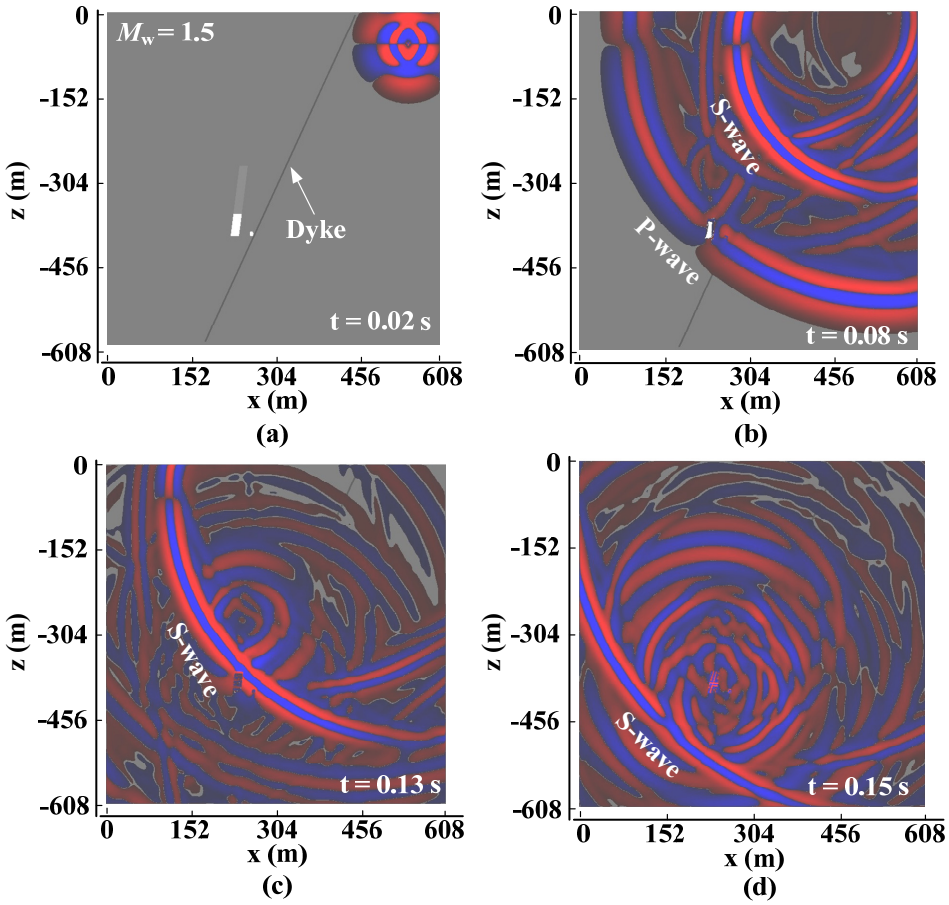

Figure 6-8: Snapshots of the horizontal velocity components at 0.02, 0.08, 0.13, and 0.15 s for the dyke model. The positive and negative values of the horizontal velocity (right and left movements) are represented by red and blue, respectively.

transition waves. The result further demonstrates that complex wave patterns can result when there are various geological and geometrical structures in a mine.

PPV contours of tunnel T1 for the dyke model are presented in Figure 6-9. It can be seen from the figure that there are zones of PPV increase and decrease. The PPV distribution is different from that shown in Figure 6-7(b), where there is no dyke. Three shielded and two enhanced zones can be observed in Figure 6-9(a). On the right side of the figure, there is a large shielded zone about 10 m away from tunnel T1. This may be due to the fact that the scattering waves, i.e., reflection waves, from the orebody and the stope are trapped and reflected back to the left side of the dyke. It would be difficult to understand this phenomenon by examining the wavefield snapshot alone, but it becomes obvious by viewing the PPV contours. A second shielded zone can be found at about 4.0 m above the tunnel roof. This may also be caused by the dyke, which can inhibit the waves and cause strong reflection waves for both the P- and S-waves (see wavefield in Figure 6-8 at t = 0.08, 0.13, 0.15 s). The third shield PPV zone is at the left bottom side, which may be attributed to the existence of tunnel T1, this shielded zone also exists in the models without the dyke. One PPV enhanced zone is around tunnel T1 and another is near the mined-out stope. The modeling results imply that dykes can influence the wave patterns in underground mines, although the maximum absolute value of ground motion is relatively low in this case (0.033 m/s). However, this is more than 5 times higher than the value predicted by the PPV_{SLB}, which gives a PPV of 0.0065 m/s at the tunnel location.

Comparing Figure 6-9(b) with (a), relatively lower PPV values are found and a relatively large shielded area is observed at the lower left part of the contour when the seismic source is located at x = 50 m, z = -58 m, which may be caused by the interaction between seismic wave propagation and open stopes. In addition, the influence of the dyke on ground motions is still

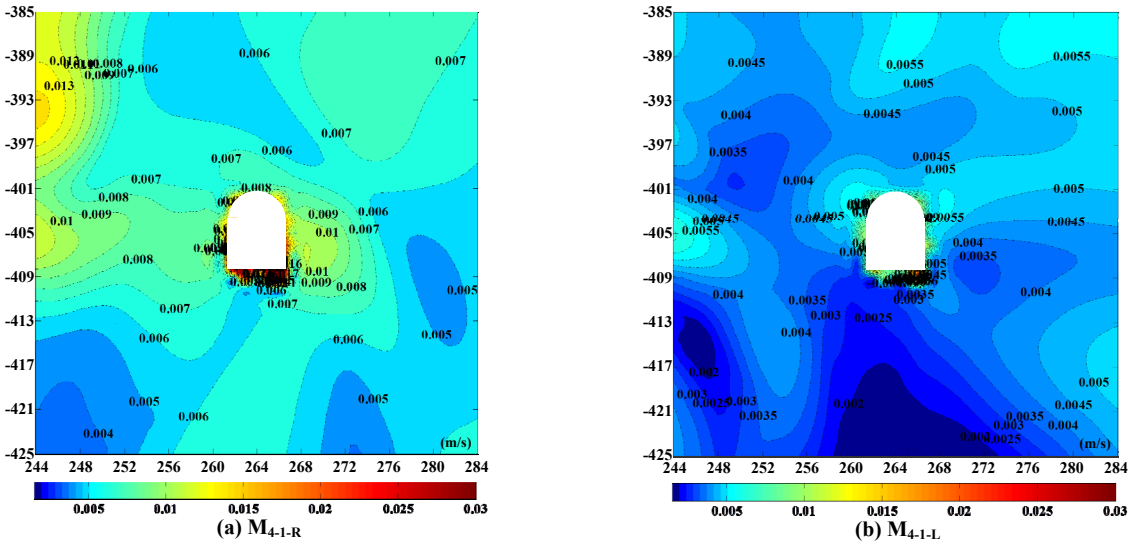

Figure 6-9: PPV contours around tunnel T1 for the dyke model. The seismic source is placed at (a) the upper-right at (x = 550 m, z = -58 m) and (b) the upper-left at (x = 50 m, z = -58 m) with a moment magnitude of 1.5 and a dip of 45°. The color scale is from 0.0015 to 0.03 m/s.

discernible. For instance, two high PPV zones are observed around the tunnel. The upper-left part of tunnel T1 is a high PPV zone due to the incoming seismic waves and the right side of tunnel T1 also shows a high PPV zone due to the multiple reflections between tunnel T1 and the dyke. Figure A - 4 shows PPV contours of the dyke model with multiple tunnels model when the seismic source is located at the upper-left corner (x = 50 m , z = -58 m).

Synthetic seismograms are plotted for two selected receivers and the results are shown in Figure 6-10. Receivers No.34 and No.38 are located on the floor. The synthetic seismograms from the dyke model ($M_{4\text{-}1\text{-}R}$) are compared with that from the background model ($M_{1\text{-}R}$) and the mining Stage 1 model ($M_{3\text{-}1\text{-}R}$). The influence of the dyke on the seismograms is apparent. The amplitudes of each velocity component are different in these models. The amplitudes of the seismograms at receiver No.38 on the right are higher than that at receiver No.34 on the left (Figure 6-10(a)). For receiver No.38 (Figure 6-10(b)), the amplitudes of the vertical velocity component are higher than that of the horizontal velocity component. This is because the location of the receiver is located on the surface of the tunnel floor. Furthermore, for receiver

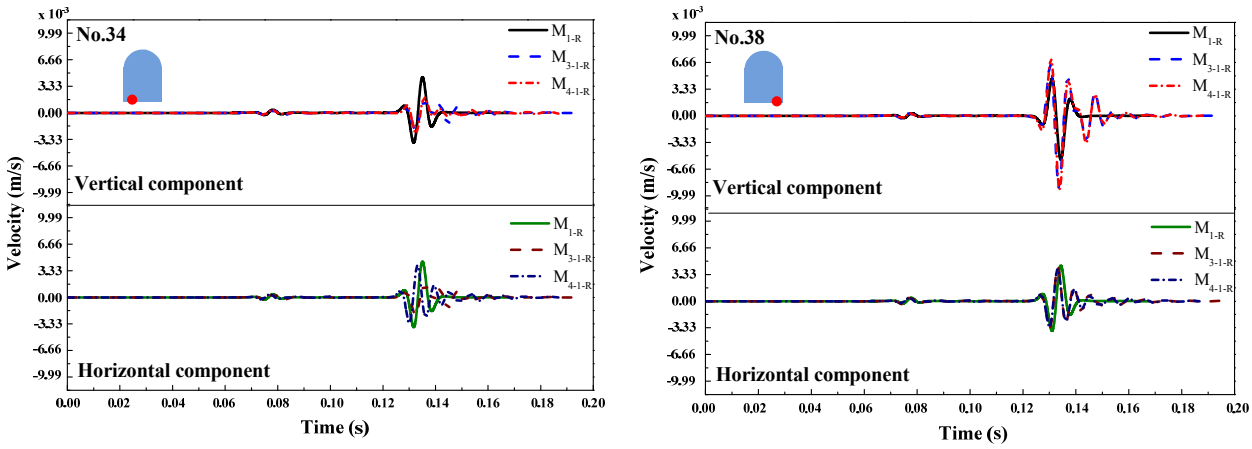

(a) (b)

Figure 6-10: Comparison of synthetic seismograms at receivers No.34 and No.38 from three different models. The receiver locations are denoted by the red dots in the figure.

No.34, the amplitudes of the two velocity components are comparable. At this location, the background model shows a large ground motion compared with models with the stope, the tunnel, and the dyke. This may be explained by the shielded effect due to the influence of the stope, the tunnel, and the dyke.

Another interesting point is the arrival time shift in the synthetic seismograms for different models. There is a small arrival time advancement in the dyke and stope models. Moreover, strong coda waves can be identified after the direct waves pass the receivers in the seismograms. When the stope and the dyke are introduced to the model, more multiple reflection waves can be generated and propagated. These coda waves may cause additional seismic loading to the tunnel and fall of ground may be expected if the rock mass around the tunnel has already been damaged by the main shock waves. These modeling results indicate that wave patterns around a tunnel can be very complex when there are more structures in the vicinity of the tunnel.

6.3.4 Influence of multiple openings on wave propagation

The multiple opening (drift) model aims at understanding the influence of multiple openings on the wave patterns. For easy comparison, two additional tunnels (tunnels T2 and T3) plus tunnel

T1 are modeled in two different cases – with and without the dyke. Snapshots of velocity component wavefields for the multiple opening model at four simulation times are presented in Figure 6-11.

The most notable influence of the multiple openings is the strong scattering waves generated in the backfilled stope and drift areas in both models, leading to extremely complex wave patterns (Figure 6-11). The wavefields from models $M_{5\text{-}1\text{-}R}$ and $M_{5\text{-}2\text{-}R}$ are similar to the wavefields from models $M_{3\text{-}3\text{-}R}$ and $M_{4\text{-}1\text{-}R}$, which means that the influence of the drifts on the wavefield is not significant. This may be due to the fact that the size of the drifts is small and the dominant frequency (100 Hz) of the seismic source is low (referring to the conclusion in Chapter 4). The P- and S-wave lengths are about 60 m and 34 m, respectively.

Figure 6-12 presents the PPV contours around tunnel T1 for the two cases with multiple tunnels. Again, the distribution of PPV is strongly non-uniform. For the $M_{5\text{-}1\text{-}R}$ model, the most

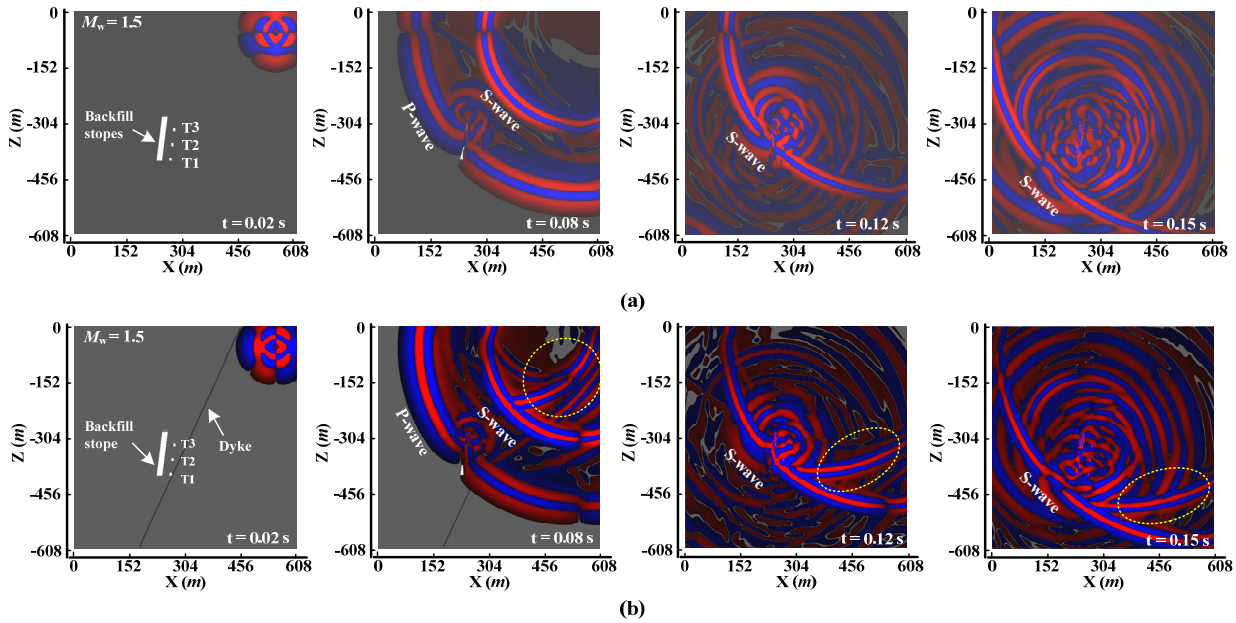

Figure 6-11: Snapshots of the vertical velocity for $M_{5\text{-}1\text{-}R}$ (a) and horizontal velocity component for $M_{5\text{-}2\text{-}R}$ (b) at 0.02, 0.08, 0.12, and 0.15 s. The positive and negative values of the vertical and horizontal components are represented by red and blue (red denotes the upward and right motions and blue stands for downward and left motion), respectively.

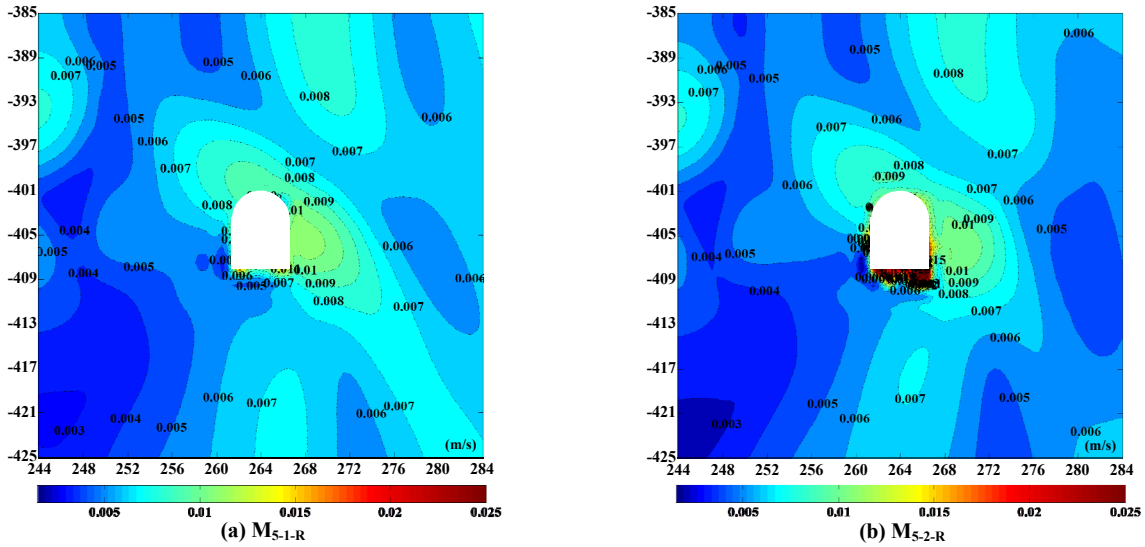

Figure 6-12: PPV contours around tunnel T1 for the multiple openings model. (a) PPV contour of multiple opening in stope at mining Stage 3 and (b) PPV contour of multiple openings in the dyke model. The color scale is from 0.002 to 0.025 m/s.

discernible change is in the right and top areas when compared with the result shown in Figure 6-7(d). The maximum PPV is lower than the PPV in the case with only one tunnel (a drop from 0.051 to 0.015 m/s). On the other hand, for the model $M_{5\text{-}2\text{-}R}$ (with dyke), the right and top areas seem to have a similar distribution of PPV when the two contours are compared (Figure 6-12 and Figure 6-9). The maximum PPV in the model with multiple tunnels is slightly lower than the PPV in the model with one tunnel (a drop from 0.043 to 0.028 m/s). In addition, PPV enhanced zones can be seen along the dyke, showing a local amplification effect. The results indicate that multiple tunnels can alter the wave patterns and reduce the ground motions around tunnel T1.

6.4 Discussion on the influence of tunnel, stope, and dyke on ground motion

The aim of this chapter is to study the influence of heterogeneity on wave patterns and ground motions. Typical heterogeneities in underground mines such as mine openings and geological structures are considered and modeled. The results show a significant influence of heterogeneity on the wave patterns. In this section, a further analysis and comparison of the results from

different models are conducted to deepen our understanding of complex wave propagation in underground mines.

Figure 6-13 presents some snapshots of the vertical velocity components of wavefields for the background ($M_{1\text{-}R}$), the single tunnel model ($M_{2\text{-}R}$), the Stope 1 excavation model ($M_{3\text{-}1\text{-}R}$), and the dyke models ($M_{4\text{-}1\text{-}R}$), at t = 0.02, 0.09, 0.14, and 0.18 s. The brightness and the contrast of the snapshots have been adjusted for each column to have a clear comparison. There are some waves that appear behind the direct P- and S- waves. It should be noted that these waves are not boundary reflection waves. It is seen from the figure that the complexity of the wavefields increase as more structures and excavations are added. Very simple wavefield of direct P- and S-waves are generated and emitted in the background model where the medium is homogeneous (Figure 6-13(a)). When one excavation is included in the model, strong scattering waves are generated and propagated around the tunnel (Figure 6-13(b)). When there is stope presence, multiple wave reflection and refraction among the openings can form very complex wavefield (Figure 6-13(c)). Strong and obvious refection waves can be identified with the presence of the dyke, and the wavefields are complex (Figure 6-13(d)). The results show that wave patterns can be changed by various structures in underground mines, and amplification or shielding of ground motions can be expected in such a case.

Figure 6-14 compares PPV contours around tunnel T1 in the four simulation cases. By comparing PPV distributions with the PPV_{SLB} distributions from the homogeneous background model (Figure 6-14(a)), the influence of mine excavations and geological structures on PPV distribution can be seen. It is seen that zones of PPV increase and decrease exist if the medium is not homogenous. The PPV_{SLB} distribution shows the wave patterns without disturbance, with PPV in the range of 0.0065 to 0.0073 m/s in the mapping area, which is in good agreement with

the PPV values estimated from the scaling law (with a 50% confidence level). Once a tunnel is considered in the model, the PPV distribution becomes strongly non-uniform (Figure 6-14(b)), with PPV values ranging from 0.006 to 0.03 m/s. In other words, PPV can be magnified more than four times due to the tunnel influence.

When there is stope presence (Figure 6-14(c)), the influence of the mined-out stope and the tunnel on PPV distribution is evident. The PPV around the tunnel reaches the order of 0.016 m/s

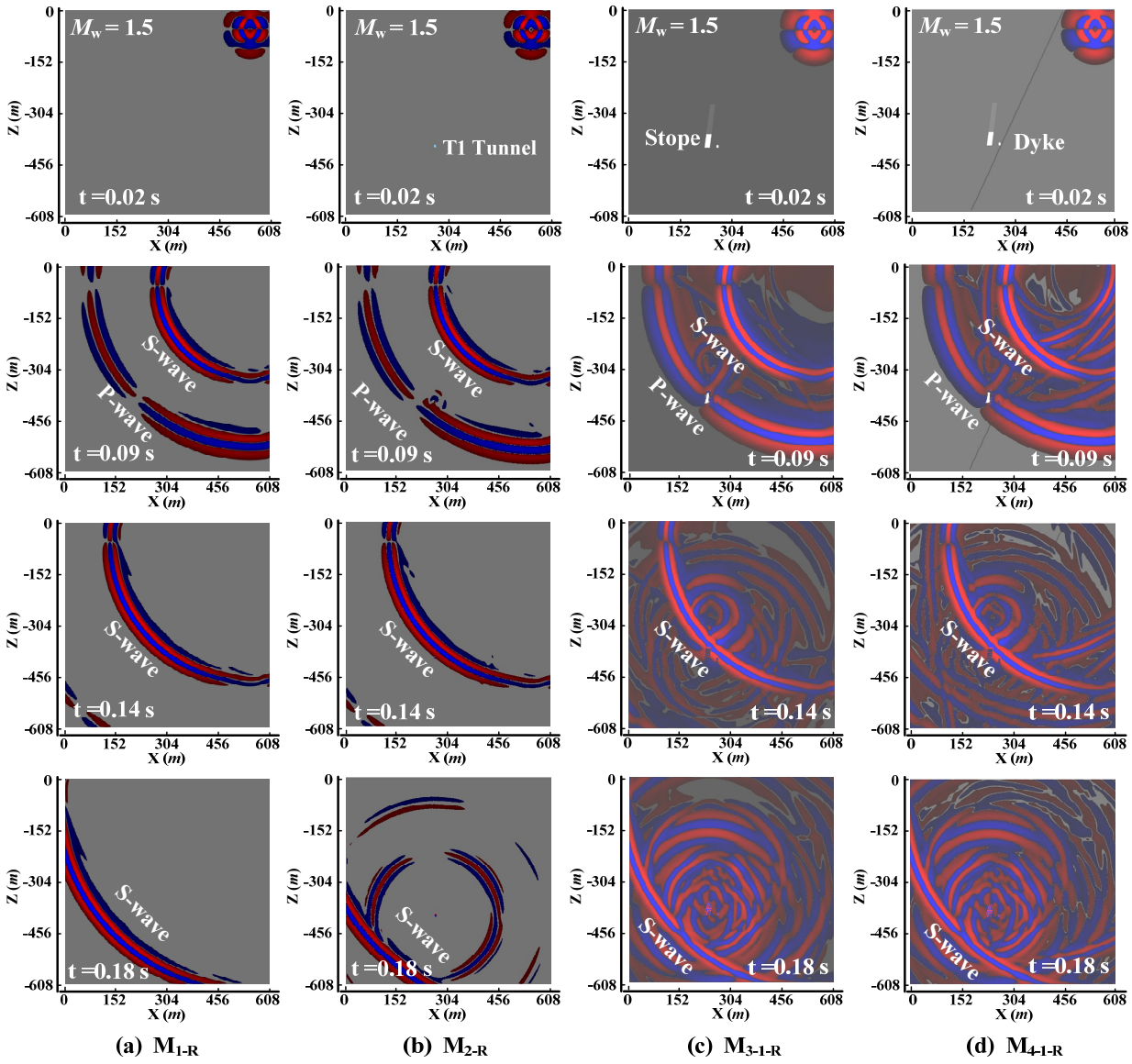

Figure 6-13: Snapshots of the vertical velocity components from four models at 0.02, 0.09, 0.14, and 0.18 s. The positive and negative values are represented by red and blue, respectively.

on both sides of the tunnel, and in a large area. The influence of the dyke on the wave patterns is interesting (Figure 6-14(d)). Although the maximum PPV is increased to 0.034 m/s on the floor, a large PPV increase on both sides of the tunnel walls, seen in the model without dyke (Figure 6-14(c)), is not seen in this case. Compared with PPV_{SLB}, the modeling results imply that heterogeneity in forms of excavation and geological structures can influence the intensity of seismic waves and distribution of ground motions. An increase or a decrease of ground motion at a particular location is possible, depending on the types and locations of heterogeneities involved.

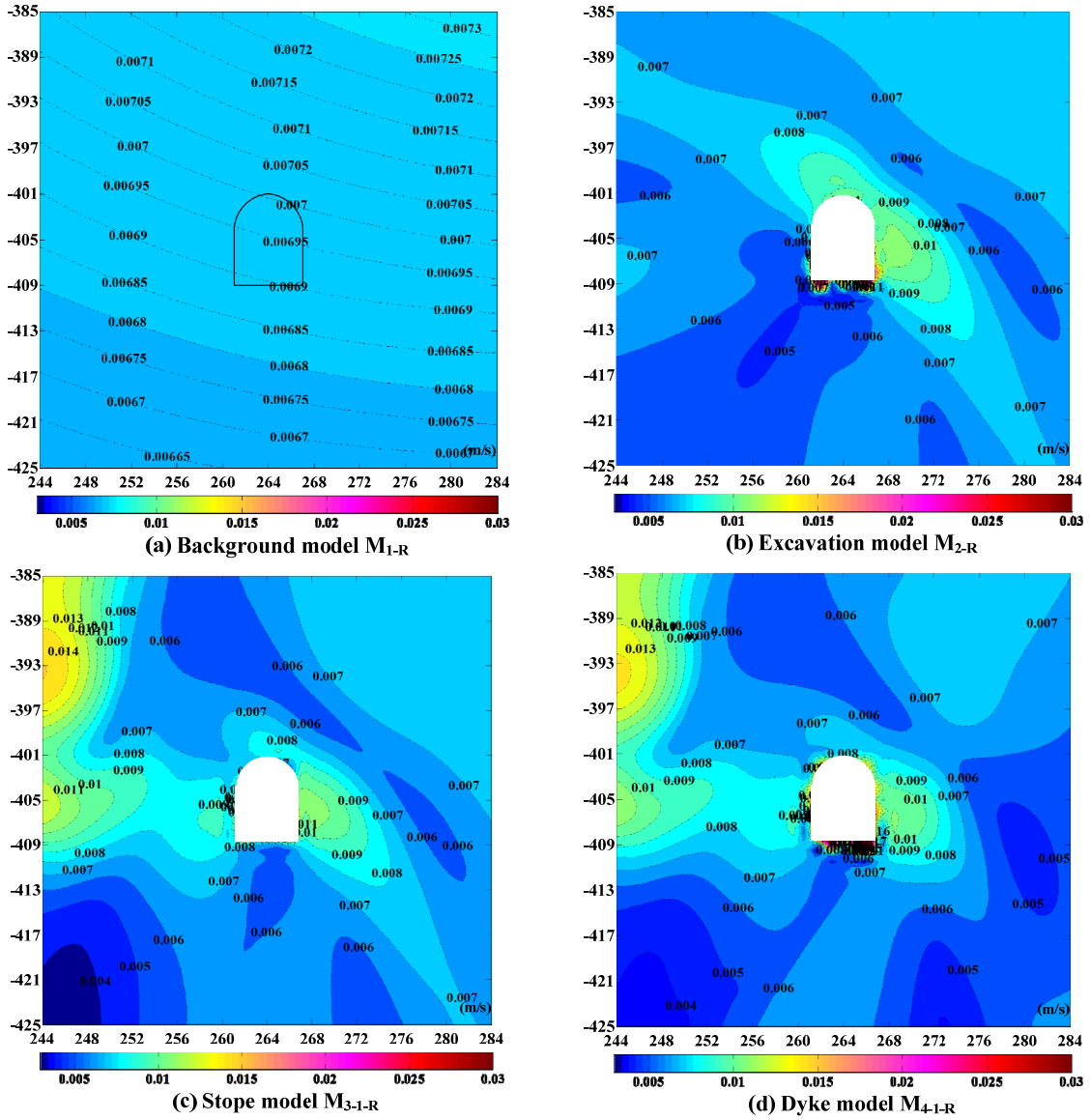

Figure 6-14: PPV contours around tunnel T1 for different models. The scales of the color bars are the same for all cases, from 0.003 to 0.03 m/s.

Figure 6-15 presents the synthetic velocity seismograms for four selected receivers of the four models. The seismograms from different models at the same receiver location are compared and several important observations can be made. For the homogeneous background model, the amplitudes for both the vertical (0.004 m/s) and the horizontal velocity components (0.0053 m/s) are similar at the four receiver locations (solid black lines). With the presence of the tunnel ($M_{2\text{-}R}$), the maximum amplitude of the vertical velocity can increase to 0.011 m/s and several peaks can be observed at receiver No.28; however, the maximum amplitude at receiver No.41 is only 0.004 m/s. This is interesting because receiver No.28 has a slightly large source-receiver distance than receiver No.41, but it has high amplitudes. A similar tendency can be observed for receivers No.38 and No.34 in model $M_{4\text{-}1\text{-}R}$ (the horizontal velocity components are denoted by red lines).

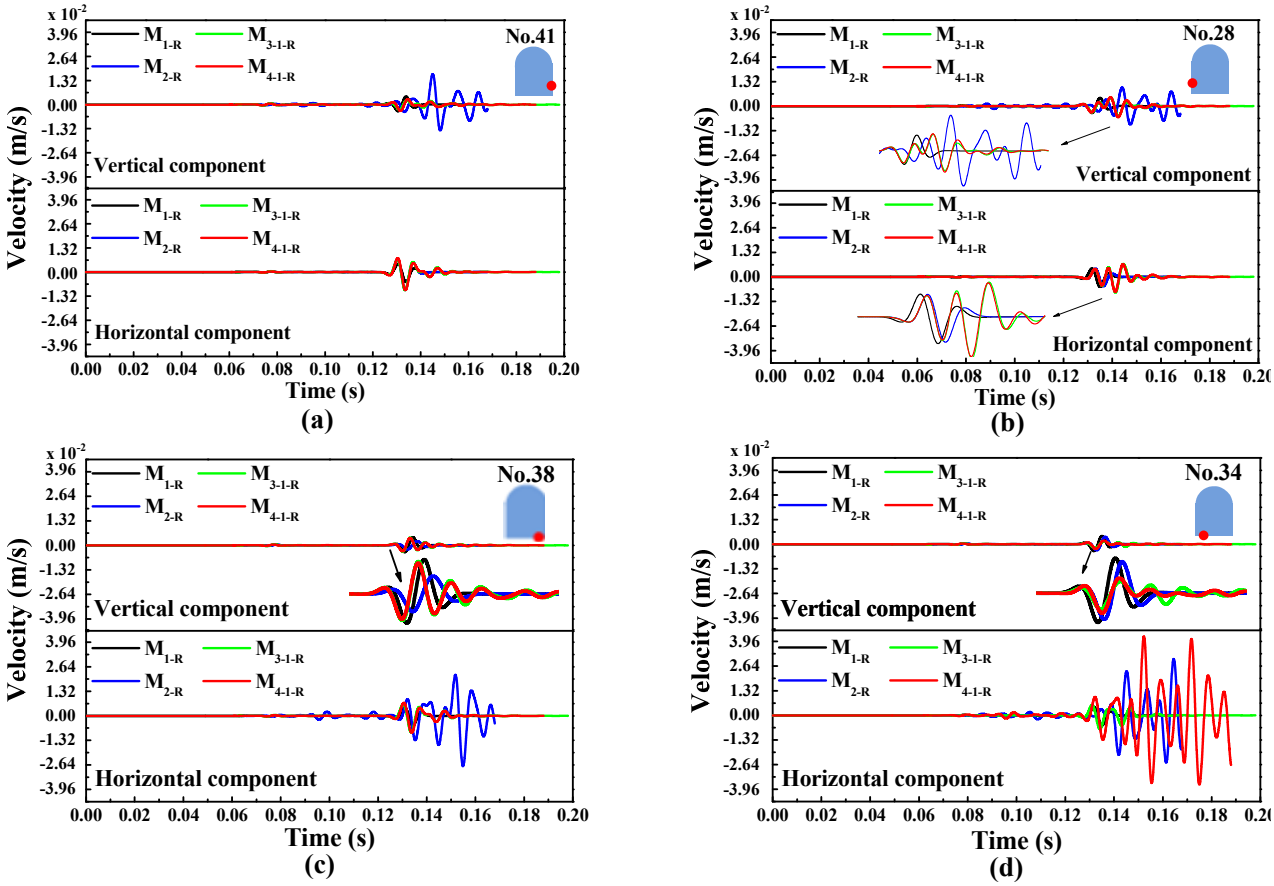

Figure 6-15: Comparison of synthetic seismograms at receivers No.41 (a), No.28 (b), No.38 (c), and No.34 (d) from different models. Amplitudes for the two velocity components of each receiver are the same for easy comparison. Receiver locations are denoted by the red dots.

Furthermore, the maximum amplitudes of the right wall receiver (No.41) in all models are larger than that of the left receiver (No.28) (roughly 1.6 times larger). For the floor receivers of No.38 and No.34, the receiver on the left (No.34) experiences higher ground motions than the receiver on the right (No.38) (about 1.8 times). Using the seismograms, it is easy to see the contributions of different velocity components to ground motion. For instance, for the receivers located on the tunnel floor, the horizontal component ground motion is stronger than that of the vertical component. Of course, the relative contribution is dictated by the influence of excavation and geology as well as seismic source characteristics.

Scattering waves can be generated due to the heterogeneity and propagated in the medium. Coda waves appear as the models become more complex. For instance, notable coda waves can be observed from the seismogram in the horizontal velocity component at receiver No.34.

Scattering waves are excited between the direct P- and S-waves, and after direct S-waves (see small oscillations between the P- and S-waves and large oscillations after the S-waves in the seismograms). In addition, several large repeated wave peaks after the direct S-waves can be found once the tunnel is added (see the blue lines for receiver No.34 for model $M_{2\text{-}R}$). Similarly, coda waves can be found in this receiver (red line) in the dyke model ($M_{4\text{-}1\text{-}R}$) and multiple wave peaks can be picked in the seismograms. This indicates that the maximum ground motion may not be directly caused by the direct S-waves; it can be caused by oscillation and shake due to the complex coda waves, which may cause repeated loading of the rock masses, potentially leading to elevated rock damage in underground mines.

P-waves seem to have little impact on seismic response in all cases due to the selected seismic source parameters in the simulations. Intensive seismic response, which results from the S-waves

can be observed at all the receivers in all models. This observation further indicates that tunnel damage can be caused by shear waves and coda waves generated from the shear waves. In addition, arrival time delay and advance due to the influence of different structures can be seen in the modeling results. A comparably large arrival time delay can be observed as more heterogeneity is included in the models.

6.5 Final remarks

In this chapter, the modeling results demonstrate the influence of geological and mine structures on seismic wave propagation. Wave propagation patterns around a tunnel can be altered due to various heterogeneities in underground mines. In particular, the following conclusions are obtained.

Scattering waves can be excited and they dominate the wavefields after the direct waves pass the tunnel. Because the existence of the tunnel, the seismic wave energy is redistributed around the tunnel, leading to a non-uniform distribution of PPV. In addition, amplification and shielding PPV zones can be found around the tunnel.

Because of the increase and decrease effect of ground motion caused by the mine-out area and backfilling, seismic response around the tunnel shows a large variation at different mining stages. When the incoming seismic waves reach the tunnel, higher PPV values can be caused by complex wave interaction. The most notable feature of the influence of dyke on seismic wave propagation is the generation of strong reflection waves for both P- and S-waves. The wavefield and wave patterns can become more complex when there are various structures. In addition, multiple openings, in combination with geological structures, may alter the wave patterns and

lead to wave shielding in some areas around the tunnel. In the meantime, scatter waves and strong coda waves are the results of the influence of heterogeneity on P- and S-wave propagation.

In summary, PPV amplification and shielding effects can occur in underground mines, particularly around excavation boundaries where mining-induced stresses are also high. As a result, rockburst caused by rock ejection due to seismic energy may occur in underground mines at certain locations. Numerical modeling of wave propagation is important for conducting forensic analysis of rockburst damage.

Chapter 7

7 FLAC/SPECFEM2D coupled numerical modeling of wavefields near excavation boundaries in underground mines

As noted in Chapter 1, the interaction between seismic wave propagation and underground excavations is important to understand strong ground motion around the excavation boundaries. In this chapter, the emphasis has been placed on studying the influence of excavation effect on ground motions in underground mines, for obtaining an improved understanding of ground motion surrounding excavations. A non-uniform velocity model is established considering the influence of confinement and rock mass failure on wave velocity. A coupled numerical method is proposed for seismic wave propagation modeling based on the non-uniform velocity model. Finally, the approach is applied to ground motion modeling around a stope due to a fault-slip seismic event. Part of this chapter was written as a paper and published in the proceedings of the ***13th International ISRM Congress 2015*** held in Montreal, Canada. Another paper has been submitted for journal publication.

7.1 Introduction

As mentioned in Chapter 1, both static and dynamic rock support designs play a critical role for safe and cost-effective mining in burst-prone mines. A comprehensive knowledge of ground motion around excavation boundaries due to seismic wave loading, normally in the form of PPV/PPA (Peak Particle Velocity/Acceleration), is important for improving dynamic rock support design and mine safety (Cai et al., 2012; Kaiser and Cai, 2013; Kaiser et al., 1996; Wang and Cai, 2014).

The determination of ground motion around excavations in deep mines is a difficult task, especially when the velocity model of the rock mass surrounding the excavations is considered (Hildyard and Young, 2002; Hildyard et al., 2005a; Sainoki and Mitri, 2014). Rock mass quality varies in different rock domains, but traditionally it is often assumed that the velocity in a rock domain is constant, forming a uniform velocity field in the same rock domain. This practice is widely used in many research fields such as geophysical surveys and earthquake engineering, which mainly focus on the seismic response on the ground surface. However, the uniform velocity assumption, even for the same rock domain, is unrealistic and inaccurate for rock masses surrounding an excavation in an underground mine. When a tunnel is excavated, stress redistribution can lead to a complex non-uniform stress field in the rock mass surrounding the excavation (Cai, 2008a). Because the wave velocity of a rock mass depends on confinement (Blake et al., 2013; Wang et al., 2005; Wepfer and Christensen, 1991) and rock mass quality (Barton, 2002; Cai and Kaiser, 2002), a non-uniform velocity field will result. It is therefore important to consider the stress field change to study ground motion near the excavation boundary in underground mines.

As shown in Figure 7-1, the confining stress (i.e., the minimum principal stress) around an excavation is zero at the boundary, and it increases gradually ($\leq R_c$ in Figure 7-1, where R_c is a critical distance that divides the velocity change profile) and reaches a constant value at locations far away from the excavation boundary ($\geq R_c$ in Figure 7-1). Hence, the distribution of confinement in the rock mass is nonlinear, which should be a function of the distance from the excavation wall to the point of interest.

Seismic wave velocity in a rock mass is confinement dependent (Asef and Najibi, 2013; Cai and Kaiser, 2002; Wepfer and Christensen, 1991). The stress distribution around an excavation is

altered due to excavation. Therefore, a key research focus is to develop a nonlinear relation between confining stress and wave velocity so as to construct a non-uniform velocity model.

Another research focus is that rock mass fracturing around excavations usually results in deterioration of rock mass quality (Hildyard and Young, 2002; Hildyard et al., 2005a), which can cause a decrease of wave velocity due to the presence of micro- and macro-fractures in the failure zones (Figure 7-1). Bohlen and Saenger (2006) stated that Excavation Damage Zones (EDZ) around openings can lead to a strong dispersion of seismic waves. Durrhem (2012) considered that fractured zones around excavations at depth can create a velocity contrast which in turn can trap the seismic wave energy, which can then enhance ground motions. Therefore, both the confinement and the failure zones around an excavation influence the ground motion pattern around the excavation. When a non-uniform velocity model is constructed, it can be used to simulate ground motion more accurately, which is important for underground engineering design.

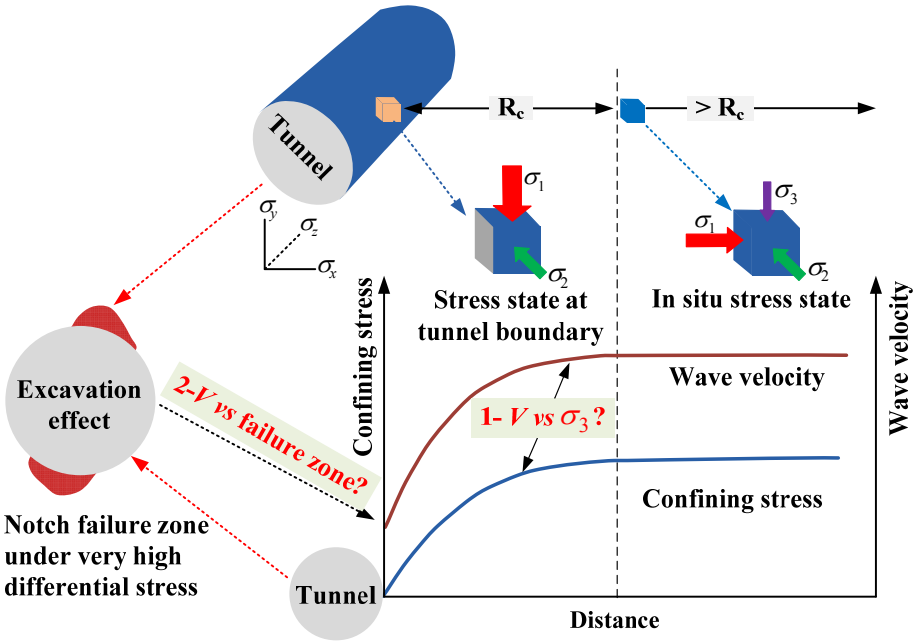

Figure 7-1: A sketch illustrating confining stress and wave velocity distribution near an excavation and key research problems in this study. R_c denotes the critical distance.

Nonlinear stress distribution usually results in a nonlinear wave velocity field around an underground excavation. It is better to use a nonlinear FEM method to solve inherently nonlinear problem and high-order elements are often required to model the wave propagation behavior efficiently (Gharti et al., 2012; Hughes, 2012). As noted in Chapter 2, SPECFEM2D and SPECFEM3D are important tools associated with the SEM method and can be used to capture the ground motion around the excavation boundaries efficiently.

7.2 A confinement-dependent nonlinear velocity model

7.2.1 Relation between wave velocity and confining pressure

The relation between confining pressure (P) and elastic wave velocity (V_p or V_s) has been investigated in laboratory for rocks (Asef and Najibi, 2013; Meglis et al., 1996; Wang et al., 2005; Wepfer and Christensen, 1991). According to the experimental data, the wave velocity of rocks is strongly dependent on confining pressure. Both P-wave velocity (V_p) and S-wave velocity (V_s) increase as the confining pressure increases. Based on laboratory test data, the wave velocity – confining pressure curve can, in general, be idealized into two parts (see Figure 7-2(a)): a nonlinear part for $P < P_c$ and a linear part for $P > P_c$, where P_c is a critical pressure. As shown in Figure 7-2(b), when the confining pressure is less than 15 MPa (i.e., P_c = 15 MPa), the wave velocity increases rapidly due to the rapid closure of microcracks and pores as the confining pressure increases. When the confining pressure is higher than 15 MPa, the variation of the wave velocity with the confining pressure is small because the rock specimens are in a highly confined state. A linear relation between wave velocity and confining pressure can be used to fit the test data in this part.

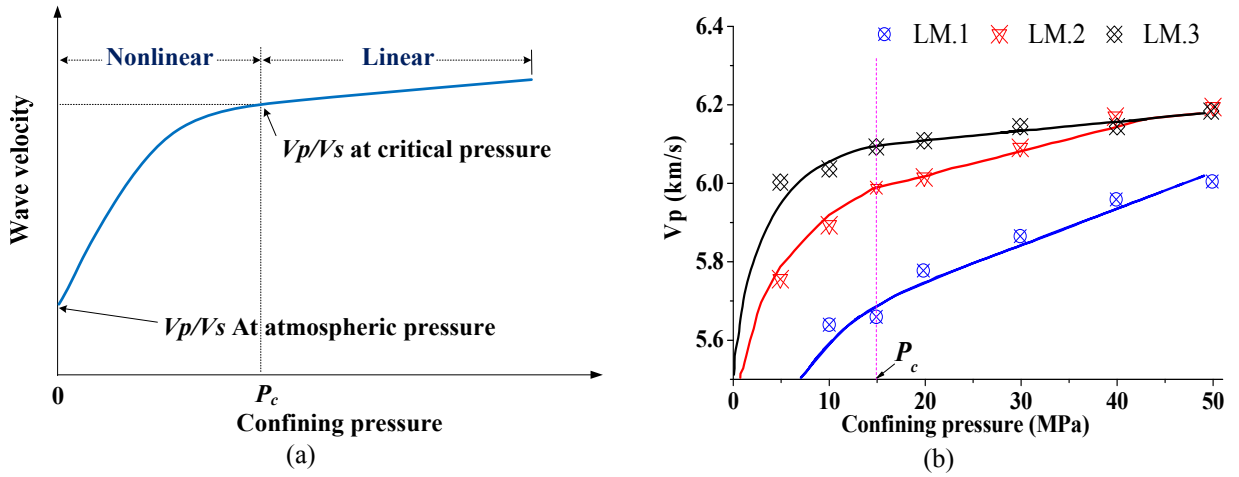

Figure 7-2: (a) Idealized wave velocity – confining pressure curve (Wang et al., 2005); (b) V_p – confining pressure curves for the Sarvak limestone (Asef and Najibi, 2013).

Elastic wave velocity of rocks is, in general, defined as a function of Young's modulus (E), Poisson's ratio (ν), and rock density (ρ). As stated above, the wave velocity of rocks is strongly confinement dependent. Hence, confining pressure should be considered when constructing a velocity model for rocks. Mathematically, a confinement-dependent velocity model can be expressed as

$$V_{p/s} = f(E, \rho, \nu, P) \tag{7.1}$$

where $V_{p/s}$ are the P- or S-wave velocities and P is the confining pressure.

7.2.2 Relation between wave velocity and confinement near an excavation boundary

In underground mines, many factors such as confining stress, rock mass quality, cavity, and water content influence the wave velocity of a rock mass. It is a challenging and difficult task to establish a relation between wave velocity and all the influencing factors. Cai and Kaiser (2002) related wave velocity to rock mass quality and depth or confinement. They concluded that at depth or under high confinement, the wave velocity is independent of rock mass quality because

joints are closed and their influence on wave velocity is small or negligible. At shallow depth or near an excavation boundary, wave velocity depends on both rock mass quality and confinement.

As stated in Section 7.1, excavation can alter the stress distribution around an opening (Figure 7-1). Furthermore, stress redistribution could potentially fracture the rock mass near the excavation boundaries and cause quality degradation of the rock mass. In other words, the excavation effect can cause a reduction of the rock mass quality, which means that the elastic modulus of the rock mass will be reduced, leading to a further change of the velocity field around the opening, in addition to the change caused by confining stress distribution alone. The elastic modulus can be used to link the wave velocity to both factors to consider the influence of rock mass quality and confinement on wave velocity.

In the following discussion, the elastic modulus is firstly established as a function of confining stress, and the relation between wave velocity and confinement is then constructed. As illustrated in Figure 7-1, the stress field in the vicinity of an excavation is non-uniform, and the corresponding wave velocity field is also non-uniform. By considering the relation between the confining pressure and the wave velocity of rocks in laboratory experiments, it is straightforward to extend this relation to rock masses near excavation boundaries. For simplicity, the confining pressure in the nonlinear velocity model shown in Eq. (7.1) can be replaced by the minimum principal stress (σ_3) around an excavation and then Eq. (7.1) becomes

$$V_{p/s} = f(E, \rho, \nu, \sigma_3) \tag{7.2}$$

Confinement can reach a very high level in some laboratory tests (e.g., up to 800 MPa (Wepfer and Christensen, 1991)) but confinement (σ_3) around an excavation cannot reach such a high level. In fact, σ_3 is zero at the excavation wall and it reaches the in situ stress level at locations

sufficiently far away from the excavation boundary. Hence, the confining stress state around an excavation is in a relatively "low confinement condition" with σ_3 varying from 0 to 27 MPa (e.g., at 1000 m depth).

As stated above, the elastic modulus is used to link confinement and wave velocity around openings in this thesis. Based on the idealized confinement–velocity curve (Figure 7-2(a)) and the "low confinement condition" near excavation boundaries, a relation between confinement and elastic modulus is proposed, which can be used to link elastic modulus to wave velocity, as shown in Figure 7-3. The elastic modulus depends on rock mass quality and confinement. According to the proposed relation, for rock masses with different qualities (e.g., red and blue solid lines in Figure 7-3 denote low and high rock mass qualities, respectively), the elastic modulus around an excavation is low at the wall boundary (E_0) and increases rapidly under low confinement, and reaches a constant value (E_{max}) far away from the wall boundary.

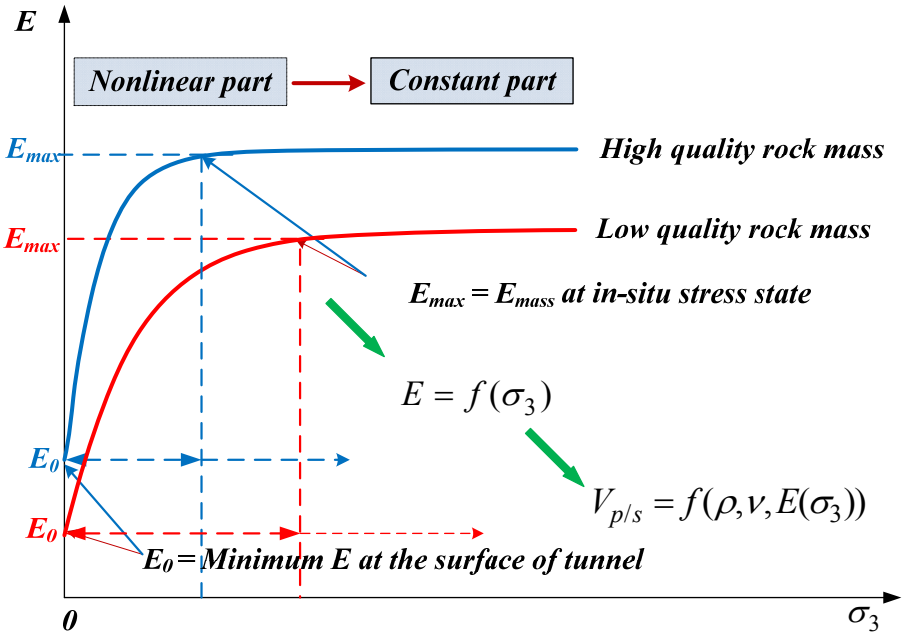

Figure 7-3: Proposed reasonable relation between confinement and elastic modulus, and wave velocity near excavation boundary.

As shown in Figure 7-3, E_0 denotes the minimum value of the Young's modulus at the excavation boundary, which cannot be negative. E_{max} is the Young's modulus of the rock mass in the in situ stress state. The maximum elastic modulus corresponds to a constant wave velocity field far away from the excavation boundary. Rock masses with different qualities will have different nonlinear behaviors when the confining stress changes from zero to the far-field stress. More details about the nonlinear behaviors of the model will be discussed in the next section.

7.2.3 A nonlinear velocity model around excavations under low confinement conditions

Three sets of experimental data of different rocks are fitted to obtain a general function to describe the proposed nonlinear velocity model (Asef and Najibi, 2013; He, 2006; Meglis et al., 1996), Figure 7-4 presents the relation between the confining pressure and the elastic modulus for the selected test data and the best-fit curves. The best fitting equations for the studied rocks are shown in Table 7-1.

Based on the fitting results (Figure 7-4 and Table 7-1), a nonlinear function is proposed to describe the relation between the elastic modulus E and confining pressure σ_3:

$$E = E_{\max} - (E_{\max} - E_0)\,\mathrm{e}^{(-\beta \times \sigma_3)} \tag{7.3}$$

where $E_{\max}$ is the maximum elastic modulus at the critical confining pressure, E_0 is the elastic modulus at the atmospheric pressure, and β is a model constant. This nonlinear function can describe the proposed curve well for rock masses at low confinement near the excavation boundary. The physical meaning of the parameters in Eq. (7.3) is clear. $E_{\max}$ can be considered as

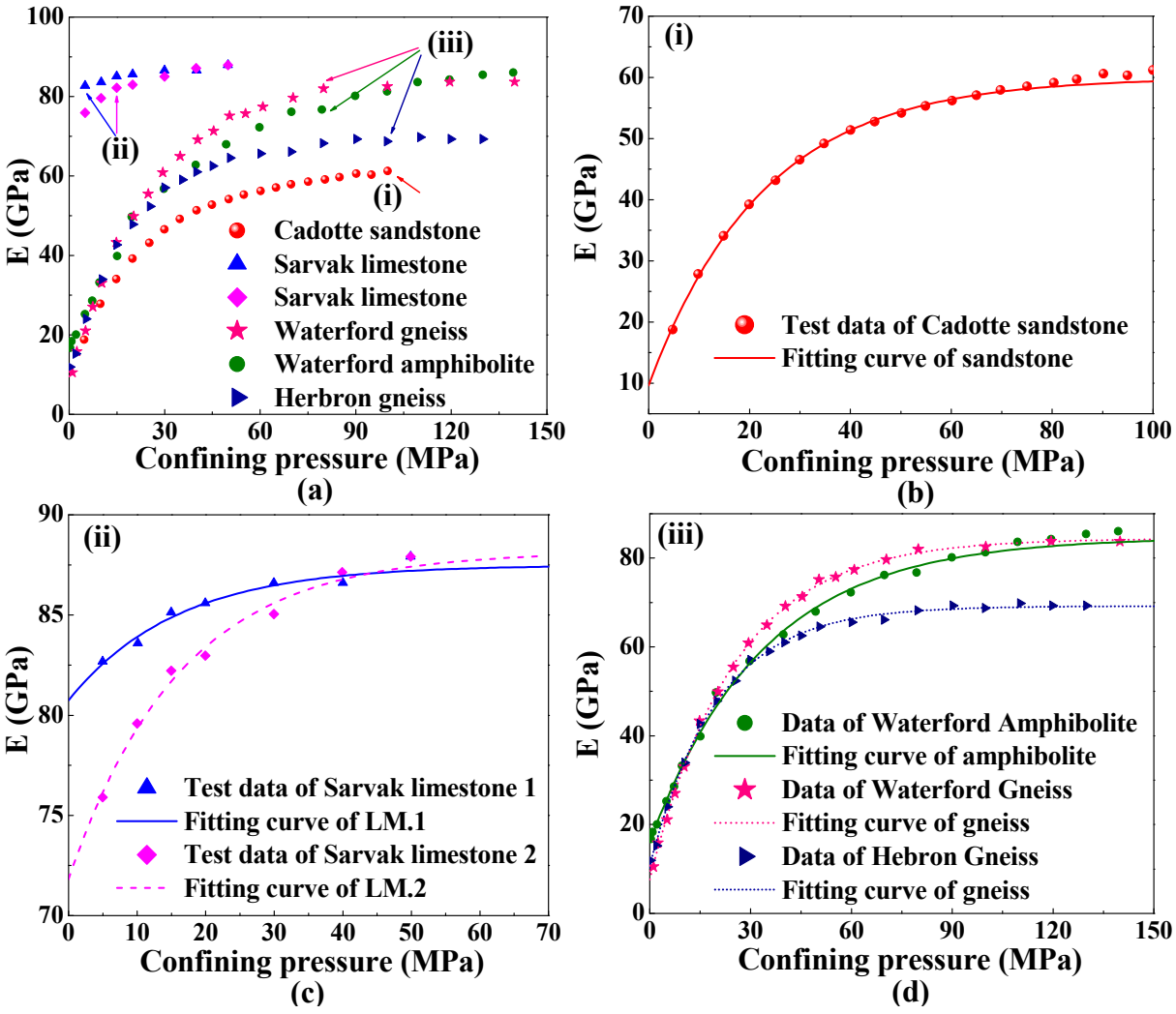

Figure 7-4: (a) Elastic modulus versus confining pressure of the experimental data; best-fit curves for (b) sandstone (He, 2006) (c) Sarvak limestone (Asef and Najibi, 2013), and (d) Waterford amphibolites and gneiss, and Hebron gneiss (Meglis et al., 1996).

Table 7-1: Best-fit equations of the experiment data

Lithology	Best-fit equation	R^2
Cadotte sandstone (Figure 7-4(b))	$E = 59.96 - 50.31e^{(-0.044\sigma_3)}$	0.999
Sarvak limestone 1 (Figure 7-4(c))	$E = 87.45 - 6.75e^{(-0.063\sigma_3)}$	0.968
Sarvak limestone 2 (Figure 7-4(c))	$E = 88.16 - 16.34e^{(-0.062\sigma_3)}$	0.981
Waterford amphibolites (Figure 7-4(d))	$E = 84.66 - 68.53e^{(-0.031\sigma_3)}$	0.997
Waterford gneiss (Figure 7-4(d))	$E = 84.38 - 76.75e^{(-0.041\sigma_3)}$	0.999
Hebron gneiss (Figure 7-4(d))	$E = 69.18 - 58.42e^{(-0.051\sigma_3)}$	0.998

the rock mass's elastic modulus in the in situ stress state, and E_0 can be viewed as the minimum elastic modulus at the excavation surface. Parameter β controls the nonlinearity of the curve and it varies for different rock masses.

The applicability of the proposed nonlinear model of Eq. (7.3) to rock masses near excavation boundaries needs to be verified using field test data. Unfortunately, because a lack of well controlled in situ experiment, field data are rarely available for the determination of the relation of elastic modulus and confining stress. Here, an alternative approach is taken to verify the proposed nonlinear model. Barton (2002) presented an empirical chart that relates seismic wave velocity, rock mass quality Q_c, depth, and porosity. Q_c is related to the rock quality index (Q_B) of the Q-system and the uniaxial compressive strength (σ_c) of intact rocks ($Q_c = Q_B \times \sigma_c/100$) (Barton, 2002). Based on the empirical chart, relations between stress level and wave velocity as well as rock mass quality can be derived. Confining stress can be converted from the buried depth in Barton's chart by incorporating the same approach of Cai and Kaiser (2002). For simplicity, it is assumed that in a case without excavation the confining stress is equal to the vertical in situ stress (assume that the in situ horizontal stress is higher than the vertical stress), which is induced by gravity with a rock density of 2700 kg/m^3. In this fashion, the proposed nonlinear model can be verified by the Barton's empirical $V_p - Q_c$ chart.

Figure 7-5 shows the elastic modulus versus confining stress from Barton's data and the fitting curves using the proposed nonlinear model (Eq. (7.3)). It is observed that the fitting curves by the proposed nonlinear model agree well with Barton's data. Again, it should be noted that the data from the Barton's empirical relation are in low confinement condition with confining pressure ranges from 0.675 to 27.0 MPa. Figure 7-4 and Figure 7-5 indicate that a large variation

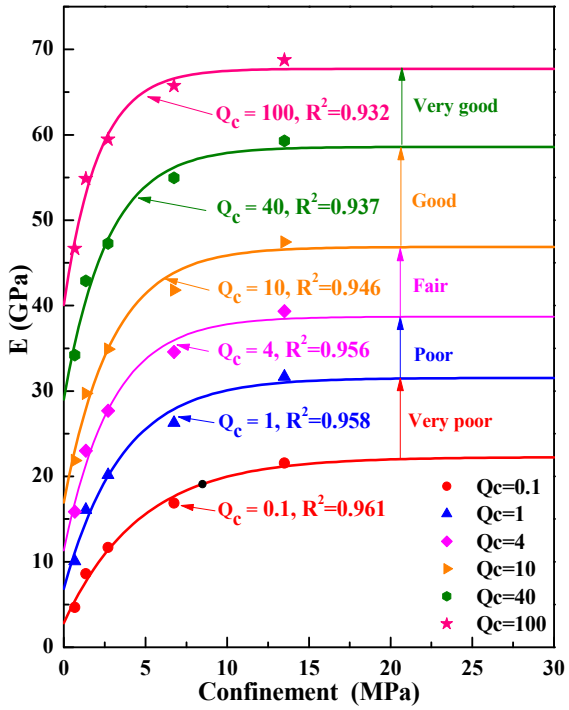

Figure 7-5: E versus confinement of Barton's data with various Q_c, and their best-fit curves.

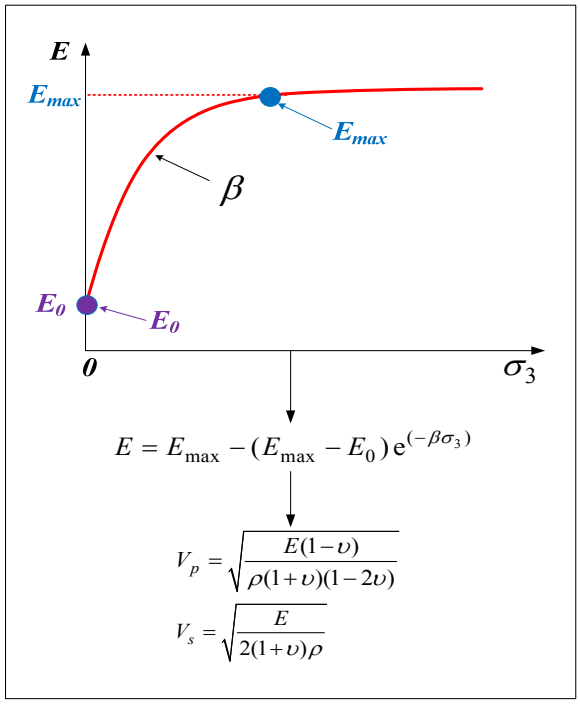

Figure 7-6: Proposed nonlinear velocity model and model parameters.

of elastic modulus exists in the low confinement zone. This also confirms that a large variation of wave velocity can be expected in the low confinement zones around excavation boundaries.

For a given rock mass, its nonlinear velocity model can be constructed using Eq. (7.3), which is further illustrated in Figure 7-6. It should be mentioned that stress distributions near the excavation boundaries are anisotropic and complex. Various representative stresses such as the σ_1, σ_3, σ_1-σ_3, and $(\sigma_1+\sigma_3)/2$ can be selected to consider the influence of stress on wave velocity field. Because the wave velocity is more sensitive to low confinement both in laboratory test results and in Barton's empirical data, for simplicity, only σ_3 is considered in the nonlinear velocity model (i.e., σ_3 is used in Figure 7-6).

7.2.4 Determination of model parameters

The variations of the confinement – elastic modulus curves with various model parameters (E_{max}, E_0, and β) are shown in Figure 7-7. Each model parameter controls the shape of the curve differently. E_{max} determines the maximum elastic modulus for rock masses at the in situ stress state. E_0 gives the minimum elastic modulus at zero confinement. As E_0 increases, the nonlinearity of the elastic modulus decreases (Figure 7-7(a)). Parameter β controls the rate of the change of the elastic modulus with confinement (Figure 7-7(b)). The elastic modulus shows a large sensitivity to confinement in the low confinement region as β decreases. It is evident that various relations between confinement and elastic modulus can be represented using different combinations of the model parameters in Eq. (7.3).

Figure 7-4, Figure 7-5, Figure 7-7, and Eq. (7.3) show that the three model parameters are closely related to rock mass quality in the low confinement region. Figure 7-8 presents the proposed model parameters as a function of Q_c based on the Barton's empirical data. Using the

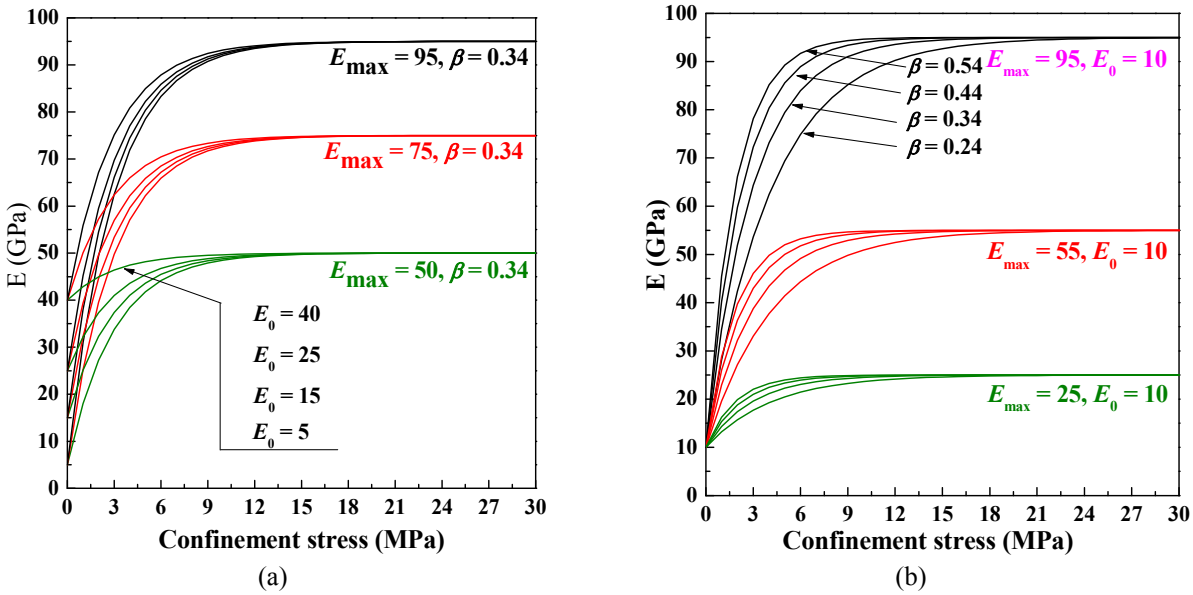

Figure 7-7: The variation of the nonlinear confinement-elastic modulus curves with model parameters: (a) E_{max}, E_0 as variables with β = 0.34; (b) E_{max}, a variables with E_0 = 10 GPa.

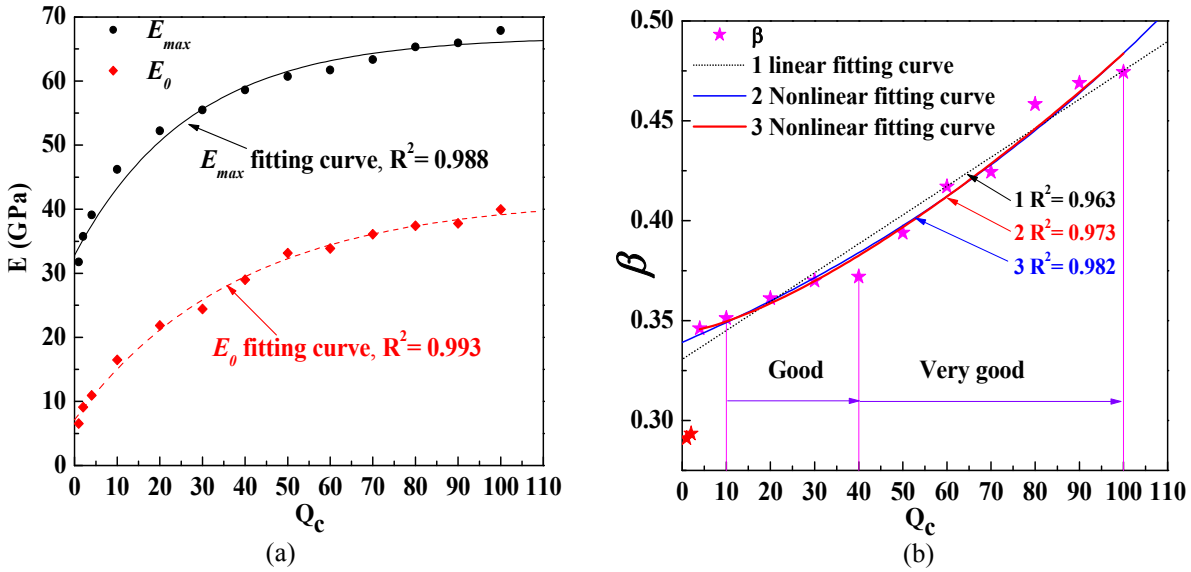

Figure 7-8: Variation of the proposed model parameters with Q_c and the corresponding best-fits.

nonlinear fitting technique, the three model parameters are estimated as a function of Q_c, as follows:

$$E_{\max} = 67.97 - 33.1 \times e^{(-0.037 Q_c)} \qquad \text{(GPa)} \tag{7.4}$$

$$E_0 = 41.73 - 34.6 \times e^{(-0.026 Q_c)} \qquad \text{(GPa)} \tag{7.5}$$

$$\beta = 0.344 + 0.00022 \times Q_c^{1.41} \tag{7.6}$$

Figure 7-8 and Eqs. (7.4) to (7.6) show that the three model parameters have a similar trend of gradual increase from their minimum values at low rock mass quality to their maximum values at high rock mass quality. As shown in Figure 7-8, all the model parameters are sensitive to rock mass quality. The Q_c values can be used to represent different rock mass states to reflect the degradation of rock mass quality due to stress-induced failure.

The model parameters E_{max} and E_0 have the dimension of GPa and β is a dimensionless model parameter. It should be mentioned that these relations (from Eqs. (7.4) to (7.6)) are fitting equations, which describe the relations of values empirically.

The proposed nonlinear model is developed by considering the influence of confining stress and rock mass quality simultaneously. For instance, according to Eqs. (7.4) to (7.6) the model parameters of E_{max}, E_0, and β are determined as 58.6 GPa, 29 GPa, and 0.384 for very good (Q_c = 40, σ_c = 240 MPa) rock masses. As shown in Figure 7-3, a nonlinear velocity model near the excavation boundaries can be established if the model parameters are known and the confining stress field is determined. In this way, a heterogeneous velocity model around an opening, which takes into account the influence of in situ stress, excavation effect, and rock mass quality, can be constructed.

7.2.5 Consideration of excavation effect in the proposed nonlinear velocity model

Underground excavation leads to in situ stress redistribution and induces rock mass degradation or damage around the excavation boundary, which can influence the wave velocity field around the opening. The influence of confinement on wave velocity is considered in the proposed nonlinear modulus model (Eq. (7.3)). The influence of failure zone on wave velocity can also be considered using the proposed model.

As noted above, different index values of rock mass quality can be used to represent different states of a rock mass, i.e., from peak to post-peak. It is observed that gradual deterioration of rock mass quality can be linked to the post-peak behavior of the rock mass. Similar to the approach of degrading GSI (Geological Strength Index) values from peak to residual (Cai et al. (2007a), Q_c can also be degraded from peak to residual. This means that the failure zone of a

rock mass can be considered by assigning a lower value of Q_c (Eqs. (7.4) to (7.6)) in the proposed modulus model.

Figure 7-9 illustrates how to consider the excavation effect in the proposed nonlinear velocity model. Both the influence of confinement (σ_3) change and degradation of rock mass quality (Q_c) around an excavation on the wave velocity field are considered. This model can be implemented in stress analysis software such as FLAC for investigating the excavation effect on velocity field, which is important for capturing ground motion around excavations. A relation between Q_c and the post-peak behavior of a rock mass is required to implement the model in FLAC. In general, a plastic parameter can be employed to describe the post-peak behavior of the rock mass, i.e., strength transition due to rock mass deterioration (Cai and Kaiser, 2014; Cai et al., 2007b; Zhao and Cai, 2010b). In the strain-softening model in FLAC, the plastic shear strain (ε_{ps}) is used to control the post-peak strength parameters.

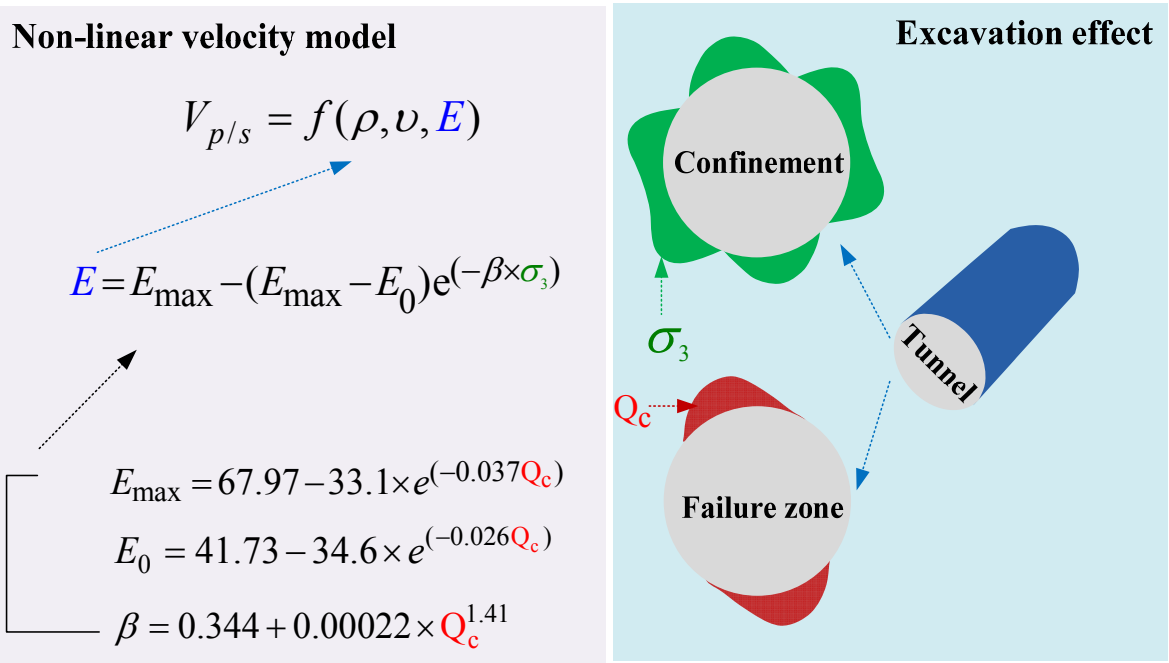

Figure 7-9: Modeling excavation effect around openings using the proposed nonlinear velocity model.

For simplicity, a bilinear decay function is used to describe the variation of Q_c with ε_{ps} in this study. A peak value of Q_c is assigned to the rock mass that behaves elastically and a residual value of Q_c is assigned to the rock mass when the residual state is reached. Linear interpolation is used for Q_c once the irreversible plastic strain occurs until the plastic strain reaches the characteristic plastic strain, and Q_c is kept at the residual value afterwards. Rock masses in the failure zone will have a lower Q_c value, which in turn leads to a lower E or wave velocity.

It is a difficult task to determine Q_c values of the peak and residual stages for a rock mass. A simple linear empirical relation between Q_c and σ_c of rock mass is derived and used based on the data of Barton (2002) in this thesis. This means that different rock mass quality values can be linked to different rock mass strengths. In this manner, a simple practical method can be employed to determine the peak and residual values of Q_c. For example, $Q_{c\text{-peak}} = 40$ and $Q_{c\text{-residual}} = 1$ can be assigned to rock masses if the peak/residual strengths of the rock mass is equal to 110 MPa and 5.5 MPa. In addition, different ε_{ps} values are used to represent different post-peak behaviors of rock mass. In general, relatively small (Figure 7-10(a), i.e., 0.001) and large (Figure

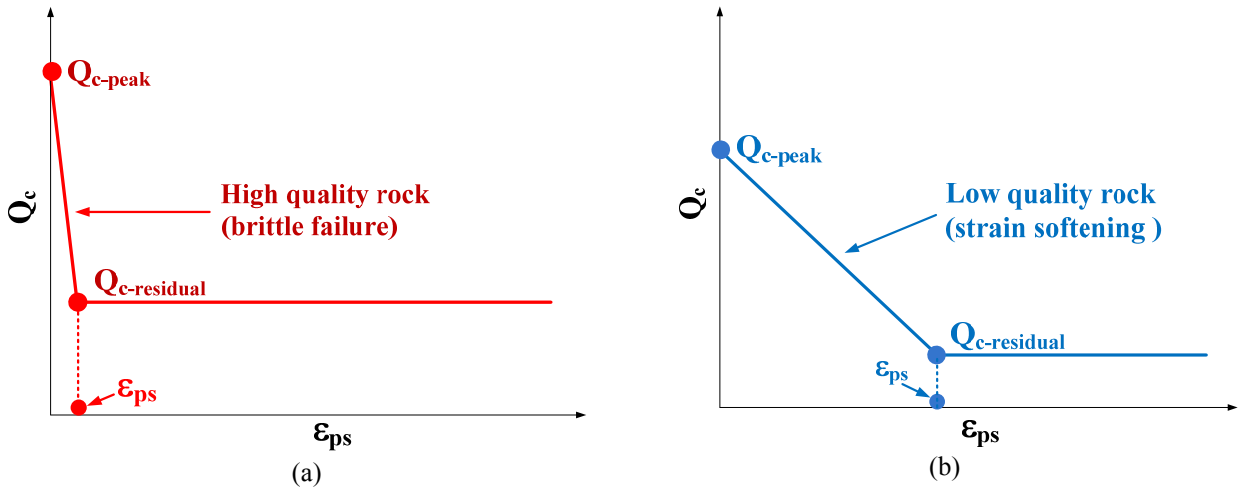

Figure 7-10: Simple relation between Q_c and ε_{ps} of the rock masses. Rock mass quality is expressed as a bilinear decay function of plastic strain. Different values of ε_{ps} are used to represent brittle (a) and strain – softening (b) behaviors of rock masses.

7-10(b), i.e., 0.006) value of ε_{ps} can be used to represent brittle and strain-softening behaviors of rock mass. In this fashion, the second excavation effect (rock mass failure) can be considered in the wave velocity model (the first excavation effect is the change of confinement). Both effects are important for determining the velocity field around underground excavations.

7.3 FLAC/SPECFEM2D coupled numerical method

7.3.1 Introduction of the coupled method

There are two tasks in investigating the excavation effect on ground motions around excavation boundaries. The first is to determine stress distribution around the excavation, followed by the determination of the velocity field. The second is to estimate ground motions around the excavation due to wave propagation. As far as the author knows, there is no numerical code that can properly handle the above two tasks simultaneously. Therefore, a coupled numerical approach is proposed in this thesis.

FLAC is a powerful numerical tool that can be used to analyze stress distribution due to excavation (Cai, 2008b; Cai et al., 2007a; Malan, 2002); it can also perform simple seismic wave propagation analysis but is not as efficient as other specialty tools (Geniş, 2010a; Xiao et al., 2005). As stated in Chapter 2, SPECFEM2D is a powerful tool to study wave propagation problems (Komatitsch and Tromp, 1999, 2002a, b), but it does not have the ability to conduct stress analysis. An explicit coupled approach is proposed in this study which considers the merits of each code to resolve this issue. In the proposed coupled method, static stress analysis is conducted firstly using FLAC to approximate stress field surrounding an excavation and seismic wave propagation is then simulated using SPECFEM2D to determine ground motions around the excavation boundaries.

7.3.2 Coupled modeling procedure

Figure 7-11 illustrates the proposed FLAC/SPECFEM2D coupled modeling procedure. Three stages are involved in the coupling process. In Stage 1, excavation modeling is conducted in FLAC. Subsequently, the nonlinear velocity model and necessary files for seismic wave modeling are constructed using FISH scripts in FLAC and transferred to SPECFEM2D in Stage 2. Finally, wave modeling is conducted using SPECFEM2D in Stage 3.

A straightforward "element-to-element" mapping method is used to prepare necessary files for SPECFEM2D in Stage 2. As shown in Figure 7-11, a mesh is generated firstly in FLAC and each element in the FLAC model is considered as an individual material in SPECFEM2D when data are transferred from FLAC to SPECFEM2D. Several special FISH scripts are written and used in Stage 2 to output data from FLAC to SPECFEM2D. All necessary files, which are required for wave modeling in SPECFEM2D, are generated by invoking the FISH scripts in FLAC. The

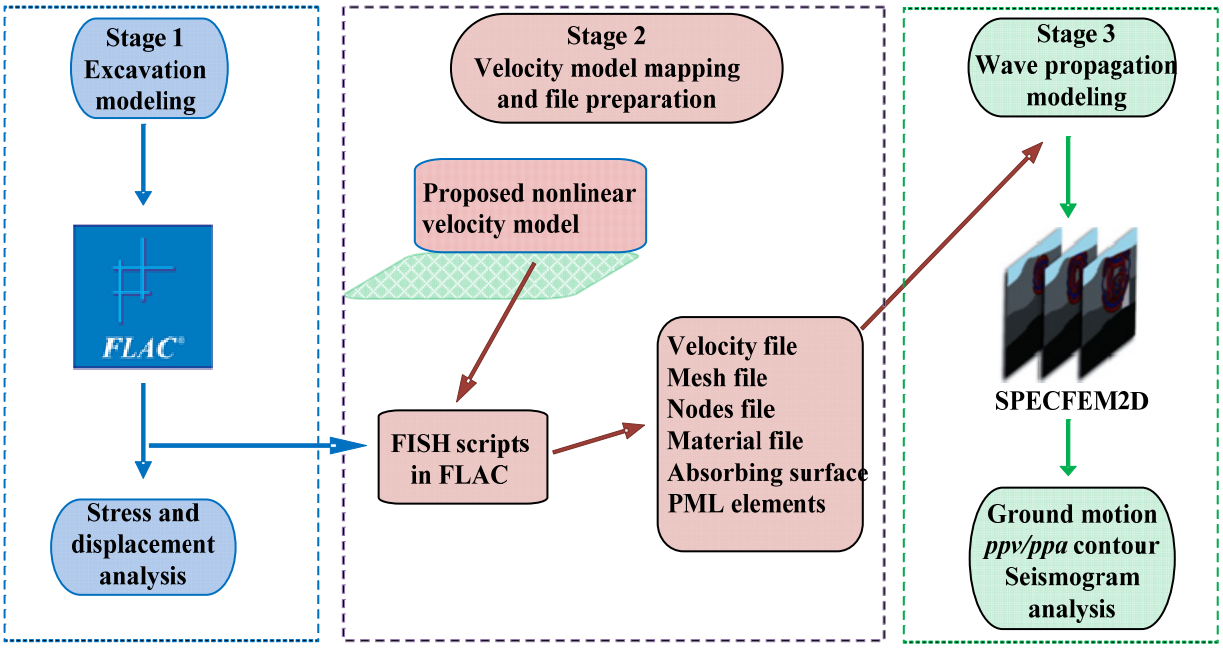

Figure 7-11: Proposed FLAC/SPECFEM2D coupled modeling procedure.

velocity model of SPECFEM2D is constructed by the scripts after the final computation state is reached in FLAC. Files that contain coordinates, elements, materials, PML (perfect match layer) elements, and velocity field, are generated and transferred according to the "element-to-element" mapping method. This coupling approach enables us to perform wave propagation modeling in a non-uniform velocity field using SPECFEM2D. The coupling approach is used to simulate wave patterns around a simple stope in next section.

7.4 Numerical implementation of the proposed coupled simulation method

7.4.1 Stope excavation model

For demonstration purposes, seismic wave propagation around a stope is simulated using the proposed coupled method. The size of the stope is 12 m (width) by 24 m (height). Based on the coupling procedure outlined in Figure 7-11, a mesh is generated firstly using the internal grid generator in FLAC. The model size is 304 m × 304 m, which has 369,664 elements with a grid spacing of 0.5 m. A close-up view of the stope model is presented in Figure 7-12, and the corresponding SPECFEM2D model and a square layout of 41 by 41 receivers (green dots with a 1.5 m spacing) are shown in Figure 7-13. In addition, receivers are placed at the surface (dark red dots with a 0.5 m spacing, from No.1 to No.124) and inside the rock masses (blue dots, from No. 125 to No. 248), as shown in Figure 7-13.

Hoek and Brown (1997) proposed a simple rule-of-thumb for post-peak behaviors of rocks, i.e., brittle failure for very good quality hard rock mass (Q_c = 40 to 100), strain-softening for average quality rock mass (Q_c = 4 to 10), and perfect plastic failure for poor quality rock mass (Q_c = 0.1 to 1). In the context of hard rock deep mining, perfect plastic failure of rock mass is rarely encountered and brittle failure is common. Hence, two cases, one for very good (Q_c = 40) and the

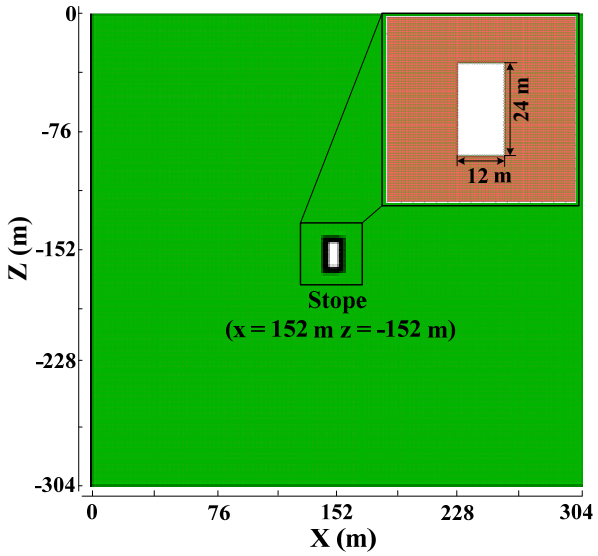

Figure 7-12: FLAC model for static stress analysis and a zoomed-in insert of the stope model showing the stope dimension.

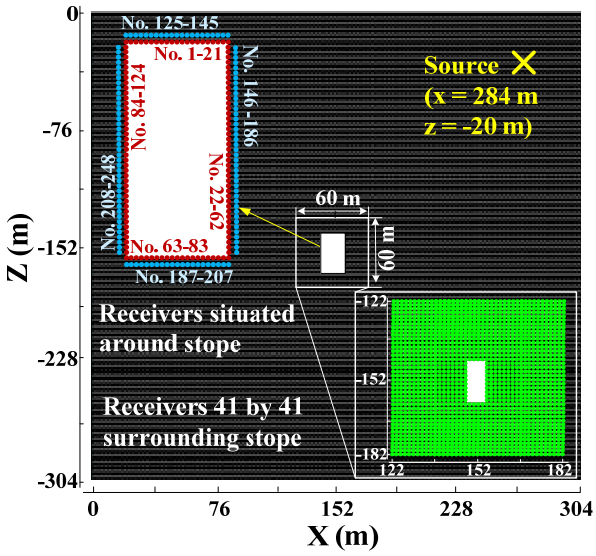

Figure 7-13: SPECFEM2D model for seismic wave modeling and the receiver layout around the stope.

other for fair ($Q_c = 4$) rock masses are considered as the host rock mass surrounding the stope. In addition, different ε_{ps} values are used to represent different post-peak behaviors of the rock mass. In general, relatively small (i.e., 0.1%) and large (i.e., 0.6%) values of ε_{ps} can be used to model brittle and strain-softening behaviors of rock mass. Suggestions by Hajiabdolmajid et al. (2002) and Zhao and Cai (2010a) are followed to determine the model parameters and to properly approximate the brittle failure and strain softening behaviors of very good and fair rock mass. The adopted rock mass deformation and strength properties are presented in Table 7-2 and the brittle parameters of the CWFS (cohesion weakening and frictional strengthening) model for a good rock mass and strain softening parameters for a fair rock mass are shown in Figure 7-14.

Table 7-2: Host rock mass properties for the FLAC model

Rock mass quality Q_c	Deformation parameters			Strength parameters of two types of host rock masses							
						Peak parameters		Residual parameters		Plastic strain (%)	
	ρ (kg/m^3)	E (GPa)	ν	ψ (°)	σ_t (MPa)	c_p (MPa)	ϕ_{fp} (°)	c_r (MPa)	ϕ_{fr} (°)	ε^c_{ps}	ε^f_{ps}
40	2500	58.6	0.26	25	12	45	10	1	50	0.1	0.1
4	2000	38.7	0.3	30	7	18	35	2	10	0.4	0.4

Note: ψ - dilation angle, σ_t - tensile strength, c - cohesion, ϕ_f - friction angle, ε_{ps} - characteristic plastic strain

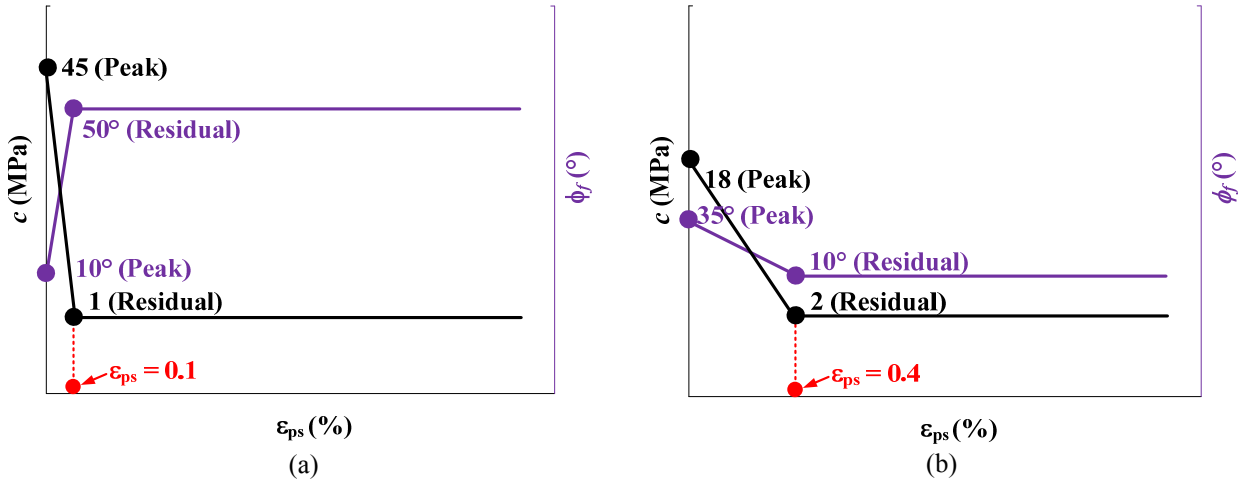

Figure 7-14: Parameters of the CWFS model for very good rock mass (a) and for fair rock mass (b).

The in situ stress field is defined by σ_1 = 60 MPa, σ_2 = 45 MPa, σ_3 = 30 MPa, where the directions of σ_1 is horizontal, σ_3 vertical, and σ_2 perpendicular to the 2D plane. Elastic and plastic stress analyses are performed in FLAC to determine the stress distribution and yield zones around the stope. Afterwards necessary input files are generated by running the FISH scripts and are transferred to SPECFEM2D. For comparison, seismic wave propagation modeling using uniform and the proposed non-uniform velocity models are performed.

7.4.2 Fault-slip seismic source

As stated in Chapter 2, the moment tensor source model is appropriate for representing a fault-slip seismic event to simulate far-field wave propagation. For point source model, only three components are required in the seismic source representation. In this chapter, a normal fault with a dip of 45° is modeled. The fault-slip source is described by six parameters in 2D modeling: origin onset time (t_0 = 0), source hypocenter (x (horizontal) and z (vertical)), and moment tensor (M_{xx}, M_{zz}, and M_{xz}). The Ricker wavelet source time function is used. The intensity of the seismic event is assumed with a moment magnitude of M_w = 2.0. The seismic source is placed at the top right (x = 284 m, z = -20 m) of the model (yellow cross in Figure 7-13).

7.4.3 Non-uniform velocity distribution around the stope

Elastic stress analyses are conducted firstly using the deformation parameters presented in Table 7-2 to investigate the influence of confinement on ground motion. Figure 7-15 shows the minimum principal stress distribution around the stope after excavation (for Q_c = 40) and the corresponding shear velocity models without and with the consideration of the influence of confinement on velocity field in SPECFEM2D. In the uniform velocity model shown in Figure 7-15(b), constant shear wave velocities of 0 and 3.06 km/s (calculated based on the deformation parameters list in Table 7-2) are assigned to the mined-out stope and the host rock, respectively. In the non-uniform velocity model shown in Figure 7-15(c), the shear wave velocity is equal to 0 inside the mined-out stope and 2.14 km/s in the tension zone. The shear wave velocities change from 2.14 to 3.06 km/s in the compressive zone, depending on the magnitude of confinement (refers to the non-uniform velocity model in Section 7.2). It is seen from Figure 7-15(a) and (c) that the distribution of the minimum principal stress indicates the distribution of the shear wave velocity around the stope. The conclusion holds true for the case of Q_c = 4. This is a good indicator that the coupling between the two numerical codes has been properly realized in the elastic analysis.

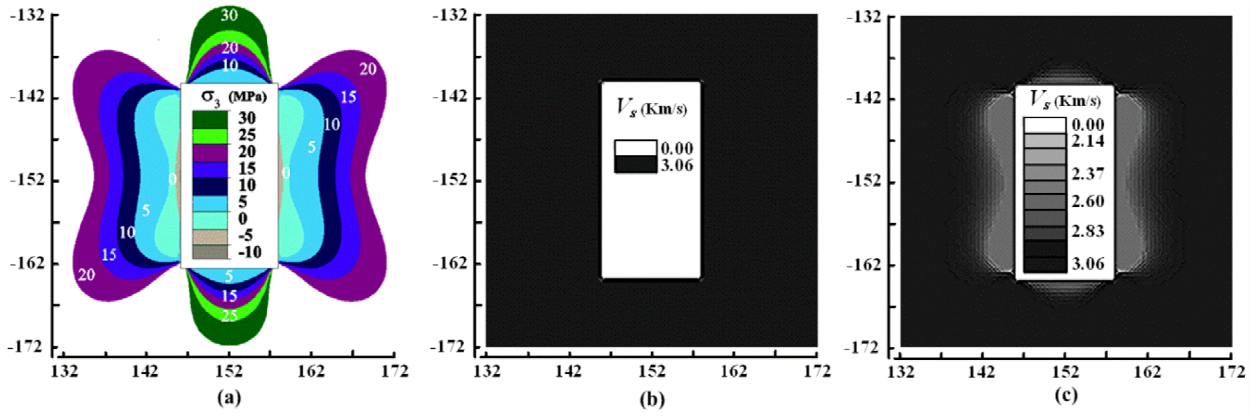

Figure 7-15: Elastic analysis result. (a) Minimum principal stress distribution in the FLAC model; uniform (b) and non-uniform (c) shear wave velocity distributions around the stope in the SPECFEM2D model.

As stated in Sections 7.1 and 7.2, ground motions around an excavation are influenced not only by confinement but also by rock mass quality. Excavation changes both confinement and rock mass quality if there is rock failure. Following the elastic stress analysis, a plastic stress analysis is conducted to examine the influence of confinement and failure zone on ground motion. Figure 7-16(a), (b), and (c) show the confinement and failure zone distribution around the stope (for Q_c = 40) in the FLAC model. Figure 7-16(d) and (e) present the corresponding shear velocity fields with the consideration of the influence of confinement only (Figure 7-16(d)) and both confinement and failure zone (Figure 7-16(d)) on the velocity fields in the SPECFEM2D model. In the failure zones, the bilinear decay functions are used to describe the relation between Q_c and plastic strain (Figure 7-10).

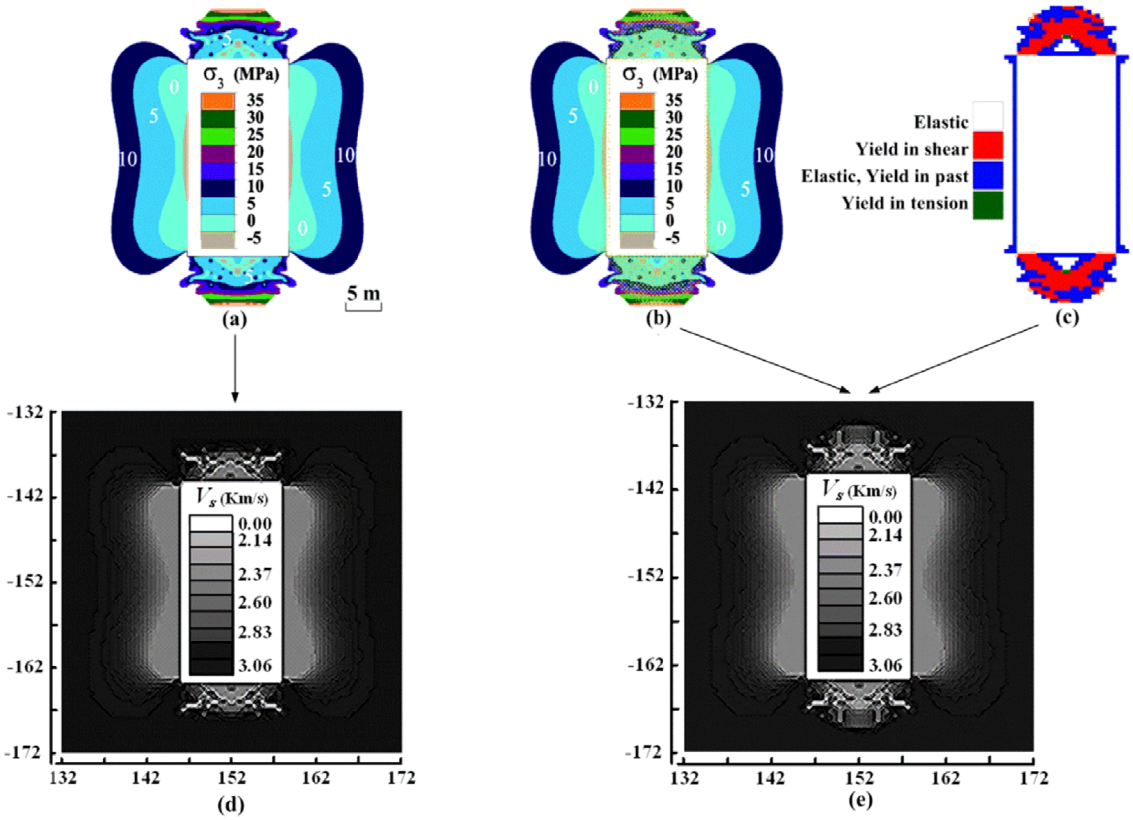

Figure 7-16: Analysis results for Q_c = 40. Distributions of confinement (a), confinement and failure zone (b), and extent and depth of failure zone (c) around the stope in the FLAC model and corresponding non-uniform shear wave velocity distributions in the SPECFEM2D model (d and e). Influence of only confinement (d) and both confinement and failure zone (e) on wavefields. Figure A - 5 in Appendix A shows the results for the case of Q_c = 4.

Figure 7-15 and Figure 7-16 show a large wave velocity variation around the stope when the confinement and rock mass failure are considered. Wave velocity is sensitive to low confinement (i.e., < 10 MPa), which has been revealed in the elastic analysis (Figure 7-15). In the plastic analysis, it is found by comparing Figure 7-15(a) with Figure 7-15(d) that low confinement leads to a significant change of the velocity field when only confinement is considered. In Figure 7-15(b) and Figure 7-15(c), a notch failure zone is formed, which is typical for hard rock masses. Once the influence of failure zone on wave velocity is considered (Figure 7-15(e)), the low velocity zones are enlarged in the roof and on the floor, which correspond to the failure zones. Field monitoring data show that the wave velocities are low in fractured zones around excavations (Cai and Kaiser, 2005; Maxwell et al., 1998).

Four velocity models are considered in the following discussion to examine the influence of confinement and rock mass failure on ground motion due to wave propagation. They are: I: uniform velocity model (Figure 7-15(b)), II: confinement-dependent model (elastic analysis case: Figure 7-15(c)), III: confinement-dependent model (plastic analysis case: Figure 7-16(d)), and IV: confinement and rock mass failure-dependent model (Figure 7-16(e)).

7.4.4 Modeling results and discussion

7.4.4.1 Wavefield analysis

Snapshots of the vertical velocity component of the four velocity models (Model I – uniform and Models II, III, and IV – non-uniform, Q_c = 40) are shown in Figure 7-17 at five wave propagation times. Direct P- and S-waves are generated and emitted in all velocity models, which can be seen at t = 0.04 s. Because the selected source model parameters represent a normal fault with a dip of 45°, relatively small P-wave-induced disturbance around the stope is expected and this is confirmed in the result. Noticeable scattering waves are produced when the S-waves

reach the top right of the stope. This observation also holds true for the case of Q_c = 4 (see Figure A - 6 in Appendix A).

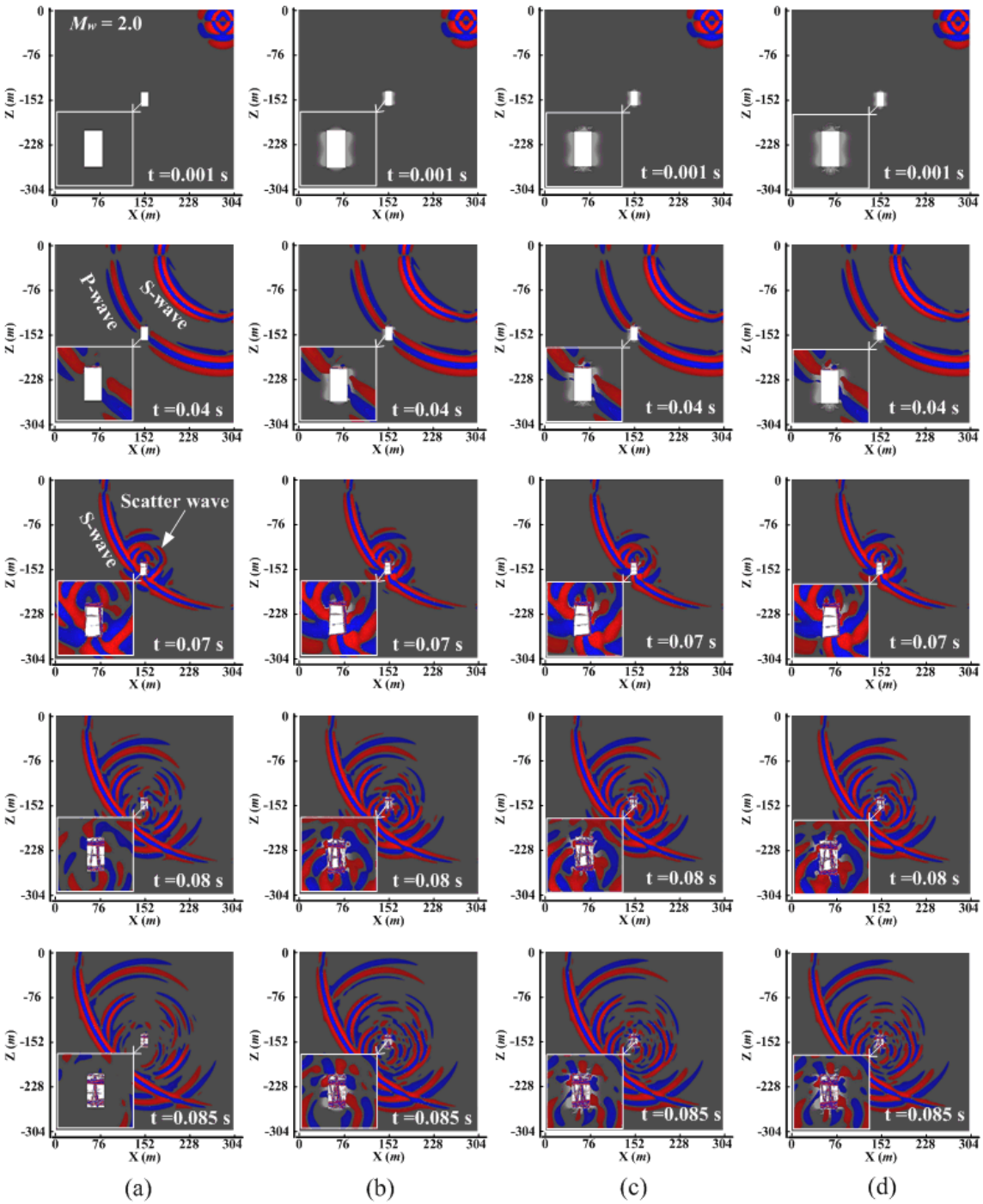

Figure 7-17: Snapshots of the vertical velocity component at 0.001, 0.04, 0.07, 0.08 and 0.085 s for velocity models of Model I (a), Model II (b), Model III (c), and Model IV (d) with Q_c = 40. The inserts at the lower-left corner show the details of wavefield around the stope. The positive (upward movement) and negative (downward movement) values of the vertical velocity component are represented by red and blue, respectively.

Compared with the result of the uniform velocity model Figure 7-17(a), more complex wavefields (see the zoom-in inserts) are observed around the stope in the non-uniform velocity models (Figure 7-17(b), (c), and (d)). This means that energy redistribution of the S-wave is expected due to the reflected and refracted waves. It also shows that wave patterns near an opening can be changed due to a non-uniform velocity field caused by an excavation. Although it is hard to identify or characterize the difference in the wavefields among the three non-uniform velocity models in Figure 7-17(b), (c), and (d), a small difference does exist and is visible in the wavefields (e.g., t = 0.085 s).

7.4.4.2 PPV contour analysis

PPV contours, mapped from a 60 m × 60 m square area with a 1.5 m receiver spacing and 41× 41 receivers around the stope (Figure 7-13), are obtained and the results are presented in Figure 7-18 to further inspect the influence of confinement and rock mass failure on the ground motion around the stope. All contours are plotted on the same color scales, from 0 to 0.38 m/s for Q_c = 40 and from 0 to 0.9 m/s for Q_c = 4. Zones of PPV increase and decrease are identified for both cases of good and fair rock masses. Large wave amplification occurs in the roof and on the right wall because these areas are facing to the incoming direction of seismic wave propagation. Shield PPV zones appear at the lower-left side of the stope (Figure 7-18(a) and (c)). The PPV increase and decrease zones around the stope demonstrate that excavation damage has a large influence on the wave patterns and ground motions.

Comparing with relatively stiff rock masses, soft rock masses may cause local large seismic response. For instance, the PPV_{max} (maximum value of PPV) for Q_c = 4 is about 0.45 m/s, which is 1.88 times higher than the PPV_{max} for Q_c = 40 (about 0.24 m/s) in the uniform velocity model (Model I, see Figure 7-18(b)). Similarly, for Model IV, the PPV_{max} in the Q_c = 4 case is about

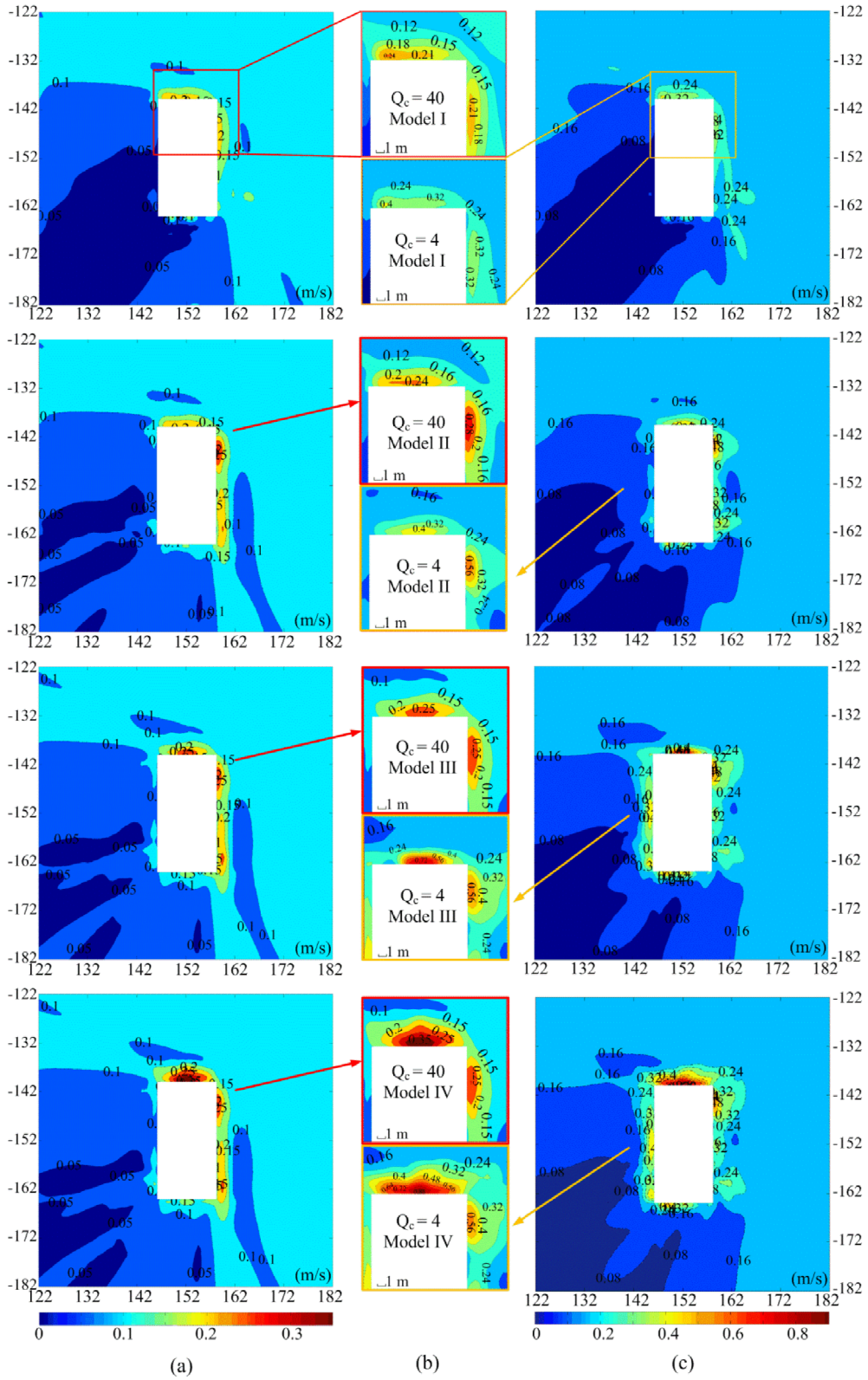

Figure 7-18: PPV contours around the stope for the four modeling cases of good (stiff) and fair (soft) quality rock masses. (a) and (c) show the PPV contours for Q_c = 40 and Q_c = 4, respectively; (b) shows the zoom-in plots with detailed PPV distributions around the stope in each case.

2.37 times higher than that in the $Q_c = 40$ case. In addition, the extent of zones with high PPV in the fair quality rock mass ($Q_c = 4$) is larger than that in the good quality rock mass ($Q_c = 40$). Hence, larger seismic response can be expected if the rock mass quality is poorer. In addition, in Model IV, if 0.24 m/s and 0.15 m/s are chosen as the reference PPV values to calculate the extents of the zones with high PPV for the cases of $Q_c = 4$ and $Q_c = 40$, the results are about 7.3 m and 3.2 m, respectively, which can be measured directly in Figure 7-18.

Comparing with the uniform velocity (Model I), relatively high PPV values and large zones with high PPV are observed in the non-uniform velocity models (Models II, III, and IV in Figure 7-18(a) and (c)). Figure 7-18(b) shows zoom-in plots of PPV distributions in the roof and on the right wall for all simulation cases. It is seen that confinement and failure zones influence the ground motions. Different from the results of Model I, higher ground motions can be observed on the right wall and large zones with high PPV can be identified in the roof and on the right wall in the results from Models II and III. For instance, PPV_{max} in Model II, which are 0.28 m/s ($Q_c = 40$) and 0.56 m/s ($Q_c = 4$) and occurring on the right wall, are larger than the PPV_{max} values of 0.21 m/s ($Q_c = 40$) and 0.32 m/s ($Q_c = 4$) in the uniform velocity (Model I).

In Model IV (confinement and failure zone-dependent), higher PPV values occur in the roof, at locations that correspond to the notch failure zone. In addition, the extent of high PPV zone in Model IV is larger than those in Models I, II, and III. For instance, the PPV_{max} values are 0.38 m/s and 0.9 m/s for $Q_c = 40$ and $Q_c = 4$ in Model IV, respectively, which are about 1.6 and 2.3 times larger than the PPV_{max} values in Model I (0.24 m/s for $Q_c = 40$ and 0.4 m/s for $Q_c = 4$). It is evident that PPV distribution can be altered and PPV values at some locations can be magnified due to the non-uniform velocity field caused by confinement change and rock mass failure.

7.4.4.3 PPV distribution along the excavation surface

As seen from Figure 7-18, high PPV values exist in the roof and on the right wall of the stope. PPV distributions along the roof and right wall surfaces of the stope are determined and the results are presented in Figure 7-19 to further investigate the site amplification effect on the excavation surface. The distances between receivers for obtaining PPV contours (Figure 7-18) and surface PPV distribution (Figure 7-19) are 1.5 m and 0.5 m, respectively. The reason for choosing a large receiver spacing for PPV contour calculation is to reduce the computation time. 124 surface receivers are placed on the stope surface with a 0.5 m spacing to find out the ground motion along the stope surface.

It is seen from Figure 7-19 that a relatively large seismic response is observed for Q_c = 4 when compared with the response for Q_c = 40, both on the roof surface (receivers No.1 to No.21) and right wall surface (receivers No.22 to No.62). This agrees with the trend inside the rock mass presented in the previous section, meaning that more intensive seismic response can be expected in soft rocks.

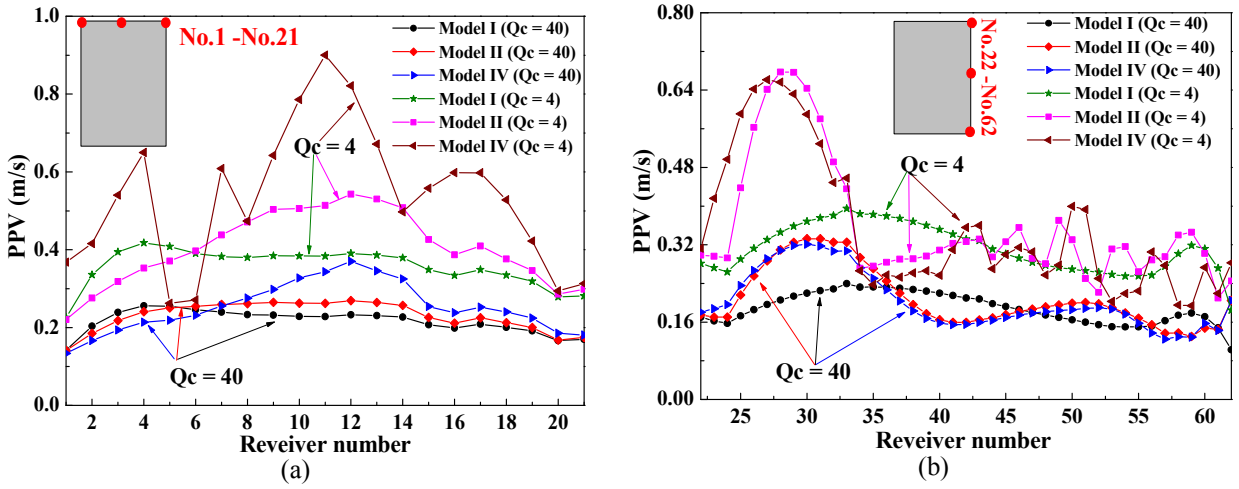

Figure 7-19: PPV distributions on the roof and side wall surfaces for the uniform and non-uniform velocity models. (a) Roof receivers, from No.1 to No.21, left to right at 0.5 m spacing; (b) right wall receivers, from No.22 to No.62, top to down at 0.5 m spacing.

Figure 7-19 also indicates that the PPV values in the non-uniform velocity models (Models II and IV) are larger than the PPV values in the uniform velocity model (Model I) at most roof receiver locations. For the roof receivers (Figure 7-19(a)), large ground motions are observed at receivers No.11 to No.12 in Model IV for both Q_c = 40 (blue right triangle) and Q_c = 4 (dark brown left triangle), which further demonstrates the influence of failure zone on ground motions. In the meantime, similar trend exists in the response in the right wall surface receivers (Figure 7-19(b)). High PPV values are identified at the upper right wall surface (i.e., receivers No.23 to No.34) in the non-uniform velocity models (Models II and IV). The variations of the PPV values in these models are primarily caused by the confinement differences.

7.4.4.4 Seismogram analysis

Synthetic seismograms at receivers No.12 and No.28 are calculated to further investigate the influence of confinement and failure zone on ground motion. The results are presented in Figure 7-20 (for Q_c = 4; Figure A - 7 in Appendix A shows the results for Q_c = 40). The velocity seismograms of the two receivers show a large difference between the uniform (Model I) and non-uniform velocity models (Models II and IV), especially after the direct S-wave reached the receivers. As expected, the P-wave has a small and the S-wave has a large disturbance to ground motion due to velocity change caused by confinement change and rock mass failure. The vertical and horizontal velocity component seismograms for both receivers are dominated by the S-waves and scatter waves.

A comparison of the seismograms of the roof and right wall receivers for Models I, II, and IV indicate that higher velocity amplitudes are produced in both velocity components, in the models that take confinement and rock mass failure into consideration. In Models II and IV, strong and long period coda waves are generated and are visible after the direct S-waves reach these

receivers. However, the amplitudes of the coda waves in Model IV are relatively lower than that in Model II for receivers No.12 (Figure 7-20(a)) and No.28 (Figure 7-20(c)). For instance, the horizontal component of receiver No.28 shows large coda waves in Model II after 0.08 s, but the coda wave amplitudes are not comparably high in Model IV (Figure 7-20(c)). It means that a failure zone might serve as a buffer zone to reduce ground motion on the stope surface but the failure zone itself might experience intensive ground motions. In addition, a slight delay of wave arrival time is visible in the seismograms, which might be caused by the interaction between seismic wave and failure zones in the low confinement zones.

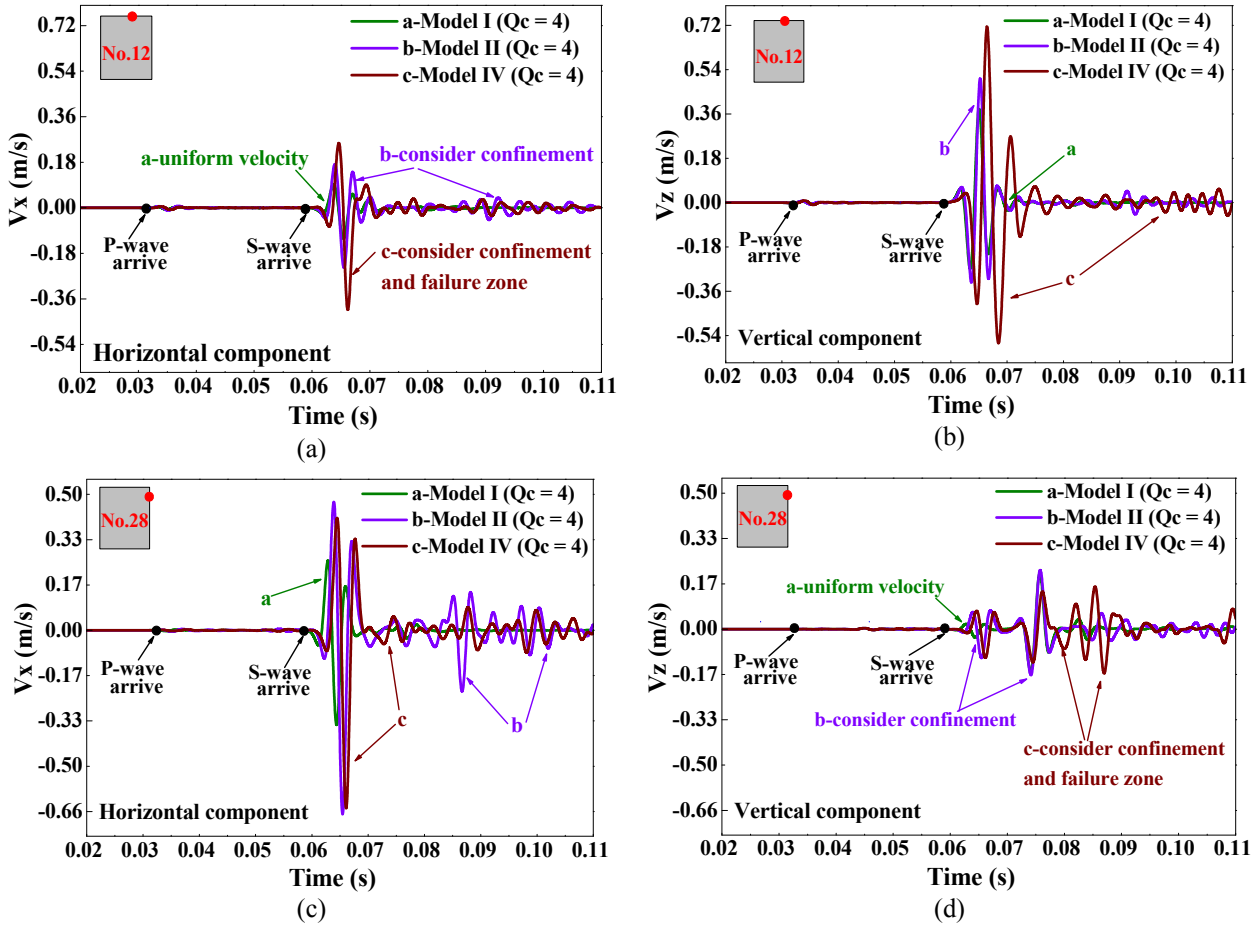

Figure 7-20: Synthetic seismograms at receivers No.12 and No.28 for the uniform and non-uniform velocity models. Horizontal (V_x)/Vertical (V_z) velocity components of No.15 and No.59 are shown in (a)/(b), and (c)/(d), respectively. The receiver is denoted by the red circle dot in the upper-left insert, for $Q_c = 4$.

The modeling results suggest that more complex seismic response and amplification of ground motion can be expected around the stope due to the influence of confinement and rock mass failure resulting from excavation. Hence, consideration of the excavation effect is important for capturing ground motion accurately around excavations. The proposed non-uniform velocity model and the FLAC/SPECFEM2D coupled approach provide a means to analyze ground motion near excavation boundaries accurately.

7.4.5 Site amplification near excavation boundaries

128 receivers are placed in four lines inside the rock masses, 2 m away from the excavation surface (blue dots in Figure 7-13) to investigate the site amplification effect. A comparison of PPV between the surface receivers (R_1, red) and inside receivers (R_2, blue) for the roof and right wall is shown in Figure 7-21. It is found that the surface receivers have stronger ground motion than the receivers placed inside the wall (i.e., 2 m away from the wall surface). For inside receiver No.136, the PPV_{max} value is 0.18 m/s (Q_c = 40) in the roof in Model IV, but the PPV_{max} value increases to about 0.38 m/s at the surface receiver No.12 in Model IV (Figure 7-21(a)). On the right side wall (Figure 7-21(b)), the PPV values show different features compared with those in the roof. In the upper right wall area (from receivers No.22/146 to No.36/160), the PPV values of the R_1 receivers are larger than those of the R_2 receivers in all models. In the lower right wall area (from receivers No.37/161 to No.62/186), the PPV values of the R_1 receivers are lower than that of the R_2 receivers for the non-uniform velocity models but are still larger than that in the uniform velocity model. The results suggest that ground motion amplification can be expected at the excavation surface. This is in general agreement with field observations (Milev and Spottiswoode, 2005; Milev et al., 1999).

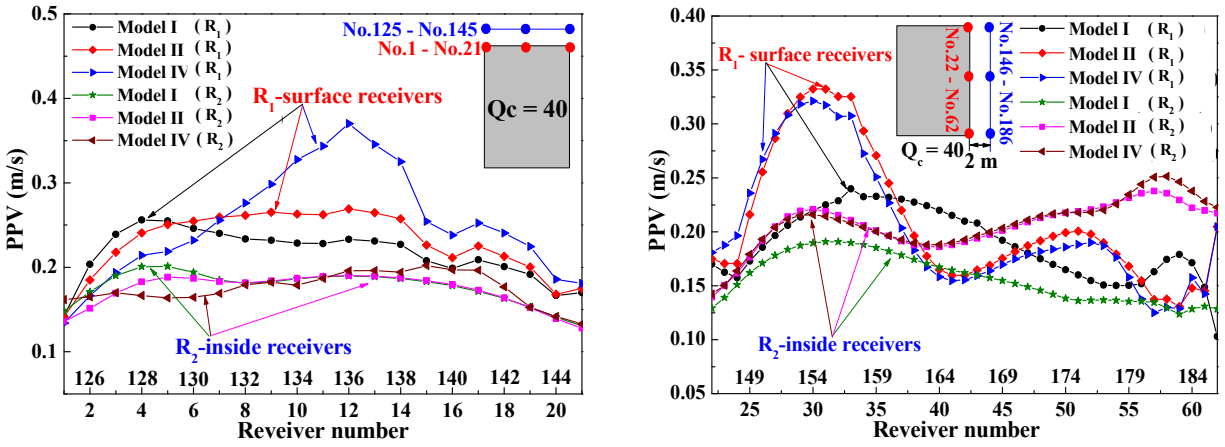

Figure 7-21: PPV distribution on the roof and right side wall area for the surfaces (red dots) and inside (blue dots) receivers. (a) Roof receivers, from No.1 to No.21 (R_1) and No.125 to No.145 (R_2), left to right at 0.5 m spacing; (b) right wall receivers, from No.22 to No.62 (R_1) and No.146 to No.186 (R_2), top to down at 0.5 m spacing.

A semi-empirical calibrated design scaling law (Kaiser et al., 1996) has been introduced to estimate PPV for dynamic support design. As a general empirical method for PPV estimation in hard rock mines, the scaling law can provide an upper bound PPV value for the dynamic support design. As mentioned in Chapters 5 and 6, PPV_{SLB} in the modeling cannot consider the ground motion alteration factors such as excavation and heterogeneity. A direct comparison between PPV_{SLB} and PPV from the numerical results (Q_c = 40) is shown in Figure 7-22. Figure 7-22(a) shows the PPV_{SLB} (with a 90-95% confidence level) contour around an un-mined stope. Contours of amplification factor for the uniform and non-uniform velocity models, which is defined as the ratio of PPV_{Model} to PPV_{SLB}, are presented in Figure 7-22(b). Figure 7-22(c) show zoom-in figures to illustrate the details of the amplification factors in the stope roof and right upper wall area for the uniform and non-uniform velocity models.

Comparing Figure 7-22(a) with Figure 7-18(a), it is seen that the PPV_{SLB} distribution and PPV_{Model} distribution in the modeling work are comparable. PPV amplifying/shielding areas are seen in Figure 7-22(b) and (c) at the upper-right/lower-left areas of the mapping areas, with

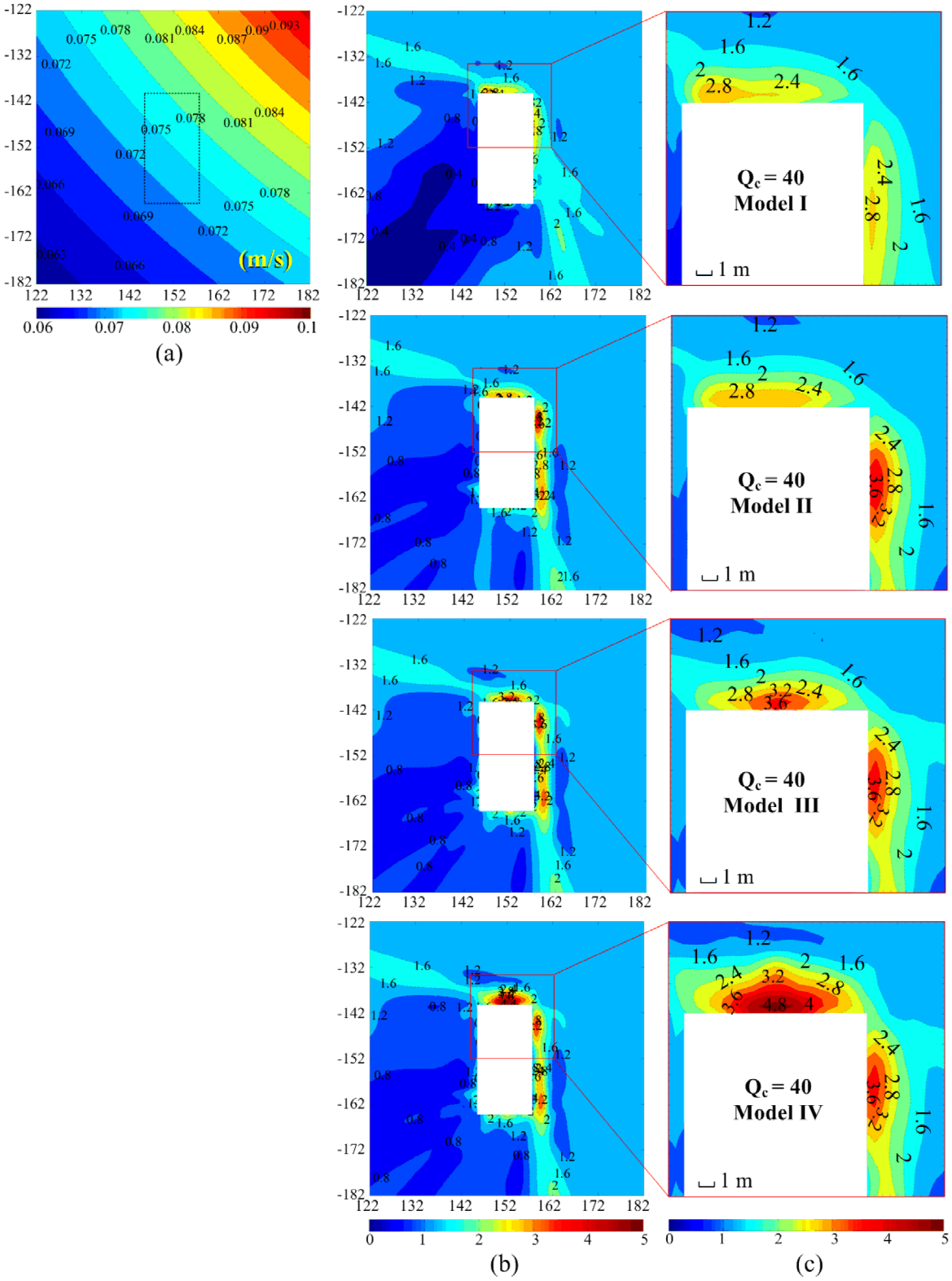

Figure 7-22: Site amplification by the stope. (a) PPV_{SLB} (m/s) contour without excavation; (b) amplification factor contours around the stope and zoom-in plots (c) showing the detailed site wave amplification in the roof and on the right wall for the uniform (Model I) and the non-uniform velocity (Models II, III, IV) models.

amplification factors of 1.6 and 0.8, respectively for Model I. It means that ground motions can be altered by man-made openings, such as drifts, ore-passes, and stopes.

Site amplification can be expected due to the excavation effect. As can be seen from Figure 7-22(b) and (c), amplification factors (related to background PPV_{SLB}) change from about 3 to 5 in the roof zones, and increase from about 3 to 4 in the right wall zones for models from Model I to Model IV, respectively. The amplification factors are the highest in the roof in Model IV in which both confinement and rock mass failure were considered. The location of the highest amplification factor is also different from that in Model I (uniform velocity model). As mentioned in Chapter 6, the data used to derive the scaling law were collected from sensors embedded relatively far away from the excavation surface. Most seismic sensors are not positioned at or near the excavation surface; hence, they cannot capture the ground motion on the surface when excavation damage dominates. The modeling results further confirm the observations made by some researchers that strong site amplification exists around the openings in the field (Hildyard and Milev, 2001; Hildyard and Young, 2002; Šílený and Milev, 2008).

This amplification phenomenon has an implication for rockburst risk assessment and dynamic rock support design. For the simulated stope, the highest PPV near the excavation boundary in the roof can be *three* times higher than the PPV_{SLB} when the boundary effect is considered with a uniform velocity model. When the boundary effect is considered with a non-uniform velocity model which is constructed based on the consideration of confinement change and rock mass failure due to excavation, the highest PPV near the excavation boundary in the roof can be *five* times higher than PPV_{SLB} value.

7.5 Final remarks

In this chapter, based on the relation between confining stress and wave velocity obtained from laboratory tests and considering low confinement condition near excavation boundaries in underground mines, a nonlinear model linking wave velocity to confinement and rock mass failure is proposed. The velocity field around an underground excavation is non-uniform and the nonlinear velocity model can define the non-uniform velocity field.

Based on the proposed nonlinear velocity model, a FLAC/SPECFEM2D coupled approach is developed and implemented to simulate ground motions around a stope due to a fault-slip seismic event. The FLAC model considers the excavation-induced stress change and rock mass failure, and passes the input data to SPECFEM2D by invoking FISH scripts. The non-uniform velocity models in SPECFEM2D are constructed based on the data transferred from FLAC, and ground motions around the excavation boundaries due to wave propagation are calculated. For comparison, ground motions in a uniform velocity model are also calculated.

The simulation results show that the difference of the velocity wavefield between the uniform and the non-uniform velocity models is large, especially in the vicinity of the stope. Very complex wavefields are generated due to the excavation effect. In the non-uniform velocity model, amplification may occur in the low confinement zones. Site amplification at the excavation surface is larger in the non-uniform velocity models due to the influence of failure zones.

Ground motion near excavation boundaries can be simulated using the proposed nonlinear velocity model and the FLAC/SPECFEM2D coupled modeling method. Using the proposed coupled method, amplification and resonance effects due to excavation can be predicted. The

most important finding from this study is that confinement change and rock mass failure can alter the velocity field around an excavation significantly and it is critical to consider this effect in ground motion simulation. Although PPV is not the only deciding factor that controls rockburst damage potential, it is one of the important factors that need to be considered carefully. As engineers move from empirical towards rationale designs, wavefield analysis using the approach proposed in this study can be beneficial. The results presented in this study provide insight to understanding ground motion patterns around underground excavation boundaries, which may facilitate more representative assessments of rockburst hazard in underground mines.

Chapter 8

8 Conclusions and future research

This thesis aims at making a contribution to better understand seismic wave propagation in underground mines. A particular emphasis is placed in understanding ground motion near excavation boundaries due to seismic wave propagation that results from a fault-slip seismic event. A literature review was firstly conducted in Chapter 2 to answer the questions why localized rockburst damage occurs and what approach can be taken to address the problem. It is found that many factors (e.g., seismic event, rock strength, and mining activities) affect rockburst damage in underground mines and an advanced numerical modeling technique can be used to address one important aspect of this issue – ground motion due to seismic wave propagation. Research findings are then presented in various aspects in five chapters (from Chapter 3 to Chapter 7) to address the question of obtaining accurate ground motion in forensic analysis of rockburst damage. The main conclusions from the thesis work are presented in Section 8.1, which are structured according to the thesis chapters. Recommendations for future work are presented in Section 8.2.

8.1 Conclusions

Firstly, from the literature review (Chapter 2) and the source parametric study (Chapter 3), it is concluded that:

- Many factors such as seismic source, excavation size and shape, internal attenuation, and geological structures contribute to localized tunnel damage after a seismic event.

- Seismic wave propagation in underground mines can be properly modeled using advanced numerical codes. SPECFEM2D is a robust tool that can be used to conduct seismic wave propagation modeling.
- Point source models can be employed to model far-field seismic wave propagation induced by a fault-slip seismic event. In particular, the DC (double-couple) point model is suitable for wave propagation modeling in the far-field.
- Ground motion depends not only on the target-source distance, but also on factors that affect wave patterns (i.e., slip direction, spatial location of tunnel with respect to seismic source, heterogeneity). Source parameters should be selected carefully when conducting wave propagation modeling.

From the study of the influence of wavelength-to-excavation span ratio on ground motion (Chapter 4), it is concluded that:

- Wavefield become more varied as the λ/D ratio decreases. In general, the PPV values around an excavation increase as the λ/D ratio increases. Furthermore, the amplification effect around an excavation increases as the λ/D ratio decreases, by either increasing the excavation span or decreasing the wavelength.
- The amplification factor becomes almost independent when the λ/D ratio is relatively large (e.g., $\lambda/D > 30$). When the λ/D ratio is greater than 30, seismic wave loading can be considered as quasi-static loading condition. On the other hand, large variations of amplification factor are expected when λ/D ratio is small (e.g., $\lambda/D < 10$) and a dynamic loading condition should be considered.

- The numerical modeling results provide additional insight to understanding ground motions near underground excavation boundaries.

From the study of the influence of attenuation on wave propagation (Chapter 5), it is concluded that:

- Seismic wave propagation is strongly influenced by the attenuation effect, especially in the far-field. The dimensionless quality factor Q can be used to account the intrinsic attenuation.
- The method to estimate the shear quality factor in hard rock mines is presented. The shear quality factor is obtained by comparing modeling results with those from the scaling laws.
- When there is no high quality field data for shear quality factor determination, a Q_s value from 40 to 80 can be used to account the attenuation effect for wave propagation simulation in hard rock mines.

From the study of the influence of heterogeneity on wave propagation (Chapter 6), it is concluded that:

- Wave propagation patterns around an excavation are altered significantly by various type heterogeneities in underground mines. Both PPV amplification and shielding effects can occur near excavation boundaries.
- For a single tunnel, scattering waves can be excited and the seismic wave energy is redistributed around the tunnel, leading to non-uniform distributions of PPV.
- Different mining stages can influence wave patterns. Seismic response around the tunnel shows large variations at different mining stages due to the mine-out area and backfilling.

- Strong scatter waves and coda waves are produced due to the influence of heterogeneities on P- and S-wave propagation. Wavefield patterns become more complex when more structures are involved. Multiple openings, in combination with geological structures such as dykes, can cause strong reflection waves that alter wave patterns.
- PPV amplification and shielding can occur around excavation boundaries. When mining-induced stresses and ground motions are high, a rock ejection type of rockburst damage may occur along a tunnel.

Finally, in the study of the coupled numerical modeling of wave propagation (Chapter 7):

- A nonlinear velocity model, which links wave velocity to confinement and rock mass quality, is presented to account for the non-uniform velocity field around excavations. This velocity model is applicable for excavation problems that result in both low confinement and rock failure for regions near the excavation boundaries. It is necessary to accurately define velocity fields around excavations in underground mines.
- A FLAC/SPECFEM2D coupled approach is developed based on the proposed nonlinear velocity model. In the proposed numerical technique, excavation-induced stress change and rock mass failure are considered in FLAC. A non-uniform velocity model is constructed in FLAC and then transferred to SPECFEM2D.
- It is seen that confinement change and rock mass failure can alter the velocity field around an opening and it is critical to consider this effect in ground motion simulation. Strong amplification normally occurs in the low confinement zones and on the excavation surface. Complex wavefields are also observed in the non-uniform velocity models. The FLAC/SPECFEM2D coupled numerical modeling method provides a new

approach for wavefield modeling in underground mines. It can also provide better velocity models for accurate source location determination in microseismic monitoring.

The results from this thesis provide some important and enlightening insights to seismic wave propagation in underground mines. Due to time and computation resource constraints, many questions could not be addressed in the thesis and they are recommended for future research.

8.2 Findings from preliminary study in 3D modeling of wave propagation

The thesis is focused on 2D seismic wave propagation simulations; however, wave propagation in an underground mine is 3D in nature. Therefore, a preliminary study of 3D modeling of seismic wave propagation is conducted and the results are presented in Appendices D and E.

8.2.1 Summary of preliminary 3D modeling work presented in Appendix D

- 3D wavefield modelling is possible but adds many challenges. A workflow to conduct 3D wave propagation modeling, from high quality mesh generation, parallel computing to data visualization using various advanced software, is developed. This workflow can facilitate efficient application of the SPECFEM3D tool for wave propagation modeling in underground mines.
- SPECFEM3D seems to provide a suitable tool for seismic wave propagation modeling in underground mines.

8.2.2 Summary of preliminary case study presented in Appendix E

- A preliminary case study in a South Africa gold mine is conducted to demonstrate the applicable of SPECFEM3D for wave modeling in underground mines.

- Source models can have a large impact on seismic wavefield. It is found that the non-point source model produces better seismic source evolution and seismograms than those obtained from the point source model. Compared with point source models, non-point source models may be better suited for both near-field and far-field wave simulations.
- The haulage tunnel and the mined-out areas have influence on seismic wave propagation. Large ground motions are observed near these areas and there are ground motion localizations at certain parts of the tunnel and in the mined-out areas.
- Combining SPECFEM3D and the kinematic source model, it is possible to capture realistic ground motion due to seismic wave propagation in underground mines. This in turn can assist in rock support design and rockburst risk management.

8.3 Recommendations and future research

Several issues are encountered during the research and addition research needs to be conducted in the future to address them. Some recommendations for future research are suggested below.

- Expand the research on near source representation of seismic sources. Dynamic source models are suitable for capturing ground motion in the near-field because it can model the physical process of fault slip. More field data should be collected and back analysis be conducted to understand the dynamic rupture process of faults in underground mines.
- Further validate the nonlinear velocity model. The proposed nonlinear velocity model needs to be further validated using field data from well-planned field experiments in

underground mines. Once this is accomplished, the nonlinear velocity model can be used with confidence to capture non-uniform velocity field in underground mines.

- Conduct more case studies to demonstrate the merits of the modeling techniques. It would be interesting to conduct forensic analyses using data from some underground mines with detailed data that include seismic source, geology, mine geometry, and rockburst damage conditions. This will promote the acceptance of conducting seismic wave modeling as an essential component in underground mine design.
- Apply the numerical modeling method to other fields such as underground cavern design, dam engineering, nuclear waste disposal, railway and highway tunnel design, etc.

References

Abercrombie, R.E., 1995. Earthquake source scaling relationships from −1 to 5 M_L using seismograms recorded at 2.5-km depth. J. Geophys. Res. Solid Earth (1978-2012), 100 (B12), 24015-24036.

Abokhalil, M., 2007. M. Sc. Thesis, Insights into the response of rock tunnels to seismicity. University of Oslo, Norway.

Agrawal, P., Sun, C.T., 2004. Fracture in metal-ceramic composites. Compos Sci Technol 64 (9), 1167-1178.

Aki, K., 1967. Scaling law of seismic spectrum. J. Geophys. Res. 72 (4), 1217-1231.

Aki, K., 1980a. Possibilities of seismology in the 1980s. B Seismol Soc Am 70 (5), 1969-1976.

Aki, K., 1980b. Scattering and attenuation of shear-waves in the lithosphere. J. Geophys. Res. 85 (Nb11), 6496-6504.

Aki, K., Richards, P.G., 2002. Quantitative seismology, 2nd Edition. Univ. Sci. Books, Sausalito, CA.

Alejano, L.R., Rodriguez-Dono, A., Alonso, E., Fdez-Manin, G., 2009. Ground reaction curves for tunnels excavated in different quality rock masses showing several types of post-failure behaviour. Tunnell. Underground Space Technol. 24 (6), 689-705.

Alford, R.M., Kelly, K.R., Boore, D.M., 1974. Accuracy of Finite-Difference modeling of acoustic-wave equation. Geophysics 39 (6), 834-842.

Ariffin, A.K., Huzni, S., Nor, M.J.M., Mohamed, N.A.N., 2006. Hybrid finite-discrete element simulation of crack propagation under mixed mode loading condition. Key Engineering Materials 306, 495-500.

Asef, M., Najibi, A., 2013. The effect of confining pressure on elastic wave velocities and dynamic to static Young's modulus ratio. Geophysics 78 (3), D135-D142.

Aydan, Ö., Ohta, Y., Geniş, M., Tokashiki, N., Ohkubo, K., 2010. Response and stability of underground structures in rock mass during earthquakes. Rock Mech. Rock Eng. 43 (6), 857-875.

Baker, C., Young, R.P., 1997. Evidence for extensile crack initiation in point source time-dependent moment tensor solutions. B Seismol Soc Am 87 (6), 1442-1453.

Bangash, T., Munjiza, A., 2002. FEM/DEM modelling of RC beams under impact. In: Proceeding of 7 th International Conference on Structures under Shock and Impact, Montreal, Quebec, Canada, 11 (7), 519-528.

Barton, N., 1984. Effect of rock mass deformation on tunnel performance in seismic regions. Advances in Tunnelling Technology and Subsurface Use 4 (3), 89-99.

Barton, N., 2002. Some new Q-value correlations to assist in site characterization and tunnel design. Int. J. Rock Mech. Min. Sci., 39 (2), 185-216.

Basabe, J.D.D., Sen, M.K., 2007. Grid dispersion and stability criteria of some common fnite-element methods for acoustic and elastic wave equations. Geophysics 72 (6), T81-T95.

Basabe, J.D.D., Sen, M.K., 2010. Stability of the high-order fnite elements for acoustic or elastic wave propagation with high-order time stepping. Geophys. J. Int 181 (1), 577-590.

Beer, G., Duenser, C., Vorauer, J., 2004. New developments in the analysis of large scale 3-D rock mechanics problems using coupled Finite Element/Boundary Element methods. In: Proceeding of the ISRM International Symposium 3rd ARMS, Millpress, Rotterdam, 1333-1336.

Beresnev, I.A., Atkinson, G.M., 2002. Source parameters of earthquakes in eastern and western North America based on finite-fault modeling. B Seismol Soc Am 92 (2), 695-710.

Berkhout, A.J., 1987. Applied seismic wave theory. Elsevier.

Bhasin, R., Hoeg, K., Abokhalil, M., 2008. Effect of seismicity on rock support in tunnels. In: Proceeding of World Tunnel Congress 2008 - Underground Facilities for Better Environment and Safety, India, 530-540.

Blake, O., Faulkner, D., Rietbrock, A., 2013. The effect of varying damage history in crystalline rocks on the P- and S-wave velocity under hydrostatic confining pressure. Pure and Applied Geophysics 170 (4), 493-505.

Boashash, B., 2003. Time frequency signal anlysis and processing. Elsevier.

Bohlen, T., Saenger, E., 2006. Accuracy of heterogeneous staggered-grid finite-difference modeling of Rayleigh waves. Geophysics 71 (4), T109-T115.

Boore, D.M., 1970. Love waves in nonuniform wave guides - Finite Difference calculations. J Geophys Res 75 (8), 1512-1527.

Boore, D.M., 2003. Simulation of ground motion using the stochastic method. Pure and Applied Geophysics 160 (3-4), 635-676.

Bormann, P., Baumbach, M., Bock, G., Grosser, H., Choy, G.L., Boatwright, J., 2002. IASPEI: New manual of seismological observatory practice (NMSOP). GeoForschungsZentrum.

Bouchon, M., 1976. Teleseismic body wave radiation from a seismic source in a layered medium. Geophys J Int 47 (3), 515-530.

Brune, J.N., 1970. Tectonic stress and the spectra of seismic shear waves from earthquakes. J. Geophys. Res. 75 (26), 4997-5009.

Cai, J.G., Zhao, J., 2000. Effects of multuiple parallel fractures on apparent attenuation of stress waves in rock masses. Int. J. Rock Mech. Min. Sci., 37 (4), 661-682.

Cai, M., 2008a. Influence of intermediate principal stress on rock fracturing and strength near excavation boundaries - Insight from numerical modeling. Int. J. Rock Mech. Min. Sci., 45 (5), 763-772.

Cai, M., 2008b. Influence of stress path on tunnel excavation response–numerical tool selection and modeling strategy. Tunnell. Underground Space Technol. 23 (6), 618-628.

Cai, M., 2013a. Fracture initiation and propagation in a brazilian disc with a plane interface: a numerical study. Rock Mech. Rock Eng.46 (2), 289-302.

Cai, M., 2013b. Principles of rock support in burst-prone ground. Tunnell. Underground Space Technol. 36, 46-56.

Cai, M., Champaigne, D., 2009. The art of rock support in burst-prone ground. Keynote leccture. In: Proceeding of 7th International Symposium on Rockburst and Seismicity in Mines (RaSIM 7): Controlling Seismic Hazard and Sustainable Development of Deep Mines, Dalian, China, 1 and 2 33-46.

Cai, M., Kaiser, P., 2002. Dependency of wave propagation velocity on rock mass quality and confinement. In: Proceeding of 5th North American Rock Mechanics symposium, University of Toronto, 615-622.

Cai, M., Kaiser, P., 2014. In-situ rock spalling strength near excavation boundaries. Rock Mech. Rock Eng. 47 (2), 659-675.

Cai, M., Kaiser, P., Duff, D., 2012. Rock support design in burst-prone ground utilizing an interactive design tool. In: Proceeding of 46th US Rock Mechanics/Geomechanics Symposium, 12-599.

Cai, M., Kaiser, P., Morioka, H., Minami, M., Maejima, T., Tasaka, Y., Kurose, H., 2007a. FLAC/PFC coupled numerical simulation of AE in large-scale underground excavations. Int. J. Rock Mech. Min. Sci., 44 (4), 550-564.

Cai, M., Kaiser, P., Tasaka, Y., Minami, M., 2007b. Determination of residual strength parameters of jointed rock masses using the GSI system. Int. J. Rock Mech. Min. Sci., 44 (2), 247-265.

Cai, M., Kaiser, P., 2004. Numerical simulation of the Brazilian test and the tensile strength of anisotropic rocks and rocks with pre-existing cracks. Int. J. Rock Mech. Min. Sci., 41(Supplement 1), 478-483.

Cai, M., Kaiser, P., 2005. Assessment of excavation damaged zone using a micromechanics model. Tunnell. Underground Space Technol. 20 (4), 301-310.

Cai, M., Kaiser, P., Morioka, H., Minami, M., Maejima, T., Tasaka, Y., Kurose, H., 2007c. FLAC/PFC coupled numerical simulation of AE in large-scale underground excavations. Int. J. Rock Mech. Min. Sci., 44 (4), 550-564.

Cai, M., Wang, X., 2015. A non-uniform velocity model and FLAC/SPECFEM2D coupled numerical simulation of wave propagation in underground mines. In: Proceeding of the 13th International ISRM Congress 2015, Montreal, Canada.

Carcione, J., 2007a. Wave fields in real media: wave propagation in anisotropic, anelastic, porous and electromagnetic media. Elsevier.

Carcione, J.M., 1993. Seismic modeling in viscoelastic media. Geophysics 58 (1), 110-120.

Carcione, J.M., 1995. Constitutive model and wave-equations for linear, viscoelastic, anisotropic media. Geophysics 60 (2), 537-548.

Carcione, J.M., 2007b. Wave felds in real media: theory and numerical simulation of wave propagation in anisotropic, anelastic, porous and electromagnetic media. Elsevier.

Carcione, J.M., Kosloff, D., Kosloff, R., 1988. Wave propagation simulation in a linear visoelastic medium. Geophys. J. Int 95, 597-611.

Chaljub, E., Komatitsch, D., Vilotte, J.-P., Capdeville, Y., Valette, B., Festa, G., 2007. Spectral-element analysis in seismology. Advances in Geophysics 48, 365-419.

Chapman, C.H., 2004. Fundamentals of seismic wave propagation. Cambridge University Press, Cambridge,UK.

Chen, C.H., Chen, J.J., 2004. Research report, CECI, Taiwan.

Chen, C.H., Wang, T.T., Jeng, F.S., Huang, T.H., 2012a. Mechanisms causing seismic damage of tunnels at different depths. Tunnell. Underground Space Technol. 28, 31-40.

Chen, J.R., 2005. The influence of seismic wave on long tunnel. In: Proceeding of the International Conference on World Long Tunnels, Taipei, Taiwan, 1181-1188.

Chen, S.G., Zhao, J., 1998. A study of UDEC modelling for blast wave propagation in jointed rock masses. Int. J. Rock Mech. Min. Sci., 35 (1), 93-99.

Chen, Z.Y., Shi, C., Li, T.B., Yuan, Y., 2012b. Damage characteristics and influence factors of mountain tunnels under strong earthquakes. Nat Hazards. 61 (2), 387-401.

Cherry, M.R., Aldrin, J.C., Boehnlein, T., Blackshire, J.L., 2013. A parallel mixed 3d grid/explicit fem scheme for computing elastic wave propagation on a Gpu using an irregular mesh. Review of progress in quantitative nondestructive evaluation 1511 (1), 75-82.

Christensen, R.M., 1982. Theory of viscoelastic: an introduction, 2nd edn. Academic Press, New York.

Close, D., Cho, D., Horn, F., Edmundson, H., 2009. The sound of sonic: a historical perspective and introduction to acoustic logging. CSEG Recorder, 34-43.

Clough, R., 1960. The finite element method in plane stress analysis. Proc Secon ASCE Conf Elec Compu, Pittsburg, PA, 345.

Cohen, G., 2002. Higher-order numerical methods for transient wave equations. Springer, Berlin, Germany.

Cristini, P., Komatitsch, D., 2012. Some illustrative examples of the use of a spectral-element method in ocean acoustics. The Journal of the Acoustical Society of America 131 (3), EL229-EL235.

Cundall, P.A., 1971. A computer model for simulating progressive, large scale movements in blocky rock systems. In: Proceeding of Intl. Symp. Rock Fracture., Nancy, France, II-8.

Cundall, P.A., 1988. Formulation of a 3-Dimensional Distinct Element model .1. a scheme to detect and represent contacts in a system composed of many polyhedral blocks. Int. J. Rock Mech. Min. Sci., 25 (3), 107-116.

Dalguer, L.A., Miyake, H., Irikura, K., 2004. Characterization of dynamic asperity source models for simulating strong ground motion. In: Proceeding of the 13th World Conference on Earthquake Engineering.

Darve, F., Servant, G., Laouafa, F., Khoa, H.D.V., 2004. Failure in geomaterials: continuous and discrete analyses. Comput Method Appl M 193 (27-29), 3057-3085.

Deng, X.F., Zhu, J.B., Chen, S.G., Zhao, Z.Y., Zhou, Y.X., Zhao, J., 2014. Numerical study on tunnel damage subject to blast-induced shock wave in jointed rock masses. Tunnell. Underground Space Technol. 43, 88-100.

Diallo, M.S., Appel, E., 2000. Acoustic wave propagation in saturated porous media: reformulation of the Biot/Squirt flow theory. J Appl Geophys 44 (4), 313-325.

Doornbos, D., 1982. Seismic moment tensors and kinematic source parameters. Geophys J Int 69 (1), 235-251.

Dou, L.M., Chen, T.J., Gong, S.Y., He, H., Zhang, S.B., 2012. Rockburst hazard determination by using computed tomography technology in deep workface. Safety Sci 50 (4), 736-740.

Dowding, C., 1984. Estimating earthquake damage from explosion testing of full-scale tunnels. Advances in tunnelling technology and subsurface use 4 (3), 113-117.

Dowrick, D.J., Rhoades, D.A., 2004. Relations between earthquake magnitude and fault rupture dimensions: How regionally variable are they? B Seismol Soc Am 94 (3), 776-788.

Du, Q.Z., Liu, L.L., Sun, J.B., 2007. Numerical modeling of seismic wavefield in anisotropic viscoelastic porous medium with the pseudo-spectral method. Acta Phys Sin-Ch Ed 56 (10), 6143-6149.

Dubinski, J., Mutke, G., 1996. Characteristics of mining tremors within the near-wave field zone. Pure Appl Geophys 147 (2), 249-261.

Dubinski, J., Mutke, G., 2005. Study of temporal changes of P-wave velocity in polish copper mines in high seismic activity zones. In: Proceeding of Rasim6: Controlling Seismic Risk, 631-634.

Durrhem, R.J., 2012. Functional specifications for in-stope support based on seismic and rockburst observations in South African mines. In: Proceeding of the Sixth International Seminar on Deep and High Stress Mining (Deep Mining 2012), Perth, Australia, 41-55.

Dziewonski, A.M., Anderson, D.L., 1981. Preliminary reference earth model (PREM). Phys. Earth Plant 25, 297-356.

Eibert, T.F., Hansen, V., Blindow, N., 1997. Full-wave 3D-modeling of ground-penetrating radars by a finite element/boundary element-hybrid technique. In: Proceeding of 1997 International Geoscience and Remote Sensing Symposium, I-Iv 227-229.

Elmo, D., Vyazmensky, A., Stead, D., Rance, J.R., 2007. A hybrid FEM/DEM approach to model the interaction between open-pit and underground block-caving mining. Rock Mechanics: Meeting Society's Challenges and Demands 1 and 2, 1287-1294.

Essen, K., Bohlen, T., Friederich, W., Meier, T., 2007. Modelling of Rayleigh-type seam waves in disturbed coal seams and around a coal mine roadway. Geophys. J. Int 170, 511-526.

Faccioli, E., Maggio, F., Paolucci, R., Quarteroni, A., 1997. 2D and 3D elastic wave propagation by a spseudo-spectral domain decomposition method. J Seismol 1 (3), 237–251.

Faccioli, E., Tagliani, A., Paolucci, R., 1989. Effects of wave-propagation in random earth media on the seismic radiation spectrum. Structural Dynamics and Soil-Structure Interaction, 61-75.

Feignier, B., Young, R.P., 1992. Moment tensor inversion of induced microseismic events - evidence of nonshear failures in the -4 less-than M less-than -2 moment magnitude range. Geophys Res Lett 19 (14), 1503-1506.

Fichtner, A., 2011. Full seismic waveform modelling and inversion. Springer, Berlin, German.

Fletcher, J.B., McGarr, A., 2005. Moment tensor inversion of ground motion from mining-induced earthquakes, Trail Mountain, Utah. B Seismol Soc Am 95 (1), 48-57.

Frohlich, C., Apperson, K.D., 1992. Earthquake focal mechanisms, moment tensors, and the consistency of seismic activity near plate boundaries. Tectonics 11 (2), 279-296.

Furumura, T., Kennett, B.L.N., Furumura, M., 1998. Seismic wavefield calculation for laterally heterogeneous whole earth models using the pseudospectral method. Geophys J Int 135 (3), 845-860.

Geniş, M., 2010. Assessment of the dynamic stability of the portals of the Dorukhan tunnel using numerical analysis. Int. J. Rock Mech. Min. Sci., 47 (8), 1231-1241.

Genis, M., Gercek, H., 2003. A numerical study of seismic damage to deep underground openings. In: Proceeding of ISRM 2003-Technology roadmap for rock mechanics, S. Afr. Inst. Min. Metall., 351-356.

Gharti, H.N., Oye, V., Komatitsch, D., Tromp, J., 2012. Simulation of multistage excavation based on a 3D spectral-element method. Computers & Structures 100 (2012), 54-69.

Gibowicz, S.J., 1990. The mechanism of seismic events induced by mining. A review. In: Proceeding of Rockbursts and Seismicity in Mines, Minneapolis, USA, 3-27.

Gibowicz, S.J., 1993. Seismic moment tensor and the mechanism of seismic events in mines. Rockbursts and Seismicity in Mines 93, 149-155.

Gibowicz, S.J., Harjes, H.P., Schafer, M., 1990. Source parameters of seismic events at heinrich tobert mine, ruhr basin, federal-republic-of-germany - evidence for nondouble-couple events. B Seismol Soc Am 80 (1), 88-109.

Gibowicz, S.J., Kijko, A., 1994. An Introduction to Mining Seismology. Academic Press, San Diego, California, USA.

Gibson, R.L., Toksoz, M.N., Dong, W., 1996. Seismic radiation from explosively loaded cavities in isotropic and transversely isotropic media. B Seismol Soc Am 86 (6), 1910-1924.

Goldstein, P., 1995. Slopes of p-wave to s-wave spectral ratios - a broad-band regional seismic discriminant and a physical model. Geophys Res Lett 22 (23), 3147-3150.

Goodman, R., Taylor, R., Brekke, T., 1968. A model for the mechanics of jointed rock. J Soil Mech Div SM3, 37-59.

Gray, J.P., Monaghan, J.J., 2004. Numerical modelling of stress fields and fracture around magma chambers. J Volcanol Geoth Res 135 (3), 259-283.

Guatteri, M., Mai, P.M., Beroza, G.C., Boatwright, J., 2003. Strong ground-motion prediction from stochastic-dynamic source models. Bulletin of the seismological society of America 93 (1), 301-313.

Guidault, P.A., Allix, O., Champaney, L., Navarro, J.P., 2007. A two-scale approach with homogenization for the computation of cracked structures. Comput Struct 85 (17-18), 1360-1371.

Gutenberg, B., Richter, C., 1956. Earthquake magnitude, intensity, energy and acceleration. Bull Seism Soc Am 46, 105-145.

Haddon, R., 1996. Use of empirical Green's functions, spectral ratios, and kinematic source models for simulating strong ground motion. Bull Seism Soc Am 86 (3), 597-615.

Hajiabdolmajid, V., Kaiser, P., Martin, C., 2002. Modelling brittle failure of rock. Int. J. Rock Mech. Min. Sci., 39 (6), 731-741.

Hanks, T.C., Kanamori, H., 1979. Moment magnitude scale. J. Geophys. Res: Solid Earth 84 (B5), 2348-2350.

Hart, R., Cundall, P.A., Lemos, J., 1988. Formulation of a 3-Dimensional Distinct Element model to mechanical calculations for motion and interaction of a system composed of many polyhedral blocks. Int. J. Rock Mech. Min. Sci., 25 (3), 117-125.

Hasegawa, H.S., Wetmiller, R.J., Gendzwill, D.J., 1989. Induced seismicity in mines in Canada - an overview. Pure Appl Geophys 129 (3-4), 423-453.

Hashash, Y., Hook, J.J., Schmidt, B., 2001. Seismic design and analysis of underground structures. Tunnell. Underground Space Technol. 16 (4), 247-293.

Hashash, Y., Park, D., Yao, J.I., 2005. Ovaling deformations of circular tunnels under seismic loading, an update on seismic design and analysis of underground structures. Tunnell. Underground Space Technol. 20 (5), 435-441.

Hatherly, P., 2013. Overview on the application of geophysics in coal mining. International Journal of Coal Geology 114, 74-84.

Hazzard, J.F., Young, R.P., 2002. Moment tensors and micromechanical models. Tectonophysics 356 (1–3), 181-197.

He, T., 2006. P- and S-wave velocity measurement and pressure sensitivity analysis of AVA response University of Alberta, Alberta, Canada.

Heal, D., 2010. Observations and analysis of incidence of rockburst damage in underground mines. Ph.D Thesis, School of Civil and Resources Engineering, University of Western Australia, p. 357.

Heal, D., Hudyma, M., Potvin, Y., 2006. Evaluating rockburst damage potential in underground mining. In: Proceeding of Golden Rocks 2006 The 41st US Symposium on Rock Mechanics (USRMS).

Hettich, T., Hund, A., Ramm, E., 2008. Modeling of failure in composites by X-FEM and level sets within a multiscale framework. Comput Method Appl M 197 (5), 414-424.

Hildyard, M., 2007a. Wave interaction with underground openings in fractured rock. Rock Mech. Rock Eng. 40 (6), 531-561.

Hildyard, M., Milev, A., 2001. Simulated rockburst experiment: Numerical back-analysis of seismic wave interaction with the tunnel. S. Afr. Inst. Min. Metall., 101 (5), 223-234.

Hildyard, M., Young, R., 2002. Modelling seismic waves around underground openings in fractured rock. Pure Appl Geophys 159 (1-3), 247-276.

Hildyard, M., Young, R., Collins, D., Pettitt, W., 2005. Seismic wave propagation to diagnose the state of fracturing. S. Afr. Inst. Min. Metall., 437-446.

Hildyard, M.W., 2007b. Manuel rocha medal recipient - wave interaction with underground openings in fractured rock. Rock Mech Rock Eng 40 (6), 531-561.

Hoek, E., Brown, E., 1997. Practical estimates of rock mass strength. Int. J. Rock Mech. Min. Sci., 34 (8), 1165-1186.

Holub, K., Rusajova, J., 2011. Peak Particle Velocity for Rockbursts in Underground Coal Mines and for Shot-Hole Explosions in Open-Pit Mines. Acta Geod Geophys Hu 46 (1), 104-114.

http://www.3ds.com/products-services/simulia/portfolio/abaqus.

http://www.ansys.com.

http://www.cervenka.cz/products/atena.

Huang, T.T., Johnstone, A., Yang, Y.F., Beduz, C., Friend, C., 2005. Finite element modeling of thermal stability and quench proagation in a pancake coil of PbBi2223 tapes. Ieee T Appl Supercon 15 (2), 1647-1650.

Hudyma, M.R., 2013. Applied mine seismology concepts and techniques, technical notes for ENGR 5356-Mine Seismic Monitoring System.

Huerta, C.I., Shin, Y., Powers, E., Roesset, J., 2000. Time-frequency analysis of earthquake records. In: Proceeding of 12th World Conference on Earthquake Engineering, Auckland, New Zealand.

Hughes, T., 2012. The finite element method: linear static and dynamic finite element analysis. Courier Dover Publications.

Idriss, I., 1985. Evaluating seismic risk in engineering practice. In: Proceedings of the 11th International Conference on Soil Mechanics and Foundation Engineering, San Francisco, 12-16 August 1985. Publication of: Balkema (AA).

Igel, H., Mora, P., Riollet, B., 1995. Anisotropic wave-propagation through finite-difference grids. Geophysics 60 (4), 1203-1216.

ITASCA, C.G., 1995. PFC-2D and PFC-3D Manuals.

Izutani, Y., Kanamori, H., 2001. Scale-dependence of seismic energy-to-moment ratio for strike-slip earthquakes in Japan. Geophys. Res. Lett. 28 (20), 4007-4010.

Jarosch, H.S., 1969. Body-wave magnitude and source mechanism. Eos T Am Geophys Un 50 (4).

Ji, S.W., Tang, Y.J., Hu, D.G., Wang, J., Tao, S.J., 2009. Analysis of typical seismic damages of highways in Wenchuan earthquake-induced hazard areas in Sichuan province. Chin. J. Rock Mech. Eng. 6 (28), 1250-1260.

Jiang, L.Z., Chen, J., Li, J., 2010. Seismic response of underground utility tunnels: shaking table testing and FEM analysis. Earthq Eng Eng Vib 9 (4), 555-567.

Jing, H.H., He, M.C., Wang, S.R., 2002. Numerical simulation study on the process of the rockburst in deep roadway. New Development in Rock Mechanics and Rock Engineering, Proceedings, 479-482.

Jing, L., 2003. A review of techniques, advances and outstanding issues in numerical modelling for rock mechanics and rock engineering. Int. J. Rock Mech. Min. Sci., 40 (3), 283-353.

Jing, L.R., Hudson, J.A., 2002. Special issue: Numerical methods in rock mechanics - Preface. Int. J. Rock Mech. Min. Sci., 39 (4), 407-408.

Kühn, D., Vavryčuk, V., 2013. Determination of full moment tensors of microseismic events in a very heterogeneous mining environment. Tectonophysics 589, 33-43.

Käser, M., Dumbser, M., Puente, d.l., Igel, H.J., 2007. An arbitrary high-order discontinuous Galerkin method for elastic waves on unstructured meshes – III. Viscoelastic attenuation. Geophys. J. Int 168, 224-242.

Kaiser, P., Cai, M., 2012. Design of rock support system under rockburst condition. Journal of Rock Mechanics and Geotechnical Engineering 4 (3), 215-227.

Kaiser, P., Cai, M., 2013. Critical review of design principles for rock support in burstprone ground - time to rethink!. Keynote Lecture. In: Proceeding of Ground Support 2013, Australian Centre for Geomechanics, Perth, 3-38.

Kaiser, P., Maloney, S.M., 1997. Scaling laws for the design of rock support. Pure and Applied Geophysics 150 (3-4), 415-434.

Kaiser, P., McCreath, D.R., D.D.Tannant, 1996. Rockburst support handbook. Geomechanics Research Centre, Sudbury, Ontario, Canada.

Kanamori, H., 1978. Quantification of earthquakes. Nature 271, 411-414.

Kanamori, H., 1983. Magnitude scale and quantification of earthquakes. Tectonophysics 93 (3-4), 185-199.

Kanamori, H., Rivera, L., 2004. Static and dynamic scaling relations for earthquakes and their implications for rupture speed and stress drop. Bull. Seismol. Soc. Am. 94 (1), 314-319.

Kang, I.B., Chen, H.W., 2003. Wavefield simulation in general elastic and viscoelastic fractured media based upon the pseudo-spectral method. Terr Atmos Ocean Sci 14 (4), 487-504.

Kelly, R.J., 1976. Guidance accuracy considerations for microwave landing system. Ieee T Aero Elec Sys 12 (3), 428-428.

Kgarume, T., 2010. Masters Thesis. Mine aftershocks and implications for seismic hazard assessment. University of the Witwatersrand.

Komatitsch, D., 1997. Méthodes spectrales et éléments spectraux pour l'équation de l'élastodynamique 2D et 3D en milieu hétérogène. Ph.D. thesis, Institut de Physique du Globe de Paris.

Komatitsch, D., Barnes, C., Tromp, J., 2000. Simulation of anisotropic wave propagation based upon a spectral element method. Geophysics 65 (4), 1251-1260.

Komatitsch, D., Erlebacher, G., Göddeke, D., Michéa, D., 2010a. High-order finite-element seismic wave propagation modeling with MPI on a large GPU cluster. J. Comput. Phys. 229 (20), 7692-7714.

Komatitsch, D., Göddeke, D., Erlebacher, G., Michéa, D., 2010b. Modeling the propagation of elastic waves using spectral elements on a cluster of 192 GPUs. Comput Sci. Res Dev. 25 (1-2), 75-82.

Komatitsch, D., Michéa, D., Erlebacher, G., 2009. Porting a high-order finite-element earthquake modeling application to NVIDIA graphics cards using CUDA. J. Parallel Distrib. Comput. 69 (5), 451-460.

Komatitsch, D., Tromp, J., 1999. Introduction to the spectral element method for three-dimensional seismic wave propagation. Geophys. J. Int. 139 (3), 806-822.

Komatitsch, D., Tromp, J., 2002a. Spectral-element simulations of global seismic wave propagation - I. Validation. Geophys. J. Int. 149 (2), 390-412.

Komatitsch, D., Tromp, J., 2002b. Spectral-element simulations of global seismic wave propagation - II. Three-dimensional models, oceans, rotation and self-gravitation. Geophys. J. Int. 105 (1), 303-318.

Komatitsch, D., Tromp, J., 2003. A perfectly matched layer absorbing boundary condition for the second-order seismic wave equation. Geophys. J. Int. 154 (1), 146-153.

Komatitsch, D., Vilotte, J., 1998. The spectral element method: an efficient tool to simulate the seismic response of 2D and 3D geological structures. B Seismol Soc Am 88 (2), 368-392.

Komatitsch, D., Vilotte, J.P., Vai, R., Castillo-Covarrubias, J.M., Sanchez-Sesma, F.J., 1999. The spectral element method for elastic wave equations - Application to 2-D and 3-D seismic problems. Int J Numer Meth Eng 45 (9), 1139-1164.

Kondrat'yev, Y.V., Daragan, S.K., Lyuke, Y.I., Peregontseva, V.Y., 1984. The spectra of longitudinal and converted seismic waves as a function of underground explosion energy. Physics of the Solid Earth 20 (4), 262-268.

Konicek, P., Soucek, K., Stas, L., Singh, R., 2013. Long-hole destress blasting for rockburst control during deep underground coal mining. Int. J. Rock Mech. Min. Sci., 61, 141-153.

Kontoe, S., Zdravkovic, L., Potts, D.M., Menkiti, C.O., 2008. Case study on seismic tunnel response. Can. Geotech. J. 45 (12), 1743-1764.

Kontogianni, V.A., Stiros, S.C., 2005. Induced deformation during tunnel excavation: Evidence from geodetic monitoring. Eng Geol 79 (1-2), 115-126.

Kosloff, D.D., Baysal, E., 1982. Forward modeling by a fourier method. Geophysics 47 (10), 1402-1412.

Kristek, J., Moczo, P., Archuleta, R.J., 2002. Efficient methods to simulate planar free surface in the 3D 4(th)-order staggered-grid finite-difference schemes. Stud Geophys Geod 46 (2), 355-381.

Kristekova, M., 2006. Time-frequency analysis of seismic signals. PhD. Thesis. Geophysical Institute, Slovak Academy of Sciences, Bratislava.

Kwiatek, G., Plenkers, K., Dresen, G., 2011. Source parameters of picoseismicity recorded at Mponeng deep gold mine, South Africa: implications for scaling relations. B Seismol Soc Am 101 (6), 2592-2608.

Lamb, H., 1904. On the propagation of tremors over the surface of an elastic solid. Philos. Trans. Royal Soc. London, Ser. A 203, 1-42.

Larsson, K., 2004. Mining induced seismicity in Sweden. Ph.D. Thesis, Lulea University of Technology, Sweden.

Latham, J.P., Munjiza, A., Garcia, X., Xiang, J.S., Guises, R., 2008. Three-dimensional particle shape acquisition and use of shape library for DEM and FEM/DEM simulation. Miner Eng 21 (11), 797-805.

Lee, M.W., Balch, A.H., 1982. Theoretical seismic-wave radiation from a fluid-filled borehole. Geophysics 47 (9), 1308-1314.

Lee, S.J., Chan, Y.C., Komatitsch, D., Huang, B.S., Tromp, J., 2009. Effects of realistic surface topography on seismic ground motion in the Yangminshan region of Taiwan based upon the spectral-element method and LiDAR DTM. B Seismol Soc Am 99 (2A), 681-693.

Lenhardt, W.A., Pascher, C., 1996. The mechanism of mine-collapse deduced from seismic observations. Pure Appl Geophys 147 (2), 207-216.

Li, D., Helmberger, D., Clayton, R.W., Sun, D., 2014. Global synthetic seismograms using a 2-D finite-difference method. Geophys. J. Int, 1-18.

Li, R.P., Uren, N.F., McDonald, J.A., Urosevic, M., 2004. Recovery of elastic parameters for a multi-layered transversely isotropic medium. J Geophys Eng 1 (4), 327-335.

Li, X.F., Li, X.F., Zhang, M.G., 2007. Review of seismic wave numerical modeling methods. Chinese Journal of Disaster Prevention and Mitigation Engineering 27 (2), 241-248.

Lightfoot, N., Goldbach, O.D., Kullmann, D.H., Toper, A.Z., 1996. Rockburst control in the South African deep level gold mining industry. Rock Mechanics Tools and Techniques 1 and 2, 295-303.

Liu, E.R., Hudson, J.A., Pointer, T., 2000. Equivalent medium representation of fracture rock. J. Geoph. Res 105(b2), 2981-3000.

Liu, Q., 2006. Spectral-element simulations of 3D seismic wave propagation and applications to source and structural inversions. Ph.D thesis. California Institute of Technology, Pasadena, California.

Lorig, L.J., Brady, B.H.G., Cundall, P.A., 1986. Hybrid distinct element boundary element analysis of jointed rock. Int. J. Rock Mech. Min. Sci., 23 (4), 303-312.

Madariaga, R., 1976. Dynamics of an expanding circular fault. B Seismol Soc Am 66 (3), 639-666.

Maday, Y., Patera, A.T., 1989. Spectral element methods for the incompressibleNavier-Stokes equations. State of the Art Survey in Computational Mechanics, New York.

Mahabadi, O.K., Cottrell, B.E., Grasselli, G., 2010. An example of realistic modelling of rock dynamics problems: FEM/DEM simulation of dynamic brazilian test on barre granite. Rock Mech. Rock Eng. 43 (6), 707-716.

Mahtab, M., Goodman, R., 1970. Three-dimensional finite element analysis of jointed rock slopes. In: Proceeding of Second Congress of the International Society of Rock Mechanics, Belgrade, 3 353-360.

Mai, P.M., Beroza, G.C., 2000. Source scaling properties from finite-fault-rupture models. B Seismol Soc Am 90 (3), 604-615.

Malan, D., 2002. Manuel Rocha medal recipient simulating the time-dependent behaviour of excavations in hard rock. Rock Mech. Rock Eng. 35 (4), 225-254.

Mandal, B., Toksoz, M.N., 1991. Effects of an explosive source in an anisotropic medium. Explosion Source Phenomenology 65, 261-268.

Mangriotis, M.D., Rector, J.W., Herkenhoff, E.F., Neu, J.C., 2013. Scattering versus intrinsic attenuation in the vadose zone: A VSP experiment. Geophysics 78 (2), B49-B63.

Marfurt, K.J., 1984. Accuracy of finite-difference and finite-element modeling of the scalar and elastic wave equations. Geophysics 49 (5), 533-549.

Martin, C.D., Kaiser, P., Christiansson, R., 2003. Stress, instability and design of underground excavations. Int. J. Rock Mech. Min. Sci., 40 (7-8), 1027-1047.

Martin, R., Komatitsch, D., 2006. An optimized convolution-perfectly matched layer (C-PML) absorbing technique for 3D seismic wave simulation based on a finite-difference method. Geophys. Res. Abstr 8, 03988.

Martin, R., Komatitsch, D., Gedney, S.D., Bruthiaux, E., 2010. A high-order time and space formulation of the unsplit perfectly matched layer for the seismic wave equation using Auxiliary Differential Equations (ADE-PML). Cmes-Comp Model Eng 56 (1), 17-41.

Maxwell, S., Young, R., Read, R., 1998. A micro-velocity tool to assess the excavation damaged zone. In: Proceeding of International Journal of Rock Mechanics and Mining Sciences and Geomechanics Abstracts, 35 235-247.

Maxwell, S.C., Young, R.P., 1995. A controlled in-situ investigation of the relationship between stress, velocity and induced Seismicity. Geophys Res Lett 22 (9), 1049-1052.

McCalpin, J.P., 2012. Paleoseismology. Environ Eng Geosci 18 (3), 311-312.

McGarr, A., 1971. Violent deformation of rock near deep-level, tabular excavations—seismic events. B Seismol Soc Am 61 (5), 1453-1466.

McGarr, A., 1984. Scaling of ground motion parameters, state of stress, and focal depth. J. Geophys. Res. 89 (B8), 6969-6979.

McGarr, A., 1992a. An implosive component in the seismic moment tensor of a mining-induced tremor. Geophys Res Lett 19 (15), 1579-1582.

McGarr, A., 1992b. The leighton, fred memorial workshop on mining induced seismicity (Montreal, August 30, 1987) - Introduction. Pure Appl Geophys 139 (3-4), 347-348.

McGarr, A., 1992c. Moment tensors of 10 Witwatersrand mine tremors. Pure and Applied Geophys 139 (3-4), 781-800.

McGarr, A., 1994. Some comparisons between mining-induced and laboratory earthquakes. Pure and Applied Geophysics 142 (3-4), 467-489.

McGarr, A., 2005. Observations Concerning Diverse Mechanisms for Mining-Induced Earthquakes. In: Proceeding of Rasim6: Controlling Seismic Risk, 107-111.

McGarr, A., Spottiswoode, S., Gay, N., 1975. Relationship of mine tremors to induced stresses and to rock properties in the focal region. B Seismol Soc Am 65 (4), 981-993.

McGarr, A., Spottiswoode, S., Gay, N., Ortlepp, W., 1979. Observations relevant to seismic driving stress, stress drop, and efficiency. J. Geophys. Res: Solid Earth (1978–2012) 84 (B5), 2251-2261.

McLaughlin, K.L., Bonner, J.L., Barker, T., 2004. Seismic source mechanisms for quarry blasts: modelling observed Rayleigh and Love wave radiation patterns from a Texas quarry. Geophys J Int 156 (1), 79-93.

Meglis, I., Greenfield, R., Engelder, T., Graham, E., 1996. Pressure dependence of velocity and attenuation and its relationship to crack closure in crystalline rocks. J. Geophys. Res. 101 (B8), 17,523-533.

Milev, A.M., Spottiswoode, S.M., 2005. Strong ground motion and site response in deep South African mines. S. Afr. Inst. Min. Metall., 7 (105), 515-524.

Milev, A.M., Spottiswoode, S.M., Stewart, R.D., 1999. Dynamic response of the rock surrounding deep level mining excavations. In: Proceeding of 9th ISRM, Paris, 1109-1114.

Miyake, H., Iwata, T., Irikura, K., 2003. Source characterization for broadband ground-motion simulation: Kinematic heterogeneous source model and strong motion generation area. B Seismol Soc Am 93 (6), 2531-2545.

Mizutani, H., Geller, R.J., Takeuchi, N., 2000. Comparison of accuracy and efficiency of time-domain schemes for calculating synthetic seismograms. Phys Earth Planet In 119 (1-2), 75-97.

Moczo, P., Kristek, J., Galis, M., Pazak, P., Balazovjech, M., 2007a. The finite-difference and finite-element modeling of seismic wave propagation and earthquake motion. Acta Phys Slovaca 57 (2), 177-406.

Moczo, P., Robertsson, J.O.A., Eisner, L., 2007b. The finite-difference time-domain method for modeling of seismic wave propagation. Advances in Geophysics 48, 421-516.

Morency, C., Tromp, J., 2008. Spectral-element simulations of wave propagation in porous media. Geophys. J. Int. 175 (1), 301-345.

Motazedian, D., Atkinson, G.M., 2005. Stochastic finite-fault modeling based on a dynamic corner frequency. B Seismol Soc Am 95 (3), 995-1010.

Mukherjee, Y.X., Mukherjee, S., Shi, X.L., Nagarajan, A., 1997. The boundary contour method for three-dimensional linear elasticity with a new quadratic boundary element. Eng Anal Bound Elem 20 (1), 35-44.

Nagarajan, A., Mukherjee, S., Lutz, E., 1996. The boundary contour method for three-dimensional linear elasticity. J Appl Mech-T Asme 63 (2), 278-286.

Nuttli, O.W., 1973. Seismic wave attenuation and magnitude relations for eastern North America. J. Geophys. Res. 78 (5), 876-885.

Nuttli, O.W., Kim, S.G., 1974. Surface-wave magnitude determination from global network of very-long period seismographs. Eos T Am Geophys Un 55 (4), 360-360.

Ogasawara, H., 2002. A review of the semi-controlled earthquake generation experiment in South African deep gold mines, in Seismogenic Process Monitoring, edited by H. Ogasawara, T. Yanagidani, and M. Ando, pp. 119-150, A.A. Balkema, Brookfield, Vt.

Oliveira, S.P., Seriani, G., 2011. Eect of element distortion on the numerical dispersion of spectral element methods. Commun Comput Phys 9 (4), 937-958.

Ortlepp, W., 1997. Rock fracture and rockbursts-an illustrative study. Monograph Series M9. South African institude of mining and metalurgy, Johannesbury, South Africa.

Ortlepp, W., Stacey, T., 1994. Rockburst mechanisms in tunnels and shafts. Tunnell. Underground Space Technol. 9 (1), 59-65.

Owen, G.N., Scholl, R.E., 1981. Earthquake engineering of large underground structures. Report no. FHWA/RD-80/195. Federal Highway Administration and National Science Foundation.

Pan, E., Amadei, B., Kim, Y.I., 1998. 2-D BEM analysis of anisotropic half-plane problems - application to rock mechanics. Int. J. Rock Mech. Min. Sci., 35 (1), 69-74.

Pan, E.N., Chen, C.S., Amadei, B., 1997. A BEM formulation for anisotropic half-plane problems. Eng Anal Bound Elem 20 (3), 185-195.

Patera, A.T., 1984. A spectral element method for fluid-dynamics - laminar-flow in a channel expansion. J Comput Phys 54 (3), 468-488.

Penzien, J., 2000. Seismically induced racking of tunnel linings. Earthquake Eng. Struct. Dyn. 29 (5), 683-691.

Peter, D., Komatitsch, D., Luo, Y., Martin, R., Le Goff, N., Casarotti, E., Le Loher, P., Magnoni, F., Liu, Q., Blitz, C., 2011a. Forward and adjoint simulations of seismic wave propagation on fully unstructured hexahedral meshes. Geophys J Int 186 (2), 721-739.

Peter, D., Komatitsch, D., Luo, Y., Martin, R., Le Goff, N., Casarotti, E., Le Loher, P., Magnoni, F., Liu, Q., Blitz, C., Nissen-Meyer, T., Basini, P., Tromp, J., 2011b. Forward and adjoint simulations of seismic wave propagation on fully unstructured hexahedral meshes. Geophys J Int 186 (2), 721-739.

Phan, A.V., Mukherjee, S., 2008. Boundary contour method fracture analysis of bimaterial interface cracks. Commun Numer Meth En 24 (12), 1685-1697.

Potvin, Y., Hudyma, M., Jewell, R., 2000. Rockburst and seismic activity in underground Australian mines-an introduction to a new research project. In: Proceeding of ISRM International Symposium.

Potvin, Y., Wesseloo, J., 2013. Towards an understanding of dynamic demand on ground support. S. Afr. Inst. Min. Metall., 113 (12), 913-922.

Prikryl, R., Klima, K., Lokajicek, T., Pros, Z., 2005. Non-linearity in multidirectional P-wave velocity: confining pressure behaviour based on real 3D laboratory measurements, and its mathematical approximation. Petrophysical Properties of Crystalline Rocks 240, 323-334.

Puente, J.d.l., Ampuero, J.P., Käser, M., 2009. Dynamic rupture modeling on unstructured meshes using a discontinuous Galerkin method. J. Geophys. Res. Solid Earth (1978-2002) 114 (B10).

Puente, J.d.l., Käser, M., Dumbser, M., Igel, H., 2007. An arbitrary high-order discontinuous Galerkin method for elastic waves on unstructured meshes. Geophys. J. Int. 169, 1210-1228.

Pyrak-Nolte, L.J., Myer, L.R., Cook, N.G.W., 1990a. Anisotropy in seismic velocities and amplitudes from multiple parallel fractures. Geophys. Res B7, 11,345-311,358.

Pyrak-Nolte, L.J., Myer, L.R., Cook, N.G.W., 1990b. Transmission of seismic waves across single natural fractures. Geophys. Res. 95 (B6), 8617-8638.

Qian, S., 2002. Introduction to time-frequency and wavelet transforms. Prentice-Hall.

Rebetskii, Y.L., 2005. Tectonic stress, metamorphism, and earthquake source model. Dokl Earth Sci 400 (1), 127-131.

Ricciardello, A., Puccio, L., Caserta, A., 2011. 3D Reassessment of the Classical Garvin's Problem. Communications in Applied and Industrial Mathematics 2 (2).

Richardson, E., Jordan, T.H., 2002. Seismicity in deep gold mines of South Africa: Implications for tectonic earthquakes. B Seismol Soc Am 92 (5), 1766-1782.

Rizk, K., Wagen, J.-F., Gardiol, F., 1997. Two-dimensional ray-tracing modeling for propagation prediction in microcellular environments. Vehicular Technology, IEEE Transactions on 46 (2), 508-518.

Rizzo, F., Shippy, D., Rezayat, M., 1985. A boundary integral equation method for radiation and scattering of elastic waves in three dimensions. International journal for numerical methods in engineering 21 (1), 115-129.

Romanowicz, B., Mitchell, B.J., 2007. Deep earth structure - Q of the earth from crust to core, in seismology and structure of the earth, edited by B. Romanowicz and A. Dziewonski, pp: 731-774, Elsevier, Amsterdam.

Roth, A., Ranta-Korpi, R., 2007. Numerical modeling and dynamic simulation of high-tensile steel wire mesh for ground support under rockburst loading. Rock Mechanics: Meeting Society's Challenges and Demands 1 and 2, 1505-1509.

Rousseau, J., Frangin, E., Marin, P., Daudeville, L., 2008. Damage prediction in the vicinity of an impact on a concrete structure: a combined FEM/DEM approach. Comput Concrete 5 (4), 343-358.

Šílený, J., Milev, A., 2008. Source mechanism of mining induced seismic events—resolution of double couple and non double couple models. Tectonophysics 456 (1), 3-15.

Sánchez-Sesma, F.J., Iturrarán-Viveros, U., Kausel, E., 2013. Garvin's generalized problem revisited. Soil Dynamics and Earthquake Engineering 47, 4-15.

Saenger, E.H., Shapiro, S.A., Keehm, Y., 2005. Seismic effects of viscous Biot-coupling: Finite difference simulations on micro-scale. Geophys Res Lett 32 (14).

Sainoki, A., Mitri, H., 2014. Simulating intense shock pulses due to asperities during fault-slip. J Appl Geophys 103, 71-81.

Salamon, M.D.G., 1981. Rockburst phenomena in the gold-mines of the Witwatersrand - a Review. T I Min Metall A 90 (Oct), A212-A213.

Sato, H., Fehler, M.C., 1998. Seismic wave propagation and scattering in the heterogeneous Earth. Springer-Verlag, New York.

Sato, H., Fehler, M.C., Maeda, T., 2012. Seismic wave propagation and scattering in the heterogeneous earth: Second Edition. Springer.

Savage, B., Komatitsch, D., Tromp, J., 2010. Effects of 3D attenuation on seismic wave amplitude and phase measurements. B Seismol Soc Am 100 (3), 1241-1251.

Sayers, C.M., Kachanov, M., 1991. A Simple technique for finding effective elastic-constants of cracked solids for arbitrary crack orientation statistics. Int. J. Solids Struct 27 (6), 671-680.

Schoenberg, M., 1980. Elastic wave behaviour across linear slip interfaces. Acoust. Soc. Am 68 (5), 1516-1521.

Seriani, G., Oliveira, S.P., 2008. Dispersion analysis of spectral-element methods for elastic wave propagation. Wave Motion 45 (6), 729-744.

Seriani, G., Priolo, E., Pregarz, A., 1995. Modelling waves in anisotropic media by a spectral element method. In: Proceeding of Third International Conference on Mathematical and Numerical Aspects of Wave Propagation, 289-298.

Seriani, G., Su, C., 2012. Wave propagation modeling in highly heterogeneous media by a poly-grid chebyshev spectral element method. J Comput Acoust 20 (2).

Shi, G.H., 1988. Discontinuous deformation analysis---a new model for the statics and dynamics of block systems. Ph. D. thesis, University of California, Berkeley.

Silva, B.G.d., Einstein, H.H., 2013. Modeling of crack initiation, propagation and coalescence in rocks. Int J Fracture 182 (2), 167-186.

Simser, B., Joughin, W.C., Ortlepp, W.D., 2002. The performance of Brunswick Mine's rockburst support system during a severe seismic episode. J S Afr I Min Metall 102 (4), 217-223.

Sochacki, J., Kubichek, R., George, J., Fletcher, W.R., Smithson, S., 1987. Absorbing boundary-conditions and surface-waves. Geophysics 52 (1), 60-71.

Sonley, E., Atkinson, G.M., 2005. Empirical relationship between moment magnitude and Nuttli magnitude for small-magnitude earthquakes in southeastern Canada. Seismological Research Letters 76 (6), 752-755.

SPECFEM2D, 2012. Manual (*version 7.0*). http://geodynamics.org/cig/software/specfem2d/specfem2d-manual.pdf.

SPECFEM3D, 2014. Manual (*version 2.1*). http://geodynamics.org/cig/software/specfem2d/specfem2d-manual.pdf.

Spottiswoode, S., McGarr, A., 1975. Source parameters of tremors in a deep-level gold mine. B Seismol Soc Am 65 (1), 93-112.

St John, C.M., Zahrah, T.F., 1987. A seismic design of underground structures. Tunnell. Underground Space Technol. 2 (2), 165-197.

Stacey, R., 1988. Improved transparent boundary formulations for the elastic-wave equation. B Seismol Soc Am 78 (6), 2089-2097.

Stacey, T.R., Ortlepp, W.D., 2000. Support appropriate for dynamic loading and large static loading in block cave mining openings. Australas I Min Met 2000 (7), 783-789.

Stein, S., Wysession, M., 2003. An introduction to seismology, earthquakes, and earth Strucutre. Oxford: Blackwell.

Stein, S., Wysession, M., 2009. An introduction to seismology, earthquakes, and earth structure. John Wiley & Sons.

Stickney, M.C., Sprenke, K.F., 1993. Seismic events with implosional focal mechanisms in the Coeur-Dalene mining district, Northern Idaho. J Geophys Res-Sol Ea 98 (B4), 6523-6528.

Tajdus, A., Flisiak, J., Cala, M., 1997. Estimation of rockburst hazard basing on 3D stress field analysis. Rockbursts and Seismicity in Mines, 273-277.

Tang, L.Z., Xia, K.W., 2010. Seismological method for prediction of areal rockbursts in deep mine with seismic source mechanism and unstable failure theory. J Cent South Univ T 17 (5), 947-953.

Tannant, D.D., McDowell, G.M., Brummer, R.K., Kaiser, P.K., 1993. Ejection velocities measured during a rockburst simulation experiment. In: Proceeding of the 3rd International Symposium on Rockbursts and Seismicity in Mines, 129-133.

Thomsen, L., 1986. Weak elastic-anisotropy. Geophysics 51 (10), 1954-1966.

Towhata, I., 2008. Geotechnical earthquake engineering. Springer Science & Business Media.

Trifu, C.I., 2001. The evaluation of failure components using the seismic moment tensor inversion. Rock Mechanics in the National Interest 1 and 2, 1335-1341.

Triviño, L.F., Mohanty, B., Milkereit, B., 2012. Seismic waveforms from explosive sources located in boreholes and initiated in different directions. J Appl Geophys 87, 81-93.

Tromp, J., Komatitsch, D., Liu, Q.Y., 2008. Spectral-element and adjoint methods in seismology. Commun Comput Phys 3 (1), 1-32.

Tshering, T., 2011. M.Sc. Thesis, The impact of earthquakes on tunnels in different rock mass quality Q. University of Oslo, Norway.

Udias, A., 1999. Principles of seismology. Cambridge University Press, Cambridge,UK.

Uhrhammer, R.A., Hellweg, M., Hutton, K., Lombard, P., Walters, A.W., Hauksson, E., Oppenheimer, D., 2011. California Integrated Seismic Network (CISN) local magnitude determination in California and vicinity. B Seismol Soc Am 101 (6), 2685-2693.

Vavrycuk, V., 2008. Velocity, attenuation, and quality factor in anisotropic viscoelastic media: A perturbation approach. Geophysics 73 (5), D63-D73.

Virieux, J., 1984. SH-wave propagation in heterogeneous media - velocity-stress finite-difference method. Geophysics 49 (11), 1933-1942.

Virieux, J., 1986. P-SV wave propagation in heterogeneous media: velocity-stress finite-difference method. Geophysics 51 (4), 889-901.

Wang, C.L., Wu, A.X., Liu, X.H., Ji, X.W., Li, X., Yan, Q.W., Huang, X.G., Hou, X.B., 2009. Mechanisms of microseismic events occurred in a deep hard-rock mine of China. In: Proceeding of 7th International Symposium on Rockburst and Seismicity in Mines (Rasim7): Controlling Seismic Hazard and Sustainable Development of Deep Mines, 1 and 2 245-250.

Wang, Q., Ji, S., Salisbury, M., Xia, B., Pan, M., Xu, Z., 2005. Shear wave properties and Poisson's ratios of ultrahigh-pressure metamorphic rocks from the Dabie-Sulu orogenic belt, China: Implications for crustal composition. J. Geophys. Res. Solid Earth (1978-2012) 110 (B8).

Wang, S.R., Zhang, H.Q., Liu, P.P., Jia, H.H., 2010. Research on the energy dissipation and stress distribution characteristics of the excavated circular tunnel under high stress conditions. Rock Stress and Earthquakes, 561-565.

Wang, T.T., Hsu, J.T., Chen, C.H., Huang, T.H., 2014. Response of a tunnel in double-layer rocks subjected to harmonic P- and S-waves. Int. J. Rock Mech. Min. Sci. 70, 435-443.

Wang, W., Wang, T., Su, J., Lin, C., Seng, C., Huang, T., 2001a. Assessment of damage in mountain tunnels due to the Taiwan Chi-Chi Earthquake. Tunnell. Underground Space Technol. 16 (3), 133-150.

Wang, X., Cai, M., 2014. Wave propagation simulation in underground mines by SPECFEM2D. In: Proceeding of the seventh international conference on deep and high stress mining, Sudbury, 723-738.

Wang, X., Cai, M., 2015. Influence of wavelength-to-excavation span ratio on ground motion around deep underground excavations. Tunnell. Underground Space Technol. 49, 438-453.

Wang, Y.B., Takenaka, H., Furumura, T., 2001b. Modelling seismic wave propagation in a two-dimensional cylindrical whole-earth model using the pseudospectral method. Geophys J Int 145 (3), 689-708.

Wei, L., Hudson, J.A., 1988. A hybrid discrete-continuum approach to model hydro-mechanical behaviour of jointed rocks. Eng Geol 49 (317-325).

Wells, D.L., Coppersmith, K.J., 1994. New empirical relationships among magnitude, rupture length, rupture width, rupture area, and surface displacement. B Seismol Soc Am 84 (4), 974-1002.

Wepfer, W., Christensen, N., 1991. A seismic velocity-Confining pressure relation, with application. Int. J. Rock Mech. Min. Sci. Abstr 28, 451-456.

Williams, J., Mustoe, G., 1987. Modal methods for the analysis of discrete systems. Comput Geotech 4, 1-19.

Wright, C., Kijko, A.J., Linzer, L.M., Smith, M., 2003. Recent research in earth structure, earthquake and mine seismology, and seismic hazard evaluation in South Africa. S Afr J Sci 99 (7-8), 389-394.

Wu, R.S., 1996. Synthetic seismograms in heterogeneous media by one-return approximation. Pure and Applied Geophys 148, 155–173.

Wu, R.S., Aki, K., 1985. Scattering characteristics of waves by an elastic heterogeneity. Geophysics 50, 582–595.

Xiao, H., He, X., Feng, T., Wang, E., 2005. Research on coupling laws between EME and stress fields during deformation and fracture of mine tunnel excavation based on FLAC (2 D). Chin. J. Rock Mech. Eng. 24 (13), 2304-2309.

Yamada, T., Mori, J.J., Ide, S., Abercrombie, R.E., Kawakata, H., Nakatani, M., Iio, Y., Ogasawara, H., 2007. Stress drops and radiated seismic energies of microearthquakes in a South African gold mine. J. Geophys. Res. Solid Earth (1978–2012) 112 (B3).

Yamada, T., Mori, J.J., Ide, S., Kawakata, H., Iio, Y., Ogasawara, H., 2005. Radiation efficiency and apparent stress of small earthquakes in a South African gold mine. J. Geophys. Res. 110 (B01305).

Yang, D.H., Zhang, Z.J., 2000. Effects of the Biot and the squirt-flow coupling interaction on anisotropic elastic waves. Chinese Sci Bull 45 (23), 2130-2138.

Yang, J., Liu, T., Tang, G., Hu, T., 2009. Modeling seismic wave propagation within complex structures. Applied Geophysics 6 (1), 30-41.

Yoshimitsu, N., Kawakata, H., Yamamoto, A., Ogasawara, H., Iio, Y., 2012. Temporal changes in attenuation of S waves through a fault zone in a South African gold mine. Geophys J Int 191 (3), 1317-1324.

Yu, Q., Tanaka, M., Ohnishi, Y., 1999. An inverse method for the model of water flow in discrete fracture network. Proceedings of the 34th Janan National Conference on Geotechnical Engineering,Tokyo, 1303-1314.

Zhang, J., Fu, B., 2008. Rockburst and its criteria and control. Chin. J. Rock Mech. Eng 27 (10), 2034-2042.

Zhao, X., Cai, M., 2010a. Influence of plastic shear strain and confinement-dependent rock dilation on rock failure and displacement near an excavation boundary. Int. J. Rock Mech. Min. Sci., 47 (5), 723-738.

Zhao, X.G., Cai, M., 2010b. A mobilized dilation angle model for rocks. Int. J. Rock Mech. Min. Sci., 47 (3), 368-384.

Zhu, J.B., Deng, X.F., Zhao, X.B., Zhao, J., 2012. A numerical study on wave transmission across multiple intersecting joint sets in rock masses with UDEC. Rock Mech. Rock Eng. 46, 1429-1442.

Zimmerman, R., Bodvarsson, G., 1996. Effective transmissivity of two-dimensional fracture networks. Int J Rock Mech Min Sci Geomech Abstr 33 (4), 433-446.

Appendix A: Additional modeling results

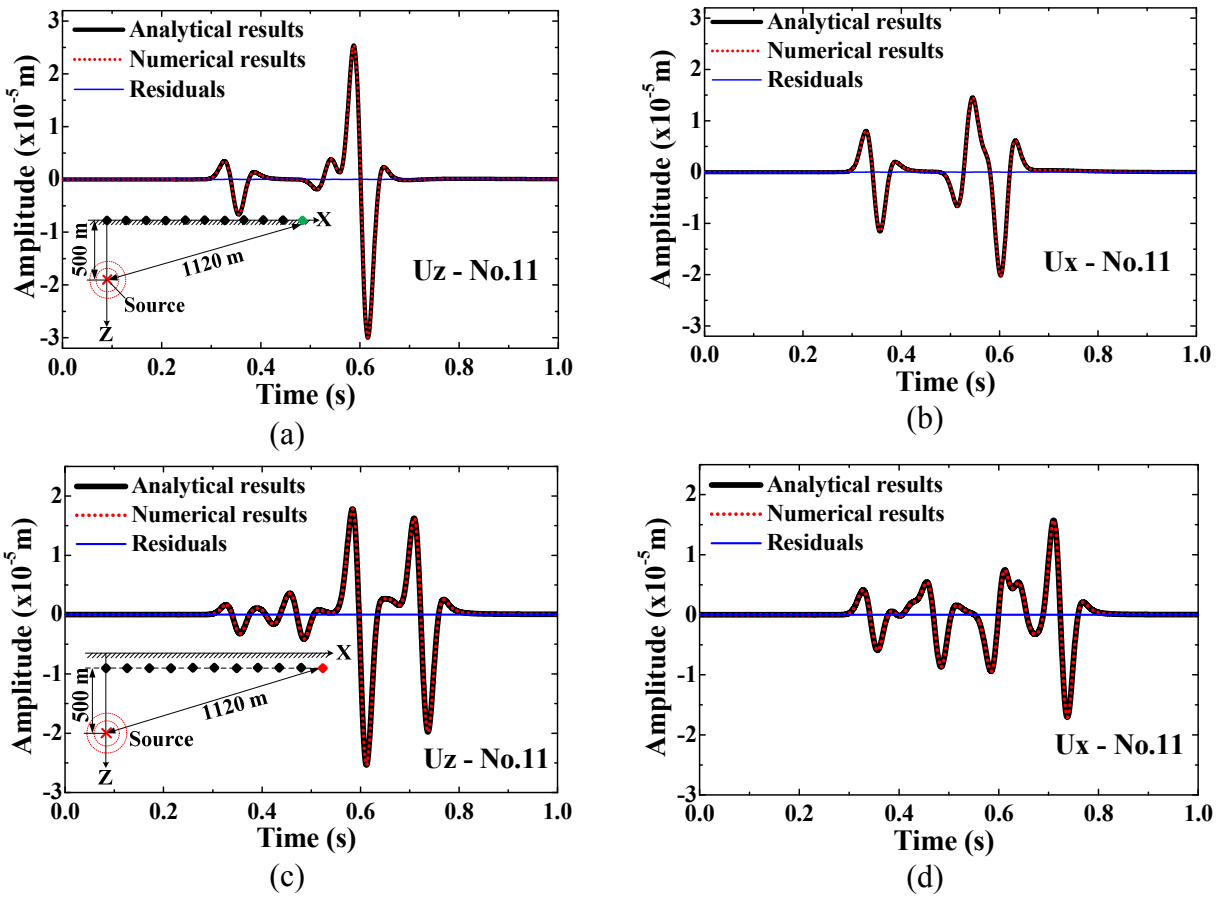

Figure A - 1: Seismograms of displacement for receiver No.11 in the two validation cases. No.11 is placed at the free surface/inside the model for cases A and B, which is shown as green/red dot in the small insert in the lower-right of (a) and (c), respectively. Components of vertical (U_z) and horizontal (U_x) displacements are shown in (a) and (c) for cases A and B, (b) and (d) for cases A and B, respectively. The modeling results (red dot line) are plotted against the analytical solutions (black solid line), and the absolute residuals (blue solid line) are displayed in the same plot.

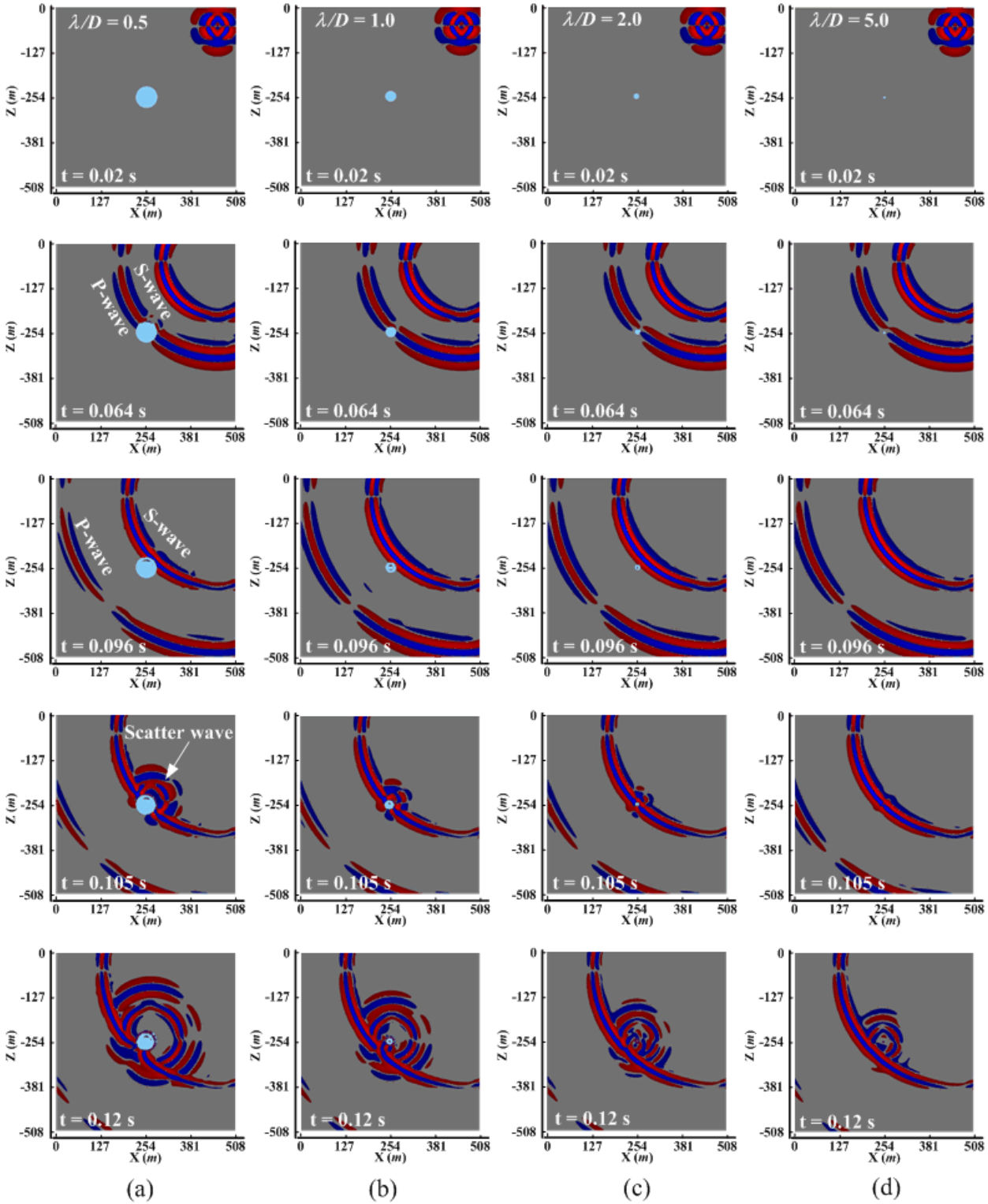

Figure A - 2: Snapshots of the vertical velocity field for the circular-shape excavation at 0.02, 0.064, 0.096, 0.105 and 0.12 s for models with λ/D ratios of 0.5 (a), 1 (b), 2 (c), and 5 (d), respectively. The positive (upward movement) and negative (downward movement) vertical velocities are denoted by red and blue, respectively.

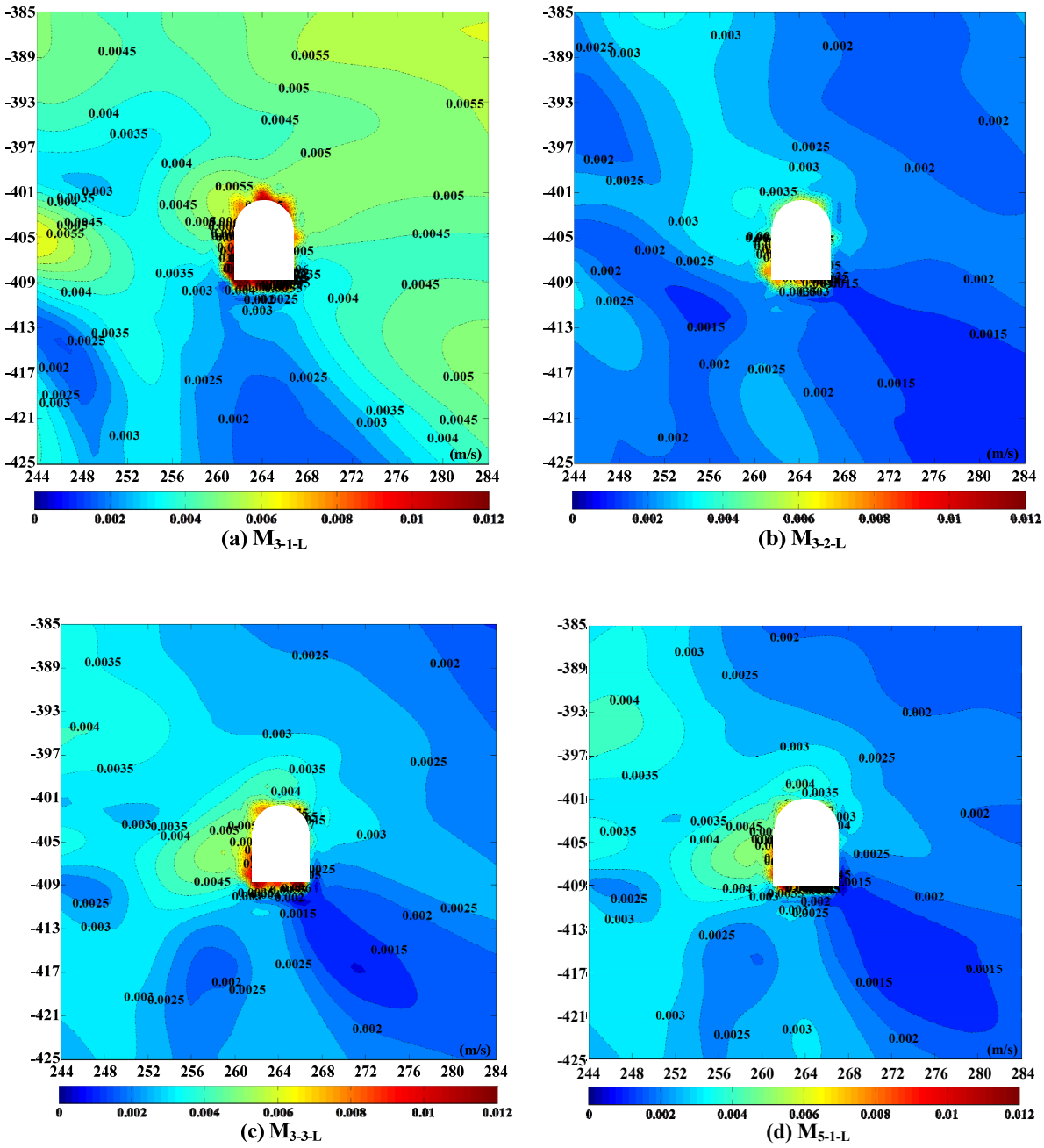

Figure A - 3: PPV contours around tunnel T1 at different mining stages when the source is located at the left up corner side of the model. (a), (b), (c), and (d) present PPV contours at the three mining stages and multiple openings case. All contours have the same color scale: 0.000 – 0.012 m/s.

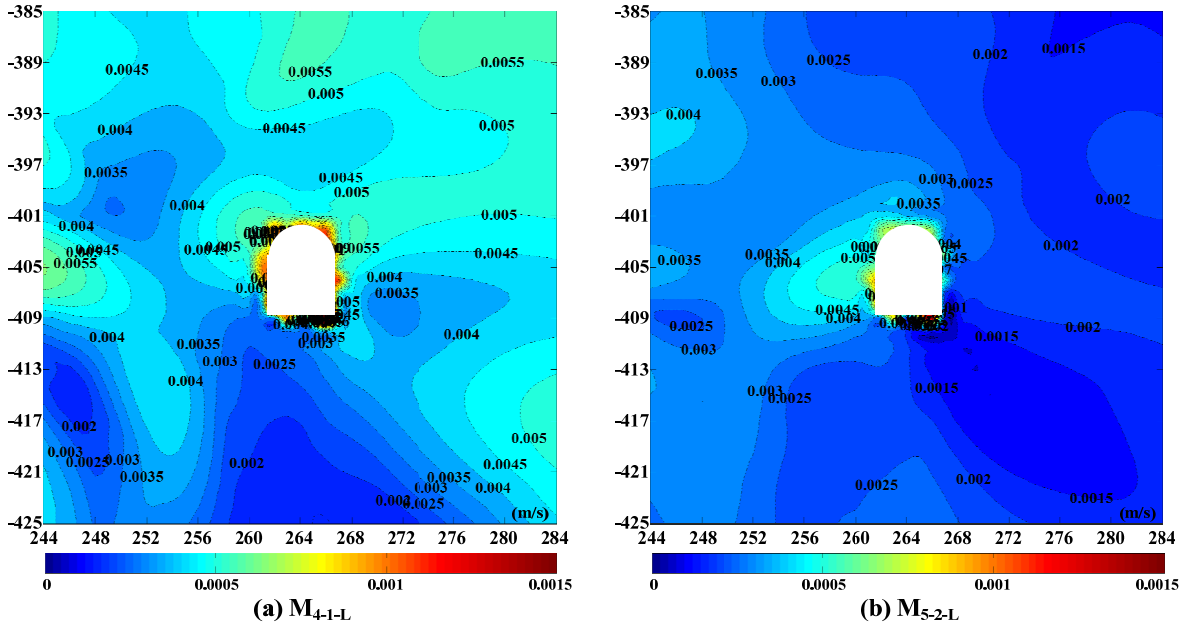

Figure A - 4: PPV contours around tunnel T1 in the dyke model and model with multiple openings and dyke, with the seismic source located in the left up corner of the model. PPV contour in the dyke model (a), and PPV contour in the dyke model with multiple openings (b).

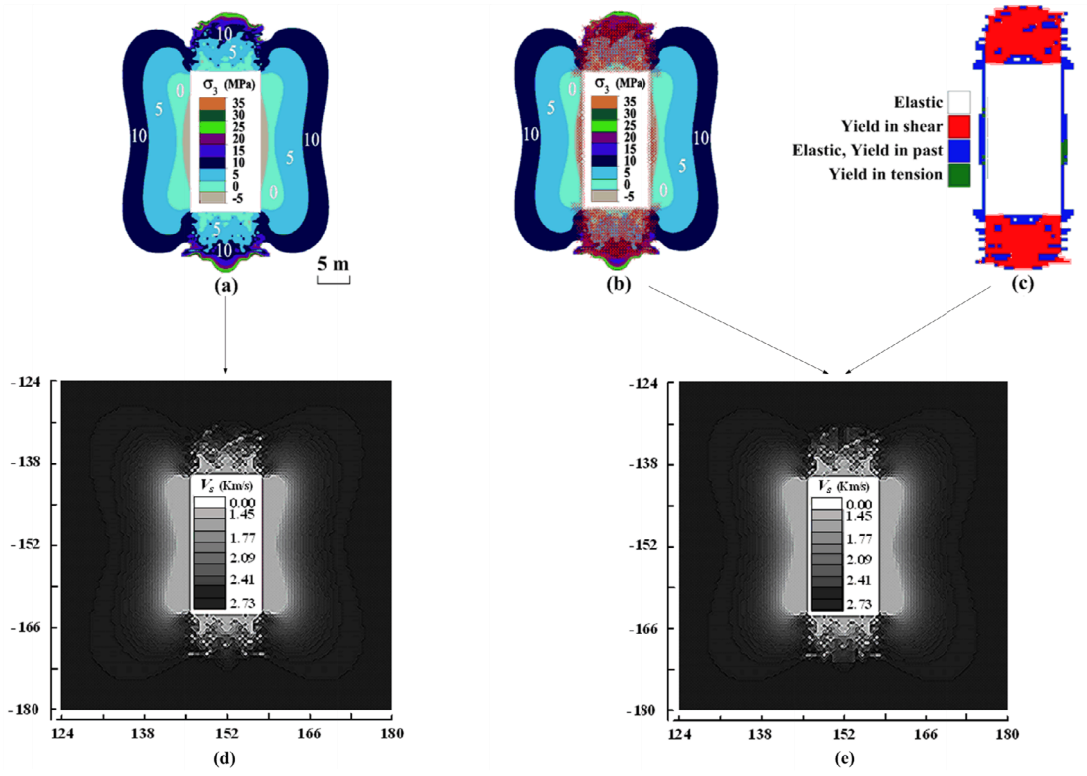

Figure A - 5: Modeling results with $Q_c = 4$. Distributions of confinement (a), confinement and failure zone (b), and the extent and depth of failure zone (c) around the stope in the FLAC model. The corresponding non-uniform shear wave velocity distributions in the SPECFEM2D model are shown in (d) and (e), which consider the influence of only confinement (d) and both confinement and failure zone (e) on wavefields.

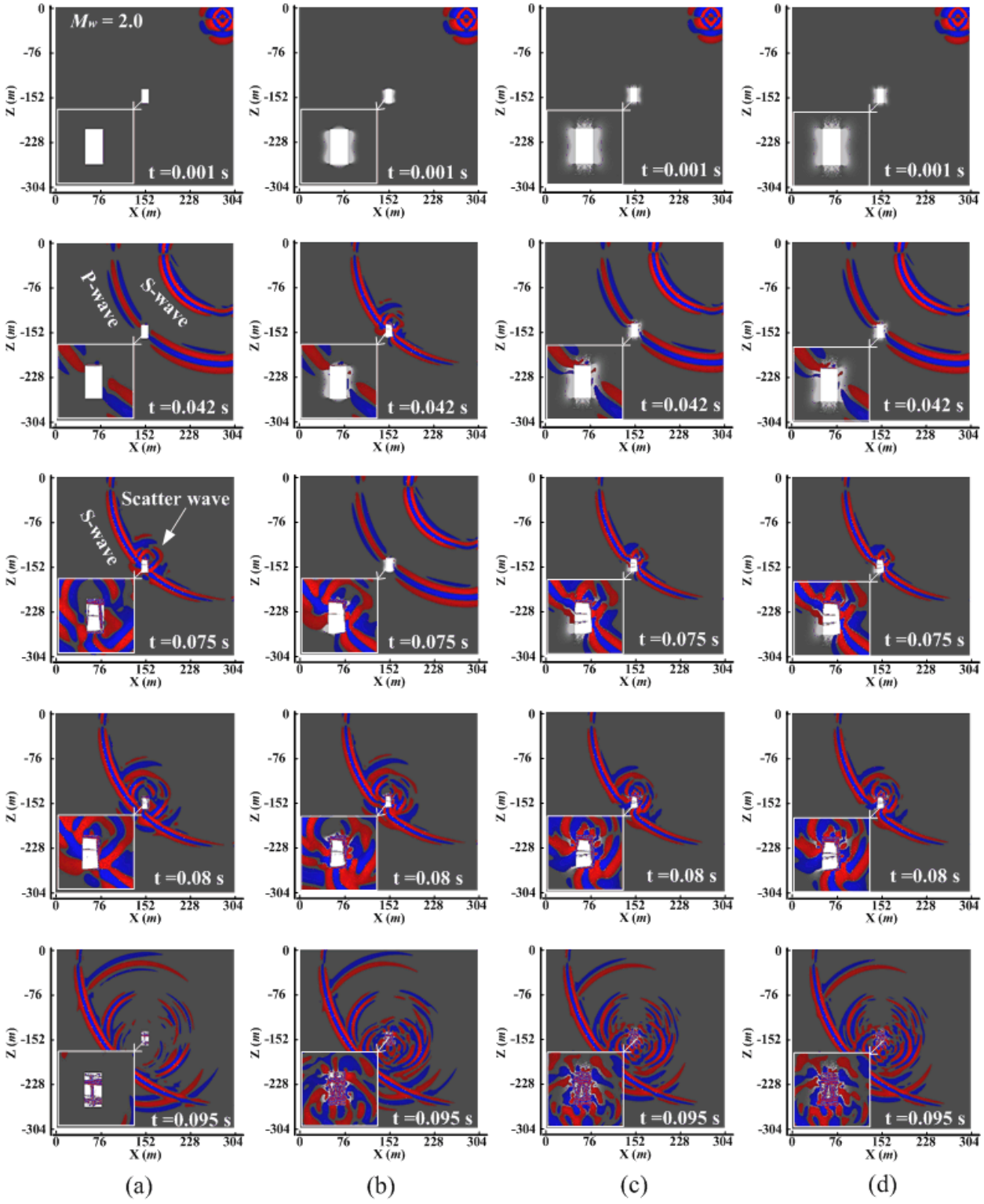

Figure A - 6: Snapshots of the vertical velocity component at 0.001, 0.042, 0.075, 0.08 and 0.095 s for velocity Model I (a), Model II (b), Model III (c), and Model IV (d) with Q_c = 4. The small insert at the lower-left corner show the details of the wavefield around the stope. Positive (upward movement) and negative (downward movement) values of the vertical velocity component are represented by red and blue, respectively.

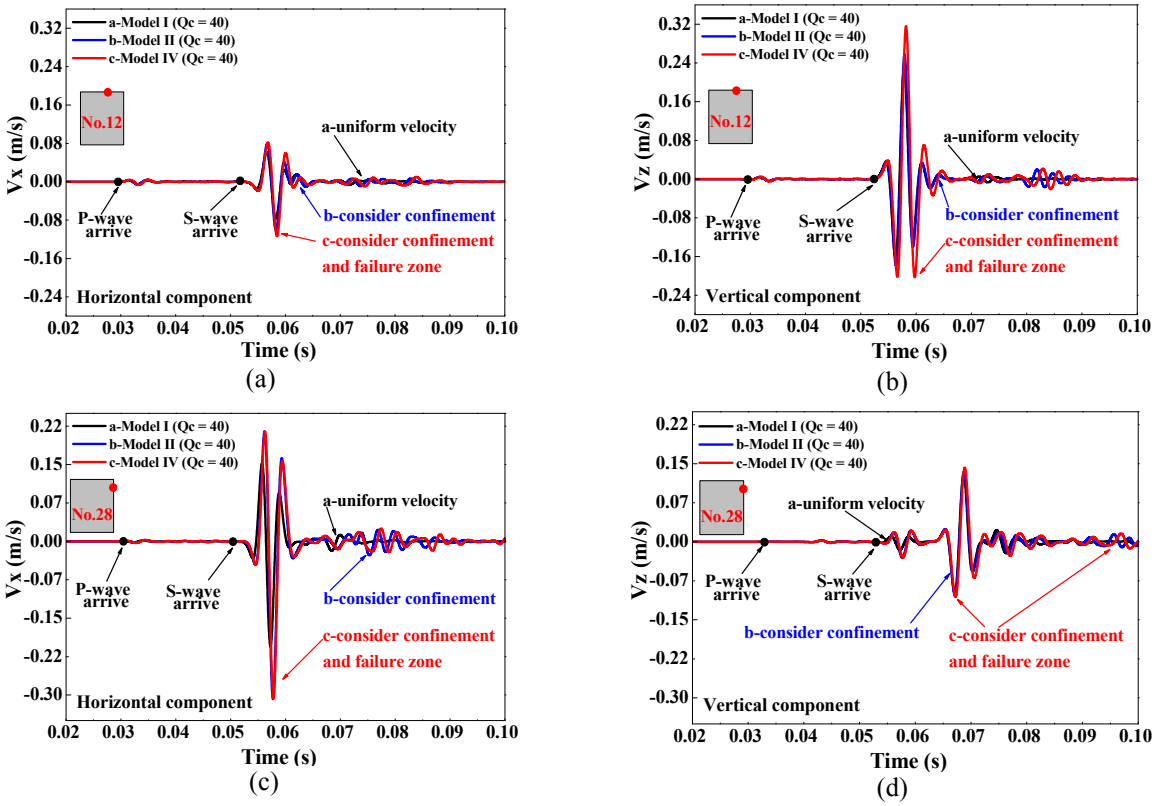

Figure A - 7: Synthetic seismograms at receivers No.12 and No.28 for the uniform and non-uniform velocity models (for Q_c = 40). Horizontal (V_x) and vertical (V_z) velocity components of receivers No.12 and No.28 are shown in (a) and (b) and (c) and (d), respectively. The receiver locations are denoted by the red dot in the upper-left inserts.

Appendix B: Magnitudes of seismic event

B.1 Magnitude scales

B.1.1 M_L - Local (or Richter) magnitude

Richter magnitude (M_L) was the first instrumental magnitude proposed and it is widely used in the field of earthquake engineering. This scale is based on the amplitude (unit: mm) of the largest seismogram wave trace on a Wood-Anderson seismograph, normalized to 100.0 km of a standard epicentral distance. The following equation can be used to calculate M_L (Gutenberg and Richter, 1956; Uhrhammer et al., 2011)

$$M_L = \log(A_p / T_d) + F_c(H, r) + C_s + C_r \tag{B.1}$$

where A_p (mm) is the peak amplitude of the recorded signal, T_d (s) is the dominant period, F_c is a correction for variation of amplitude with the earthquake's depth H (m) and distance r (m) from the seismometer, C_s and C_r are correction factors for the site and the receiver, respectively. Normally, if the local magnitude is lower than M_L = 6.5, it can reflect accurately the amount of seismic energy released from an earthquake. However, the local magnitude scale will progressively underestimate actual energy release and will not be appropriate once the magnitude surpass this threshold. This phenomenon is known as the "saturation" of the Richter magnitude scale, and more details about the topic can be found in Lomnitzadler and Lomnitz (1979) and Holschneider *et al.* (2011).

B.1.2 M_N - Nuttli magnitude

Nuttli magnitude (M_N) is a version of the Richter scale specifically for use in eastern North America (Nuttli, 1973). The Nuttli magnitude scale is based on the maximum amplitude of the Rayleigh surface waves for a frequency of 1 Hz. M_N is determined by

$$M_N = \log(\frac{A_p}{2}) + 1.66\log(r) - \log(T_d) - 0.1 \quad \text{(B.2)}$$

B.1.3 M_s - Surface-wave magnitude

Surface-wave magnitude (M_s) was developed to avoid the "saturation" issue of the Richter magnitude for event magnitudes above $M_L = 6.5$, and the determination of the magnitude scale basically follows a similar procedure to measure signal strength and other parameters as the Richter's method. The only difference in the measurement of the surface-wave magnitude is that it measures the peak wave amplitude (i.e., the largest absolute value) from surface waves that have periods of 20 s, from long-period seismographs at a teleseismic distance (Kanamori, 1978; Nuttli and Kim, 1974). Comparing with the Richter magnitude scale, the distance for seismograph record does not limit within 100 km of the epicenter for the surface-wave magnitude. In light of no distance consideration, the teleseismic records of large-to-moderate magnitude earthquakes worldwide are assigned to surface-wave magnitude. However, M_s also suffers the issue of saturation, at about $M_s = 8.0$.

B.1.4 M_b - Body-wave magnitude

Body-wave magnitude (M_b) for short-period body-wave is measured from peak motions recorded at distances up to 1000 km on instruments with a passband in the range of 1 to 10 Hz (Jarosch,

1969). M_b scale is the principal magnitude used in the tectonically "stable" eastern part of North America and Canada (McCalpin, 2012). There is no exception for this magnitude scale and it will be saturated at M_b = 6.0 to 6.5.

B.1.5 M_w – Moment magnitude

Moment magnitude (M_w) is the most recently developed scale to circumvent the issue of saturation in other magnitude scales. M_w is fundamentally different from other scales. Compared with other magnitude scales which rely on measured seismogram peaks at certain distance from the epicenter, the M_w scale depends on seismic moment (M_0) that represents directly the amount of energy released at the source, not just on the type of seismic wave used. The seismic moment is defined as (Aki and Richards (2002) and Kanamori (1983))

$$M_0 = \mu_s A D_s \tag{B.3}$$

where μ_s (dyne/cm^2) is the average shear rigidity of the faulted rocks, A (cm^2) is the area of the fault face, and D_s (cm) is the average slip displacement over the entire fault surface. The seismic moment tensor is a quantity that depends on the fault strength and orientation. Once the seismic moment is known, a standard way of converting seismic moment to moment magnitude can be found in Hanks and Kanamori (1979) and Kanamori (1983)

$$M_W = \frac{2}{3}\log M_0 - 10.73 \tag{B.4}$$

where M_w is the moment magnitude and M_0 (dyne·cm) is the seismic moment.

Based on database from the Geological Survey of Canada (GSC), Sonley and Atkinson (2005) proposed a empirical relation between the moment magnitude and Nuttli magnitude for small magnitude

$$M_W = 1.03 M_N - 0.61 \tag{B.5}$$

B.2 Relation among various magnitudes and source intensity determination

B.2.1 Relation among different magnitudes

Figure B - 1 shows the relation among different magnitude scales. Clearly, while other magnitude scales will saturate at several different magnitude levels, there is no magnitude saturation if the moment magnitude is used. Hence, the moment magnitude scale solves the saturation issue and can be employed to describe large seismic events.

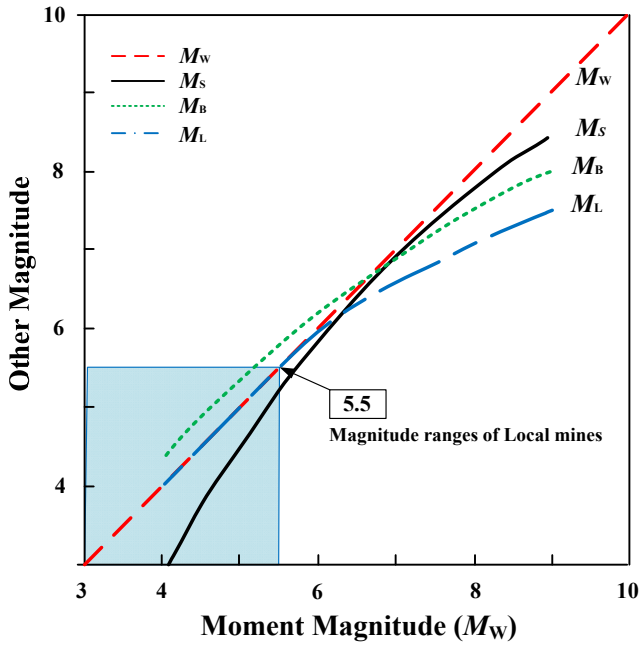

Figure B - 1: Relation among various magnitude scales. Magnitude range of large rockbursts in underground mines is shown in the left bottom square (from Idriss (1985), Kanamori (1983), and Towhata (2008) with some amendments).

The moment magnitude and the Richter magnitude will provide roughly equivalent intensity before the Richter magnitude reaches a saturation level of M_L = 6.5, and the curves of M_L and M_w overlap partly in the graph (Figure B - 1), which means that both scales can be used for large seismic events in underground mines because the magnitudes of seismic events in underground mines are, in general, less than M_L = 5.5, and most large seismic events are between M_L = 3 to 4.

The local Richter magnitude scale M_L and the Nuttli scale M_N are widely used to quantify intensity of seismic source in underground mines (Kaiser et al., 1996). The difference between the M_L and M_N scales is expressed by the difference in the value of magnitude for the same seismic event. Hence, all the above three magnitude scales (M_w, M_L, and M_N) can be correlated to each other and each of them can be used to properly quantify seismic intensity in underground mines.

It is important to note that M_w can be connected directly to the physical process of faulting. As discussed above, M_w is calculated from the seismic moment M_0, which is directly related to the energy released from the seismic source. Hence, the M_w scale has a clear and rigorously meaning of the physical process of the source movements. On the contrary, other magnitude scales (such as M_L, M_s, and M_b) have no direct tie to the physical process of faulting because they rely on the measurement of recorded waveforms at site stations. Furthermore, both the M_L and the M_w scales can provide roughly equivalent intensity in the context of underground mines. It is therefore appropriate to employ the M_w scale to consider the intensity of a seismic source in wave propagation simulations.

B.2.2 Source intensity determination of forward wave propagation modeling

For forward seismic wave propagation modeling, the first and the most important information is the intensity of the seismic source. In other words, source parameters of the seismic event need to be determined. In the context of forward simulation, assume that the magnitude M_w of a seismic source is known, the seismic moment can be determined from Aki and Richards (2002)

$$M_0 = 10^{\frac{3}{2}(M_W + 10.73)} \tag{B.6}$$

where M_0 (dyne·cm) is the seismic moment and M_W is the moment magnitude.

Once the seismic moment M_0 is known, for a DC (double-couple) model (assume that information of the fault area and other parameters such as strike ϕ_s, rake γ_r, and dip δ_d are known) of fault slip in 2D, three elementary moment tensor components for the far-field P-SV system can be expressed by

$$\begin{aligned} M_{xx} &= -M_0(\sin\delta_d \cos\gamma_r \sin 2\phi_s + \sin 2\delta_d \sin\gamma_r \sin^2\phi_s) \\ M_{xz} &= -M_0(\cos\delta_d \cos\gamma_r \cos\phi_s + \cos 2\delta_d \sin\gamma_r \sin\phi_s) \\ M_{zz} &= M_0 \sin 2\delta_d \sin\gamma_r \end{aligned} \tag{B.7}$$

where M_{xx}, M_{zz}, and M_{xz} are the components of the moment tensor, which can represent the seismic source in 2D wave simulation. In this manner, the moment tensor source can be employed to denote the seismic source of a fault.

Appendix C: Joint time frequency analysis (JTFA)

It is well known that seismograms recorded at stations are not stationary but non-stationary signals (Boashash, 2003; Huerta et al., 2000). Various frequency components exist in the seismograms because of the seismic wave interactions with drifts, stopes, dykes, or other geological structures in underground mines. Therefore, the seismograms computed from a numerical model that includes several types of heterogeneities will also be non-stationary and contain different frequency components. This appendix aims at examining frequency changes in seismograms. The dominant frequency can be identified from such an analysis.

C.1 Brief introduction of JTFA and non-stationary seismograms of waves

A seismogram is often plotted in the time domain, but the time amplitude representation is not always the best representation of the seismogram (Qian, 2002). In many cases, the most distinguished information of the seismograms is hidden in the frequency content and sometimes the frequency spectrum is more useful because it can provide information on what frequencies exist in the seismograms. Whether a certain frequency component in wave seismograms exists or not can be identified using the Fourier Transform (FT), which converts the signals from the time domain into the frequency domain. The FT technique provides the frequency content in time series; however, it cannot show the exact time when these frequency components appear and there is no temporal information.

The most complete and informative characterization of a signal can be obtained by its decomposition in the time-frequency plane, an elegant way of separating phase (i.e., travel time)

and amplitude information (Kristekova, 2006). A Joint Time Frequency Analysis (JTFA) maps a one-dimensional signal into a two-dimensional function of time and frequency, which can be used to describe the spectral content of the signal change with respect to time (Huerta et al., 2000). Furthermore, time-frequency distribution can show how energy is distributed over the time and frequency domains simultaneously (Boashash, 2003).

The seismic waves recorded in seismograms exhibit clearly non-stationary characteristics of waves (Huerta et al., 2000). Around a tunnel, the frequency content in recorded seismograms induced from a fault-slip event is complex, which is a result of the influence of source, path, medium, and site effect on the signals. The seismograms can contain signals of various frequencies due to the scattering and attenuation of propagating seismic waves. The non-stationarity of the seismograms means that the frequency amplitude can vary with time, which can be related to the intensity of the ground motion. Hence, a time-frequency representation is suitable for describing time localization of seismograms; the frequency components are known in the seismograms, and the arrival time can be identified the in time domain. The JTFA is conducted in the following to understand better the seismograms obtained from the numerical modeling.

C.2 Analysis of synthetic seismograms using JTFA

The spectral energy density function can be obtained by means of a FT analysis, which can show the frequencies that are present in the seismograms. Hence, the FT method is used first to identify the frequencies hidden in the seismograms. Next, the JFTA method is used to reveal where and when the frequency content changes.

C.2.1 Background (homogeneous) model

Figure C - 1 presents the joint time-frequency representations for two seismograms. The receiver locations are indicated by red dots in the middle inserts showing the shape of the tunnel and the receiver location (the tunnel is not excavated in this case). The lower middle inserts show the spectra of the two velocity components based on the FT analysis. The time-frequency representation and the waveform of each velocity component are shown in Figure C - 1(a) and (b) for receivers 34 and 38. It should be noted that the actual frequency is shown in the FT power spectra and the normalized frequency (ranges: 0.0 to 0.5) is shown in the JTFA.

For the homogeneous model, the seismograms for the two velocity components are very simple. The FT results indicate clearly that there is only one notable spike at 125 Hz for both the

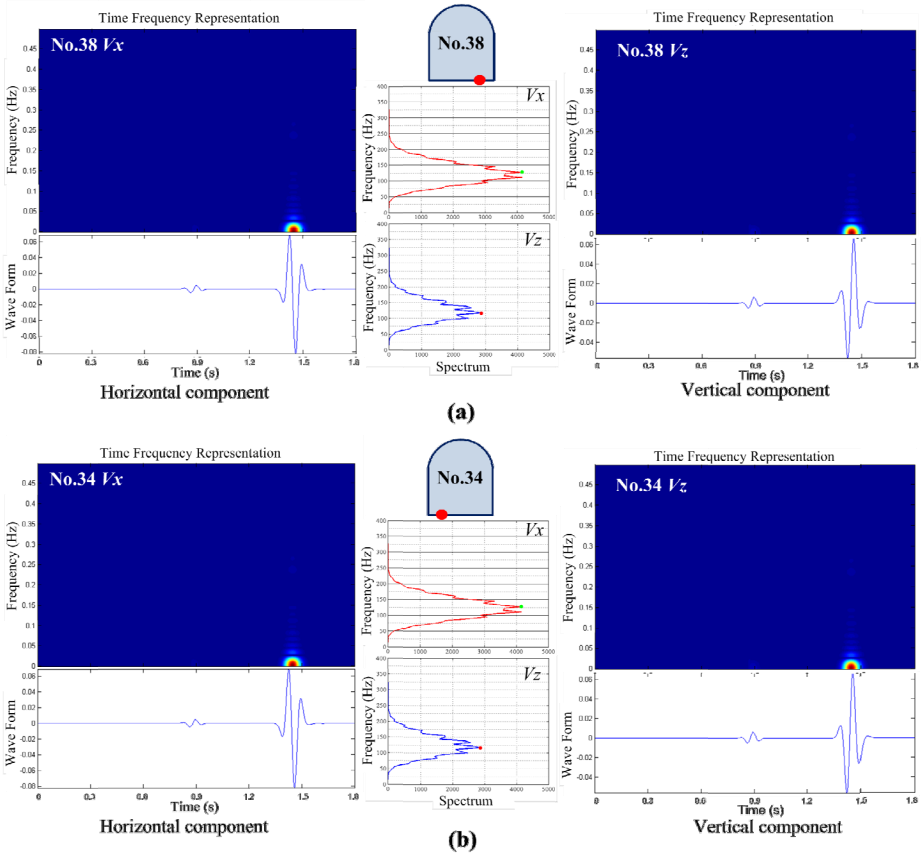

Figure C - 1: Joint time-frequency representations of the two velocity components of the synthetic seismograms for receivers No.34 and No.38 (homogeneous model $M_{1\text{-}R}$).

horizontal and vertical velocity components. The result from the JTFA shows when the notable frequency appears in the time domain. It also shows that the S-waves have more seismic energy than the P-waves. Similar results are found for other receivers.

C.2.2 Tunnel model

In this analysis, the model contains a tunnel. The joint time-frequency representations for two floor receivers (No.34 and No.38) are shown in Figure C - 2. The horizontal velocity component becomes more complex due to the influence of the tunnel. The vertical velocity component has one spike in the power spectrum, roughly at 120 Hz and 100 Hz for receivers No.34 and No.38, respectively. The horizontal velocity has three main frequency components, at 100, 150, and 200 Hz. However, more energy seems to concentrate at 150 Hz and 100 Hz for receivers No.34 and No.38, respectively. This may be due to multiple wave reflections that can generate relatively high frequency components in the seismograms. For receiver No.34, the strong ground motion is caused by the coda waves after the direct waves have arrived. Similarly for receiver No.38, strong coda waves around 100 Hz cause large ground motion at the point.

The three main frequency components identified on the time series can provide a good understanding on the influence of excavation on seismic wave. For instance, according to the FT analysis, dominant frequencies at 100, 150, and 200 Hz are identified for the horizontal velocity signals at the two receivers. It is noticed from the JTFA that the sequence of these frequencies for receiver No.34 is in the order of 100, 200, and 150 Hz in the time series. For receiver No.38, the order is 200, 150, and 100 Hz in the time series. Besides, seismic energy distribution

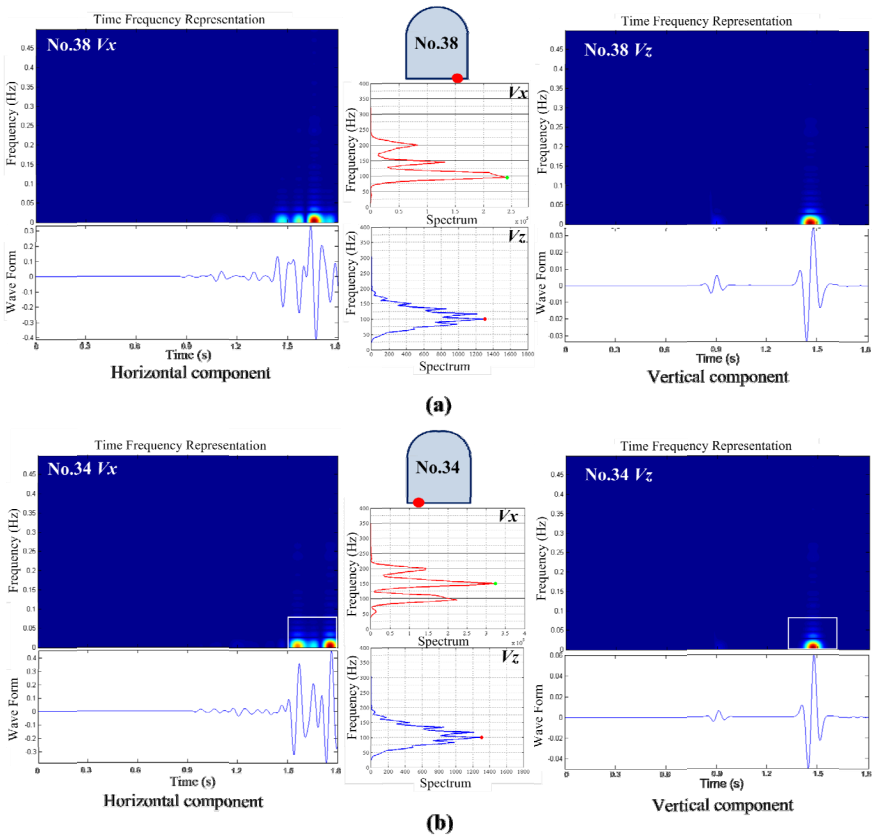

Figure C - 2: Joint time-frequency representations of the two components of the velocity synthetic seismograms for receivers No.34 and No.38 (single tunnel model $M_{2\text{-}R}$).

can also be identified in the time series. Clearly, more seismic energy appears at receiver No.34 than at receiver No.38. Based on the above analysis, it can be concluded that the JTFA is a useful tool to understand seismic wave characteristics in the frequency domain.

C.2.3 Backfilled stope model

For ease of comparison, the same receivers (No.34 and No.38) are selected and analyzed for the backfilled stope model and only the first mining stage (Stage 1) is considered. The joint time-frequency representations are shown in Figure C - 3. Various frequency components can be found. According to the FT analysis results, one (150 Hz) and two spikes (100 and 175 Hz) of frequencies are observed in the spectra of the horizontal and vertical velocity seismograms for receiver No.34. For receiver No.38, the horizontal component presents mainly two frequency

components (110 and 170 Hz), and several frequencies (such as 76, 98, 120, 150 Hz) can be observed for the vertical component. The seismic energy of the horizontal component is higher than that of the vertical component. These results indicate that more frequency components exist due to the presence of the stope.

The JTFA results reveal clearly the energy distribution for each frequency component. For receiver No.34, the direct S-waves play an important role in influencing the ground motion. The frequencies of 150 Hz (horizontal) and 100 Hz (vertical), and 175 Hz in the vertical component have contributed to the seismic response. For receiver No.38, the direct S-waves also play an important role in influencing the seismic response. However, the main frequency for the horizontal component drops from 150 to 110 Hz. The S-waves arrive firstly at receiver No.38 with a dominant frequency of about 110 Hz. Then the dominant frequency increases to 150 Hz

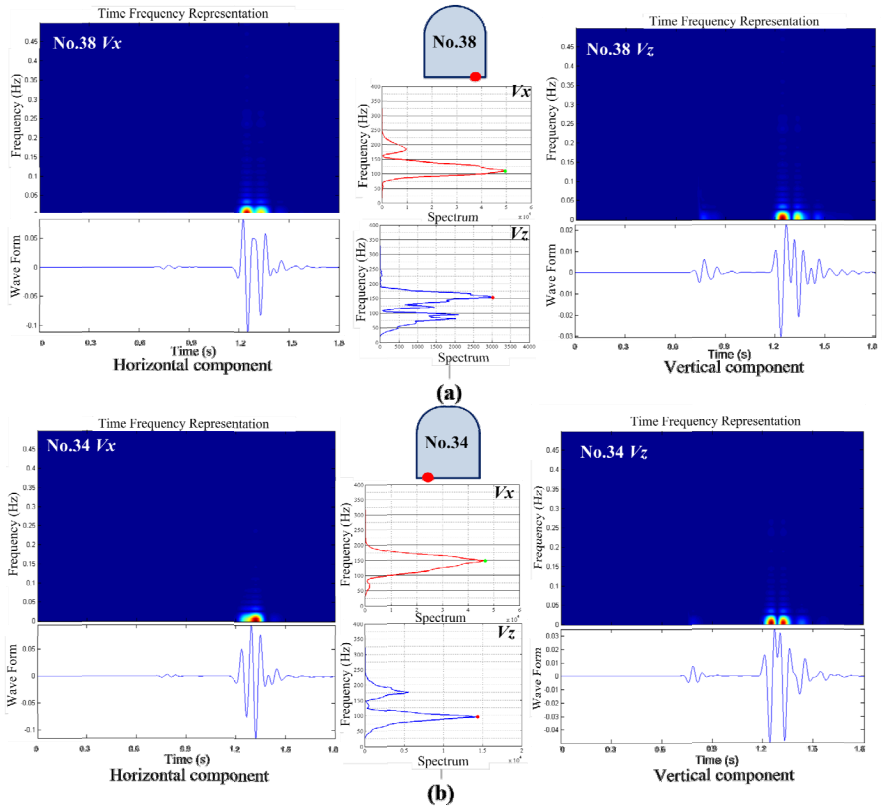

Figure C - 3: Joint time-frequency representations of the two components of the velocity synthetic seismograms for receivers No.34 and No.38 (backfilled model $M_{3\text{-}1\text{-}R}$).

due to the interaction of the S-waves with the scatter waves resulted from the direct P-waves. For the vertical component, the main frequency with the largest amount of seismic energy increases is from 100 to 150 Hz and more frequency components can be found in the coda waves, which have a relatively low seismic energy.

C.2.4 Dyke model and model with multiple openings

The results from the dyke model ($M_{4\text{-}1\text{-}R}$) and the model with multiple openings ($M_{5\text{-}2\text{-}R}$) are analyzed using JTFA. For model $M_{4\text{-}1\text{-}R}$, the joint time-frequency representations for the two floor receivers (No.34 and No.38) are shown in Figure C - 4. When the 3 m wide dyke is added to the model, the horizontal velocity component of receiver No.38 is centered around 150 Hz at two different times in the coda waves. In addition, 100 and 200 Hz frequency components can be noticed in Figure C - 4(a). For receiver No.34, the horizontal component has a concentration at 150 Hz (Figure C - 4(b)). Moreover, the seismic energy of the horizontal component is higher than that from the vertical component.

The maximum horizontal ground motion for receiver No.34 occurs at t = 1.5 s with a dominant frequency of 150 Hz; however, for receiver No.38, large ground motions with a dominant frequency of 150 Hz occur at two times: t = 1.6 s and t = 1.8 s. This may be resulted from the strong coda waves that are caused by the dyke. Because the dyke is located near the right wall of the tunnel, strong scatter waves are generated and propagated back and forth between the drift and the dyke. In addition, the coda waves can provide additional seismic energy to rocks near the tunnel boundary, which is evident in the horizontal component at receiver No.38 (Figure C - 4(a)).

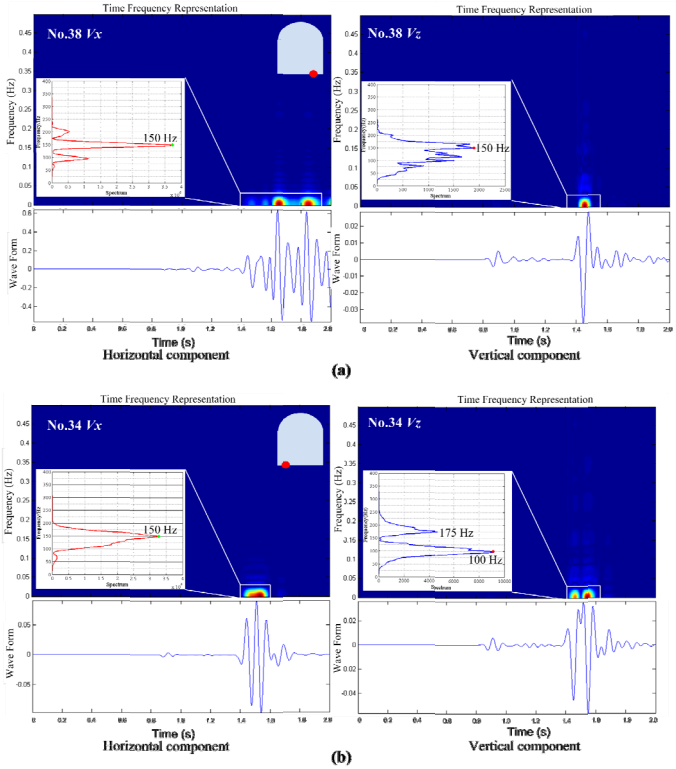

Figure C - 4: Joint time-frequency representations of the two components of the velocity synthetic seismograms for receivers No.34 and No.38 (dyke model $M_{4\text{-}1\text{-}R}$).

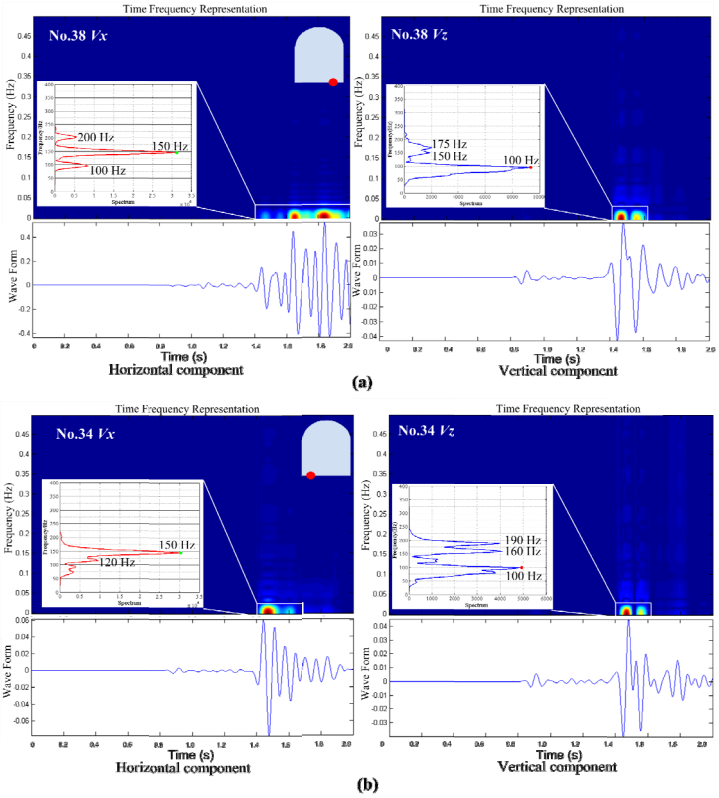

Figure C - 5: Joint time-frequency representations of the two components of the velocity synthetic seismograms for receivers No.34 and No.38 (dyke model with multiple drifts $M_{5\text{-}2\text{-}R}$).

Compared the results from Figure C - 5 with that from Figure C - 4, it is seen clearly that the horizontal components for both two receivers have the same frequency spikes (except that receiver No.34 has an addition spike at 120 Hz in model $M_{5\text{-}2\text{-}R}$). The vertical components have a large difference in both receivers, showing the influence of multiple openings on seismic wave propagation. The distance between tunnel (T2) and the bottom tunnel (T1) is 40 m. Additional openings (T3 and T4) in the model shows an energy absorption effect, which can be seen in the power spectra. Compare with that in model $M_{5\text{-}2\text{-}R}$, relatively low energy of the frequency components can be found in model $M_{5\text{-}2\text{-}R}$.

The results obtained from the above analysis show that the effect of the influence of different structures on seismic waves can be studied using JTFA. The advantage of JTFA is that it can reveal addition information hidden in the seismograms. For different models, the frequency component for each receiver can increase or decrease when comparing with the result from the background model (125 Hz for all different components of the receivers). In general, the multiple scattering waves produce relatively high frequency components in the seismograms. Hence, the existence of tunnel will produce relatively low frequency components because high frequency components can be absorbed by these openings. In addition, the coda waves between the direct P- and S-waves and after the direct S-waves may cause additional dynamic loading to the rock masses near the tunnel boundaries.

Appendix D: A preliminary study using SPECFEM3D

The thesis focuses on 2D wavefield simulations, which are useful to gain insight into wave propagation; however, a comprehensive and quantitative understanding of wave propagation in an underground mine requires a 3D model with a proper seismic source and realistic medium. Therefore in this Appendix D, the emphasis has been transferred from 2D to 3D modeling of seismic wave propagation. The applicability of SPECFEM3D is firstly validated using a simple excavation model by comparing the modeling results with that from 2D modeling.

D.1 Introduction

Considering that underground mining environments are 3D in nature, 3D modeling is therefore required to understand wave propagation in underground mines. Three key areas should be considered to conduct 3D wave propagation simulation using SPECFEM3D. (1) 3D modeling demands advanced mesh generation technique in the pre-processing stage due to the complexity in underground mines (i.e., geological structures with high spatial variations, various geometries of mine stopes and drift system). Powerful advanced mesh generation tools such as CUBIT, Gmsh, and ANSYS are needed. (2) 3D modeling requires a powerful computing resource in the computation stage. Parallel computation with multiple CPUs and GPUs could reduce computation time significantly. (3) 3D modeling needs advanced data visualization techniques in the post-processing stage. Software such as ParaView, Matlab, and Origin can assist scientific visualization. A preliminary 3D study is conducted and the results are presented in this appendix.

D.2 A simple excavation tunnel

D.2.1 Model description

A simplified 3D excavation model is constructed with the density, P-wave and S-wave velocities of the rock mass as 2700 kg/m^3, 5874 m/s, and 3400 m/s, respectively. As shown in Figure D - 1(a), the model dimension is 300 m × 400 m × 400 m. An air filled circular tunnel (blue), with a diameter of 8 m and a length of 100 m, is located in the middle of the model (x ranges from 100 to 200 m, y ranges from 246 to 254 m, and z ranges from -246 to -254 m, see Figure D - 1(b)). The model has 403,384 elements with a total of 419,765 nodes; the average element size is about 0.5 m for the rocks around the excavation tunnel and 5.0 m for the remaining rocks.

A seismic source is located at the upper right of the model (x = 150 m, y = 100 m, z = -100 m) (red dot-cross in Figure D - 1(b)), represented by the moment tensor source model with a magnitude of M_w = 1.5 and with a dominant frequency of 100 Hz and a slip direction defined by strike/dip/rake of 0°/45°/-90°. This is to ensure that the maximum ground motion is in the y-z plane.

Receivers (green dots) are placed in three cross-sections (x-y, y-z, z-x) of the tunnel to calculate PPV contours in these planes, as shown in Figure D - 1(b). Figure D - 1(c) and (d) show the detailed receiver layouts in the model. In each plane, 41 by 41 receivers with a 5 m grid spacing are placed in a square area of 200 m × 200 m to generate PPV contours. The four edges of the model are set as absorbing boundaries. It took about 5 hours to run this 3D excavation model when 12 CPUs (Inter Xeon E5-2687w with 3.1 GHz) and 2 GPUs (Quadro K5000 with 4G memory and Tesla K20c with 4G memory) are used.

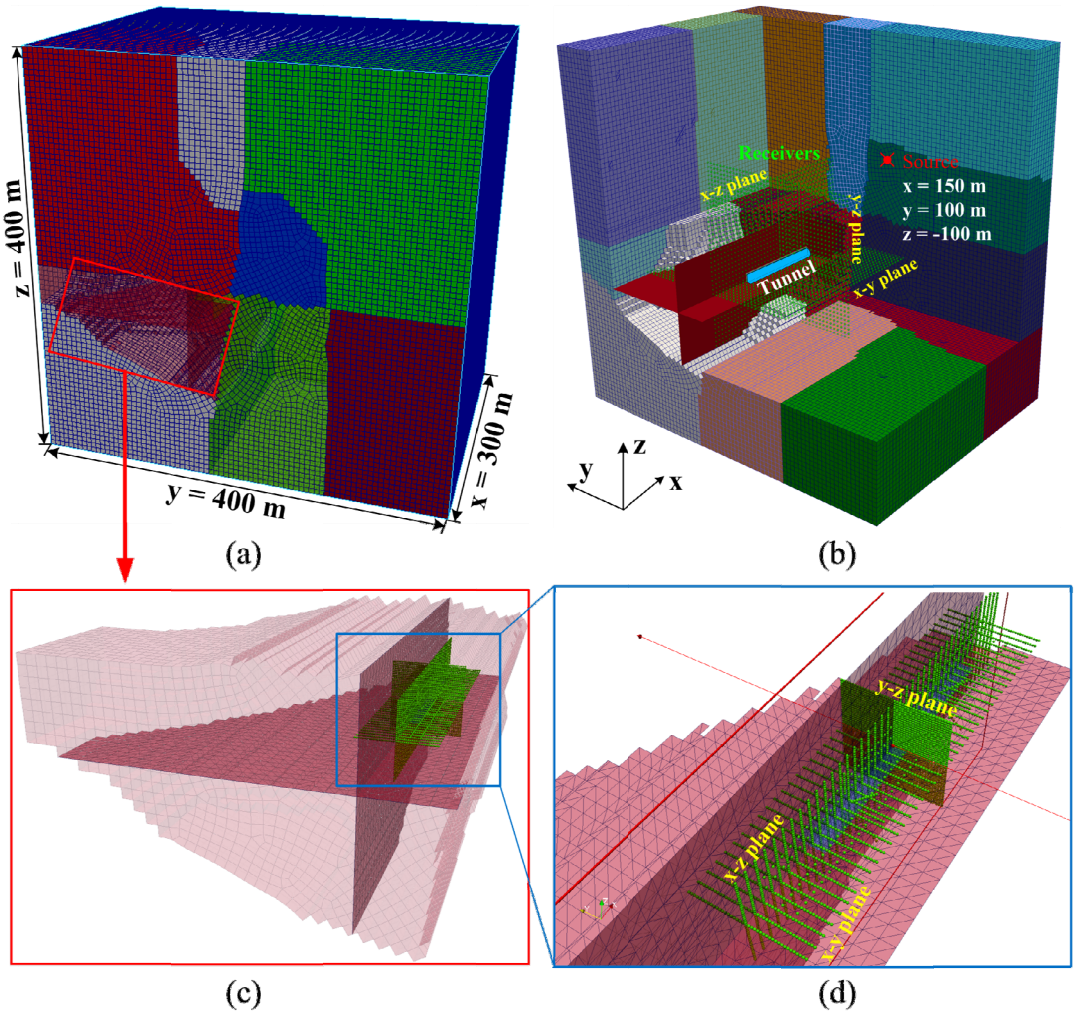

Figure D - 1: (a) Spectral-element mesh of a simple 3D excavation model; (b) interior section of the mesh that highlights the tunnel location, seismic source, and receivers; (c) receiver layout around the tunnel and (d) a zoom-in plot to show the details of the receivers. The model is partitioned into 12 sub-domains (indicated by different colors) for parallel computing.

D.2.2 Modeling results and discussion

Due to the selected seismic source location and source parameters as well as model set up, seismic wave propagation in the y-z plane should follow the same pattern and possess similar characteristics to wave propagation in 2D in the y-z plane. Hence, the 3D modeling results can be compared with that presented in Section 6.2. A background model without the tunnel is also simulated to compare results.

Figure D - 2 presents a series of snapshots of the isosurfaces of the vertical velocity component (V_z) for the background and the tunnel excavation models at four propagation times. It is observed from Figure D - 2(a) and (b) that direct P- and S-waves are generated and propagated in the y-z plane in which the seismic source is located. Furthermore, seismic waves also propagate in other spatial directions (see yellow dash line highlighted areas in Figure D - 2 at t = 0.072 s and 0.096 s). The wave radiation patterns in the y-z plane from the 3D modeling are the same as that from the 2D simulation.

The influence of the tunnel on the seismic wavefield can be found at t = 0.072 s in Figure D - 2(c), which shows some reflection waves caused by the tunnel. Detailed plots of the wavefield can be found in Figure D - 3, which show the velocity isosurfaces in the range of -0.01 and 0.01 m/s. Comparing Figure D - 3(a) with (b) and (c), the effect of tunnel excavation on the wavefield can be seen clearly. Some reflection and scattering waves are generated due to the tunnel.

PPV contours of the background model and the tunnel excavation model in the three cutting planes are shown in Figure D - 4 and Figure D - 5, respectively. Figure D - 4(a) shows the cross-cutting planes and the receivers are denoted by the green dots. It is seen from Figure D - 4 that the PPV contours are closely related to the mechanism of the seismic source (a normal fault with a dip of 45° located in the y-z plane). Figure D - 4(c) shows the same PPV pattern as that presented in Section 6.2. The PPV distributions in the three cutting planes indicate that the radiation patterns of the seismic wave are correctly modeled in the background model using SPECFEM3D.

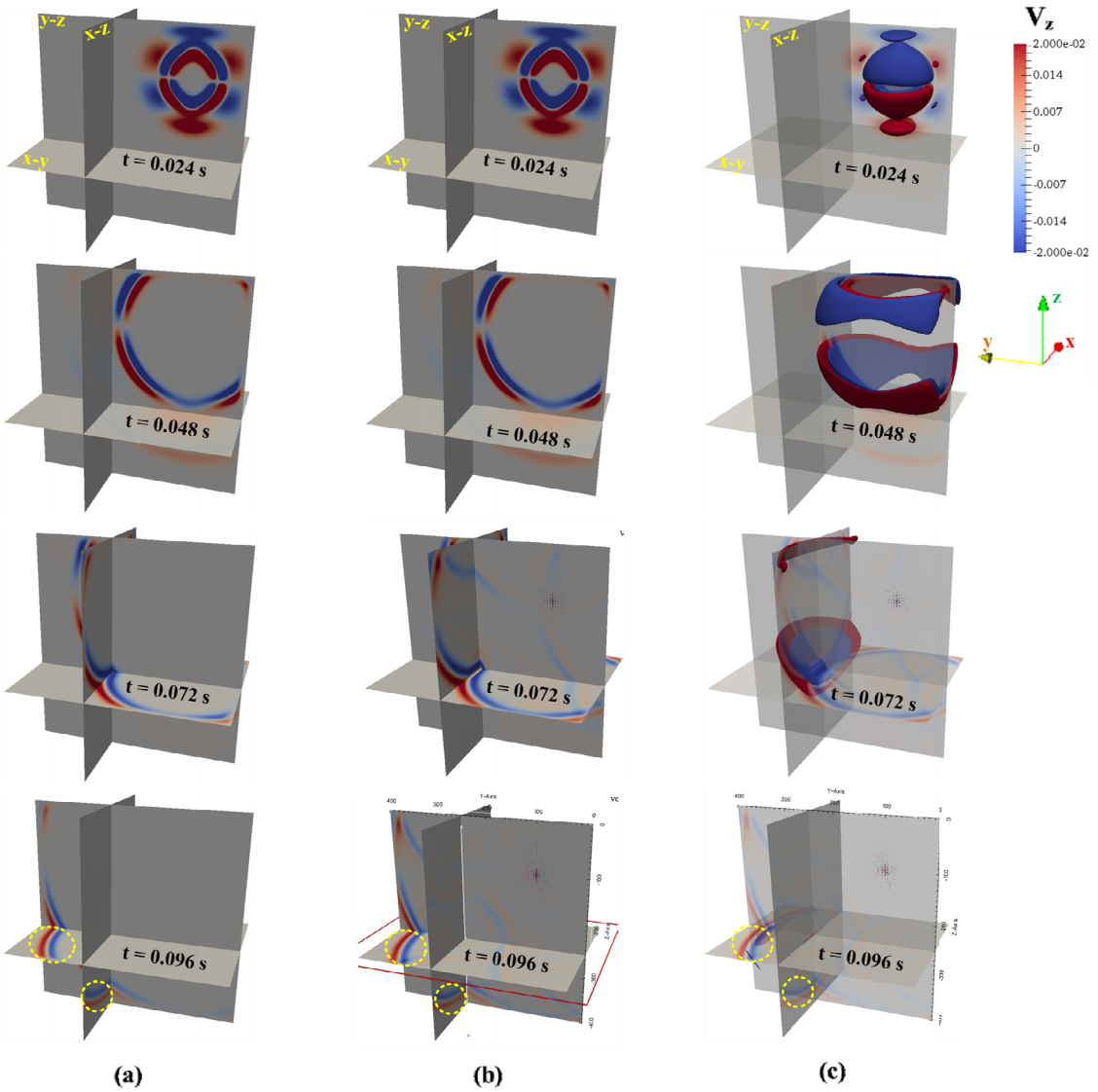

Figure D - 2: Snapshots of the vertical velocity component for the background model (a) and the tunnel excavation model (b) at four propagation times. (c) Shows the isosurfaces of V_z (ranges from -0.02 to 0.02 m/s). Red and blue indicate positive (upward) and negative (downward) velocities, respectively.

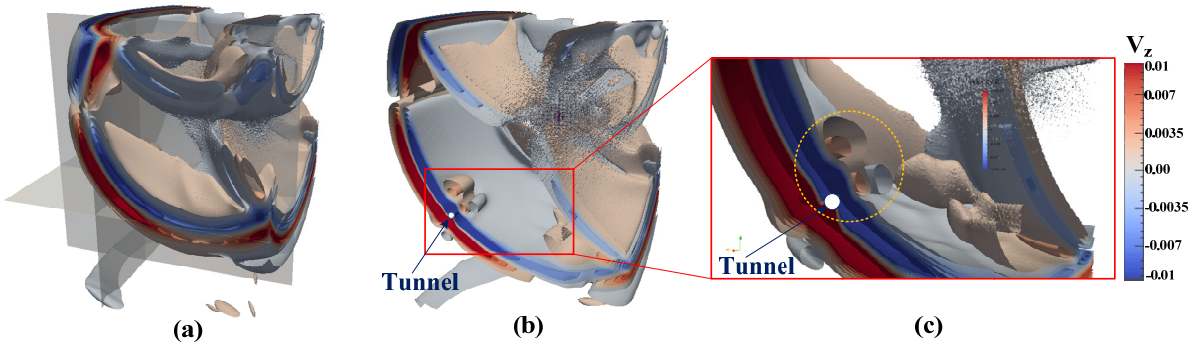

Figure D - 3: Influence of the tunnel on seismic wavefield (vertical velocity component). (a) and (b) show the velocity contours (-0.01 - 0.01 m/s) for the background model and the tunnel model, respectively. (c) Shows an enlarged area around the tunnel.

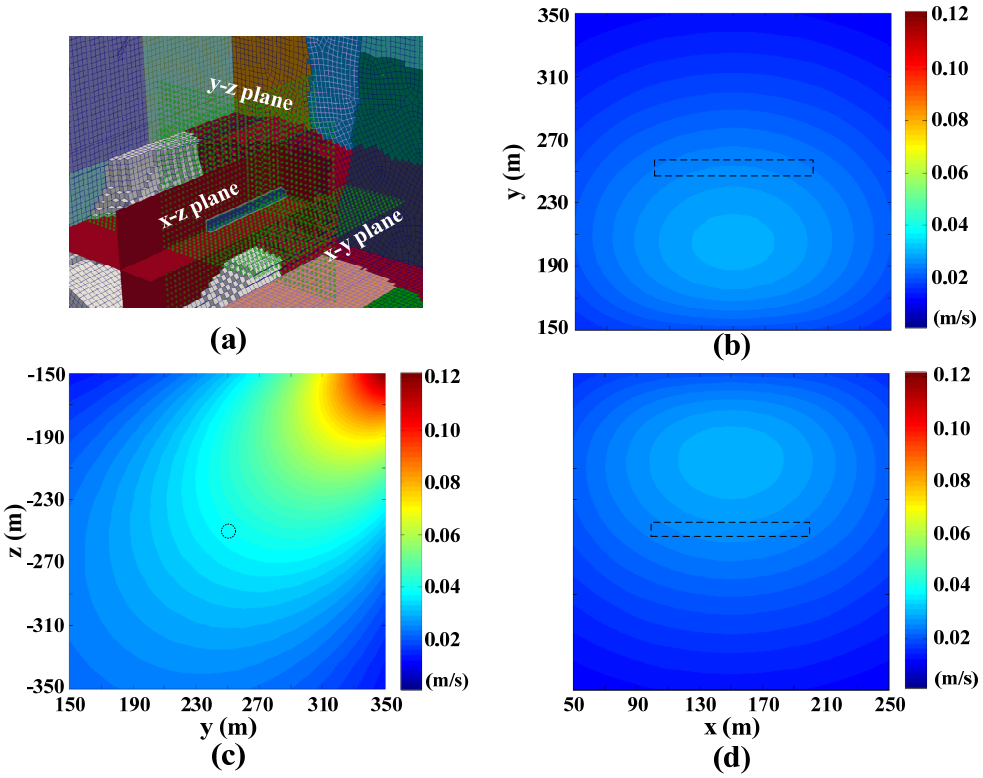

Figure D - 4: PPV contours in three cross-sections for the background model. (a) Three cutting planes in the model. PPV contours in the x-y plane (b), y-z plane (c), and x-z plane (d).

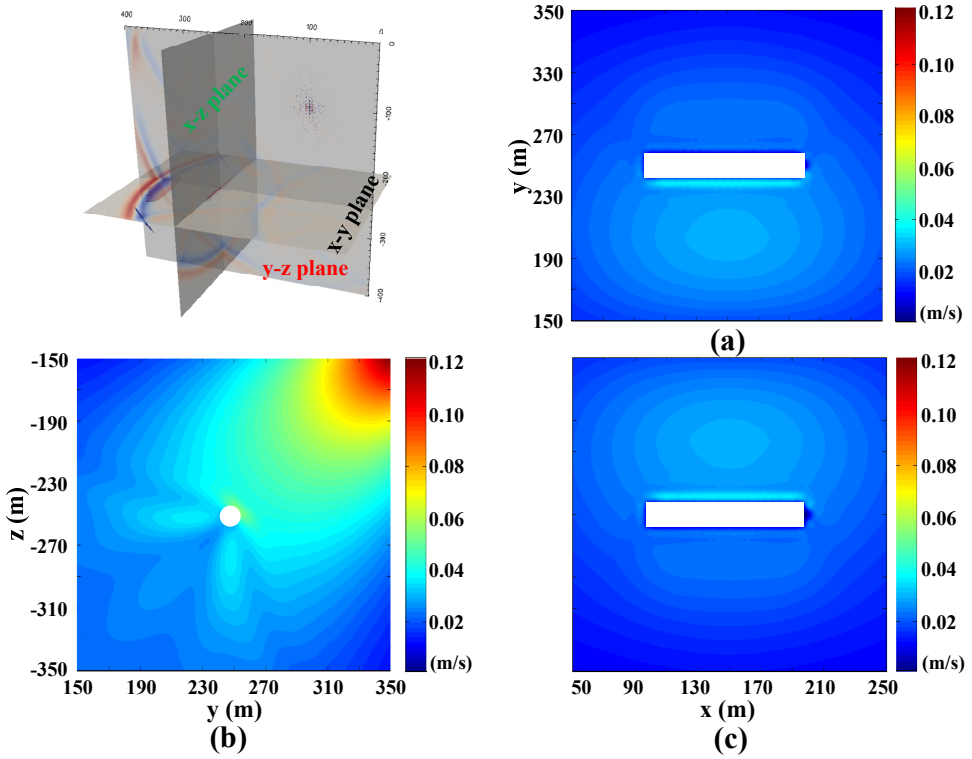

Figure D - 5: PPV contours for the tunnel model. PPV contours in the x-y plane (a), y-z plane (b), and x-z plane (c).

The influence of the 100 m long tunnel on the PPV distribution can be seen in Figure D - 5. PPV contours are altered around the tunnel when compared with the results shown in Figure D - 4. Detailed PPV contours around the tunnel are shown in Figure D - 6, which can be used to compare the 3D results with the 2D results. Relatively strong ground motions are identified on the right tunnel wall side (Figure D - 6(a)) and in the roof areas (Figure D - 6(b)) because these areas are facing the seismic wave propagation direction, which can also be clearly seen in the y-z plane (Figure D - 6(c)). Furthermore, strong ground motions are localized along the tunnel surface. As expected, the maximum ground motion occurs in the y-z plane. PPV contours such as these provided by SPECFEM3D can be used to assess ground motions near excavation boundaries in underground mines. PPV contours and each velocity component in the cutting planes are presented from Figure D -7 to Figure D -12.

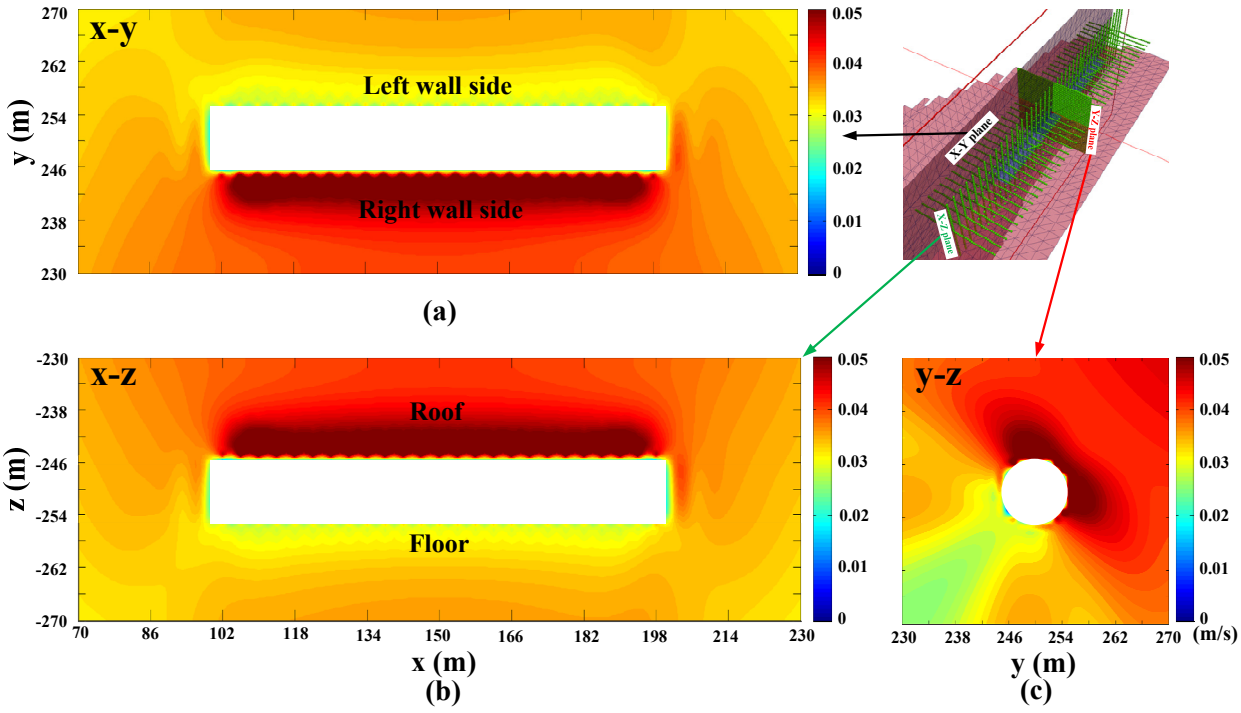

Figure D - 6: PPV contours around the tunnel in the x-y plane (a), x-z plane (b), and y-z plane (c).

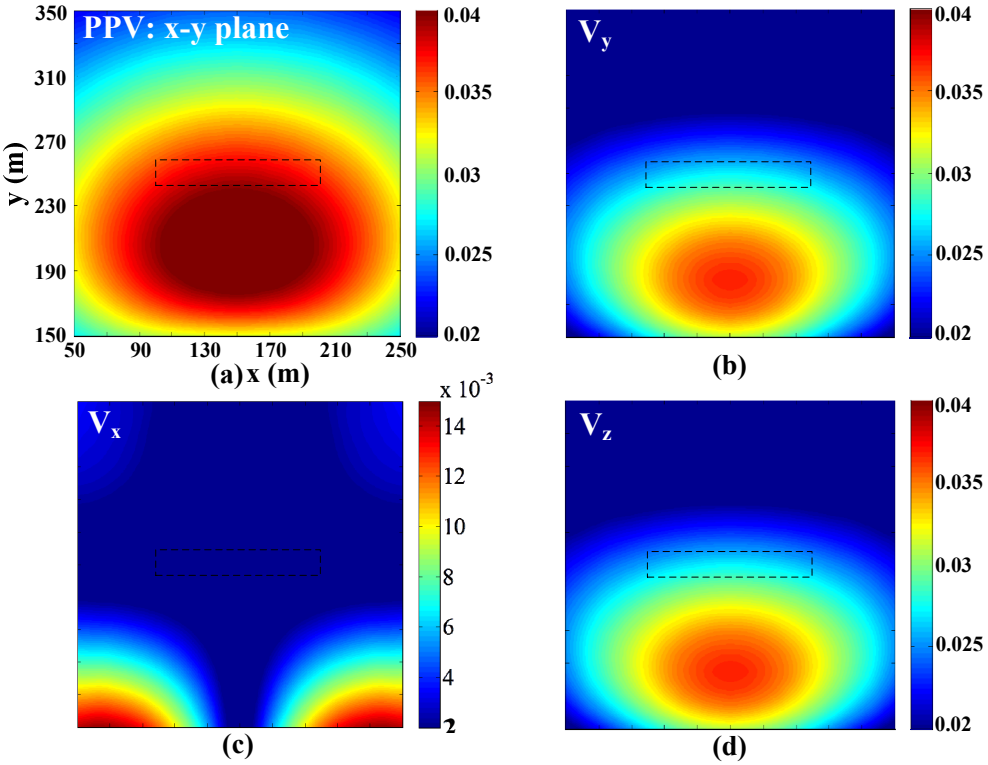

Figure D - 7: PPV contours in the x-y plane for the background model (a). Contours in the x-y plane for velocity components V_y (b), V_x (c), and V_z (d).

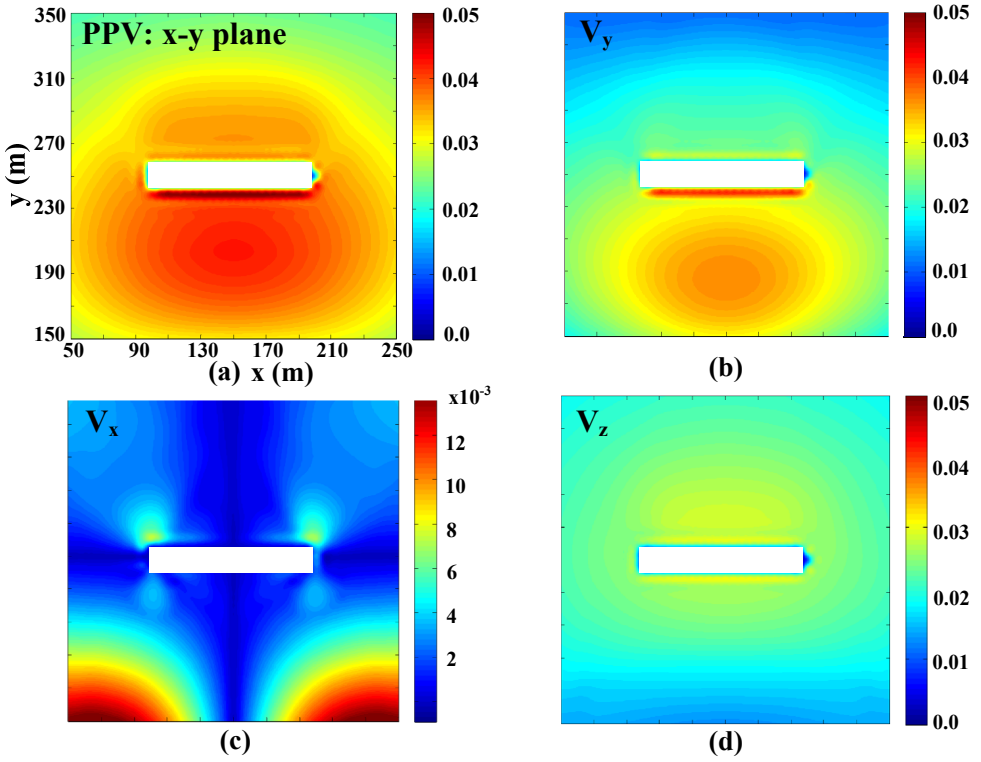

Figure D - 8: PPV contours in the x-y plane for the tunnel excavation model (a). Contours in the x-y plane for velocity components V_y (b), V_x (c), and V_z (d).

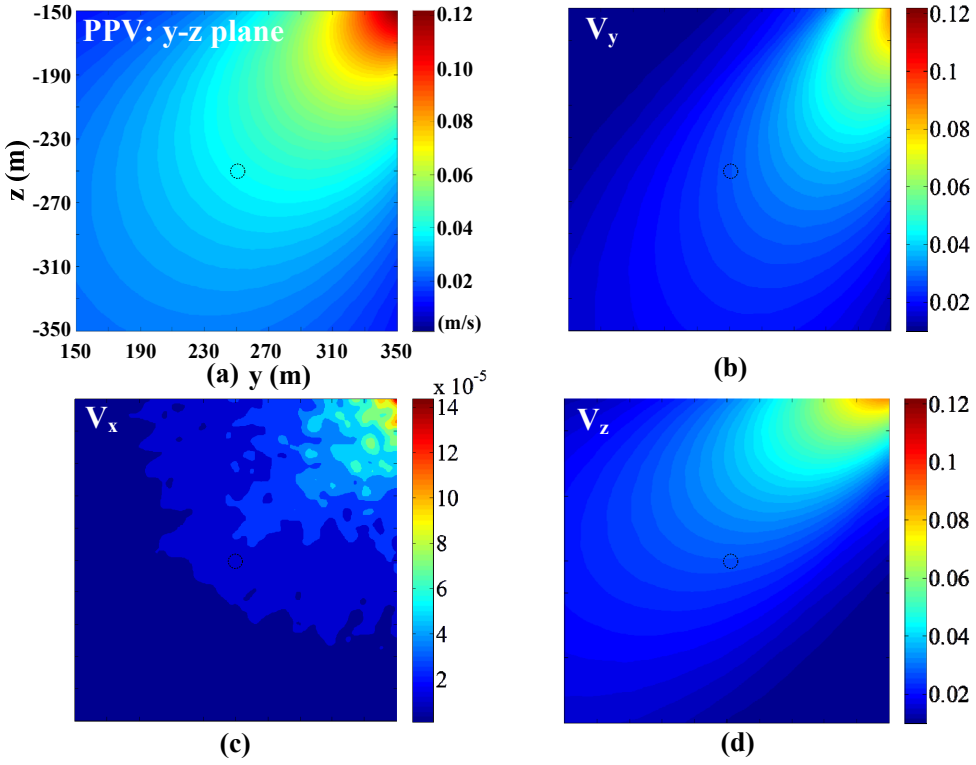

Figure D - 9: PPV contours of in the y-z plane for the background model (a). Contours in the y-z plane for velocity components V_y (b), V_x (c), and V_z (d).

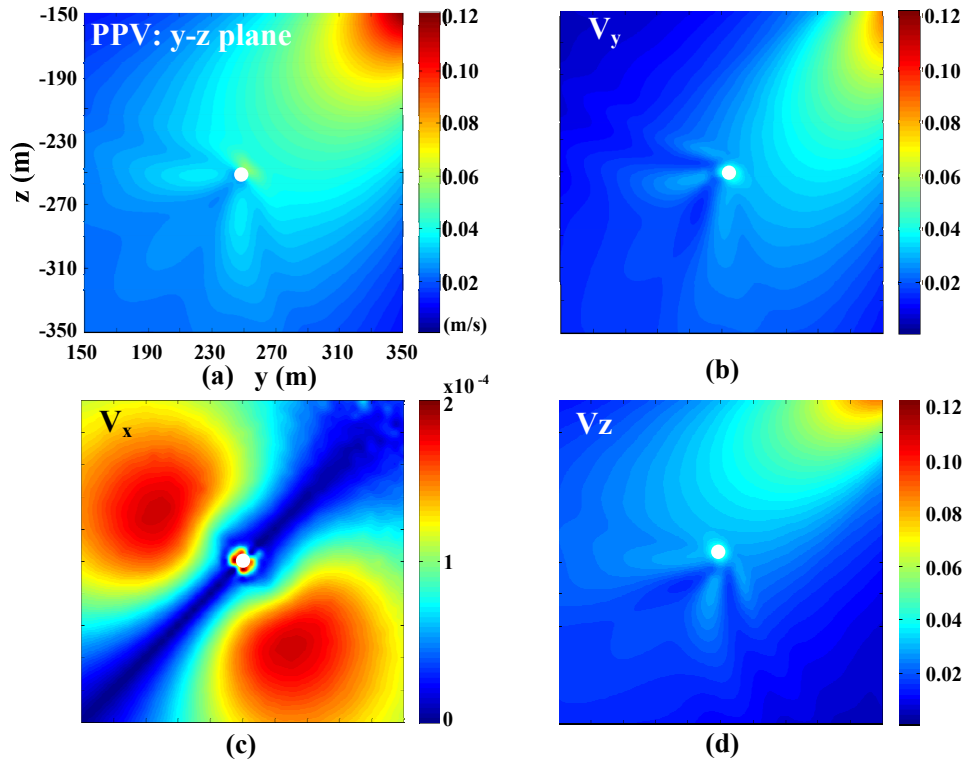

Figure D - 10: PPV contours in the y-z plane for the tunnel excavation model (a). Contours in the y-z plane for velocity components V_y (b), V_x (c), and V_z (d).

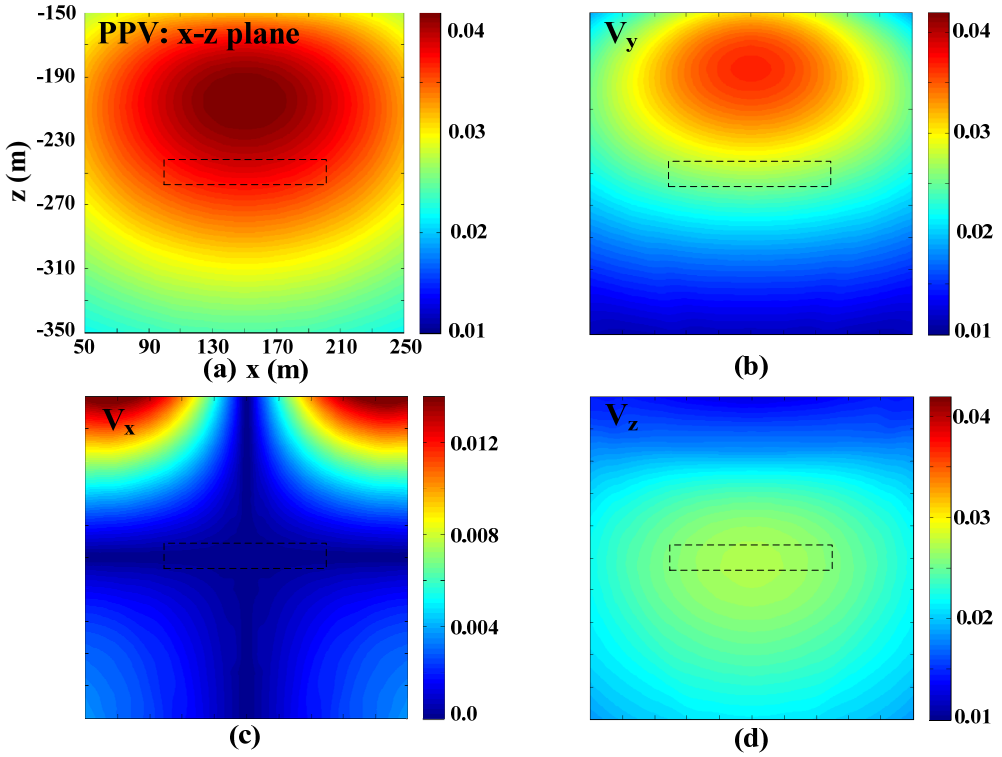

Figure D - 11: PPV contours in the x-z plane for the background model (a). Contours in the x-z plane for velocity components V_y (b), V_x (c), and V_z (d).

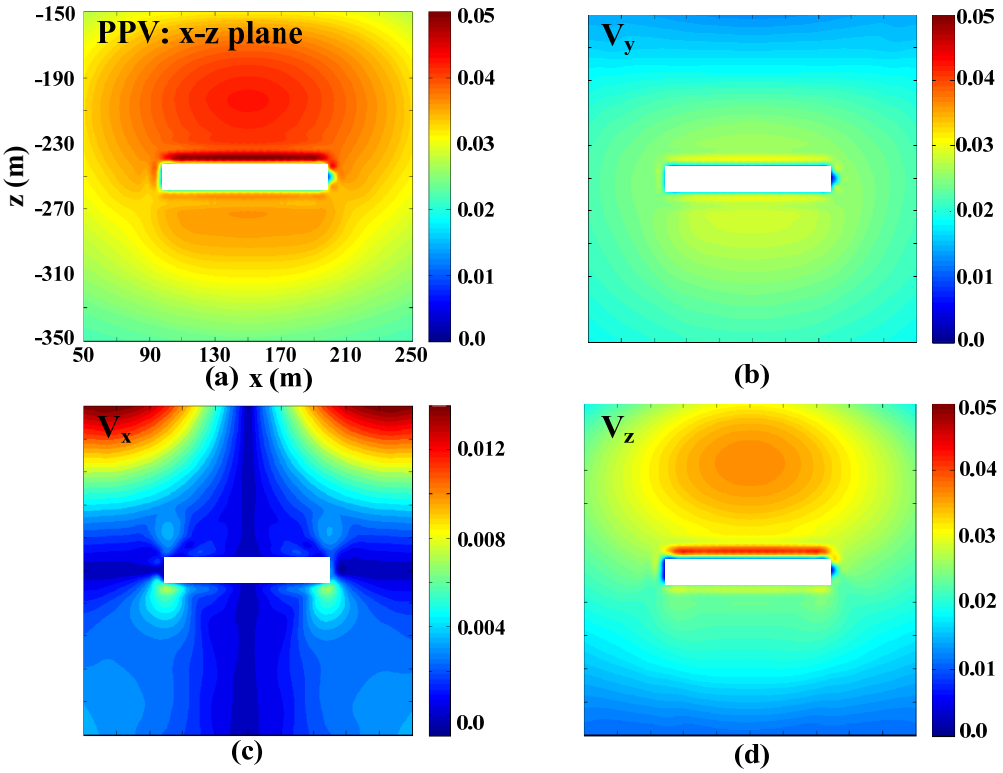

Figure D - 12: PPV contours of in the x-z plane for the tunnel excavation model (a). Contours in the x-z plane for velocity components V_y (b), V_x (c), and V_z (d).

D.3 Summary

The results from SPECFEM3D are compared with that from SPECFEM2D in the y-z plane. It is seen that the ground motions in y-z plane from SPECFEM3D agree well with that from SPECFEM2D because the 3D problem can be treated as a 2D P-SV problem for the given seismic source condition. Ground motion is a combination of the three velocity components. In this case, V_x contributes less to the total ground motion compared with V_z and V_y. Based on the 3D modeling results from the background and tunnel models in this section and results from the 2D modeling in Chapter 6, it is seen that SPECFEM3D is a valid tool that can be used to conduct seismic wave propagation simulation in underground mines that can have complicated geometries and heterogeneous media. In the Appendix E, a case study which considers real mine geometry and rock mass properties is conducted.

Appendix E: A case study at Mponeng mine in South Africa using SPECFEM3D

The simulation work conducted in here serves to further demonstrate the capability of the SPECFEM3D tool for wavefield modeling in a complex underground mining environment, through the incorporation of various rock domains, mined-out stopes, and a drift system in the model. In addition, this modeling work demonstrates how to better represent seismic sources in the near-field in SPECFEM3D because the seismic source mechanism in the near-field is not well understood. This case study can be viewed as a preliminary study of a rockburst event. This type of study may provide a better understanding of localized rockburst damage in underground mines for improved rock support design.

E.1 Introduction

Many scientific studies have been conducted in South African gold mines to understand the seismicity in front of tabular stopes (McGarr, 1971; McGarr et al., 1975; McGarr et al., 1979). Many small seismic events and large tremors in South African gold mines were caused by high stress concentrations due to excavation (McGarr, 1971; McGarr et al., 1975). Dense seismic networks were installed in the inferred seismogenic areas in advance of excavation to better observe seismic events in front of stopes, (Yamada et al., 2007; Yamada et al., 2005). It has been concluded that relatively large seismic events in South African gold mines are frequently the results of rock shear failure, similar to natural earthquakes in terms of mechanisms and source parameters (McGarr, 1994; McGarr et al., 1979; Richardson and Jordan, 2002; Spottiswoode and McGarr, 1975).

Mponeng mine is a gold mine in South Africa's North West Province, one of the deepest underground gold mines in the world. Some studies have been conducted in this gold mine to address mine seismicity and rockburst problems (Kwiatek et al., 2011; Yamada et al., 2007; Yamada et al., 2005). Figure E - 1(a) shows the mining layout and a research area, denoted by different colors. Nine triaxial borehole accelerometers (green triangles) were installed within 200 m along a haulage tunnel at a depth of 2650 m (Ogasawara, 2002; Yamada et al., 2005). Five mining-induced seismic events (red circles) were observed from February to October, 1996. Here, seismic event 1 is selected to conduct the case study.

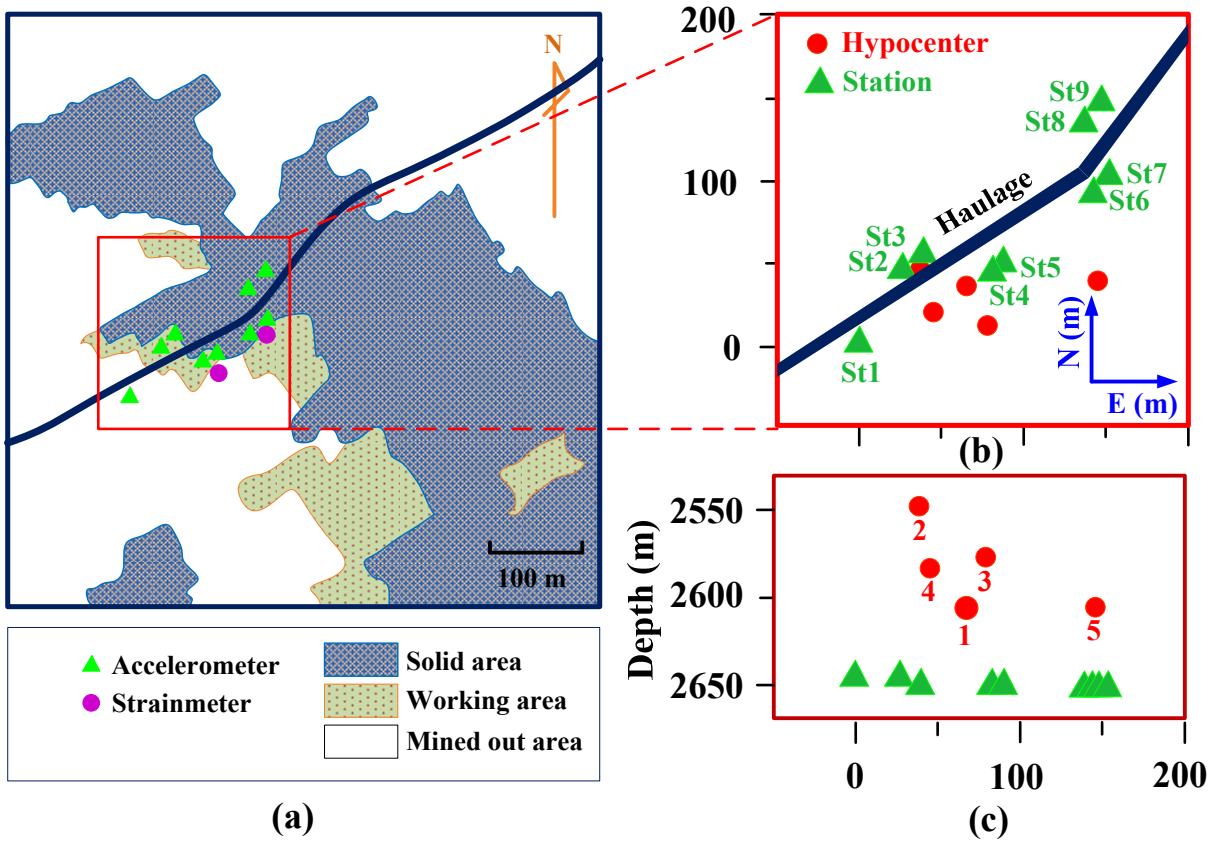

Figure E - 1: (a) Receiver stations and mining layout. For the gold reef, blue/green/white areas stand for solid gold reef/working/mined-out areas from mining activities from February to October 1996, respectively. The haulage tunnel is denoted by the dark blue line. Accelerometers and strain-meters are installed along the haulage tunnel and are denoted by the green triangles and pink circles, respectively; (b) an enlarged map view that highlights the research area and nine receivers (denoted by green triangles in E-N cross-section); (c) receiver locations (green triangles) and derived five hypocenters (red circles) projected in the vertical cross-section that passes through the tunnel axis. (E, N) = (0, 0) corresponds to the St1 (receiver 1) location (after Yamada et al. (2005)).

This seismic event was considered as a fault rupture event. Yamada et al. (2005) estimated from their study that the rupture speed was about 2500 m/s (which is 65% of the shear wave velocity of the rock). After a series inverse analyses, they found that the dynamic rupture process of the event and other nearby events were similar to that of large natural earthquakes.

E.1.1 Study area description

A research area of 200 m × 200 m is determined (Figure E - 1(b)) that includes seismic event No.1 to conduct this case study (Figure E - 1(c)) to conduct this case study. More details about this seismic event are discussed in Section E.2. Figure E - 2 illustrates the configuration of the study area, which consists of the gold reef, the host rock, open stopes, and the haulage tunnel. The rock types above and below the reef are basalt and quartzite, respectively. The gold reef thickness is 0.2 to 0.3 m and is dipping 20° towards the southeast. The open stopes (height 1 m) are about 50 m above the haulage tunnel, which has a width of 5 m. Accelerometers (green triangles) are installed at a depth of 15 m from the collars in sub-horizontal boreholes to avoid the influence of the tunnel on seismograms.

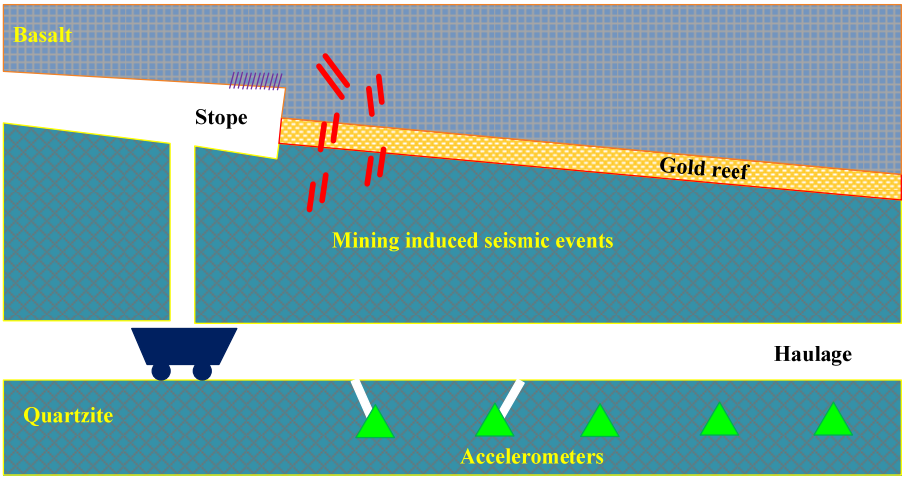

Figure E - 2: Schematic view of the observation system at Mponeng mine. Accelerometers (green triangles) are installed in the walls using 15 m long sub-horizontal boreholes. The width of the haulage tunnel is 5 m. The gold reef width ranges from 0.2 to 0.3 m and the height of the stope is about 1 m. There are no faults and dykes causing offsets of the reef and the stope in and around the observation area. Modified from Yamada et al. (2005).

During the mining period from February to October, 1996, more than 25,000 seismic events were recorded. The recorded waveform data have very high signal-to-noise ratios and the wave amplitudes were low in the tail portion of the recorded waveforms at all the receivers, which suggests that the medium in this study area is relatively homogeneous (Yamada et al., 2007). In addition, Ogasawara (2002) investigated the site effect and concluded that there was no large site effect because there were no faults, dykes, and other major structures in and around this observation area. The field data collected at this study area therefore provide a good opportunity to conduct a case analysis.

E.2.2 Model set up

SPECFEM3D is a powerful solver for wave simulation but it does not have a good pre-processor to create high quality hexahedral meshes. Hence, a challenge for successful application of 3D wave simulation is mesh generation. CUBIT (http://www.csimsoft.com/) is a powerful mesh generation tool and it can generate high quality hexahedral meshes for very complex geometries. It is used in this study.

It is found that generation of high quality hexahedral mesh is not an easy task, even for simple models. The complex model geometry (especially the mined-out stope and the gold reef area) is decomposed into many meshable sub-volumes to generate a high quality hexahedral mesh. Based on the geometry provided in Figure E - 1and Figure E - 2, a 3D model is constructed and shown in Figure E - 3. The model size is 200 m × 200 m × 150 m, and the volume is divided into 311 sub-volumes that can be properly meshed. The model is meshed with an average element size of 2 m along the haulage tunnel, 0.5 m for the orebody (the thickness of gold reef is simplified to 0.5 m), and 3 m for other rocks. The mesh is refined near the tunnel (as shown in

Figure E - 3). As a result, this model contains 524,938 spectral elements and 544,483 nodes. The whole mesh is partitioned into 12 sub-domains for parallel computation.

Table E - 1 lists the material properties. The parameters are estimated from field observation and laboratory tests. Table E - 2 shows spatial location of each receiver. Figure E - 4(a) presents shear velocity model and layout of receivers in the 3D model. Nine receivers are placed along the haulage tunnel to have a direct comparison between the synthetic seismograms and the recorded waveforms, as shown in Figure E - 4(b) and Figure E - 1. Attenuation is not considered in order to reduce computation time because of the large number of elements in the model.

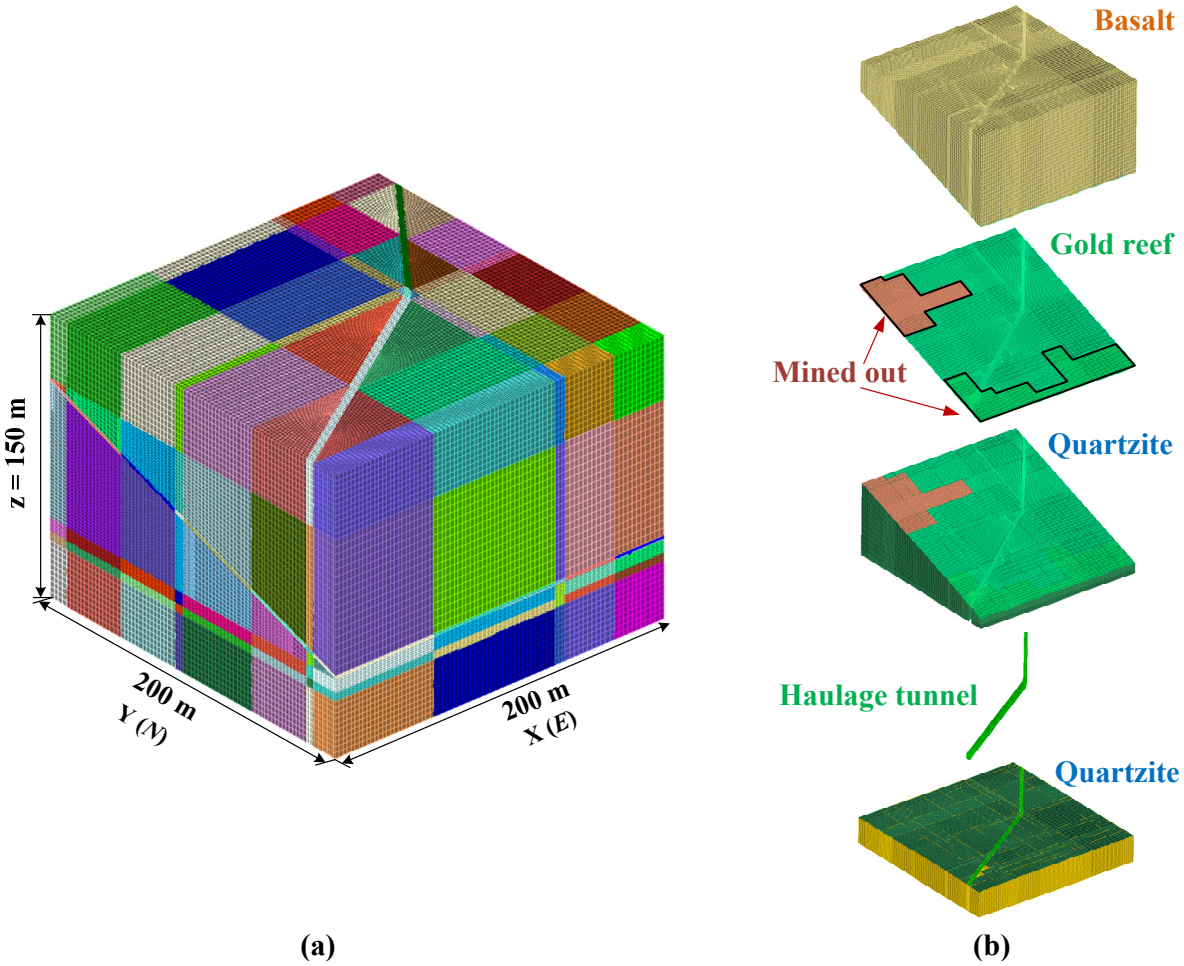

Figure E - 3: (a) Spectral element mesh of the model, which is decomposed to 311 meshable sub-volumes; (b) perspective decomposition view of the rock domains and structures (basalt, gold reef, quartzite, mined-out area, and haulage tunnel) in the spectral-element mesh after combining the sub-volumes.

Table E - 1: Model material properties

	ρ (kg/m^3)	ν	V_p (m/s)	V_s (m/s)
Basalt	2740	0.24	6200	4000
Gold reef	2850	0.22	6500	4200
Mined-out stope	1	N/A	300	0
Quartzite	2680	0.26	6000	3800
Haulage tunnel	1	N/A	300	0

Table E - 2: Spatial locations of nine receivers and the source-receiver distances

	St. 1	St. 2	St. 3	St. 4	St. 5	St. 6	St. 7	St. 8	St. 9
x (m)	0	26.4	38.8	81.6	88.7	142.6	152.1	137.7	146.1
y (m)	0	45.8	56.5	44.6	49.4	91.1	102.4	134.5	147.6
z (m)	120	120	120	120	120	120	120	120	120
r (m)	86.16	57.74	53.4	48.6	52.5	105.2	118.2	129.3	143.9

Notes: Location of each receiver is denoted by (x, y, z), which is derived from East/North/ Depth. The depth (z) for all receivers is 120 m and r denotes the source-receiver distance (m).

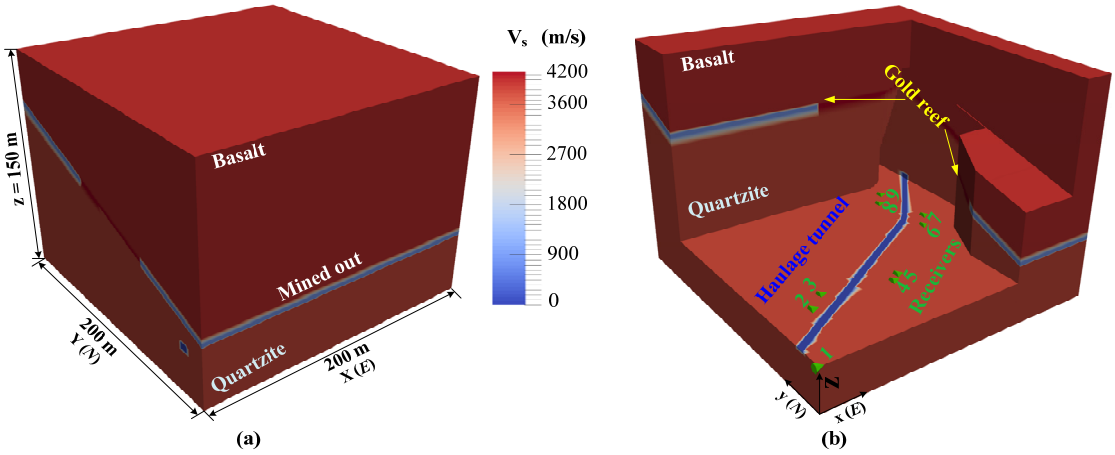

Figure E - 4: (a) Shear wave velocity model for various computation domains. Shear wave velocities are represented by the color scale; (b) receivers for synthetic seismogram calculation are denoted by green triangles and are numbered from 1 to 9.

E.2 Seismic source representation

In the thesis, moment tensor point sources were used to represent far-field fault-slip seismic events. In this case study, however, a point source representation may not be appropriate and a non-point source model is required for near-field source models. This is because the seismogenic

area is only 50 m above the tunnel and the receivers. Near-field source representation therefore holds the key to obtaining a good understanding of the near-field source seismic response. As noted in Chapter 2, kinematic (dislocation model) and dynamic (crack model) fault source models are two non-point source models. The moment tensor and the finite kinematic source models are investigated here to provide a preliminary insight of the influence of the seismic source model on seismic response.

The overburden stress is about 70 MPa in this study area and stress concentrations due to stope excavation usually cause seismic events in the front of the stopes, as shown in Figure E - 2. As stated above, those seismic events are the result of shear failure of rocks (McGarr, 1971) and are similar to natural earthquakes in terms of source mechanism and parameters (McGarr, 1994; Spottiswoode and McGarr, 1975). Considering the quality of the recorded waveforms and the derived normal fault-slip mechanism from Yamada et al. (2005), seismic event No.1 (Figure E - 1(c)) is selected for this case study.

Seismic event No.1 occurred on July 9, 1996 and it had a moment magnitude of M_w = 1.4 and its hypocenter was derived at East = 62.7 m, North = 39.0 m, and depth = -2605.6 m, which corresponds to x = 62.7 m, y = 39.0 m, and z = 75.6 m in the simulation model. Based on the inverse analysis from Yamada et al. (2005), information on the fault and the auxiliary planes corresponding to this event are determined as 59.8°/75.1°/-91.3° and 245°/15°/-85° for the strike/dip/rake, respectively. The derived parameters indicate that this event is a normal fault seismic event, which corresponds well with the vertical stress concentration near the stope mining front. Based on these data, source parameters for the moment tensor point source model and the finite kinematic source model can be determined to represent this seismic event. The

source parameters for the moment tensor point source model are determined in the same manner as discussed in Chapter 4.

For the kinematic source model, the fault plane is divided to a series of sub-faults and each sub-fault is considered as a point source (Boore, 2003; Doornbos, 1982; Miyake et al., 2003). According to the type of rupture model (i.e., unilateral or bilateral rupture) and the rupture velocity (i.e., sub-shear or super-shear), the space-time distribution of each sub-fault slip is estimated. Source parameters, such as nucleation point position, rupture area, rupture velocity, rise time, time function need to be determined. The length and width of the rupture area and the number and size of the sub-faults can be estimated from the intensity of the seismic event according to empirical relations (Beresnev and Atkinson, 2002; Dowrick and Rhoades, 2004; Haddon, 1996; Mai and Beroza, 2000; Wells and Coppersmith, 1994).

In this preliminary study, the kinematic seismic source parameters are determined through a comparison of the recorded and the synthetic seismograms using the trial-and-error method. After conducting a large number of iterative simulations, one possible schematic representation of the potential fault plane and the source rupture model was derived and is shown in Figure E - 5. The fault plane ($\phi_s/\delta_d/\gamma_r$ = 59.8°/75.1°/-91.3°) and the hypocenter ((x, y, z) = (62.7, 39.0, 75.6) m), which are derived by Yamada et al. (2005) in their inverse analysis, are shown in Figure E - 5(a). The point source model is shown in Figure E - 5(b) and the kinematic rupture source model is illustrated in Figure E - 5(c) and (d). The derived fault area is considered as a square shaped fault plane (21 × 21 m^2) (Yamada et al. (2005)), which is divided into 7 × 7 = 49 sub-faults. The center of the fault plane corresponds to the hypocenter of seismic event No.1. For each sub-fault, a moment tensor source model is used and the sum of the seismic moments for the 49 sub-faults is constrained by the seismic moment of the event that has a moment of M_w = 1.4 ($M_0 = 1.6\times10^{18}$

dyne·cm). Based on the results by Yamada et al. (2005), the rupture velocity is estimated as 2500 m/s (65% shear wave velocity). The time interval between each sub-fault is 0.0012 s in the model. Figure E - 6 shows workflow for the 3D seismic wave modeling in this section.

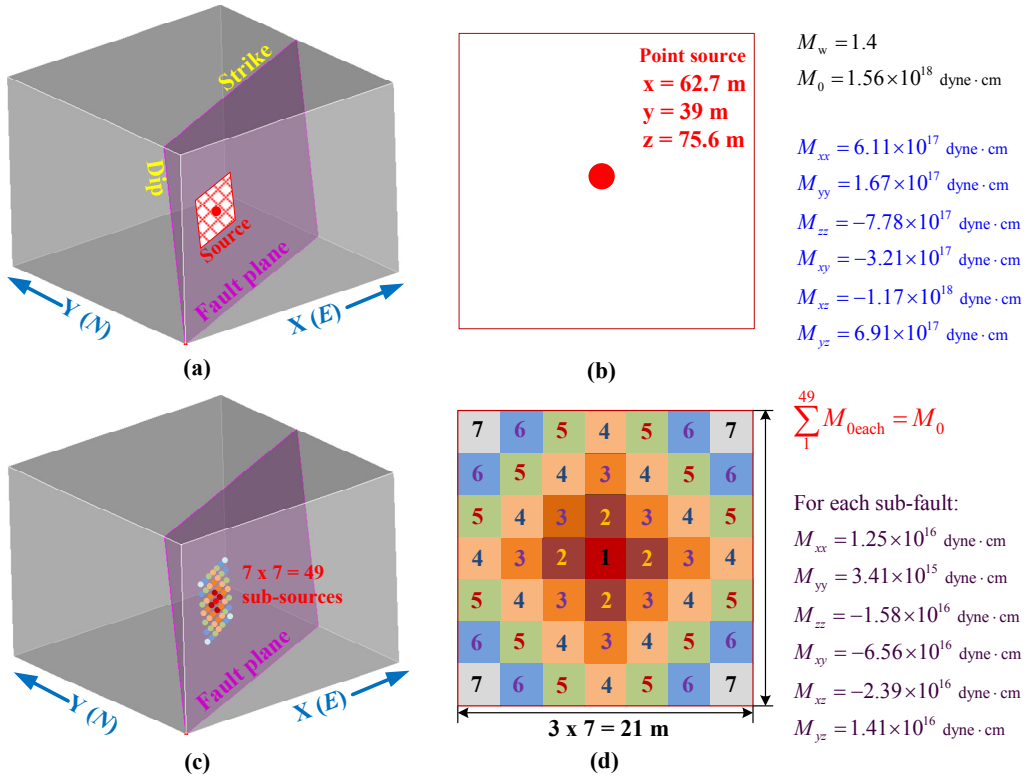

Figure E - 5: (a) Derived potential fault plane and the seismic source hypocenter; (b) the point source model. The kinematic rupture source model is shown in (c) and (d).

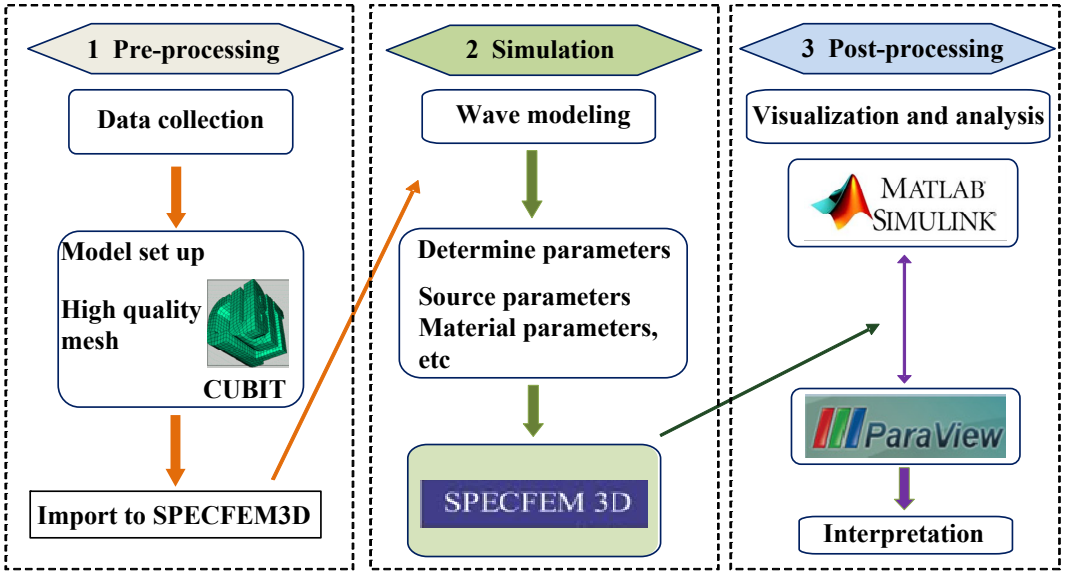

Figure E - 6: Workflow for 3D seismic wave propagation modeling.

E.3 Modeling results and discussion

E.3.1 Source radiation evolution

The focus of this study is to understand the influence of different source models on the seismic response in the near-field. Source radiation evolutions of different source models are firstly examined by visual inspection of the vertical velocity component contours in the area near the seismic source. As shown in Figure E - 7, contours of the vertical velocity component (V_z) are used to visualize seismic wave evolution at different times. Figure E - 7(a) and (d) show the wave radiation patterns for the moment tensor point source model and the kinematic rupture source model, respectively. It is seen that the wave radiation patterns are different for the two source models. The kinematic rupture source model seems to model the characteristics of fault plane slip better than the point source model when the near-field wave patterns are considered.

Figure E - 7(b) and (c) present the V_z contours in the fault plane. In the point source modeling results, the maximum V_z value (about 180 m/s) is observed at t = 0.004 s, which could not be shown in Figure E - 7(b) for the given velocity range (-3 to 3 m/s). As the waves propagate, the V_z values decrease quickly, which suggests that all seismic energy is released when the point source is triggered. On the other hand, the kinematic characteristic of the fault plane is observed when the kinematic rupture source model is used (Figure E - 7(c)). In this case, the maximum V_z (about 30 m/s) is obtained at t = 0.008 s when all the 49 sub-faults are triggered or activated at t = 0.0072 s, which could not be shown in Figure E - 7(c) for the given velocity range (-3 to 3 m/s). This makes sense because the activation of a fault slip cannot be finished instantly and there is a process of fault rupture propagation. Hence, the kinematic source rupture model is preferred for

near-field source representation compared with the point source model. This will be further discussed using the seismograms in the following section.

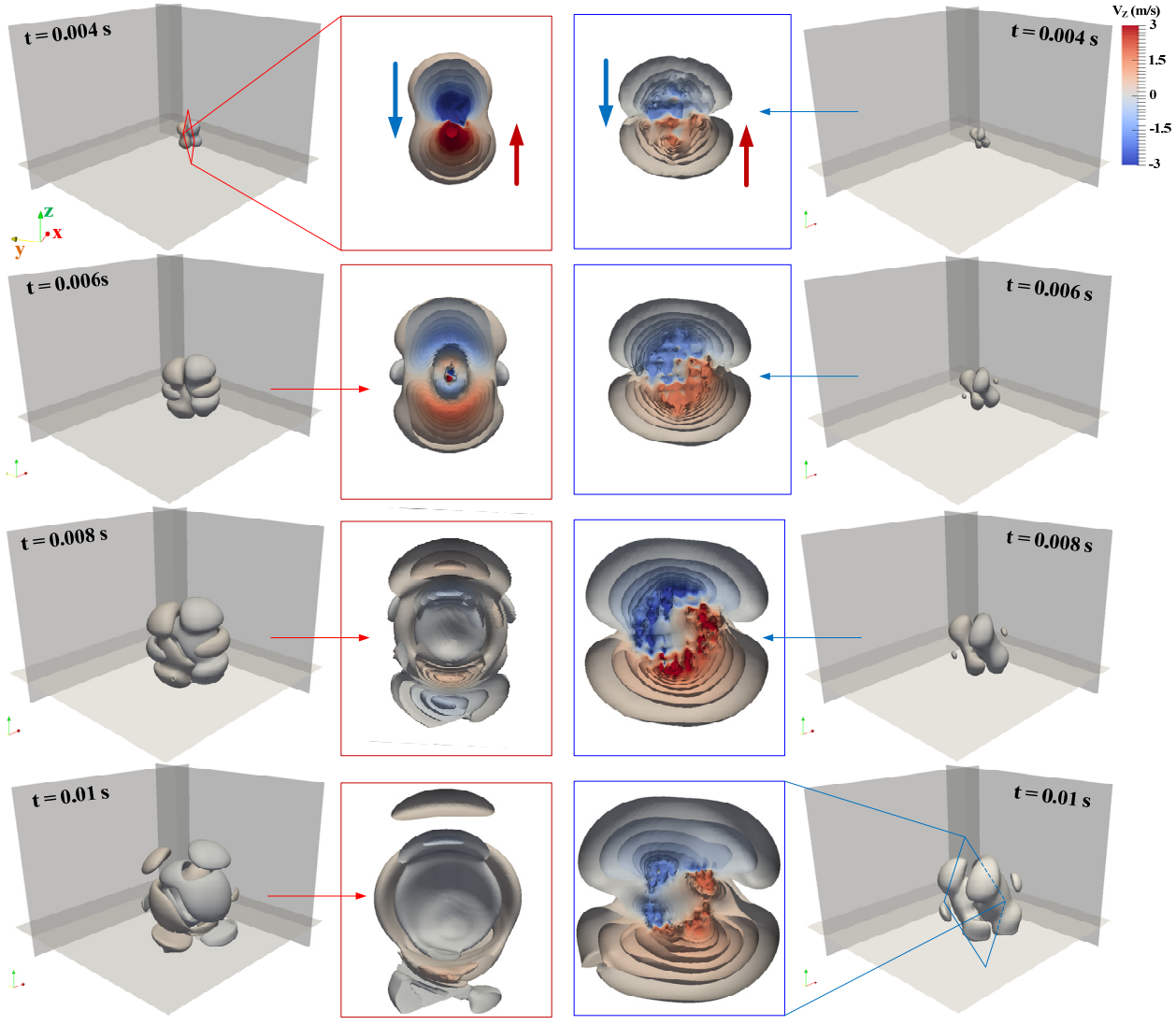

Figure E - 7: Contours of the vertical velocity component (V_z) at four propagation times (t = 0.004, 0.006, 0.008, and 0.01 s) for the moment tensor point source model (a) and the kinematic non-point source model (d). The V_z contours along the fault plane are shown in (b) and (c) for the point source and non-point models, respectively. It should be noted that the velocity values at some locations are much higher than 3 m/s but the velocity is scaled from -3 to 3 m/s.

E.3.2 Influence of the haulage tunnel and mined-out areas on the wavefield

The geological settings are relatively simple in this model, which provides a good case for studying the influence of the haulage tunnel and the mined-out areas on wave propagation. Isosurfaces of the vertical velocity component are used to examine the wavefield (Figure E - 8).

Figure E - 8 presents the V_z isosurfaces at five propagation times for the point and the non-point (kinematic rupture) source models. Different V_z values are selected to generate the isosurfaces to compare the results from the two source models. At early stages of wave propagation (t = 0.06 s and t = 0.01 s), small but detectable differences in the wavefields are observed. The kinematic rupture source model can model the fault area better than the point source model in the near-field source representation. At later stages of wave propagation, the wavefields have similar patterns. Again, the wavefield difference in the early stage of wave propagation around the source area could be expected because different seismic source models are used.

In addition, the influence of the haulage tunnel and the mined-out areas on the wavefields can be seen from results for both source models, as indicated by the red dash line circled areas in Figure E - 8 at t = 0.03 s and t = 0.04 s. Complex wavefields are observed around the areas of the haulage tunnel and the mined-out stope. The types of complex wavefields can only be captured when detailed geometries of the tunnel and stopes are properly considered in numerical modeling.

A homogenous model (rock mass is assumed uniform in the model and it uses the property of quartize) was considered to further examine the influence of the haulage tunnel and mined-out areas on seismic wave propagation, V_z contours of the kinematic rupture source model at t = 0.04 s for the homogenous model and the heterogeneous model (which includes different rock

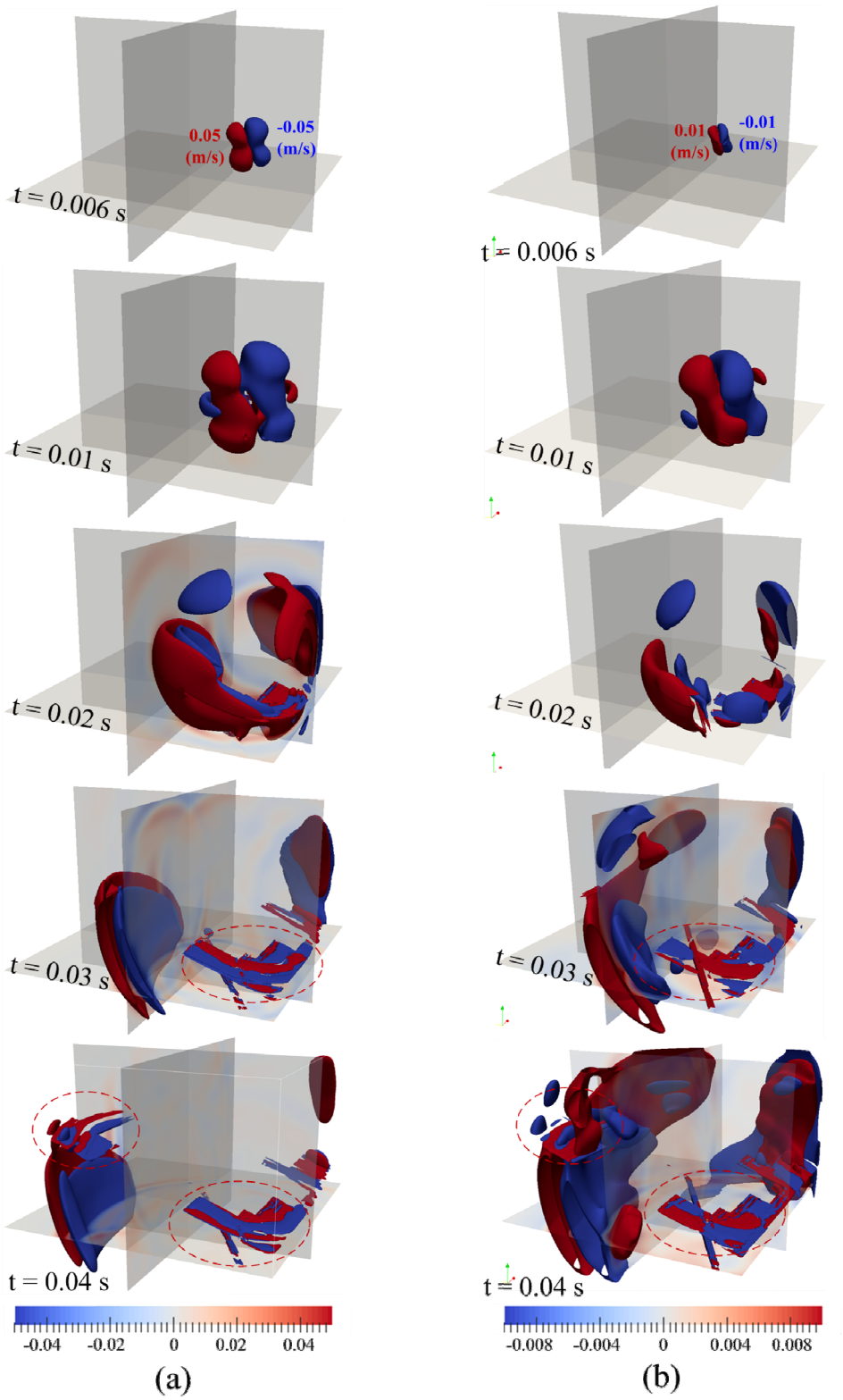

Figure E - 8: Isosurfaces of the vertical velocity component (V_z) at five propagation times (t = 0.006, 0.01, 0.02, 0.03, 0.04 s) for the moment tensor point source model (a) and the kinematic non-point source model (b). V_z isosurfaces are plotted for -0.05 to 0.05 m/s (a) and -0.01 to 0.01 m/s (b) for the point and non-point source models, respectively. Red and blue indicate upward and downward velocities, respectively.

domains, haulage tunnel, and mined-out areas) are dissected into different V_z values and are shown in Figure E - 9.

It is seen that large wave velocities are generated around the haulage tunnel and the mined-out area when compared with the results from the homogeneous model (Figure E - 9(a)), indicating that mine structures can alter ground motions. The maximum vertical velocity is 0.035 m/s in the homogenous model; however, in the heterogeneous model, the maximum vertical velocity is V_z = 0.1 m/s and it appears on the top of the haulage tunnel and the mined-out area in the south-east side of the gold reef (Figure E - 9(b)). Only a certain part of the haulage tunnel is subjected to this strong ground motion (blue area in Figure E - 9(b)). Although there are many other factors that cause rockburst damage, the pattern of elevation ground motions suggests that these areas may be more prone to failure if all other factors are equal. Furthermore, relatively large V_z values (0.025 to 0.05 m/s) are observed around the top of tunnel and the mined-out areas Figure E - 9(b). Moreover, the wavefield is affected by the gold reef and the two rock domains. For example, the influence of different rock types on the velocity field is clear when smaller V_z values (-0.01 and 0.01 m/s) are selected. As shown in the bottom plots Figure E - 9(a) and (b), a simple velocity field is observed in the homogeneous model while a complex and elevated velocity fields are found in the heterogeneous model. Similar to the results discussed in Chapter 6, tunnels and mined-out areas as well as geology can influence the wavefield and an accurate investigation of the problem requires 3D wave propagation modeling such as Figure E - 9 presented in this case study.

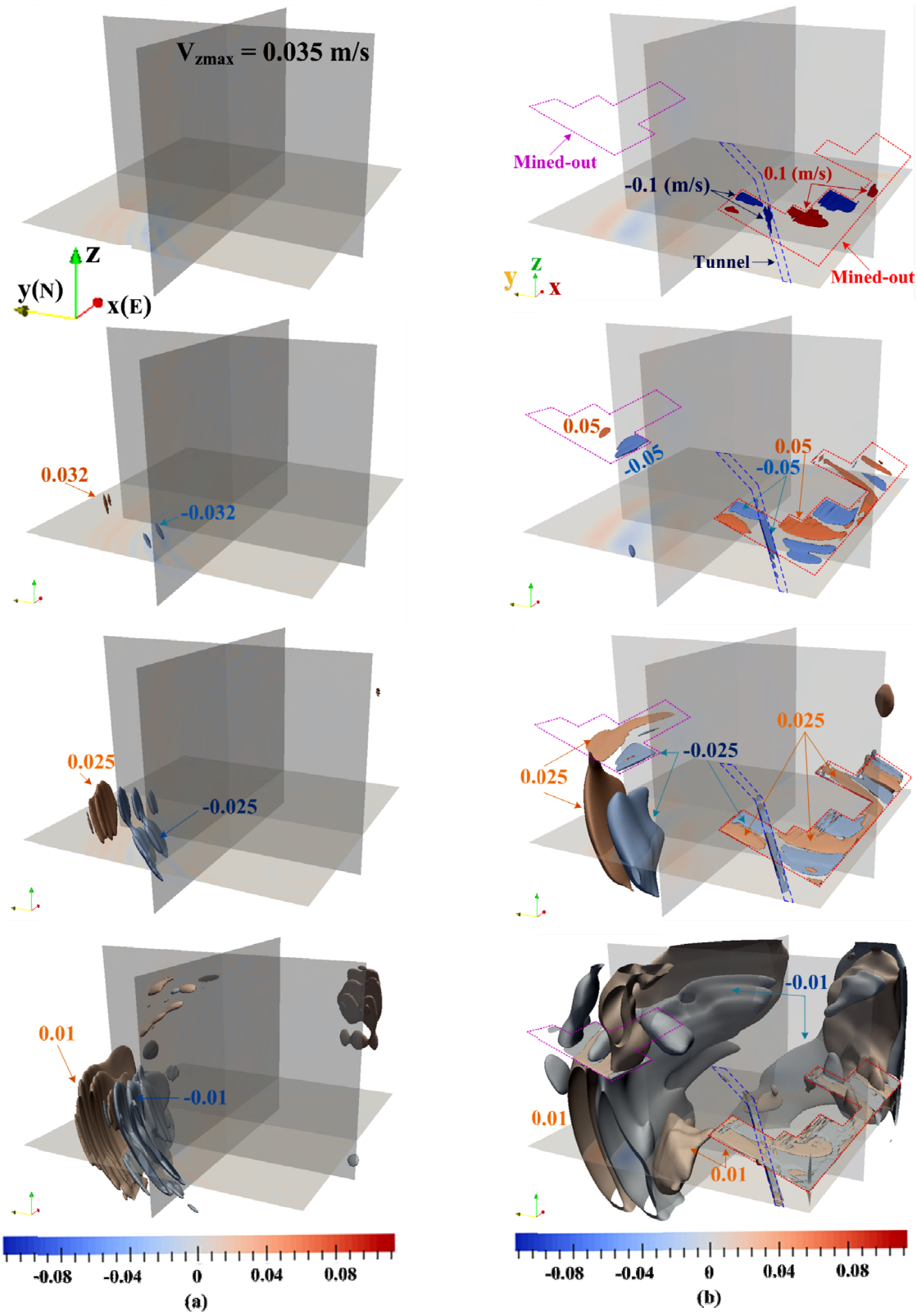

Figure E - 9: Anatomy of V_z contours for the kinematic rupture source model at t = 0.04 s for the homogenous model (a) and the heterogeneous model (b). Various V_z values are selected to show the influence of the tunnel and the mined-out areas on velocity distribution to better illustrate the V_z distribution,

E.3.3 Comparison between the recorded waveforms and the synthetic seismograms

Figure E - 10 presents the field recorded and the synthetic seismograms at six stations of the horizontal velocity component in the x direction (V_x), which are denoted by the black and red lines, respectively. Velocity components of V_y and V_z are not available from the literature and will not be compared here. For receivers 1, 2, and 9, field data are also not available. Some receivers such as St.3, St.4, and St.5 are located very close to the source (as shown in Table E - 2, the distance is around 40 to 50 m from the receivers to the lower edge of the kinematic source). The modeling results only reproduce some portions of the seismograms. Many high frequency components are observed in the recorded seismograms but are not captured in the numerical modeling. Despite this, the maximum amplitude (except St.3) and the initial portion of the seismograms are captured properly.

On the other hand, for receivers St.6, St.7, and St.8 located in the far-field (with a source center-receiver distance from 105 to 130 m (refer to Table E - 2), the simulated seismograms agree well with the recorded seismograms (Figure E - 10), especially in the second portion of the seismograms. Some high frequency components are visible in the simulated seismograms, but to a lesser extent compared with the field data. The amplitudes of the simulated seismograms in the first portion of the seismograms are slightly higher than the amplitudes in the recorded seismograms. This may be caused by seismic wave attenuation. High frequency wave components can be attenuated quickly as waves propagate at distances far away from the source area and a relatively stable wave frequency (say corner frequency) may dominate in the far-field seismograms. The influence of attenuation is not considered in the present simulation due to a constraint of availability of computation resources and it is suggested to check this influence in future studies. Despite of this limitation, the synthetic seismograms are comparable to the field

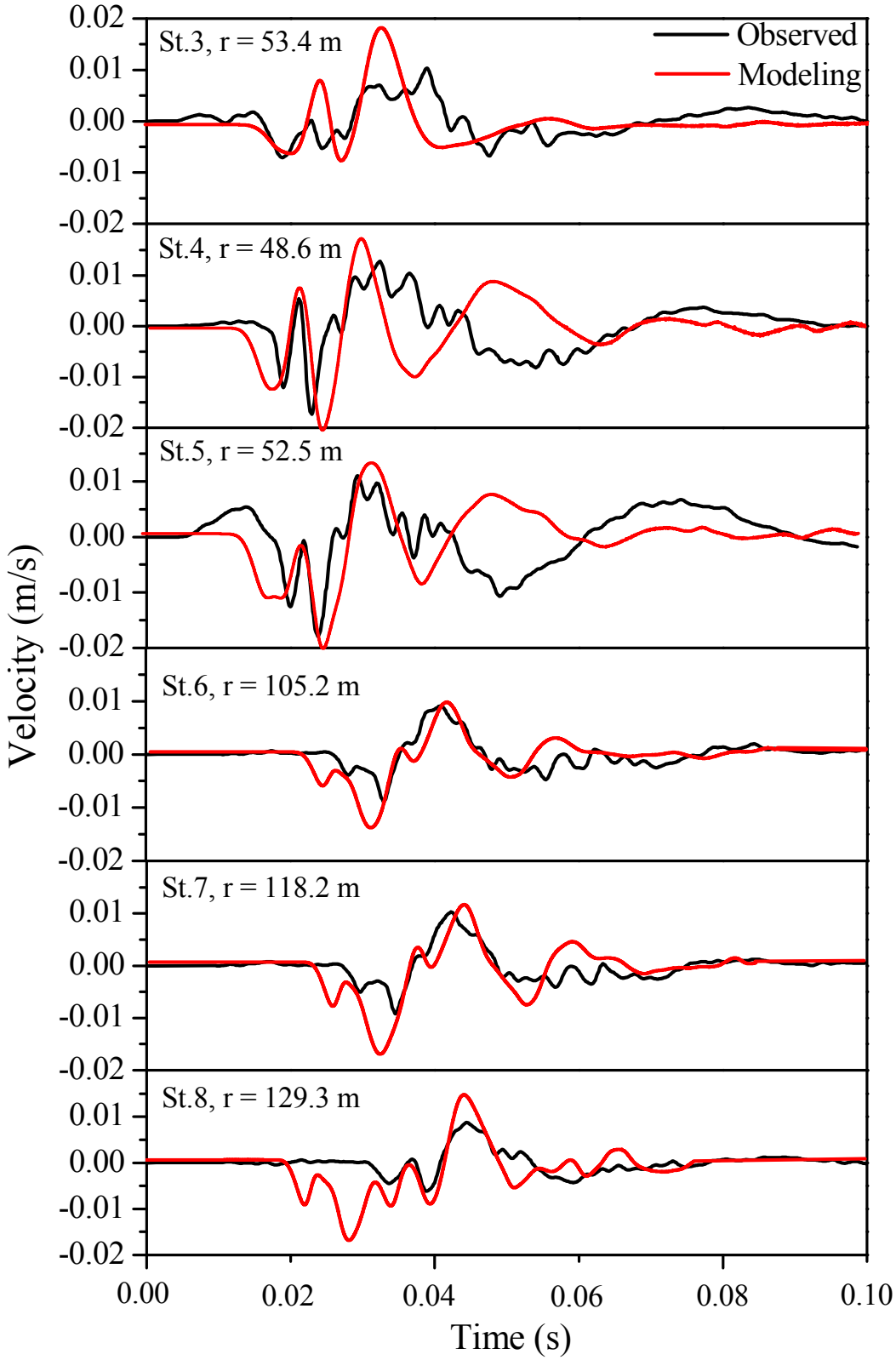

Figure E - 10: Field recorded (solid black lines) and synthetic (dashed red lines) seismograms of V_x using the non-point seismic source model.

waveforms. The modeling result indicates that high frequency wave components could influence ground motion.

The synthetic seismograms of the three velocity components (V_x, V_y, and V_z) for the non-point source model are shown in Figure E - 11. The velocity components of V_x, V_y, and V_z are denoted as red, green, and blue lines, respectively. Six stations, from St.3 to St.8, are selected to show the seismic response at different locations near the haulage tunnel.

It is seen from Figure E - 11 that the seismic responses in terms of the velocity components vary at each station. The seismic response at a station depends not only on the source-target distance, but also on the spatial location relative to the seismic source. For instance, a high vertical velocity component is observed at St.3 (V_{zmax} = -0.041 m/s). The source center-target distance of St.3 is about 53.4 m, which is slightly larger than that for St.4 (48.6 m) and St.5 (52.5 m). Considering the locations of the modeled fault (x = 62.7, y = 39, z = 75.6) and St.3 (x = 56.5, y = 38.8, z = 120) as well as the fault mechanism (dip-slip fault), it is then possible to explain the high vertical velocity component at the receiver.

In most cases, the horizontal velocity components (particularly V_y) have a large contribution to ground motions (see the green lines in Figure E - 11). As mentioned above, all the receivers are installed about 15 m inside the quartzite and are parallel or sub-parallel to the walls of the haulage tunnel. Different ground motions can occur around the haulage tunnel at locations that have similar source-target distances. For example, large ground motion variations can be expected if a receiver is placed at the top, bottom, right or left walls of the tunnel. In addition, high velocity amplitudes occur several times due to seismic wave interactions with geological and mine structures.

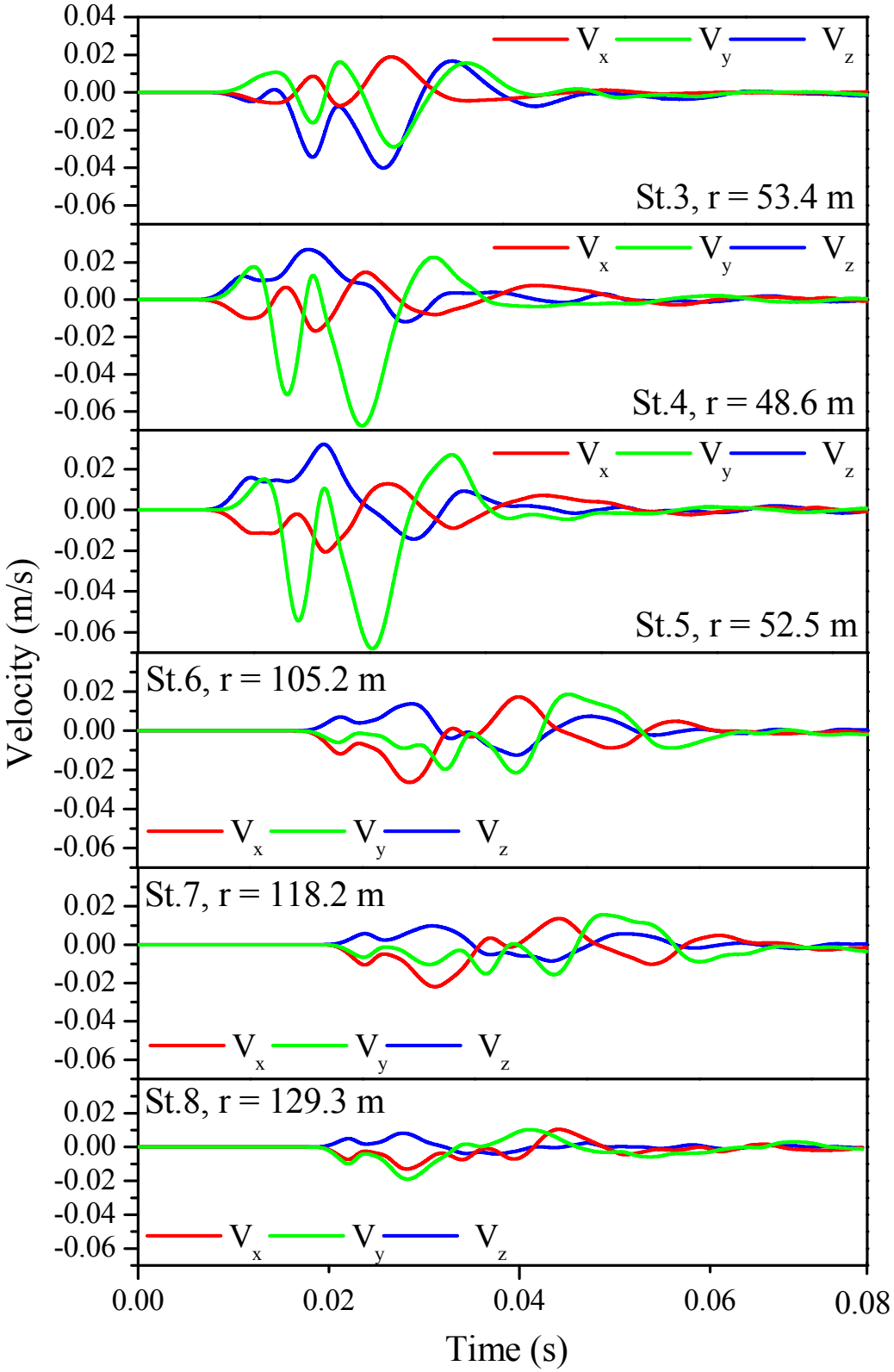

Figure E - 11: Synthetic seismograms of the three velocity components (V_x, V_y, and V_z) for the non-point seismic source model. Red, green, and blue lines denote the V_x, V_y, and V_z, respectively. Stations from 3 to 8 are selected to illustrate the modeling results.

A comparison between the recorded and the synthetic V_x seismograms from the point and non-point source models at two stations (St.4 and St.7) are shown in Figure E - 12. Black, red, and blue lines stand for the recorded seismograms and synthetic seismograms from the point and non-point source models, respectively. The seismograms from the point source model do not match well with the recorded waveforms for both St.4 and St.7. However, the synthetic seismograms from the non-point source model agree with the recorded waveforms well, especially for the first portion of St.4 and the second portion of St.7. This further suggests that the non-point source model could be a better source representation than the point source model when the near-source wavefield is of interest.

It can be seen from Figure E - 12 that there are some discrepancies between the simulated and the recorded waveforms in some portions of the seismograms. For instance, although negligible, there is a shift of the first arrival P-wave at St. 4; there is also a misfit in the seismogram for the propagation time between 0.025 and 0.05 s. The misfit is relatively large in the first part of the seismogram at St.7, although the simulated waveform resembles the recorded one well (from t = 0.02 to 0.035 s). This is not surprising because we are dealing with very complex geological,

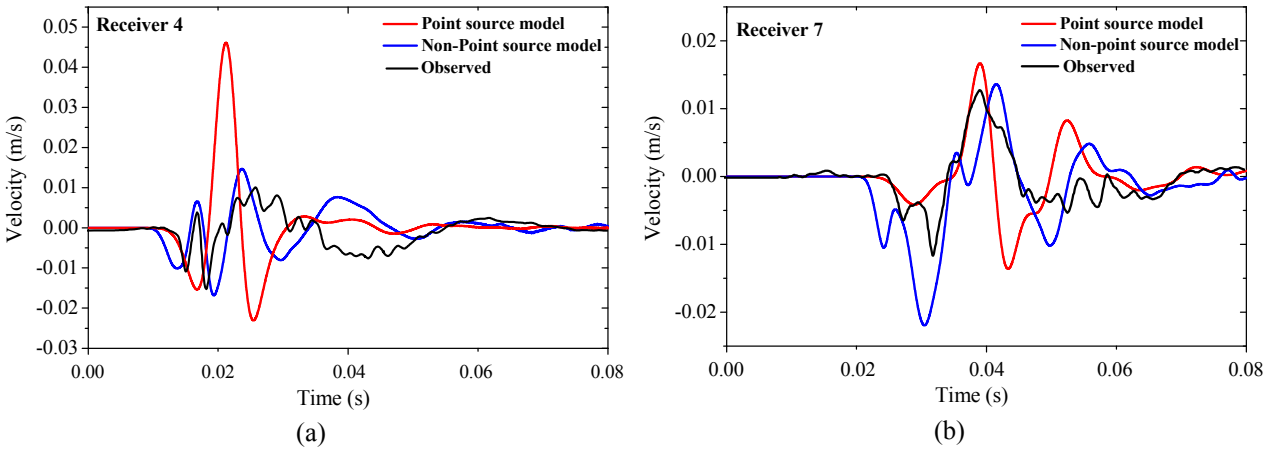

Figure E - 12: Recorded and synthetic seismograms of the horizontal velocity component (V_x) at St.4 (a) and St.7 (b) for the point and non-point source models.

geometrical, and geotechnical conditions in a deep underground mine. In addition, the seismic response in the near-field is also less understood. Even though the recorded seismograms cannot be reproduced exactly, the agreement between the results from the non-point source model and the field data suggests that the adopted non-point source model captures the major wavefield response. Hence, non-point source models should be considered in numerical modeling when studying near-field wave propagation.

E.3.4 PPV comparison of results from numerical modeling and the design scaling law

Scaling laws are known to provide an estimation of PPV for the far-field, but not for the near-field. Without capping the PPV in the near-field or near-source areas, scaling laws will hence over predict PPV in these areas. Furthermore, the scaling laws do not consider the spatial distribution of wave propagation due to a fault-slip event, and it will over predict PPV in some orientations in the far-field.

Figure E - 13 presents recorded maximum V_x values (pink balls) and the maximum V_x (red circles) from the numerical modeling. For reference, other two velocity components (V_y and V_z), at the time of maximum V_x, are also plotted in Figure E - 13. All amplitudes of each velocity component are plotted as absolute values. The contributions from different velocity components at each receiver can be observed from this figure. It can be seen that V_y makes a large contribution to the ground motion for St.4 and St.5, and V_z makes a large contribution to the ground motion for St.3, St.6, and St.7. In addition, the maximum values of V_x from the numerical modeling are in agreement with the field data at most stations.

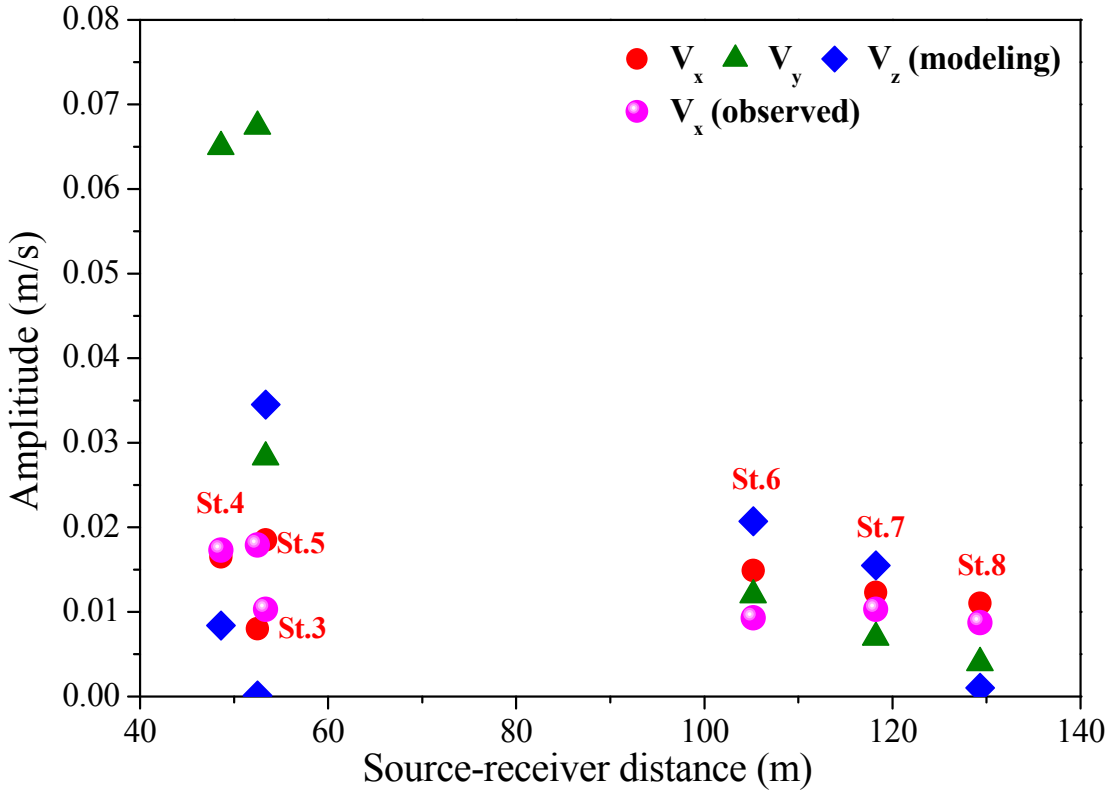

Figure E - 13: Maximum V_x recorded in the field (pink balls) and from numerical modeling (red circles), along with the corresponding V_y (green triangles) and V_z (blue diamonds) values when V_x reached its peak value in the numerical modeling at 6 receiver stations.

As discussed in Chapter 7, site amplification can alter ground motion in rocks near the excavation surface. Twelve surface receivers (six are placed on the walls and six on the roof) were placed around the haulage tunnel in the numerical model, which correspond to the receivers that were installed inside the quartzite. Again, no surface receivers were installed in the field; hence, it is not possible to compare the modeling results with the monitoring data.

Figure E - 14 presents PPV values for three types of receivers from the numerical model and PPV values from the scaling law at different confidence levels (10%, 33%, 50%, 67%, and 90%). It should be noted that the estimated PPV values are based on the field data from Creighton mine in Canada, not from Mponeng mine in South Africa. The reason why these PPV values are plotted in Figure E - 14 is to provide a reference for comparison. All the PPV values of the

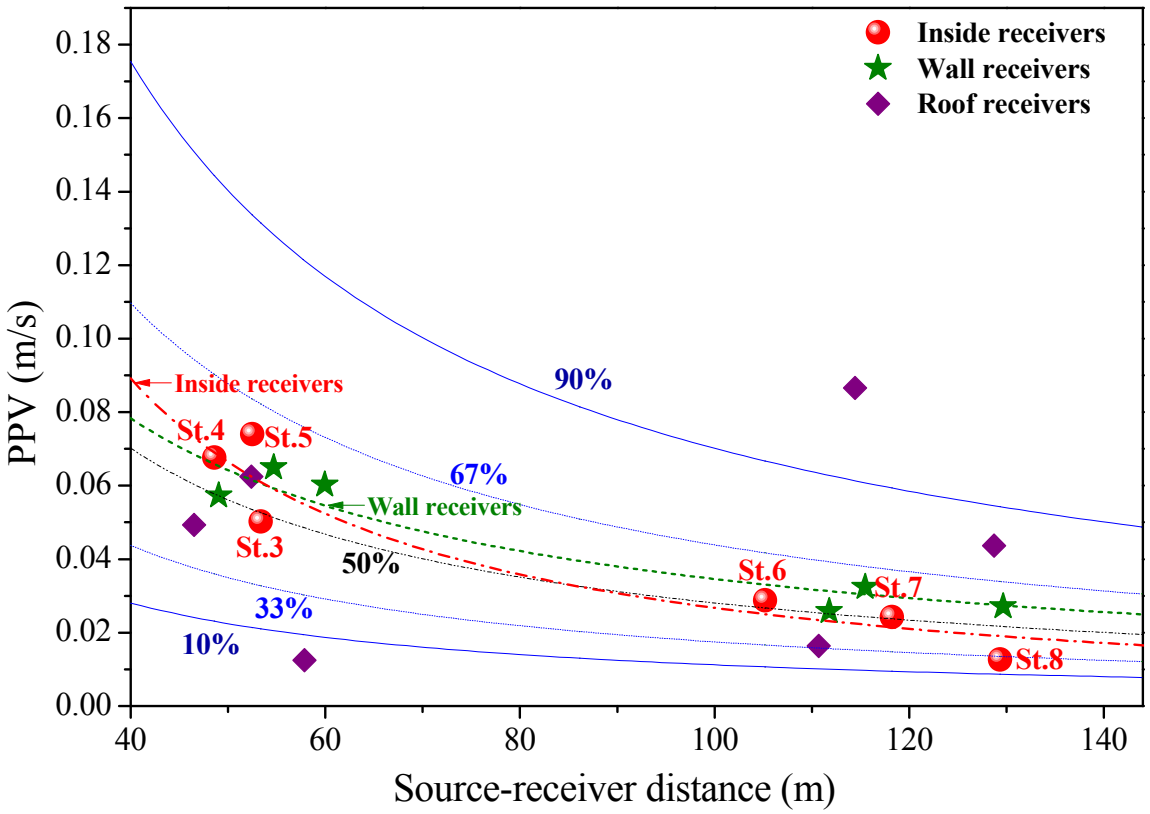

Figure E - 14: PPV distributions for three types of receivers form the numerical model. PPV values from the scaling law are also plotted at different confidence levels. PPV values estimated from the scaling law are based on field data from Creighton mine in Canada.

eighteen receivers (six inside receivers – red balls, six wall surface receivers – green stars, and six roof surface receivers – purple diamonds) are calculated using Matlab based on the synthetic seismograms from the numerical modeling. Although the scaling law is derived using data from hard rock mines in Canada, it still seems that it is applicable to this case study. As shown in Figure E - 14, the PPV values from the numerical modeling agree with the PPV ranges estimated from the scaling law. The modeled PPV values are more close to that from the scaling law at the average confidence level and with some PPV variations. For the insider receivers (red balls) without less influence of the tunnel, the PPV values agree with that from the scaling law with an average confidence level. Although some higher and lower PPV values are observed, the PPV fitting line (red dash line) fits the average PPV fitting line (solid black line) well. For the wall

receivers (green stars) with a large influence of tunnel, the PPV values are slightly higher than the PPV values from the scaling law with the average confidence level. The PPV fitting line (dash green line) of the wall receivers is slightly higher than the average PPV fitting line, indicating the tunnel can affect the ground motion and higher ground motions are expected at the tunnel surface. For the roof receivers (purple diamonds), the PPV distribution is complex in the tunnel roof. High and low PPV values are found in the roof receivers, which again indicate that the PPV is influenced by the tunnel surface. As can be seen from Figure E - 14, only one roof receiver has very high PPV and one roof receiver has very low PPV values, which is exactly what is predicted by the scaling law with a confidence level of 90% and 10%. In addition, for the wall and inside receivers, all the modeling results lie in the confidence level ranges from 33% to 67% (e.g., ±1 standard deviation of normal distribution). The modeling results of this case study further validated the applicability of the scaling law in underground hard rock mines.

Due to different spatial locations of the receivers, various site amplifications will appear at various surface locations around the tunnel. Compared with the ground motion at the inside receivers, site amplification is observed at the roof and wall receivers for certain locations (Figure E - 14). For instance, the PPV values of roof and wall receivers near St. 7 are 3.7 and 1.4 times larger than the PPV at the inside receiver St.7. The PPV values of roof and wall receivers near St. 8 are 3.5 and 2.2 times larger than PPV value at the inside receiver St.8. This result further demonstrates the site amplification effect can be caused by seismic wave interaction with underground structures.

E.4 Summary

A case study of seismic wave propagation in a South African gold mine is conducted to demonstrate the applicability of SPECFEM3D for wavefield modeling and to increase the confidence of 3D modeling in the near-field. Two source models, i.e., point moment tensor and kinematic rupture source models are considered for near-field seismic source representation. Through numerical tests using the trial-and-error method, the parameters for the non-point source model were determined and the obtained synthetic seismograms agree with the field observation data. The modeling results demonstrate the influence of geology and excavation on ground motion. It is seen that the non-point source model could be a better representation of the fault-slip seismic source than the point source model when near-field seismic response is of interest. Another benefit from this case study is that techniques such as high quality mesh generation, parallel computing using CPUs and GPUs, and post-processing have been acquired for wave propagation modeling using SPECFEM3D. This increases the confidence of using SPECFEM3D for realistic ground motion modeling in complex underground mines.

In many cases, rockburst damages in tunnels are caused by seismic events occurring not far away from the damage locations. Near-field wavefield analysis should be conducted in such cases. Ground motion in the near-field is complex and not well understood. As noted by Potvin and Wesseloo (2013), due to a lack of reliable near-field data, traditional approaches to define ground motion in the near-field may be inadequate and more or less oversimplified. It should be noted that the kinematic rupture source representation used in this study should be viewed as a high level preliminary approximation. It describes only the kinematic features of a fault slip event and it does not consider the dynamic features of fault slip, such as the constraint of in situ stress,

stress drop, and fracturing mechanism. More studies are needed in this study area, using more refined models that are quantitatively constrained by in situ stress and other properties from geophysical observations.

Curriculum Vitae

Name: Xin Wang

Post-secondary Education and Degrees:

China University of Mining and Technology, Beijing
Beijing, P.R. China
2005-2009 B.A.

China University of Mining and Technology, Beijing
Beijing, P.R. China
2009-2012 M.A.

Laurentian University
Sudbury, Ontario, Canada
2012-2015 Ph.D.

Related Work Experience:

Research Assistant
Laurentian University
2012-2015

Researcher at GRC
MIRARCO-Mining Innovation
2012-2015

PhD Thesis Related Publications:

Wang, X., Cai, M., 2014. Wave propagation simulation in underground mines by SPECFEM2D. In: Proceeding of Proceedings of the seventh international conference on deep and high stress mining, Sudbury, 723-738.

Wang, X., Cai, M., 2015. Influence of wavelength-to-excavation span ratio on ground motion around deep underground excavations. Tunnelling and Underground Space Technology 49, 438-453.

Cai, M., Wang, X., 2015. A Non-uniform velocity model and FLAC/SPECFEM2D coupled numerical simulation of wave propagation in underground mines. In: Proceeding of the 13th International ISRM Congress 2015, Montreal, Canada.

Wang, X., Cai, M., 2015. FLAC/SPECFEM2D coupled numerical simulation of wavefields near excavation boundaries in underground mines. Computers and Geoscience (Submitted).

Other publications:

Yang, SL., Ding, X.P., Wang, X., Lin, L., 2013. Analysis of floor failure depth by using electric profiling method in longwall gangue backfill mining. Journal of Coal Science and Engineering (China) 19 (3), 282-289.

Zhong, SH., Wang, X., 2012. Study on environmental cost (EC) variation of coal enterprise. Disaster Advances 5 (4), 1571-1573.

Zhong, SH., Wang, X., 2011. Improvement and application of earned value analysis in coal project management. Procedia Engineering 26, 1983-1989.

Zhao, SS., Pan. WD., Wang. X., Liu, J.D., 2011. Prediction technology of coal and gas outburst in Xuandong coal mine. In: Proceeding of Advanced Materials Research, 255 3731-3734.